# Strategic Enhancement of Ionic and Electronic Conductivities in Organic Frameworks for Efficient Energy Storage Devices

विद्या वाचस्पति की

उपाधि की अपेक्षाओं की आंशिक पूर्ति में प्रस्तुत शोध प्रबंध

A thesis submitted in partial fulfilment of the requirements of the degree of Doctor of Philosophy

द्वारा / By

**दीपक पुंजाजी रासे/ Deepak Punjaji Rase**

पंजीकरण सं. / Registration No.: 20193671

शोध प्रबंध पर्यवेक्षक / Thesis Supervisor: Prof. R. Vaidhyanathan



भारतीय विज्ञान शिक्षा एवं अनुसंधान संस्थान पुणे

**INDIAN INSTITUTE OF SCIENCE EDUCATION AND RESEARCH PUNE**

**2024**

Dedicated to

My parents and family members

Prof. R. Vaidhyanathan
Professor
Department of Chemistry,
IISER Pune

# Certificate

I certify that the work incorporated in the thesis entitled "*Strategic Enhancement of Ionic and Electronic Conductivities in Organic Frameworks for Efficient Energy Storage Devices*" submitted by *Deepak Rase* has been carried out by the candidate at the Indian Institute of Science Education and Research (IISER), Pune, under my supervision. The work presented here or any part of it has not been included in any other thesis submitted previously for the award of any degree or diploma from any other University or Institution. I further certify that the above statements made by him/her in regard to his/her thesis are correct to the best of my knowledge.

**Date:** 10 July 2024

**Prof. R. Vaidhyanathan**

**Place:** Vancover, BC

(Research Supervisor)

# Declaration

Name of Student: Deepak Punjaji Rase

Reg. No.: 20193671

Thesis Supervisor(s): Prof. Ramanathan Vaidhyanathan

Department: Chemistry

Date of joining program: 01/08/2019

Date of Pre-Synopsis Seminar: 17/01/2024

Title of Thesis: **Strategic Enhancement of Ionic and Electronic Conductivities in Organic Frameworks for Efficient Energy Storage Devices.**

I declare that this written submission represents my idea in my own words and where others' ideas have been included; I have adequately cited and referenced the original sources. I also declare that I have adhered to all principles of academic honesty and integrity and have not misrepresented or fabricated or falsified any idea/data/fact/source in my submission. I understand that violation of the above will be cause for disciplinary action by the Institute and can also evoke penal action from the sources which have thus not been properly cited or from whom proper permission has not been taken when needed.

The work reported in this thesis is the original work done by me under the guidance of Dr./Prof. Ramanathan Vaidhyanathan.

**Date:** 10/07/2024          **Deepak Rase**

# Acknowledgment

I want to express my sincere appreciation to my PhD supervisor, Dr. Ramanathan Vaidhyanathan, for their unwavering support that has been crucial throughout this incredible journey of my life. I am incredibly grateful to Dr. Vaidhyanathan for giving me the freedom to pursue different projects without any hesitation. Additionally, I am thankful for the insightful discussions and invaluable scientific guidance that Dr. Vaidhyanathan has provided me with, along with numerous helpful suggestions. I am incredibly grateful for his unwavering dedication to research, as it has not only been a great source of inspiration for me, but has also significantly improved my skills in interpreting experimental results and generating innovative research ideas. I am incredibly grateful for the guidance and support he has provided me, as it has had a tremendous impact on my growth, both in my professional and personal life.

I want to express my deep gratitude to my Research Advisory Committee (RAC) members, Dr. Avinash Kumbhar and Dr. Musthafa Muhammed. Their extensive knowledge in electrochemistry and timely guidance have been invaluable in helping me navigate through various scientific challenges. I am incredibly grateful for their guidance, as it has been absolutely pivotal in helping us achieve this milestone.

I would like to express my sincere appreciation to my research collaborators, Prof. Stefan Kaskel from Technical University Dresden in Germany, Dr. C. P. Vinod, and Dr. T. G. Ajithkumar from NCL Pune, as well as their students, for their invaluable assistance and for granting me access to their research facilities. I am truly grateful for their support. I am incredibly grateful for their contributions, which have greatly enriched my projects and played a key role in their success.

I would like to express my sincere appreciation to the Indian Institute of Science Education and Research (IISER), Pune. The leadership of Prof. S. S. Bhagwat and former Director Prof. Jayant B. Udgaonkar has created an incredible research environment and provided exceptional research facilities. I am truly grateful for their support. I am extremely grateful for the financial support provided by IISER Pune. It has played a crucial role in supporting my academic pursuits, including the PhD fellowship and travel grants for international conferences. I cannot express enough how invaluable this support has been to me.

 Looking back on my academic journey, I am incredibly grateful to Dr. S. A. Salunke (SPPU Pune) for introducing me to experimental chemistry during my MSc days. Their guidance and passion for scientific research ignited my own love for it. I am incredibly grateful for her mentorship, as it not only laid the foundation for my career but also instilled in me the resilience to navigate through challenges.

I am extremely thankful of my family's unwavering support. All of this would not have been possible without them. My mother, grandfather, and sister have shown me unwavering love and support, and I am immensely appreciative of their sacrifices. I am so appreciative of their unwavering support throughout these trying times.

I am immensely appreciative of my path because it has given me priceless experiences and the bravery to take on any obstacles that I may encounter. It has also given me a lot more confidence. I am immensely appreciative of every uncertain moment I have encountered. Every one of them has helped me realise the value of tenacity and has ultimately brought me success. These encounters have motivated me to take on the upcoming task with uncompromising determination.

Deepak Rase

# List of Acronyms

| Materials related | Units |
|---|---|
| **POF**: Polymeric Organic Frameworks | °C : Degree Celsius |
| **MOF**: Metal Organic Framework | **mmol**: Milli moles |
| **COF**: Covalent Organic Frameworks | **µL**: Micro liter |
| *Instrument and measurement related* | **mL**: Milliliter |
| **FE-SEM**: Field Emission-Scanning Electron,<br><br>**HR-TEM:** High Resolution Transmission Electron Microscopy<br><br>**SAED:** Selected Area Electron Diffraction | **µm**: micrometer<br>**cm**: centimeter<br>**mm**: milimeter |
| **TGA**: Thermogravimetric analysis | **nm:** nanometer |
| **PXRD**: Powder X-Ray Diffraction<br>**SCXRD:** Single Crystal X-ray diffraction | **hrs**: hours |
| **AFM:** Atomic Force Microscopy | **min**: Minutes |
| **BET**: Brunauer Emmett Teller | **mol**: moles |
| **GCD**: Galvanostatic charge-discharge | **gm**: Gram |
| **EDLC**: Electrical Double Layer Capacitance | **Å** : Angstrom |
| **CE**: Counter Electrode | **Csp:** specific capacitance |
| **WE**: Working Electrode | **MHz**: Megahertz |

| | |
|---|---|
| **RE**: Reference Electrode | **V**: volts |
| **CV:** Cyclic Voltammogram | **mV:** Millivolts |
| *Chemicals related* | **M**: Molar |
| **DMF**: N, N-Dimethyl formamide<br>**DMSO:** Dimethyl sulfoxide<br>**NMP:** N-Methyl-2-pyrrolidone | **A**: Ampere<br>**mA**: Milliampere<br>**µA**: microampere |
| **ACN:** Acetonitrile | **F**: Farad |
| **MeOH:** Methanol | **mg**: Milligram |
| **EtOH:** Ethanol | **K**: Kelvin |
| **H$_2$SO$_4$:** Sulphuric Acid | **THF:** Tetrahydrofuran |
| **OH$^-$** : Hydroxide ion, **H$^+$:** Hydrogen ion**, Li$^+$:** Lithium ion**, Na$^+$:** Sodium ion, **K$^+$:** Potassium ion **Zn$^+$**: Zn ion. | **mA/g:** milliampere/gram |
| **NEt$_4^+$BF$_4^-$:** tetraethylammonium tetrafluoroborate<br>**EMIMBF$_4$:** 1-Ethyl-3-methylimidazolium tetrafluoroborate | **mAh/g:** milliampere hour/gram |

# Table of Contents

# Table of Contents

# Table of Contents

# Synopsis

In this thesis we explored innovative approaches to developing polymer-based solid-state electrolytes for flexible zinc-air batteries (ZABs) and supercapacitors. Initially, a Bakelite-type organic polymer featuring viologen, triazine, and phenolic groups is introduced. This polymer structure integrates free hydroxide ions, counterbalanced by cationic viologen centres, facilitating efficient hydroxide ion transport through weak interactions. Computational analyses and electrochemical methods confirm the structural features conducive to effective ion transport and reveal a substantial energy barrier for $Zn^{2+}$ penetration, mitigating crossover effects. The polymer, when coated on filter paper, exhibits impressive conductivity and power density, enabling practical applications in flexible batteries that demonstrate reliable performance.

Further advancements focus on enhancing hydroxide ion conductivity in viologen-Bakelite polymers by incorporating specific monomers. These polymers, integrated into rechargeable ZABs, show significantly improved conductivity and power density, with stable operation over extended periods. The study also successfully develops a flexible, rechargeable zinc-air battery with practical utility, showcasing the potential of these cationic polymers for high-performance energy storage.

Additionally, a novel approach involves incorporating conducting polypyrrole into a polyimide covalent organic framework (COF), resulting in a substantial increase in electronic conductivity. This composite material enables the assembly of a carbon-free quasi-solid-state capacitor with high energy and power densities. The synergy between the redox-active COF, polypyrrole, and organic electrolytes allows for a wide-voltage window, enhancing device performance and stability.

Finally, the research presents a sulphonated COF designed for solid-state lithium-ion conduction. By solidifying a customized liquid electrolyte within the COF channels, the charge-carrier concentration is amplified, and structural imperfections are rectified. This approach ensures efficient mobilization of lithium ions and improves the overall performance and stability of the material as a solid-state electrolyte, presenting a promising solution for enhancing safety and energy density in lithium-ion batteries.

# Chapter 1: Hydroxide Ion Conducting Viologen-Bakelite Organic Frameworks for Flexible Solid-State Zinc-Air Battery Applications

Polymer-based solid-state electrolytes represent a promising avenue for the development of safe,
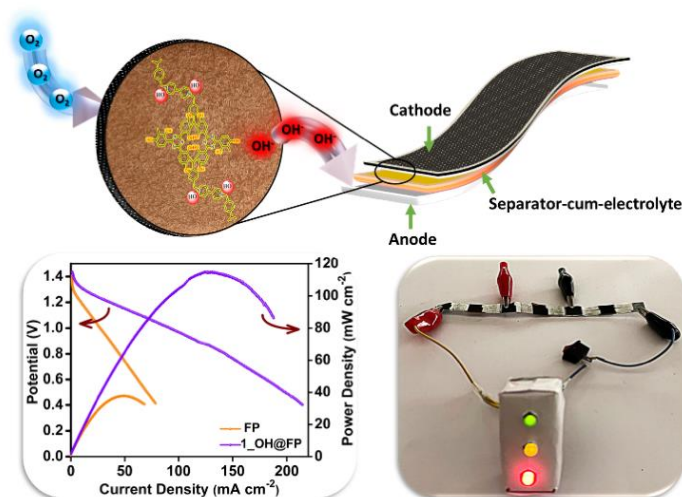


lightweight, and flexible batteries. In this study, we introduce a robust Bakelite-type organic polymer adorned with viologen, triazine, and phenolic groups. This flexible structure incorporates free hydroxide ions, counterbalanced by cationic viologen centers, within the polymeric framework. Activation of aromatic groups and heteroatoms under an applied potential initiate a push-pull mechanism, facilitating the transport of hydroxide ions through weak interactions like electrostatic, van der Waals, and hydrogen bonding. Computational analyses confirm the structural features conducive to efficient hydroxide ion transport. Notably, minimal KOH wetting is required to maintain a humid environment for Grotthuss-type transport. The resulting hydroxide ion conductivity reaches $1.4 \times 10^{-2}$ S cm$^{-1}$ at 80 °C and 95% RH, sustained for over 15 hours. Further advantage is achieved by coating the polymer as a thin solid-state separator-cum-electrolyte on readily available filter paper, exhibiting a conductivity of $4.5 \times 10^{-3}$ S cm$^{-1}$. Utilizing this composite in a zinc-air battery (ZAB) yields a remarkable maximum power density of 115 mW cm$^{-2}$ and a high specific capacitance of 435 mA h g$^{-1}$, marking it among the best-performing polymer electrolyte-based batteries reported. Additionally, a flexible battery with this polymer-coated paper demonstrates an open-circuit voltage (OCV) of 1.44 V, successfully powering a demo traffic signal with three batteries in series. Through electrochemical methods and molecular dynamics simulations, we ascertain the diffusion coefficient of OH− ions, underscoring the efficiency of hydroxide ion transport through the complex multifunctional backbone of the polymer. Importantly, calculations reveal a substantial energy barrier for Zn$^{2+}$ penetration, mitigating undesirable crossover effects. These findings underscore the potential of readily accessible C–C-linked cationic polymers as solid-state electrolytes for ZABs and other anion-conducting membranes.

## Chapter 2: Designed Enhancement in Hydroxide Ion Conductivity of Viologen-Bakelite Organic Frameworks for Flexible Rechargeable Zinc-Air Battery
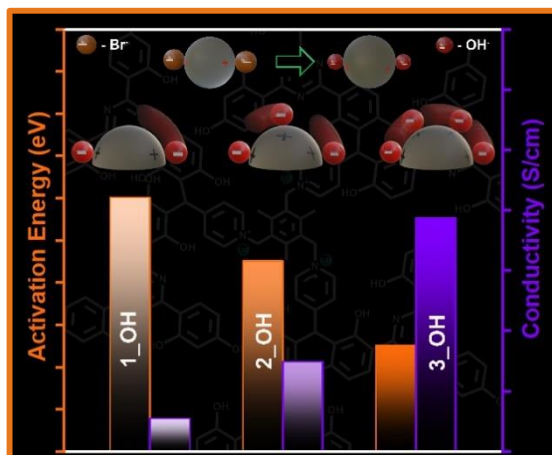


Quasi-solid-state rechargeable zinc-air batteries (ZABs) offer promising prospects for portable clean energy, owing to their high energy and power density, safety features, and cost-effectiveness. Unlike traditional ZABs with alkaline aqueous electrolytes, polymer or gel-based electrolytes can effectively mitigate zinc dissolution and dendrite formation, enhancing battery performance. However, gel electrolytes often suffer from capacity fade due to solvent loss, limiting their ability to deliver high-energy, high-power ZABs. Therefore, the development of polymers with both high hydroxide-ion conductivity and chemical durability is crucial. In this study, we introduce robust cationic polymers with controlled mobile hydroxide ions as solid-state hydroxide ion transporters. Through the strategic incorporation of "by-design" monomers, we increase viologen-hydroxide-ion concentration, resulting in polymers with enhanced ionic conductivity. Notably, polymers prepared with monomers containing four hydroxide ions exhibit superior conductivity compared to those with three hydroxide ions. The conductivity improvement from $7.30 \times 10^{-4}$ S cm$^{-1}$ to $2.96 \times 10^{-3}$ S cm$^{-1}$ at 30 °C and 95% RH demonstrates the effectiveness of this approach.

We further apply these polymers in rechargeable ZABs (RZABs), utilizing 3_OH@PVA (polyvinyl alcohol) as the electrolyte membrane and Pt/C+RuO2 catalyst. The resulting RZABs demonstrate a significant increase in power density compared to those with a PVA interlayer, reaching 158 mW cm-2. Remarkably, the device exhibits minimal initial charge-discharge voltage gap and maintains stable operation over extended periods, highlighting its robust performance. Additionally, we successfully develop a flexible and rechargeable zinc-air battery (F-RZAB) with a maximum power density of 79 mW cm-2, showcasing the practical utilité of our cationic Viologen-Bakelite polymer-based electrolyte. Overall, this study represents a significant advancement in hydroxide-ion conducting solid-state electrolyte development, particularly in the realm of flexible secondary ZABs, offering promising prospects for future energy storage applications.

## Chapter 3 : Incorporating Conducting Polypyrrole into a Polyimide COF for Carbon-Free Ultra-High Energy Supercapacitor
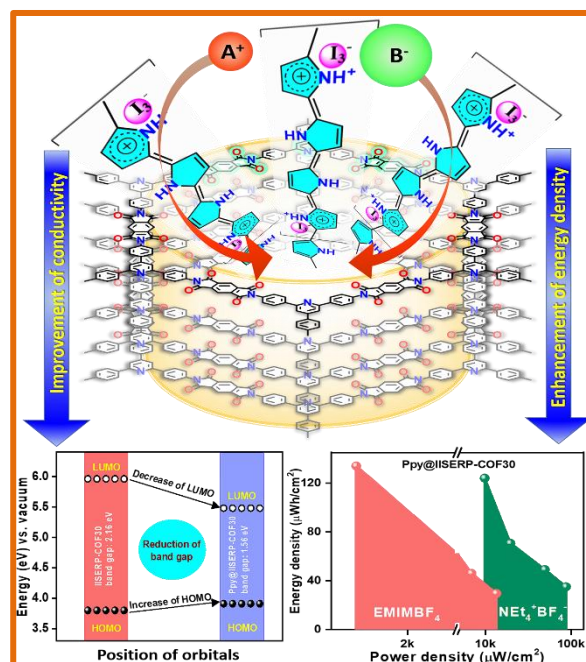


Redox-active covalent organic frameworks (COFs) are adept at storing charges but suffer from limited electronic conductivity. Typically, their capacitive behaviour relies on storing H+ ions in an acidic electrolyte, confined within a narrow voltage window of 0–1 V. While widening this window could enhance energy and power density, it risks compromising COF stability. However, COFs possess large pores that allow for the storage of bulky, polarizable ions, enabling higher energy density under wider voltage ranges. In this study, we present a COF–electrode–electrolyte system operating at elevated voltage regimes without the need for conducting carbon or redox-active oxides. By synthesizing conducting polypyrrole (Ppy) chains within a polyimide COF, we achieve a remarkable increase in electronic conductivity, approximately 10,000-fold. This composite enables the assembly of a carbon-free quasi-solid-state capacitor, exhibiting significant pseudo-capacitance (358 mF cm$^{-2}$ at 1 mA cm$^{-2}$) in an aqueous gel electrolyte.

The synergy between the redox-active polyimide COF, polypyrrole, and organic electrolytes allows for a wide-voltage window spanning from 0 to 2.5 V, resulting in high energy (145 $\mu$Wh cm$^{-2}$) and power densities (4509 $\mu$W cm$^{-2}$). By amalgamating polyimide-COF and polypyrrole into a single material, we minimize charge and mass transport resistances, further enhancing device performance. Both computational modelling and experimental validation demonstrate that even a partial translation of intrinsic electronics from modules/monomers to the COF imparts excellent electrochemical activity. These findings unveil COF-confined polymers as promising carbon-free energy storage materials, offering potential solutions to the challenges faced in conventional energy storage systems.

## Chapter 4: Sulphonated Covalent Organic Framework For Solid State Li Ion Conduction
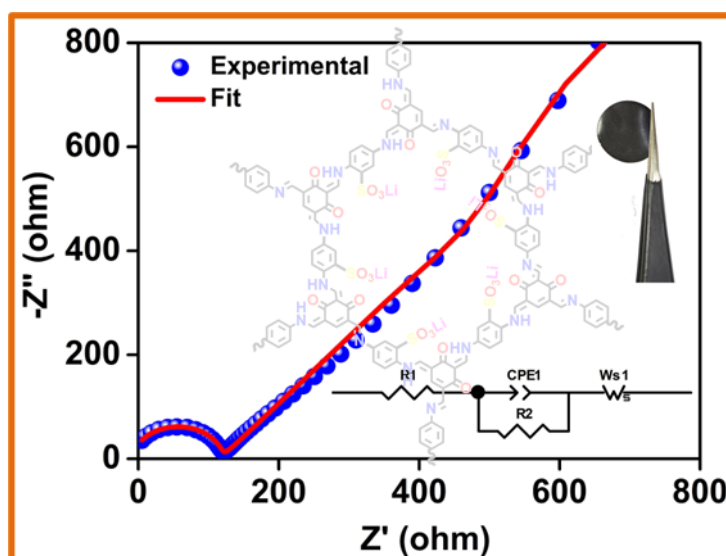


Solid-state electrolytes possessing high $Li^+$ conductivity, flexibility, durability, and stability present an appealing avenue for enhancing safety and energy density. However, achieving these stringent criteria poses challenges for current solid polymeric or ceramic electrolyte technologies.

A promising solution is introduced here: an electrolyte-mediated single-$Li^+$-conductive covalent organic framework (COF), representing a distinct class of high-quality solid-state $Li^+$ conductors. Through in situ solidification of a customized liquid electrolyte, the charge-carrier concentration within the COF channels is amplified. This process also separates $Li^+$ cations from both COF walls and molecular chains while rectifying defects through crystal soldering. This means that the unique approach of solidifying a liquid electrolyte directly within the COF structure enhances the number of lithium ions available for conduction, ensures these ions are efficiently mobilized within the COF without being hindered by interactions with the framework or each other, and simultaneously repairs any structural imperfections in the COF, thereby improving the overall performance and stability of the material as a solid-state electrolyte.

# Introduction

In the coming decades, there will be a significant surge in global energy demand driven by population growth, the emergence of new electrical devices, and industrial expansion. However, existing energy generation systems will prove insufficient to meet this escalating demand due to environmental pollution and depletion of fossil fuel resources. One primary concern is the combustion of carbon-based fossil fuels in vehicles, which has been a primary source of greenhouse gas emissions for decades, contributing significantly to adverse effects on the global climate.[1-3] To tackle these challenges, significant efforts have been directed towards exploring and advancing new energy storage and conversion technologies.[4] (Figure I.1)
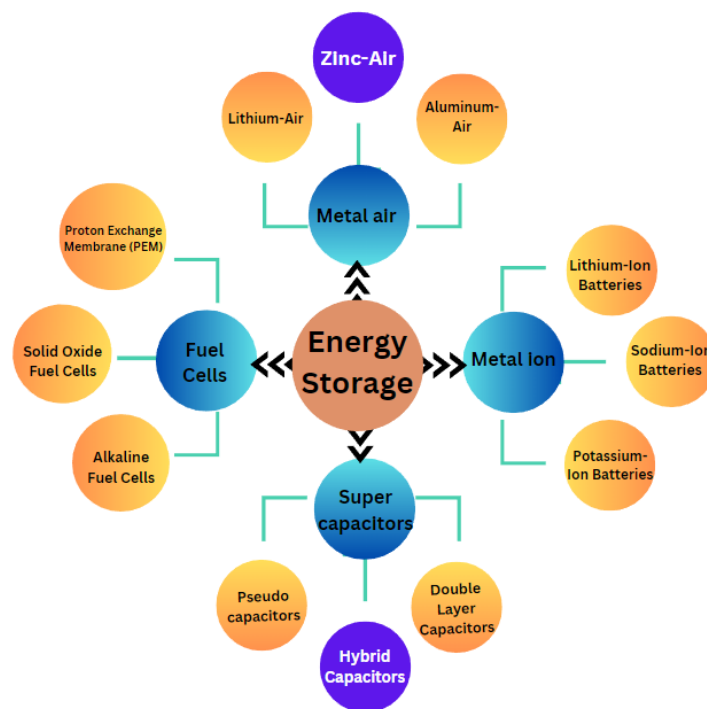


**Figure I.1:** Flow chart showing all types of energy storage devices of modern era.

Electrical energy storage with rechargeable capability is indispensable in modern life, finding extensive use in various applications such as smartphones, tablets, portable computers, digital cameras, and electric vehicles. At the circuit level of electronic devices, energy is typically stored in either batteries or capacitors. In both cases, stored energy generates an electric potential that drives a unidirectional flow of electrons during charging or discharging, thereby producing an electric current that powers connected electrical devices within a circuit.

The classification of capacitors and batteries is based on two fundamental parameters: energy density and power density. Energy density quantifies the amount of energy stored in a given volume or weight, while power density describes the rate at which energy is stored or discharged from the device. Batteries

store a significant amount of electrical energy electrochemically, offering high energy density. They convert chemical energy into electrical energy when needed, delivering a steady electrical charge to power a device. In contrast, conventional capacitors exhibit high power density and can release a burst of energy rapidly. They store electrostatic energy on their surfaces under an applied electric field.[5] (Figure I.2)
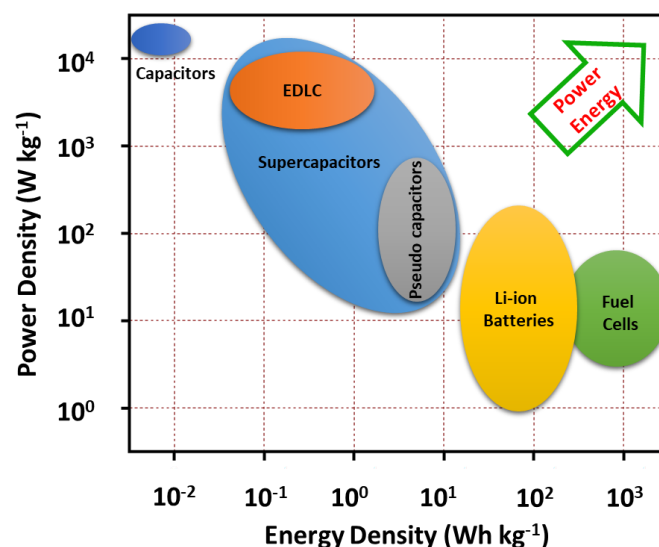


**Figure I.2:** The Ragone plot showing the position of battery and capacitor in terms of energy density and power density.

Both batteries and capacitors play essential roles in powering devices, with capacitors providing rapid energy supply and batteries offering sustained energy over a more extended period. Although the components configuring batteries and capacitors share similarities in electrodes and electrolytes, their working principles differ significantly.

Given the demand for renewable and environmentally friendly energy sources, significant research endeavours have recently concentrated on leveraging porous materials for electrochemical energy storage and conversion. There has been a notable emphasis on designing and creating materials based on polymeric organic frameworks (POFs) or covalent organic frameworks (COFs) for various electrochemical applications. These include developing electrodes and membranes for fuel cells, supercapacitors, and batteries.

## I.1 Porous Materials in Energy Storage

Porous materials have become a prominent field of study in recent decades, providing a flexible pore structure, easily implemented design methods, and a wide range of uses. This innovation has completely transformed the process of creating porous materials that are designed for specific targets. Porous materials offer numerous advantages.[6-8] They exhibit an high surface area and a variety of pore diameters, ranging from extremely small to very large, which may be precisely regulated

via synthetic methods. Moreover, these permeable networks demonstrate exceptional resistance to heat and chemicals, depending on their strong chemical bonds and structural arrangement.[9-15] One of the key attributes of porous materials is their ability to host various guest molecules within their tunable pores, enabling a wide array of applications spanning gas capture/storage and purification,[16-22] catalysis,[23-27] optics,[28-41] energy-related processes,[42-51] and even biological applications.[52] This versatility underscores the importance of porous materials in addressing contemporary challenges across multiple fields.
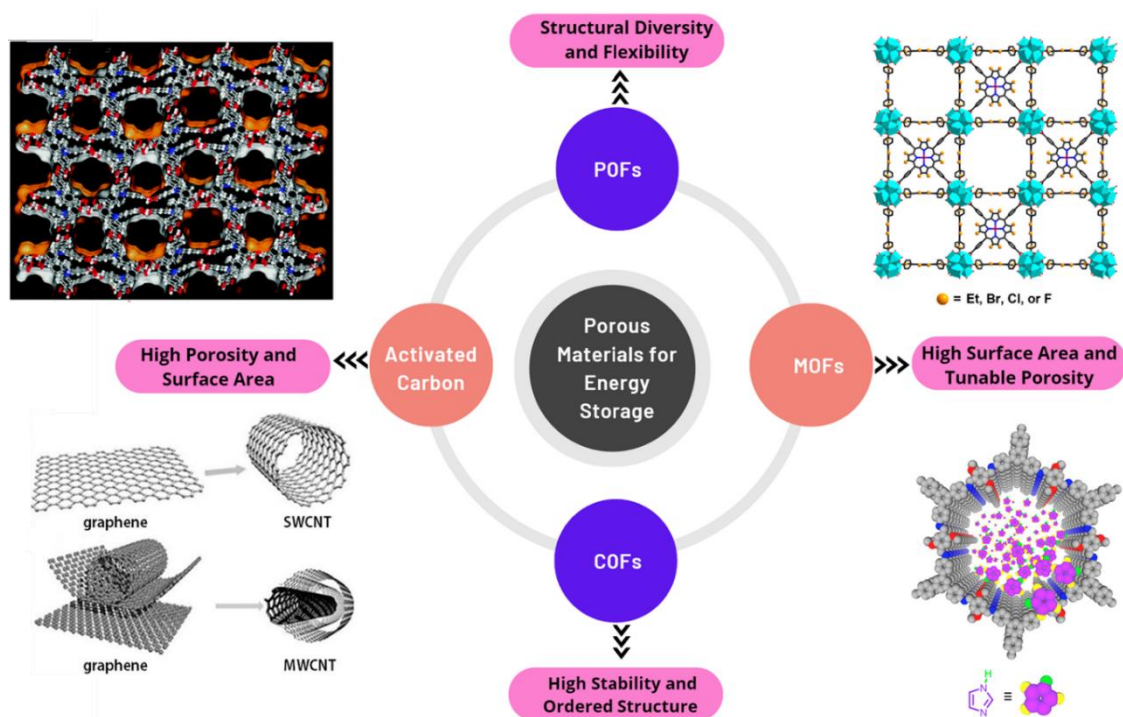


**Figure I.3:** Schematic showing porous materials in energy storage.

Porous materials can be broadly categorized into two different classes: those with inorganic backbones and those with pure organic backbones. The former category includes well-known materials such as zeolites, porous metal oxides/nitrides, porous silica, and Metal-Organic Frameworks (MOFs), [53-66] which are hybrid materials consisting of both inorganic and organic components. Conversely, organic porous materials encompass Polymeric Organic Frameworks (POFs),[11, 16, 22] Covalent Organic Frameworks (COFs),[23, 24] Hydrogen-Bonded Frameworks (HOFs),[67-69] porous organic cages,[18, 22] and more.

Porous materials play a crucial role in energy storage applications due to their high surface area and tunable properties. Each of these materials has unique properties such as high surface area and tunable porosity (MOFs), high stability and ordered structure (COFs), structural diversity and flexibility (POFs) and high porosity and surface area (activated carbon) that make them suitable for specific applications.[50, 70] (Figure I.3)

## I.1.1 Polymeric Organic Frameworks (POFs):

### I.1.1.1 Bakelite-type Chemistry:
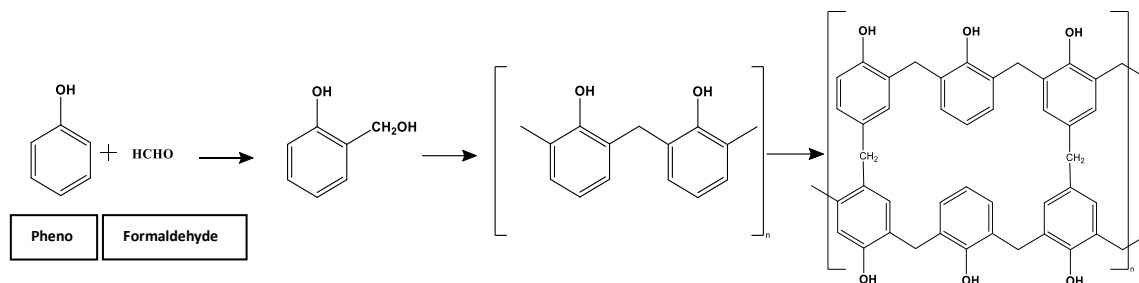


**Figure I.4:** Synthetic procedure of Bakelite polymer by condensation reaction.

Bakelite, a polymer formed from the condensation reaction of phenol and formaldehyde monomers, stands as a significant player among commercially produced polymers, finding ubiquitous utility in our daily lives.[70] Renowned for its hardness, stability, and chemical resistance, Bakelite boasts a diverse array of applications, ranging from the commonplace switches to intricate machinery and equipment. (Figure I.4)
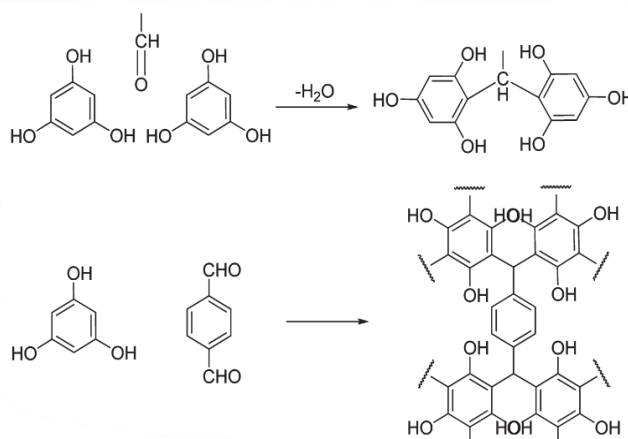


**Figure I.5:** Polymerization reaction between carbonyl group and phloroglucinol (1,3,5-trihydroxybenzene), and fully condensed structure between dialdehyde and phloroglucinol.

A novel series of microporous polymeric organic frameworks (POFs) is introduced, synthesized via solvothermal methods using phloroglucinol (1,3,5-trihydroxybenzene) and various benzaldehyde derivatives by Kanatzidis and co-workers in the year 2011.[71] These POFs, fabricated through Bakelite-type chemistry without the need of the catalysts, manifest as uniform, spherical particles with exceptional surface areas reaching up to 917 $m^2$ $g^{-1}$. Notably, the micropores exhibit remarkable uniformity in size, resembling the gas adsorption isotherms observed in crystalline microporous zeolites, despite the amorphous nature of these materials. (Figure I.5)

**1.1.1.2 Viologen chemistry:**

Viologens, organic compounds represented by the formula $(C_5H_4NR)_2^{n+}$, exhibit diverse properties and applications. These compounds, akin to 4,4'-bipyridyl, are characterized by modified pyridyl groups in some instances.[72] The formation of viologens involves the alkylation of basic nitrogen centres within 4,4'-bipyridyl, resulting in the quaternization process:
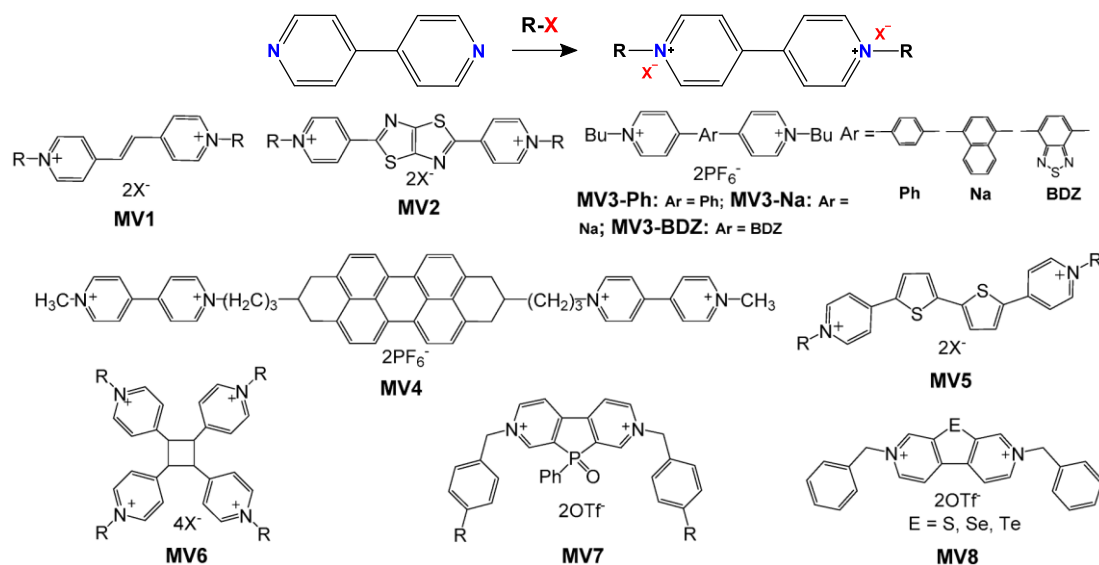


**Figure I.6:** Structures of various viologen derivatives with a bridging group or a spacer between two pyridyl groups.

This alkylation, a form of quaternization, is commonly achieved using small alkyl halides like methyl chloride or methyl bromide. Notably, when employing such alkylating agents, water-soluble viologen salts are often obtained. Researchers have explored a wide range of alkyl substituents, including methyl, long-chain alkyl, and benzyl derivatives, each offering distinct properties and potential applications.[73] (Figure I.6)

In 2022, our laboratory successfully synthesized three cationic viologen-functionalized polymers (IISERP-POF9, POF10, and POF11) using a Bakelite chemistry approach without the need for metal catalysts. These polymers displayed outstanding stability in both organic solvents and aqueous solutions, along with impressive thermal resistance. Their polymeric microporous frameworks demonstrated efficient capturing abilities for oxo-anion pollutants such as $CrO^{2-}$ and $MnO^{4-}$ from water, even at low concentrations and with rapidity.[74] (Figure I.7)

Out of the three polymers, IISERP-POF11 shown a higher ability to capture ions. The improvement can be ascribed to the reduced dimensions of the core resorcinol group in contrast to the phloroglucinol group found in the other two polymers. As a result, the empty spaces within IISERP-POF11 were less

crowded, which allowed for a more precise accommodation of oxo-anions and led to a greater capacity for catching them.
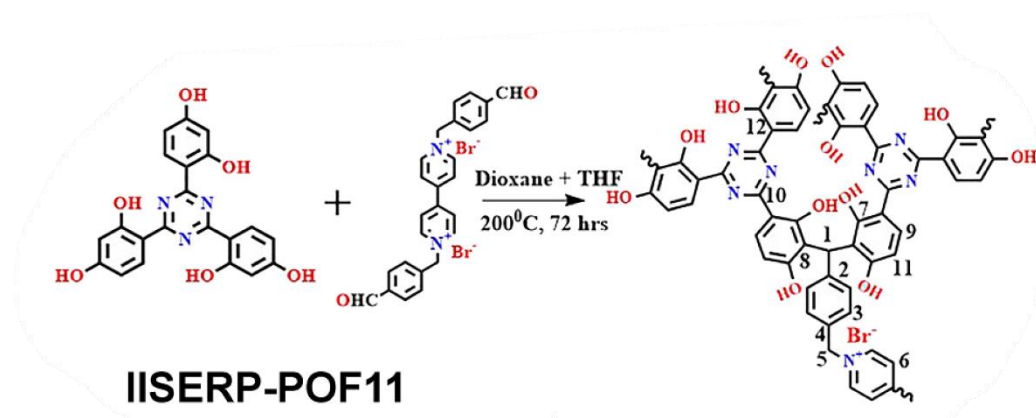


Figure I.7: Synthetic procedure of IISER-POF11.

Leveraging this advantageous property, we selected POF11 for the capture of OH⁻ ions, with the intention of employing it as a solid-state hydroxide ion conducting polymer in Zinc-air batteries.

## I.1.2 Zinc Air Battery:

Zinc–air batteries (ZABs) are being recognised as extremely potential power sources for personal and portable electronic devices, and are receiving significant interest in research. The electrolyte is a critical element that significantly influences the entire performance of ZABs, including important characteristics such as energy density, rechargeability, and operating voltage.

The functioning of rechargeable Zn–air batteries involve four key components: a Zn metal anode, electrolyte, separator, and air cathode.[75-77] During charging and discharging cycles, the Zn metal anode undergoes oxidation/reduction reactions. The electrolyte facilitates ion/electron transfer, while the separator prevents short circuits by isolating the cathode and anode. The air cathode, equipped with OER and ORR electrocatalysts, promotes oxygen reduction and evolution reactions.[78-81]

During the process of discharge, oxygen from the air electrode is reduced to hydroxide ions through the oxygen reduction reaction (ORR) at a point where three phases interact. Simultaneously, the Zn anode undergoes a reaction with hydroxide ions to produce $Zn(OH)_4^{2-}$, which then breaks down into ZnO.[82, 83]

$$\text{Zinc electrode: } Zn + 4OH^- \rightarrow Zn(OH)_4^{2-} + 2e^- \tag{1}$$

$$Zn(OH)_4^{2-} \rightarrow ZnO + H_2O + 2OH^- \tag{2}$$

$$\text{Air electrode: } O_2 + 4e^- + 2H_2O \rightarrow 4OH^- \tag{3}$$

$$\text{Overall reaction: } 2Zn + O_2 \rightarrow 2ZnO \tag{4}$$
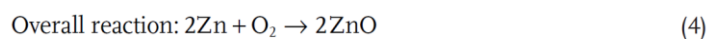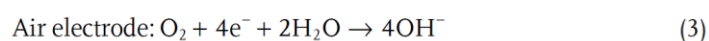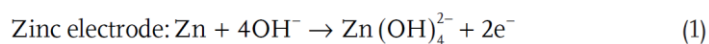
During the charging process, electric energy is accumulated by means of the oxygen evolution reaction (OER) taking place at the interface between the air electrode and the electrolyte. Simultaneously, zinc is deposited on the surface of the cathode by a reduction reaction involving ZnO.

$$\text{Zinc electrode: } ZnO + H_2O + 2OH^- \rightarrow Zn(OH)_4^{2-} \quad \quad (5)$$

$$Zn(OH)_4^{2-} + 2e^- \rightarrow Zn + 4OH^- \quad \quad (6)$$

$$\text{Air electrode: } 4OH^- \rightarrow O_2 + 4e^- + 2H_2O \quad \quad (7)$$

$$\text{Overall reaction: } 2ZnO \rightarrow 2Zn + O_2 \quad \quad (8)$$
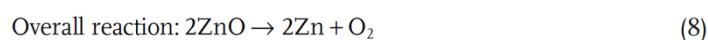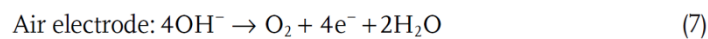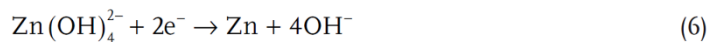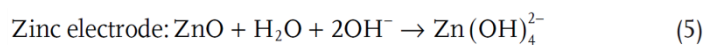
Both discharge and charge processes involve reactions with the theoretical voltage value of 1.66 V, yet they are kinetically sluggish. Efficient bifunctional electrocatalysts are essential to speed up the OER and ORR reactions and improve battery performance.[84-88] (Figure I.8)
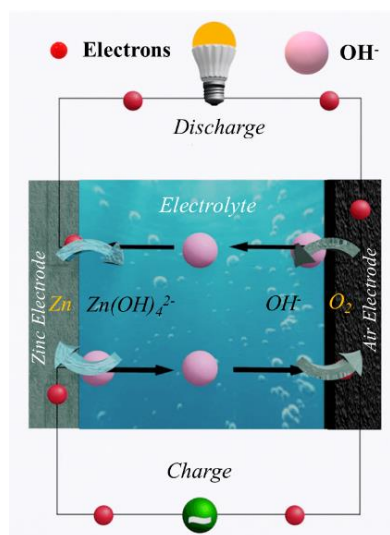


**Figure I.8:** Schematic showing working of rechargeable Zinc-air battery.

Zinc-air batteries are categorised into two varieties based on their electrolyte: aqueous zinc-air batteries with aqueous solution electrolytes and flexible all-solid zinc-air batteries with polymer-gel electrolytes. Presently, zinc-based batteries frequently employ alkaline electrolytes because of their cost-effectiveness and superior ionic conductivity, which guarantees the stability of the zinc electrode.[89, 90] However, these electrolytes are vulnerable to environmental factors such as $CO_2$ and humidity. In particular, $CO_2$ can cause the formation of $K_2CO_3$ in the electrolyte, leading to detrimental effects on the air electrode's integrity.[91] To function effectively in diverse environmental conditions, zinc-air batteries need to address issues such as electrolyte evaporation and absorption of water from the surroundings. Electrolyte evaporation can result in battery expansion, while water absorption affects the transfer of $OH^-$ ions.[92-94] (Figure I.9)

**I.1.2.1 Quasi Solid-State Zinc Air Batteries:**
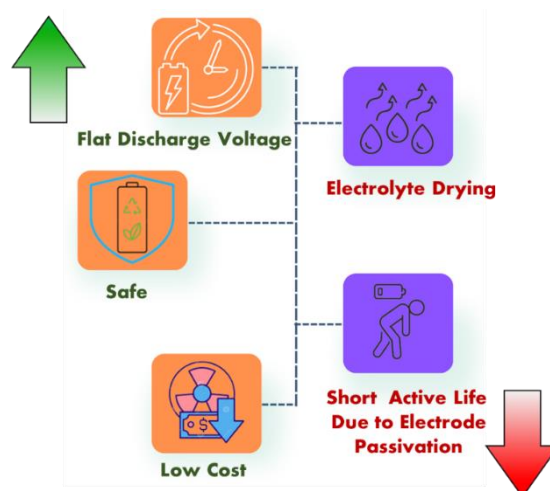


**Figure I.9:** Schematic showing advantages and challenges while working on ZABs.

In contrast to liquid electrolytes, Solid-state electrolytes (SSEs) have gained attention as a promising solution to address drawbacks in traditional liquid electrolytes, particularly in new battery chemistries. In the realm of zinc-based battery systems, solid-state ZIBs offer distinct advantages over aqueous systems, simplifying internal structures and enhancing safety. These SSEs are broadly categorized into solid-polymer materials and quasi-solid gel materials.[95] Solid-polymer materials mitigate issues like Zn corrosion and cathode dissolution while ensuring safety and dendrite inhibition, although improvements in ionic conductivity are still needed. Quasi-solid gel materials, composed of polymer matrices and salts/solvents, offer efficient ion migration channels and favourable mechanical properties, making them suitable for wearable and biomedical applications. However, challenges remain in improving ionic conductivities, electrochemical stabilities, mechanical strength, and interfacial resistance. Polymer-based electrolytes offer distinct advantages for ZABs. These include minimal electrolyte
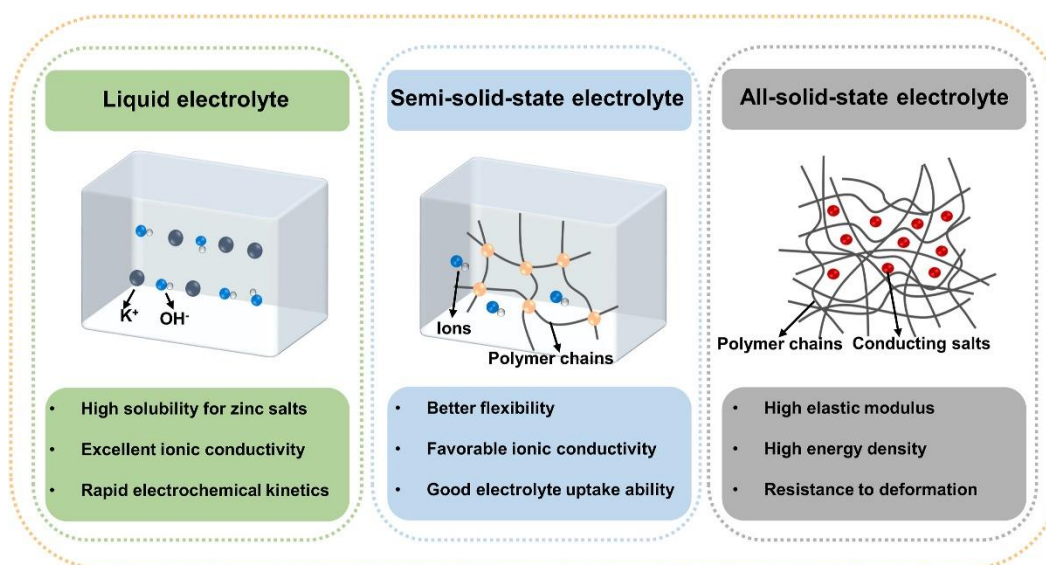


**Figure I.10:** The main types and merits of various electrolytes in ZABs.

leakage, stabilization of the three-phase interface, and suppression of dendrite formation. Such characteristics contribute significantly to enhancing the efficiency and reliability of ZABs, making polymer-based electrolytes a preferred choice in their development (Figure I.10).[96]

## I.1.2.2 Mechanism of ion transport

Understanding the mechanisms underlying OH⁻ transport in solid electrolytes is crucial for enhancing ion conductivity and overall battery performance. A dusty fluid model (DFM), initially developed for proton transport, has been widely utilized to study proton exchange membranes like Nafion. This model enables predictions regarding changes in alkaline membrane conductivity and other membrane
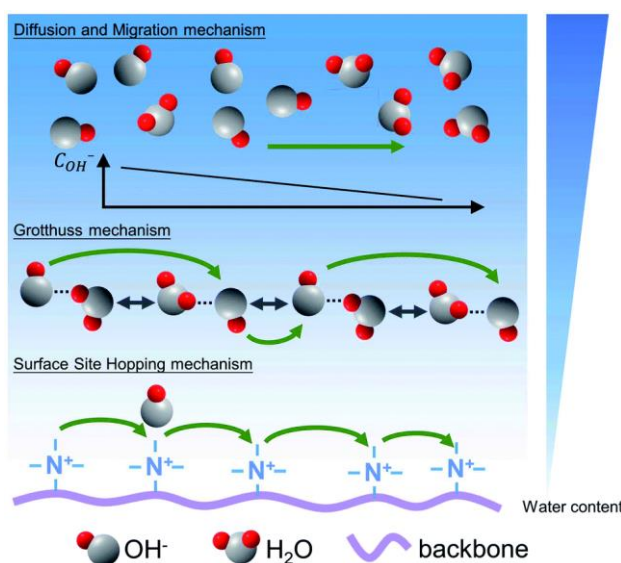


**Figure I.11:** Possible transport mechanisms for the hydroxyl anion in aqueous basic solid electrolytes.

properties with varying relative humidity, offering insights into alkali ions' conduction processes. Broadly, OH⁻ transport in aqueous basic solid electrolytes can be categorized into three forms: 1) Surface site hopping mechanism 2) Grotthuss mechanism 3) Diffusion and migration mechanism. (Figure I.11)

Each mechanism plays a distinct role in facilitating OH⁻ transport within the solid electrolyte, contributing to its overall conductivity. Understanding these mechanisms aids in devising strategies to optimize ion transport and enhance battery performance effectively.[97]

## I.1.2.3 Previous reports on flexible solid-state zinc-air batteries

Zhang and his co-workers created an alkaline gel called PVAA-cellulose solid-state electrolyte (SSE) by physically connecting ultrafine fibres of cellulose with PAA and PVA molecules through cross-linking. This gel is composed of a combination of materials that have small holes caused by the attraction of hydrogen atoms, resulting in an intricate structure that improves the absorption of alkaline

solutions and allows for the movement of ions over several paths. The PVAA-Cellulose solid-state electrolyte (SSE) demonstrates superior performance due to its high ionic conductivity of 123 mS cm$^{-1}$, efficient retention of water, and increased dimensional stability. In addition, the PVAA-Cellulose material exhibits enhanced mechanical strength as a result of the interconnected network generated by the entangled fibres and polymers. This leads to a tensile strength of 0.87 MPa and an elongation at break of 818%.
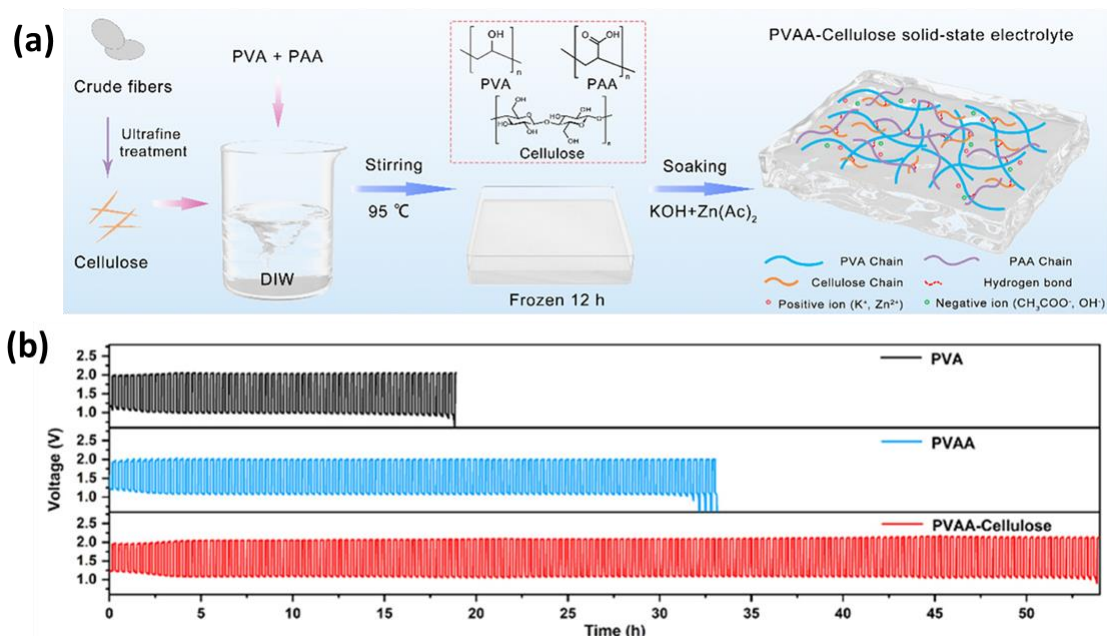


**Figure I.12:** (a) Synthetic procedure of the PVAA-Cellulose SSEs. (b) Galvanostatic discharge–charge cycling curves of the button-type solid-state ZABs using PVA, PVAA, and PVAA-Cellulose SSEs at 3 mA cm$^{-2}$.

The PVAA-Cellulose solid-state electrolyte (SSE) when included into a Zn-air battery (ZAB) allows for a power density of 74 mW cm$^{-2}$, a specific capacity of 724 mAh g$_{Zn}^{-1}$, and an OCV of 1.42 V. PVAA-Cellulose has the remarkable capability to inhibit the growth of dendrites and oxidised zinc species on the zinc electrode. This promotes the creation of stable ion transport pathways and guarantees outstanding reversibility between metallic Zn and Zn(OH)$_4^{2-}$. The utilisation of PVAA-Cellulose SSE in the ZAB leads to an extended stability in charge-discharge cycle, lasting for a duration of 54 hours. Furthermore, the flexible solid-state ZABs with PVAA-cellulose SSEs exhibit remarkable flexibility, signifying substantial potential for practical use.[98] (Figure I.12)

Zhong and his co-workers invented a new type of polymer electrolyte that uses quaternary ammonium hydroxides. This electrolyte is being used for the first time in flexible zinc-air batteries. The ionic conductor used in this study was tetraethylammonium hydroxide (TEAOH), whereas the polymer host in the electrolyte was poly(vinyl alcohol) (PVA). This combination demonstrated remarkable water retention properties, guaranteeing a good duration of storage and operational longevity of the flexible zinc-air batteries.
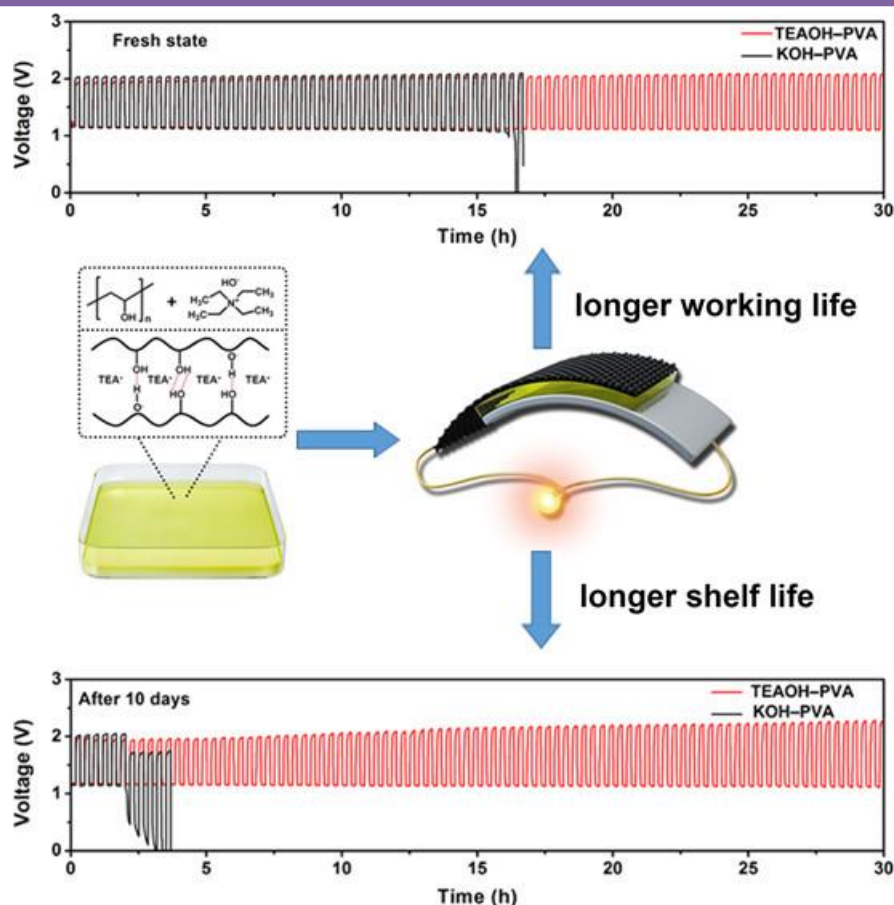
**Figure I.13:** TEAOH-PVA electrolyte exhibiting superior shelf-life stability and longevity of zinc-air battery systems.

The integration of the TEAOH-PVA electrolyte into zinc-air batteries (ZABs) resulted in an extension of the discharge time to 25 hours and a cycling stability of over 30 hours, surpassing the performance of the KOH-PVA electrolyte. The TEAOH-PVA electrolyte demonstrated a consistent ionic conductivity of around 30 mS cm$^{-1}$, in contrast to the variable performance of the KOH-PVA electrolyte. Furthermore, the TEAOH-PVA electrolyte maintained almost comparable discharge performance and cycling life even after being stored for 2 weeks when used in ZABs. In contrast, the KOH-PVA electrolyte experienced a considerable decline in performance after only 6 days of storage.[99] Consequently, the TEAOH-PVA electrolyte exhibited substantially superior shelf life compared to the KOH-PVA electrolyte for ZABs, highlighting its potential for enhancing the stability and longevity of zinc-air battery systems. (Figure I.13)

Lojoiu and co-workers proposed a method to avoid instability in the benzylic position and promote the separation of phases. They achieved this by attaching methyl diallyl ammonium groups to a poly(phenylene oxide) (PPO) backbone using a spacer that is six carbons long (PPO-6CH$_2$-Q). The ion exchange capacity (IEC) of each anion exchange membrane (AEM) was regulated by manipulating the proportion between DAPCl and PPO-6CH$_2$-Q. The use of atomic force microscopy (AFM) allowed for the observation of distinct phase separation in the PPO-6CH$_2$-3x membrane, resulting in very efficient

OH− ion conductivity at normal room temperature. Phase separation improves OH− ion conductivity by forming distinct hydrophilic channels within the membrane, which provide efficient pathways for ion transport, enhance water retention, and maintain structural integrity. These membranes demonstrated outstanding alkaline stability in 1 M KOH at 60°C, exhibiting only 8% drop in ionic conductivity after a 360-hour stability test.

In addition, in order to tackle the inability of attaching N-spirocyclic quaternary ammonium cationic groups to polymer backbone structures, the UV-curing approach was used to attach the N, N-diallyl piperidinium chloride (DAPCl) monomer to the adapted PPO polymer backbone. Studies have demonstrated that incorporating multi-cation side chains into ion exchange membranes improves their chemical stability and OH− conductivity. A zinc-silver flow battery, specifically using PPO-6CH$_2$-3x, obtained a maximum power density of 153 mW/cm$^2$. Additionally, the PPO-6CH$_2$-2x membrane has great potential for use in alkaline batteries, namely rechargeable ZSAFB, due to its low zincate ion crossover and high-power density of 137 mW/cm$^2$.[100, 101] (Figure I.14)
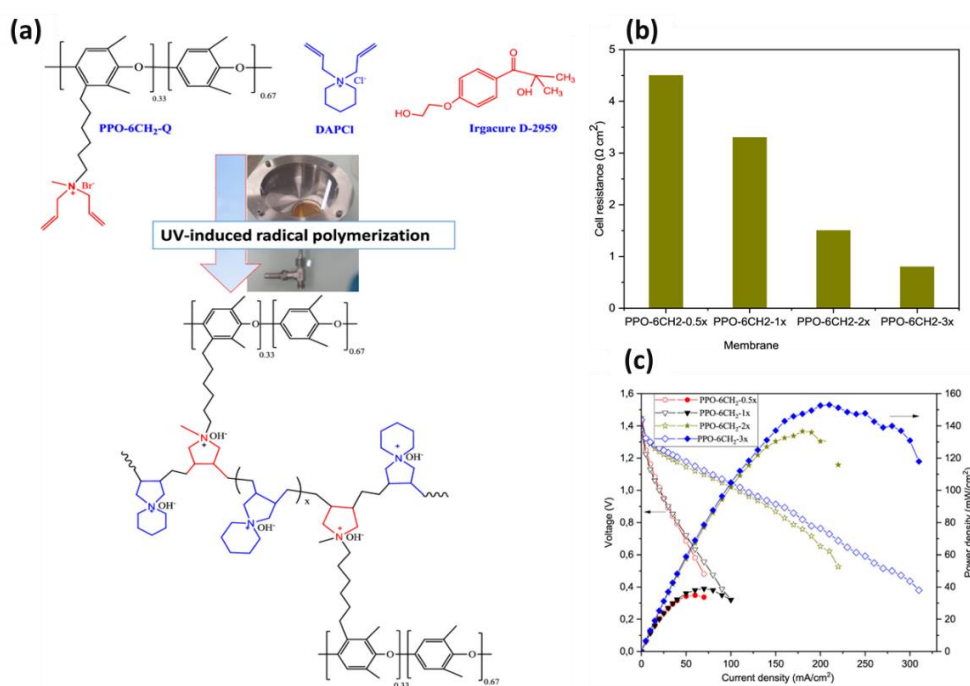


**Figure I.14:** (a) Schematic diagram of the AEM fabrication protocol. (b )Zn slurry-airflow battery (using the prepared AEMs) resistance (c) and power density measured at RT, with flow rates of the Zn slurry and synthetic air of 160 and 100 mL/min, respectively.

The preservation of alkaline stability is a notable obstacle for the practical use of anion exchange membranes (AEMs) in diverse electrochemical applications, such as alkaline batteries. The breakdown of ionomers can be attributed to the chemical instability of the fixed functional groups, polymer backbone, and/or spacer. The rapid deterioration of most polymer-based anion exchange membranes (AEMs) in alkaline environments at high temperatures is primarily attributed to cationic degradation.

A very recent work where Panda and co-worker introduced a viologen-functionalized cationic covalent organic framework (vTAPA) incorporating chloride ions as counter anions to maintain overall framework charge balance. This COF demonstrated remarkable alkaline stability when exposed to various concentrations of alkaline solution (ranging from 1 M to 12 M) for 72 hours at 25 °C. The exceptional stability of vTAPA prompted further exploration by replacing chloride ions with hydroxide ions using mild tertiary ammonium salts (specifically tetramethyl-, tetraethyl-, and tetrabutyl-ammonium hydroxide), resulting in derivatives named Methyl@vTAPA, Ethyl@vTAPA, and
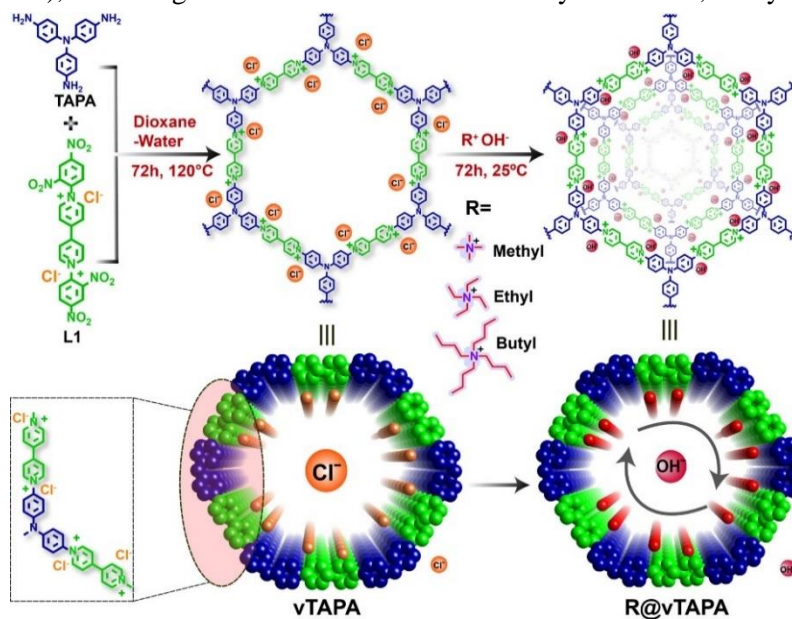


**Figure I.15:** Schematic representation of the synthesis of vTAPA COF followed by synthesis of R@vTAPA.

Butyl@vTAPA, respectively. The inclusion of hydroxide ions within these exchanged COF structures facilitated hydroxide ion conduction throughout the network. Notably, Butyl@vTAPA exhibited significantly enhanced hydroxide ion conductivity, reaching $1.05 \times 10^{-4}$ S cm$^{-1}$ at 90 °C under 98% relative humidity (RH). This conductivity level represents an approximately 1000-fold improvement compared to the pristine vTAPA COF.[102] (Figure I.15)

**I.1.2.4 Glimpses of our work: (Chapter 1 and Chapter 2)**

Based on the findings from the aforementioned studies aiming to develop a robust, chemically, and thermally stable polymer material with high ionic conductivity for application in Quasi Solid-State Zinc-Air Batteries (QZABs), it is apparent that achieving all these properties in a single material presents a challenge. Therefore, to address this gap, we endeavoured to synthesize a series of C-C bonded polymers by combining two distinct chemistries: Viologen and Bakelite. Our goal was to create a polymer that exhibits high hydroxide ion conductivity, chemical and thermal robustness, and flexibility, suitable for serving as the electrolyte in QZABs.

In chapter 1 we used recently synthesized viologen-bakelite polymers which demonstrated excellent ion exchange abilities for oxo-anion pollutants such as $CrO^{2-}$ and $MnO^{4-}$ from water[74] and here are the few highlights of the work:

- Novel Cationic Polymer Electrolyte: The study introduces a unique Bakelite-type organic polymer covalently decorated with viologen, triazine, and phenolic moieties, offering a novel approach to solid-state electrolyte design.

- Hydroxide Ion Transport Mechanism: The flexible structure of the polymer incorporates cationic viologen centres and counter-balancing free hydroxide ions, enabling efficient hydroxide ion transport through weak electrostatic, hydrogen-bond, and van der Waals interactions.

- High Hydroxide Ion Conductivity: The polymer electrolyte exhibits high $OH^-$ ion conductivity, reaching a value of $1.4 \times 10^{-2}$ S cm$^{-1}$ at 80 °C and 95% RH, offering promising performance for practical battery applications.

- Enhanced Battery Performance: The polymer-coated filter paper composite demonstrates improved conductivity and is successfully utilized as a solid-state separator-cum-electrolyte in zinc–air batteries, achieving a high power density of 115 mW cm$^{-2}$ and high specific capacitance of 435 mAh g$^{-1}$.

- Computational Insights: Computational modelling clarifies how heteroatoms contribute to the movement of electrons throughout the polymer structure, which helps in the transportation of hydroxide ions. Molecular dynamics simulations confirm favourable hydroxide ion diffusion and high barriers against undesirable zinc ion penetration, highlighting the polymer's potential as a solid-state electrolyte.

Later we synthesized two novel polymers with a systematic improvement in cationic sites analogous to the polymer presented in chapter 1. Here are the few highlights of the work presented in chapter 2:

- The improvement in conductivity obtained upon incrementing the number of hydroxide ions in each monomeric unit resulted in the following values: 2.70 x 10$^{-4}$ S cm$^{-1}$ (30 °C), 7.30 x 10$^{-4}$ S cm$^{-1}$ (30 °C), and 2.96 x 10$^{-3}$ S cm$^{-1}$ (30 °C) for polymers 1_OH, 2_OH, and 3_OH, respectively.

- The best hydroxide ion-conducting polymer, i.e., 3_OH, showed excellent ionic conductivity cycling stability and reproducibility over multiple batches.

- A self-standing membrane was prepared using PVA and 3_OH, which exhibited excellent flexibility and retained hydroxide ion conductivity comparable to the pelletized form of polymer.

- The membrane was utilized for a quasi-solid-state rechargeable zinc-air battery, delivering a power density of 158 mW cm$^{-2}$ with a high specific capacity of 742 mAh g$^{-1}$. The battery showed remarkable cycling stability for up to 67 hours when 3_OH@PVA was used as an electrolyte cum separator. The F-RZAB device delivered an open-circuit voltage (OCV) value of 1.38 V in an open-air atmosphere, with a highest power density of 79 mW cm$^{-2}$.

## I.1.3 Covalent Organic Frameworks (COFs)

Covalent organic frameworks (COFs) are a type of porous organic materials that are known for their crystalline structure. COFs, initially introduced by Cote et al., are polymers that are generated by rigid cross-linking monomers that are symmetrically well-defined.[103] These individual molecules can join together using stiff linear connectors or other elements that provide connections, leading to organised polymeric formations with clearly defined openings. The arrangement of the cross-linking nodes and linkers dictates whether the COFs adopt a two-dimensional (2D) or three-dimensional (3D) network structure. (Figure I.16)
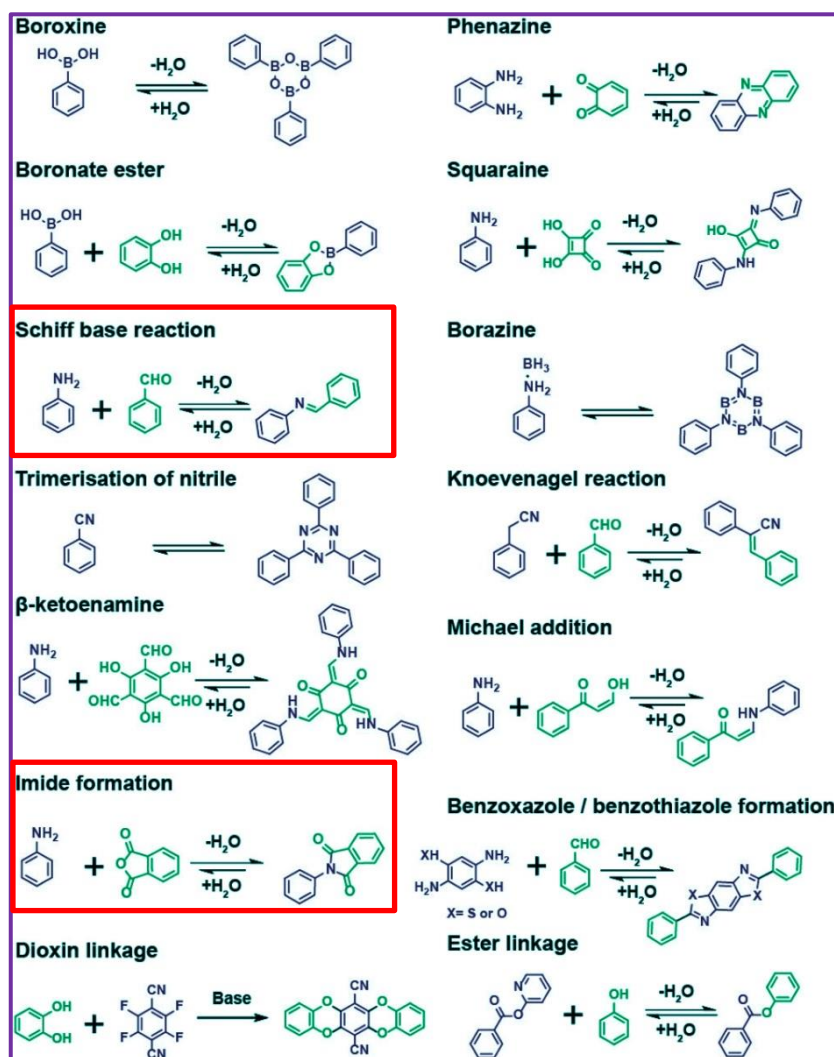


**Figure I.16:** Covalent linkages for COF formation. Highlighted boxes show chemistries used our work.

In 2D COFs, interlayer $\pi$-$\pi$ interactions contribute to network stabilization and crystallization, while 3D COFs are connected in three dimensions, often containing tetrahedral linkers and various topologies like gra, bnn, and ctn.[104] The crystalline nature, ordered porous structure, and high surface area of COFs make them highly valuable for a range of applications in porous materials research. Researchers employ diverse chemistries to develop novel COFs with
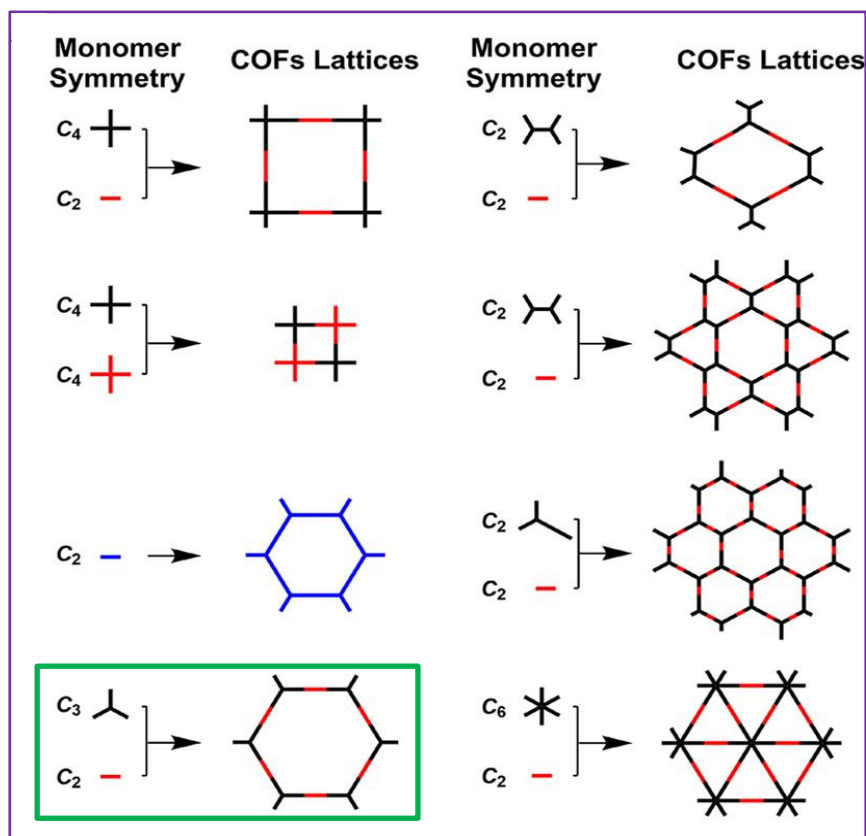
**Figure I.17:** A diagram showing the different 2D and 3D topologies of the COFs constructed from the particular choice of symmetry of linkers.

different functionalities, topologies, and stabilities. One common method involves Schiff's base formation between aldehydes and amines, leveraging the availability of a vast library of aldehydes and amines in the literature.[105] (Figure I.17)

### I.1.3.1 Advantages of Covalent Organic Frameworks (COFs)

- **Modular Design Flexibility:** COFs offer unmatched design flexibility compared to zeolites and metal-organic frameworks (MOFs). Their modular structures enable precise control over composition, shape, pore size, and surface functionality, facilitating customization for specific applications. The incorporation of functional groups enhances redox, photo, and catalytic activities, as well as metal-specific binding sites.

- **Exceptional Chemical Stability:** COFs are characterized by strong covalent bonds, ensuring excellent chemical stability even in extreme environments. Unlike MOFs, COFs are less susceptible to framework collapse or degradation, maintaining structural integrity under harsh conditions.

- **High Surface Area:** COFs possess high surface areas due to longer building units and well-defined pore structures. This feature enhances gas adsorption capacity, making COFs efficient

for gas and charge storage applications. Their ordered structure ensures facile access to pre-coded binding centres or reactive sites, making them excellent support materials or composites.

- **Adjustable Pore Size:** Tunable pore sizes in COFs enable selective adsorption of ions, molecules, or gases, ideal for separation processes and charge storage applications. By adjusting monomer size, geometry, and self-organization capability, pore size can be tailored for specific guest molecules.
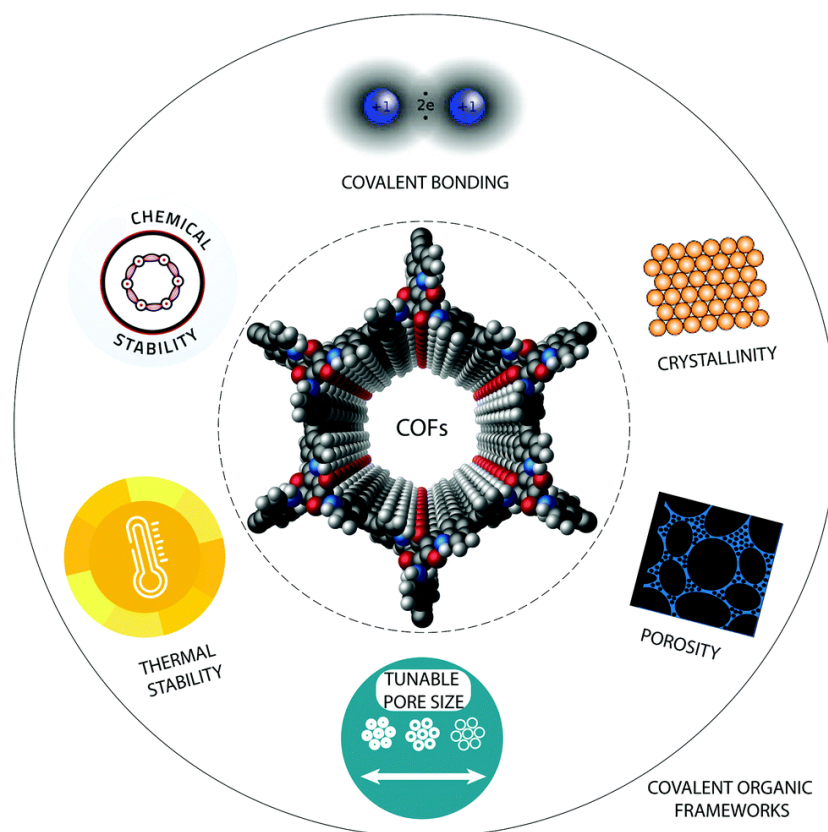


**Figure I.18:** Schematic showing advantages of Covalent Organic Frameworks (COFs).

- **Tunable Functionality:** COFs offer versatile tunable functionality, allowing the incorporation of various functional groups during synthesis or post-synthetic modifications. Conjugated functional groups or nanoparticles can alter electrical and optical properties, while redox-active groups facilitate electron transfer reactions, expanding applications in electronics, optoelectronics, and energy storage.

- **Superior Thermal and Chemical Stability:** COFs exhibit excellent thermal and chemical stability due to their covalent linkages, enabling them to withstand elevated temperatures and harsh chemical environments without structural degradation. This robustness makes COFs suitable for catalysis, gas storage, and separation processes.

- **Environmentally Friendly and Non-Toxic:** COFs are environmentally friendly and non-toxic, primarily composed of organic building units. Free from toxic metals or harmful substances, COFs are biocompatible and safe for various applications, including drug delivery, water purification, and electronics, contributing to green technology initiatives (Figure I.18).

## I.1.3.2 Strategies to design the COFs

### 1. Polyimide based COFs

Polyimide (PI) is a type of polymer that can be identified by the inclusion of cyclic imide groups in its molecular composition. PI is well-known for its remarkable stability, demonstrating great thermal stability, chemical resistance, radiation resistance, and superior mechanical characteristics. The exceptional stability of PI greatly expands its possible uses, especially in advanced sectors like aircraft, electronics, and optics.[106]

Polymers can be categorised into three distinct categories according to the chemical composition of their repeating units: aliphatic, semi-aromatic, and aromatic polymers. Aromatic PIs, characterised by structural units that are coupled with nitrogen heterocycles and benzene, have higher stability in comparison to aliphatic or semi-aromatic PIs. The material properties of PI are significantly affected by the characteristics of the monomers employed. The stiffness and adaptability of the resulting PI can be evaluated by analysing the bond length and bond angle parameters of the connecting groups. In addition, PI is created through the alternating presence of electron donors (amine chains) and electron acceptors (anhydride chains), resulting in either intermolecular or intramolecular transfer of charge between the two monomers. (Figure I.19) This phenomenon impacts various properties of PI, including colour, photoconductivity, electrical conductivity, and melting point. As new monomers are introduced or novel polymerization methods are adopted, the development space for PI continues to expand, promising further advancements in its applications and properties.



phthalic anhydride     aniline     2-phenylisoindoline-1,3-dione
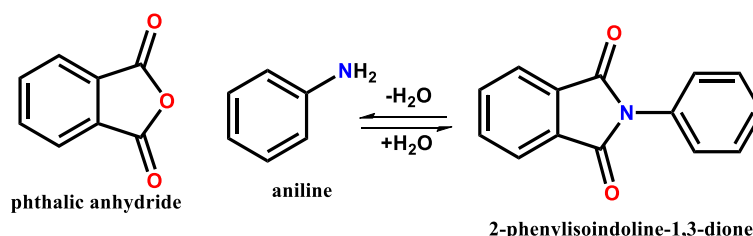
**Figure I.19:** Imide bond formation chemistry.

A method to develop novel COFs with big pores involves the process of imidization, where extended aromatic dianhydride and triamine building units are combined. The condensation reaction between phthalic anhydride and aniline results in the elimination of water and the formation of N-phenylphthalimide, an imide product.[107] Expanding on this chemical reaction, phthalic anhydride is transformed into pyromellitic dianhydride (PMDA), while aniline is transformed into triangular building units of different sizes, such as tris(4-aminophenyl)amine (TAPA, 7 Å), 1,3,5-tris(4-aminophenyl)benzene (TAPB, 9 Å), or 1,3,5-tris[4-amino(1,1-biphenyl-4-yl)]benzene (TABPB, 13 Å). The measurements are taken from the centre of the molecule to the nitrogen atom in the amine group. (Figure I.19)

Illustrated in Figure I.20 is the reversible covalent bonds formation, conferring self-healing and error-correction capabilities during crystallization to avoid the formation of disordered amorphous kinetic products. The tube-sealing method, although executed under more extreme conditions, typically necessitates precursor molecules with good solubility in the solvent to yield high-quality crystals. While crystals obtained through this method boast exceptional crystallinity, the lengthy reaction period and limited scalability restrict its widespread use.[108]

In recent years, researchers have focused on exploring low-cost and scalable synthesis methods for PI-COFs. These methods include solvothermal synthesis,[52, 109-117] condensation polymerization synthesis,[118] high-temperature solid-state synthesis,[119] interfacial synthesis, and ionothermal
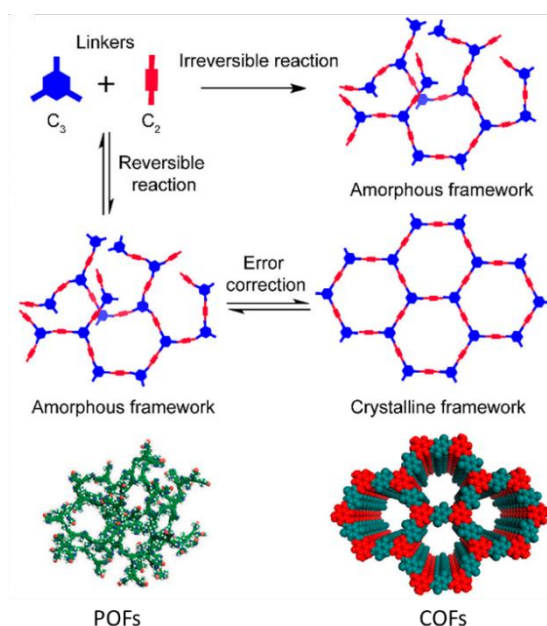


**Figure I.20:** Schematic representation of crystalline and amorphous covalent organic framework formation by reversible and irreversible reactions.

synthesis.[118, 120] These efforts aim to overcome the limitations of traditional synthesis approaches and facilitate the large-scale production of PI-COFs for various applications.

The interaction between PMDA and TAPA results in the formation of a two-dimensional crystalline covalent organic framework (COF) with hexagonal pores measuring 33 Å. This COF is referred to as PI-COF-1. Replacing TAPA with bigger amines leads to the formation of distinct 2D crystalline COFs with larger hexagonal pores. When TAPB is used, the resulting product is PI-COF-2 with pore size of 37 Å. On the other hand, when TABPB is used, the resulting product is PI-COF-3 with pore size of 53 Å. Connecting the linear and triangular building blocks through imidization is anticipated to result in two-dimensional structures that are based on the boron nitride net (BNN).[109, 121] (Figure I.21)
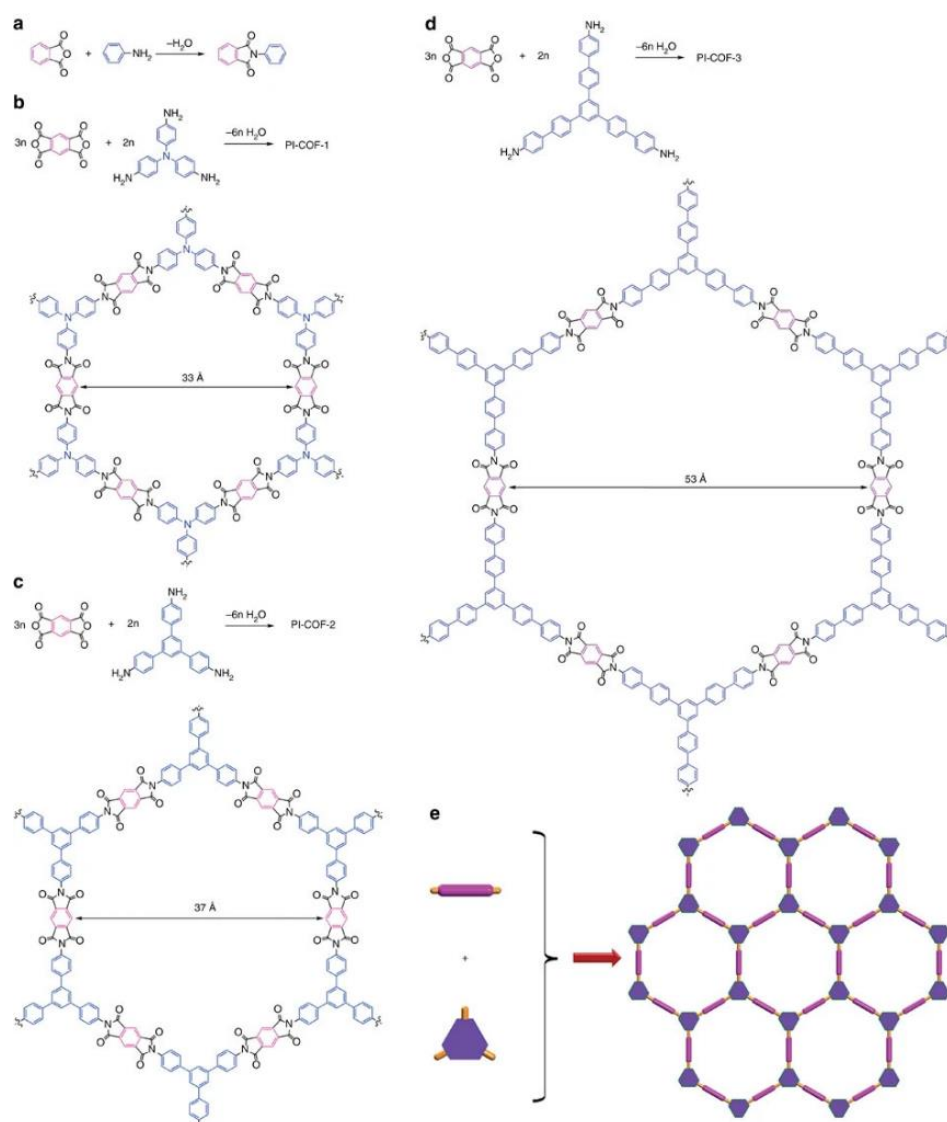
**Figure I.21:** (a) The chemical reaction between phthalic anhydride and aniline produces a monomer called N-phenylphthalimide. (b) The process of combining the extended dianhydride, pyromellitic dianhydride (PMDA), and the extended triamine tris(4-aminophenyl)amine (TAPA) results in the formation of a 2-dimensional crystalline polyimide COF with a pore size of 33 Å. This material is referred to as PI-COF-1. (C) The combination of PMDA and the extended triamine 1,3,5-tris(4-aminophenyl)benzene (TAPB) undergoes condensation to produce a two-dimensional crystalline polyimide covalent organic framework (COF) with a pore size of 37 Å. This COF is referred to as PI-COF-2. (d) The combination of PMDA and the elongated triamine 1,3,5-tris[4-amino(1,1-biphenyl-4-yl)]benzene (TABPB) results in the formation of a two-dimensional crystalline polyimide covalent organic framework (COF) with a pore size measuring 53 Å. This particular COF is referred to as PI-COF-3. (e) The condensation of linear and triangular construction blocks results in the formation of a two-dimensional structure that is based on the boron nitride net (BNN).

## 2. Designing Schiff bond-based COFs

The choice of Schiff base chemistry for constructing COFs has garnered significant attention from materials researchers due to several advantageous features. Firstly, the preparation process is versatile, allowing for variable reaction conditions and easy scale-up, even at room temperature. Secondly, there

is a vast library of molecular precursors available, offering diversity in the selection of functional groups. Thirdly, Schiff-based COFs exhibit easy dispersity in solution, enabling deposition on substrates and facile fabrication of self-standing films. Additionally, these COFs have demonstrated potential in physicochemical and electrochemical applications, boasting substantial stability even under harsh conditions and applied potentials.

The reversible polarizability and flexibility of Schiff bonds provide anchimeric assistance to other framework moieties and guest molecules without structural degradation of the COFs. Moreover, the free lone pair on Schiff-bond nitrogen serves as a basic site for interacting with Lewis acidic entities, facilitating adherence to metallic substrates—an advantageous feature for device fabrication. Despite a compromise on the crystallinity of 2D-COFs, the versatile advantages of Schiff links provide dynamic organization, enabling the exploitation of their properties for futuristic applications. Schiff-bonded COFs are particularly suitable for electrochemical applications due to their facile electrode or electrolyte fabrication with easily scalable materials, making them an ideal choice for such purposes.

Crystalline COFs offer precise control over functional groups' positions, aiding in predictable characterization through diffraction methods and establishing a structure-property relationship. This structural uniformity is advantageous for various applications, including energy conversion and storage. With their composition primarily comprising lightweight components, COFs exhibit impressive gravimetric capabilities for storing both guest molecules and energy. (Figure I.22)



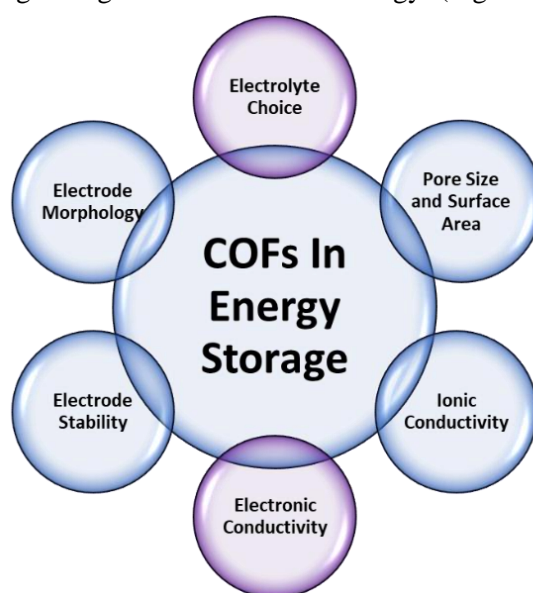**Figure I.22:** COFs properties which play crucial role in energy storage.

- **Pore Size and Surface Area:** The energy density of COF-based energy storage systems depends on their specific surface area and pore size. Tailoring pore sizes allows for optimal charge storage, with larger surface areas facilitating higher energy densities by accommodating more ions at the electrode-electrolyte interface.

- **Electrolyte Choice:** The choice of electrolyte has a substantial effect on the energy density. Ionic liquids and high-concentration aqueous electrolytes increase the range of voltages that COF-based supercapacitors can withstand, hence improving their energy storage capacity.

- **Electrode Thickness:** The energy density of COF electrodes is directly influenced by their thickness, as thicker electrodes have a higher capacity for charge storage. Nevertheless, it is essential to strike a balance between electrode thickness and energy density in order to sustain sufficient power density.

- **Faradaic and Non-Faradaic Processes:** Supercapacitors based on covalent organic frameworks (COFs) can function through both Faradaic processes involving redox reactions and non-Faradaic processes involving electrostatic adsorption. Although Faradaic processes have the advantage of increased energy efficiency, they may provide challenges in terms of cyclic stability.

- **Ionic Conductivity:** Efficient charge and ion transport within COF electrodes are crucial for high energy efficiency. Improving COF materials' ionic conductivity enhances overall efficiency.

- **Electrode Stability:** COFs exhibit strong covalent connections, contributing to their stability. Strategies such as structural optimization aim to enhance electrode stability, critical for maintaining efficiency over multiple charge-discharge cycles.

- **Rate Capability:** COFs have diverse rate capabilities, which affect their capacity to rapidly charge or discharge. Swift response rates are crucial for applications that necessitate prompt energy supply, such as regenerative braking in electric automobiles.

- **Electrode Morphology:** COF electrode morphology and structure influence response rates. Hierarchical structures or nanoscale engineering can improve charge transport and response rates.

- **Electrolyte Compatibility:** The choice of electrolyte affects response rates, with certain electrolytes offering faster ion mobility for rapid charge and discharge processes.

Covalent organic frameworks (COFs) are polymers that can be designed for charge storage applications due to their organised pores and crystalline structure. Supercapacitors play a crucial role in the

advancement of hybrid energy devices. Combining these frameworks with a large surface area in the assembly of the capacitor can help in the advancement of strong and durable solid-state supercapacitors.

## I.1.4 COFs as Supercapacitor Electrodes

Supercapacitors, also known as ultra-capacitors, are a specialized type of capacitor designed to store electrical charge at much higher levels than ordinary capacitors, while operating within lower voltage limits. They are capable of undergoing frequent charge-discharge cycles even at high currents, serving as a bridge between electrolytic capacitors and rechargeable batteries, thus slightly increasing energy density. In recent years, supercapacitors have attracted considerable research interest because of their superior power density, economical maintenance, broad thermal operating range, and prolonged cycle life in comparison to electrolytic capacitors.

These energy storage devices have a dielectric liquid working as an electrolyte, together with two electrodes possessing large surface areas that are separated by an insulating substance, facilitating the transfer of ions. The electric double layer created at the interface between the electrode and electrolyte stores electrical charge by separating easily dissociable electrolytes. This interface commonly employs carbonaceous materials with a large surface area, which allows for high capacitance outputs. While charging, the charge that builds up at the interface between the electrodes counteracts the potential bias created on the surface of the electrode. A greater surface area accessible to the electrolyte results in higher capacitance values.

Supercapacitors can be categorized on the basis of their charge storage mechanism as electric double-layer capacitors (EDLC)[122] and pseudo-capacitors. EDLCs exhibit static charge storage solely at the electrode-electrolyte interface using high surface area electrodes. Conversely, pseudo-capacitance arises from the redox behaviour of the electrolytes at the electrode surface, with near-surface faradaic reactions primarily contributing to high capacitance.

### I.1.4.1 Electric Double-Layer Capacitors (EDLCs):

Electric double layers are formed at the interface between the electrode and electrolyte in electrostatic double-layer capacitors (EDLCs), allowing for the storage of electrical energy. Upon the application of a voltage, ions from the electrolyte gather on the surface of the porous electrodes, resulting in the formation of a double layer. The mechanism depicted in Figures I.23 (a & b) results in unique curve properties observed in cyclic voltammetry (CV) and galvanostatic charge-discharge (GCD) measurements, which are caused by the physical adsorption and desorption of ions on the electrode surfaces.[123] The technology behind EDLCs facilitates rapid and reversible charge-discharge cycles, resulting in a high power density. EDLCs are renowned for their extended cycle life, low internal resistance, and exceptional performance even at high current densities. They are utilised in situations

that necessitate rapid energy transfer, such as regenerative braking systems in hybrid vehicles and power backup systems.[5]

## I.1.4.2 Pseudo-capacitors:
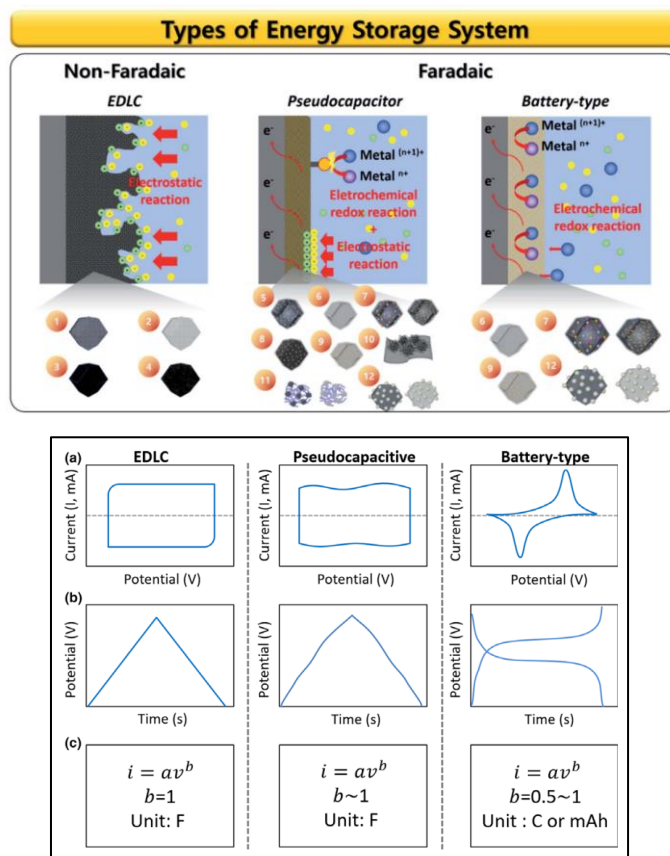


**Figure I.23:** Schematic diagram comparing the fundamental charge storage mechanisms of electrode materials in batteries and supercapacitors. (a-c) Criterion for distinguishing EDLC, pseudocapacitive, and battery materials.

Pseudo-capacitors, also referred to as redox supercapacitors, store energy by undergoing redox reactions at or the nearest electrode surface. In contrast to EDLCs, pseudo capacitors involve faradaic charge storage, where reversible redox reactions takes place between the electrode and the electrolyte. This results in specific curve characteristics in galvanostatic charge-discharge (GCD) and cyclic voltammetry (CV) profiles (Figure I.23). This redox reaction allows pseudo capacitors to store more energy per unit volume compared to EDLCs. By combining the fast charging-discharging capabilities of EDLCs with the higher energy storage capacity of batteries, pseudo capacitors strike a balance between power density and energy density. This makes them well-suited for applications requiring both high-energy storage and rapid power delivery.[5]

## I.1.4.3 Previous reports on hybridization of COFs with other materials for supercapacitor applications

While COFs offer promising benefits for energy storage, overcoming limitations such as low electronic conductivity and specific capacitance is crucial. Addressing these challenges will enable the full exploration of COFs in supercapacitor applications, with ongoing advancements aiming to enhance their performance and applicability. Their properties can be enhanced through synergistic hybridization with other materials for energy storage applications. Hybridization with carbon nanomaterials, organic conducting polymers, and transition metal-based nanomaterials can address this challenge.

**I.1.4.3.1 Hybridization using Carbon Nanomaterials**: The incorporation of carbon nanomaterials such as activated carbon (AC), graphene, carbon nanotubes (CNT), and CNF through hybridization provides a means to overcome the issues of low electrical conductivity and electrochemical stability in MOFs and COFs. Lei et al. investigated the development of a film made of electrically conductive DAAQ-BTA COF on 3D graphene (COFDAAQ-BTA-3DG), which allows for convenient utilisation of electrochemically active DAAQ components in comparison to 2D COF powder. The resulting COFDAAQ-BTA-3DG electrode exhibited a specific capacitance of 31.7 mF cm$^{-2}$ at 0.5 mA cm$^{-2}$ with a retention of 7.6 mF cm$^{-2}$ after 2000 cycles. Wei et al. synthesized TpPa-COF/single-walled CNTs (SWCNTs) through in situ polymerization, achieving an enhanced specific capacitance of 153 F g$^{-1}$ at 0.5 A g$^{-1}$ due to SWCNTs' high electrical conductivity. Additionally, COFs were hybridized with CNF via the in situ solid-state inclusion method to enhance electrical conductivity. These hybrid materials, characterized by p-p interactions between DqTp and CNF, delivered a high areal capacitance of 464 mF cm$^{-2}$.[124] (Figure I.24)
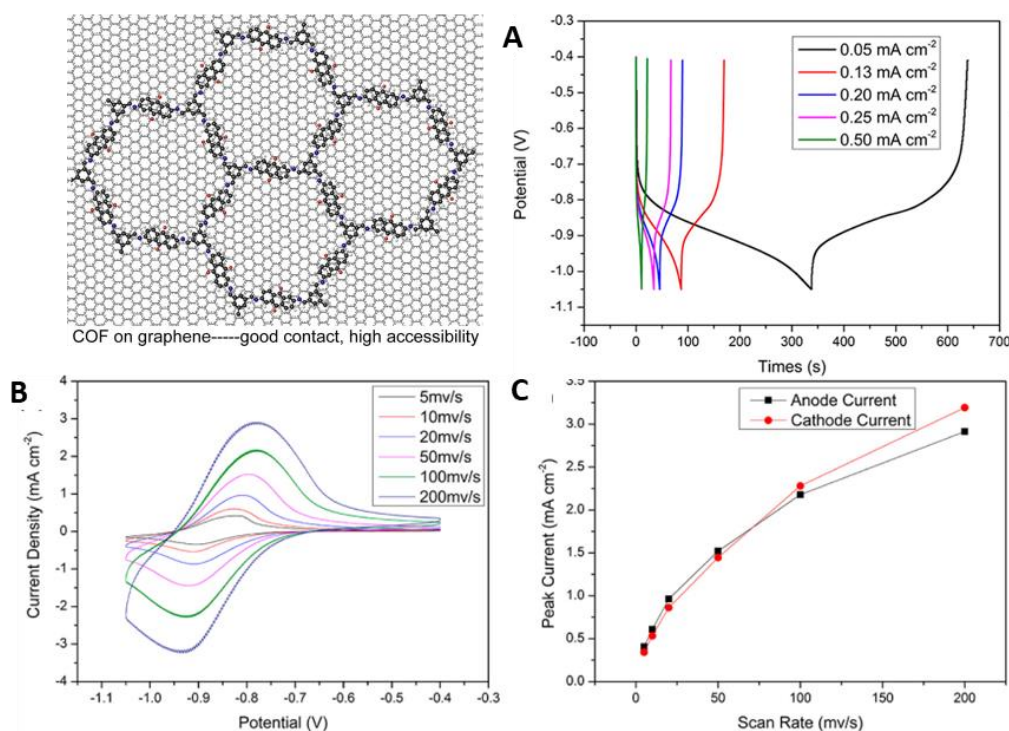


**Figure I.24:** Galvanostatic charge–discharge curves at different current densities (B) CV curves of COFDAAQ-BTA-3DG at different scan rates in 1 mol/L KOH electrolyte (C) and the relationship of peak current with scan rate.

Sun et al. investigated the possibility of a 2D/2D COF-GO hybrid as a high-performance supercapacitor electrode, citing its huge surface area, plentiful active sites, and doped heteroatom.[125] They created
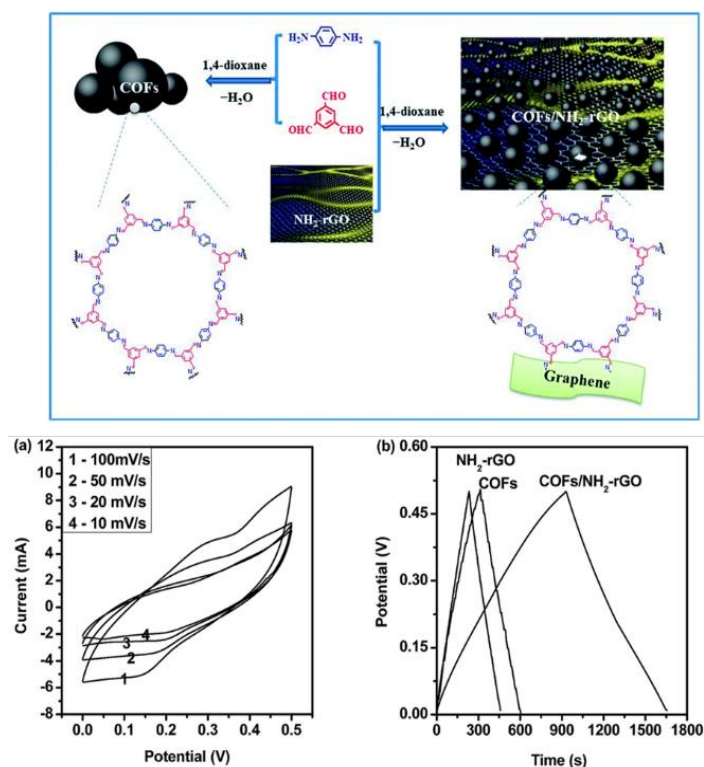


**Figure I.25:** Scheme showing synthesis of COFs and COFs/NH2–rGO (a) CV curves of COFs/NH$_2$–G. (b) galvanostatic charge–discharge curves of synthesized materials at current density of 0.2 A g$^{-1}$.

conjugated COF/graphene composites by crosslinking COFs with amine-functionalized graphene via C-N linkages. These conductive graphene and active COF composites had a specific capacitance of 533 F g$^{-1}$ in a 1.0 M Na$_2$SO$_4$ electrolyte.[126] (Figure I.25)

In recent research carried out in our laboratory, we created a composite electrode by mixing a covalent organic framework (COF) with carbon and integrating it with redox-active KI in an H$_2$SO$_4$ electrolyte for the first time. This novel composite electrode combines the redox activity of COF with the electronic conductivity of carbon, resulting in superior capacitive performance. We attained a high areal capacitance of $270 \pm 11$ mF cm$^{-2}$ and gravimetric capacitance of $57 \pm 8$ F g$^{-1}$ by fabricating flexible solid-state devices using the COF-redox-electrolyte combination. The addition of KI to the H2SO4 electrolyte has resulted in a significant increase of nearly eight times in the solid-state gravimetric specific capacitance. In addition, the imine-COF component maintains a remarkable 89% of its capacity even after 10,000 cycles, demonstrating exceptional cycling stability. (Figure I.26)

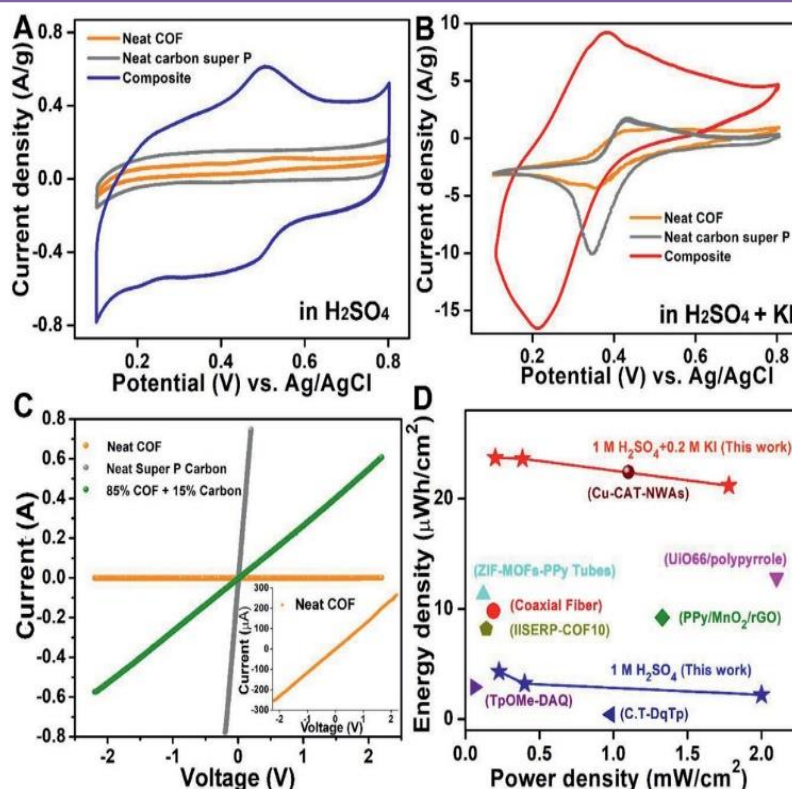**Figure I.26:** The CVs displayed in this figure were obtained by conducting measurements in a three-electrode configuration at a scan rate of 2 mV s$^{-1}$. The composite material was loaded with 2 mg and Toray carbon paper was used as the working electrode. (A) Cyclic voltammetry (CV) plots comparing the neat COF, super P carbon, and the composite material were obtained using 1 M H$_2$SO$_4$ as the electrolyte. (B) Comparative CV plots of the pristine COF, super P carbon, and the composite were obtained separately using 1 M H$_2$SO$_4$ + 0.2 M KI as an electrolyte. (C) Comparative I–V graphs of the coefficient of friction (COF), carbon, and the composite were obtained using a four-probe conductivity set-up. The carbon imparts electronic conductivity to the poorly conducting COF. Conductivity at a temperature of 60 °C: IISERP-COF has a conductivity of 3.2 × 10$^{-4}$ S cm$^{-1}$, super P carbon has a conductivity of 1.5 × 10$^1$ S cm$^{-1}$, and the composite material consisting of 80% COF, 15% carbon, and 5% Nafion has a conductivity of 7.3 × 10$^{-1}$ S cm$^{-1}$. (D) The Ragone plot relies on comparing the geometrical areal energy and power densities of developed electrodes with the most high-performing MOF and COF materials.

**I.1.4.3.2 Hybridization with conducting polymers**: Researchers have investigated the use of conducting polymers to improve the specific capacitance, electrical conductivity, and mechanical flexibility of MOFs and COFs, while preserving the inherent porous structure of these materials. For instance, polymerizing electronically conducting polymers within COFs has been explored as a solution by Dichtel and co-workers. In order to accomplish this, they utilised electropolymerization of EDOT within the pores of redox-active 2D COF films. This process led to the formation of poly(3,4-ethylenedioxythiophene) (PEDOT)-modified COF films, as depicted in Figure I.27. These films demonstrate the ability to measure the electrochemical accessibility of their redox-active groups in a quantitative manner. They also allow for the usage of films that are at least 1μm thick, which can handle high charging rates of up to 1600 C without affecting performance. (Figure I.27)

Our latest study introduces a novel approach to improve the conductivity of a 2D COF with low conductivity. This is achieved by converting it into a conducting quasi-3D COF by the use of polypyrrole chains to create covalent pillars between the layers. We suggest utilising cross-linking polypyrrole chains as "conjugation bridges" to create a three-dimensional framework and enhance the electrical conductivity of the system. This transformation is accomplished by means of Clauson-Kaas
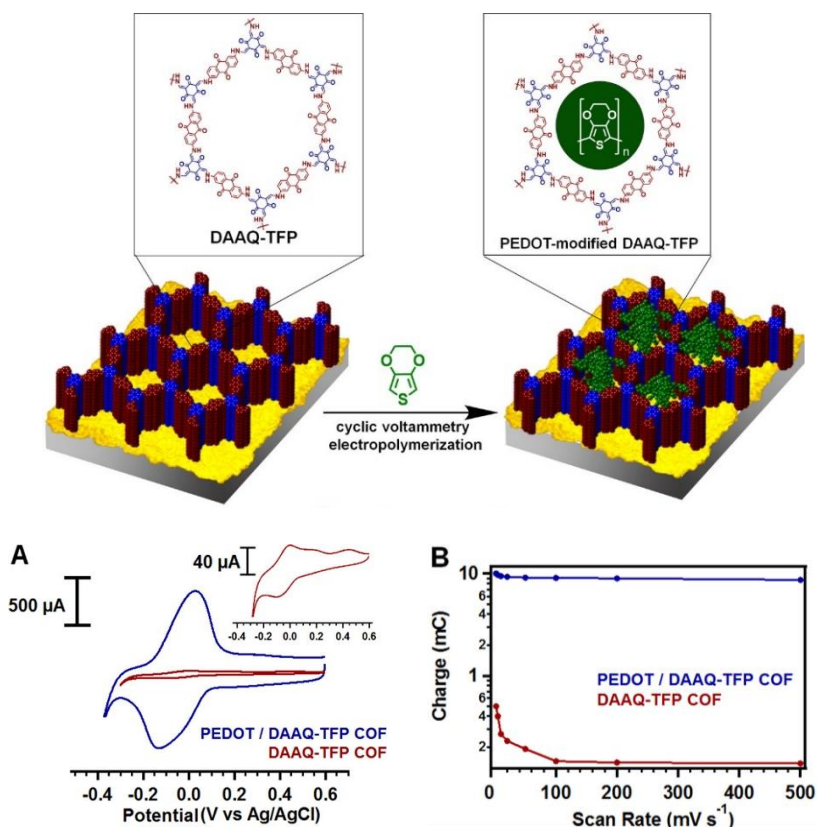
**Figure I.27:** Electrochemical performance of a PEDOT-modified and as-synthesized DAAQ–TFP COF film. (A) CV response at 20 mV s–1 in 0.5 M H2SO4 of a PEDOT-modified DAAQ–TFP film, 1 μm-thick (blue), and the same as-synthesized DAAQ–TFP film before EDOT polymerization (red). The inset presents the cyclic voltammetric response for the unmodified film using an expanded current scale. (B) The integrated charge associated with the oxidative wave of a PEDOT-modified DAAQ–TFP COF film (blue) and unmodified DAAQ–TFP COF film (red) recorded over various scan rates indicate that the PEDOT-modified films store more charge and tolerate faster scan rates than the unmodified films.

pyrrole modification. Throughout the process, the COF maintains its structure as the nitro groups are converted to amino groups and then to pyrrole groups before being anchored with polypyrrole. (Figure I.28)



**Figure I.28:** Illustration of Stepwise Postsynthetic Modification Strategy Transforming 2D IISERP-COF20-NO2 into a Quasi-3D Structure, IISERP-COF20-Ppy.

The 3D COF obtained demonstrates the utmost level of crystallinity among the COF flakes, as verified by the selected area electron diffraction (SAED) patterns.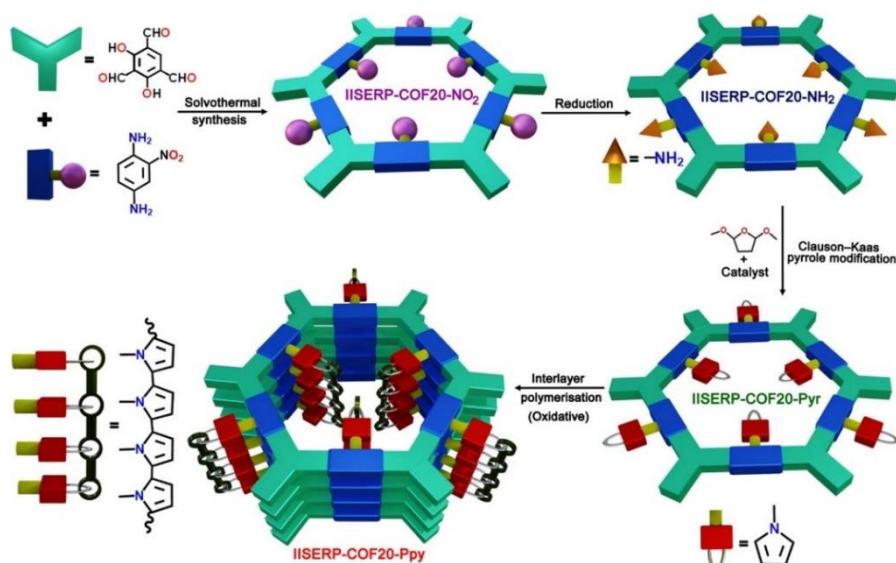 The inclusion of polypyrrole in the COF results in a lowering of the band gap, as seen by electrochemical and optical studies (optical: 1.69 eV; electrochemical: 1.34 eV). This reduction in band gap leads to an electrical conductivity of $1.5 \times 10^{-2}$ S m$^{-1}$. An examination of the performance of capacitors made from a non-conducting COF that has been modified with nitro-functional groups, compared to capacitors made from a 3D COF that is coupled with polypyrrole, shows that the latter has around six times higher capacitance. This suggests that the polypyrrole-linked 3D COF has improved electronic activity. The process of covalently interweaving 2D COFs with electron-rich polypyrrole chains offers a flexible and finely regulated method for converting 2D COFs into electrically enhanced 3D structures.[127]

## I.1.4.4 Glimpse of our work

In chapter 3 we deliberately used a very simple strategy to enhance the electronic conductivity by growing a highly conducting, cost effective polypyrrole in to the COF channels (Figure I.29). Herein we synthesized chemically robust polyimide COF with high surface area ang large pore volume. Electrically conductive polypyrrole (Ppy) chains are incorporated into a polyimide COF structure to significantly enhance electronic conductivity by approximately 10,000 times. This composite material is utilized to construct a carbon-free quasi-solid-state capacitor, which demonstrates remarkable pseudo-capacitance (358 mF cm$^{-2}$@1 mA cm$^{-2}$) when operated in an aqueous gel electrolyte. The collaborative effect between the redox-active polyimide COF, polypyrrole, and organic electrolytes enables the capacitor to achieve a wide-voltage window (0–2.5 V), resulting in exceptionally high energy (145 µWh cm$^{-2}$) and power densities (4509 µW cm$^{-2}$).
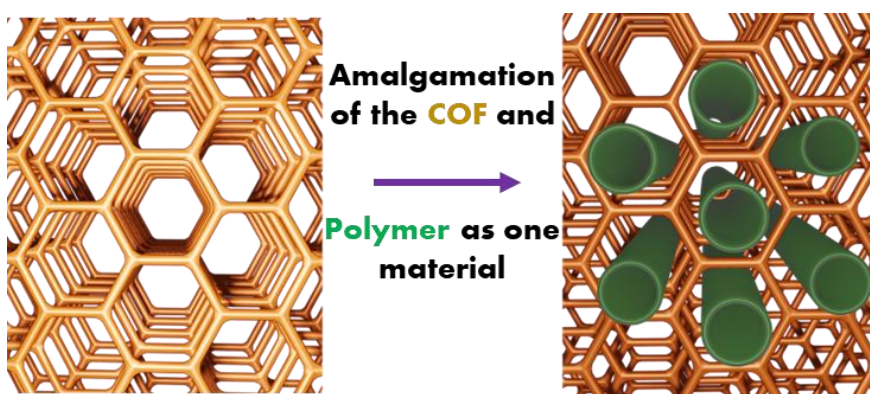


**Figure I.29:** Schematic showing utilization of COF channels by amalgamating COF and conducting polymer as one material.

## I.1.5 COFs as solid-state Li ion conductor

Lithium-ion batteries (LIBs) have become a highly regarded choice for powering flexible electronics, proving to be a dependable technology for a extensive range of applications including energy storage systems, mobile electronics, power tools, aerospace, automotive, and maritime industries. Their high power and energy densities, in comparison to competing battery technologies, have attracted substantial attention from both academia and industry. Nevertheless, despite their extensive usage, there is still a significant risk of fire linked with Lithium-ion Batteries (LiBs), especially when used in electric vehicles, aeroplanes, and submarines.[128]

### I.1.5.1 Working Principle of Li Ion Battery

As commonly understood, a Lithium-ion battery (LIB) is composed of two electrodes: the cathode and the anode, which are parted by a nonaqueous electrolyte serving as both an ion conductor and electron insulator. The electrode materials typically feature a layered structure capable of undergoing lithiation and de-lithiation processes. A typical configuration of a lithium-ion cell involves the connection of a



$$C_6 + LiMO_2 \underset{\text{Discharge}}{\overset{\text{Charge}}{\rightleftharpoons}} Li_xC_6 + Li_{(1-x)}MO_2$$
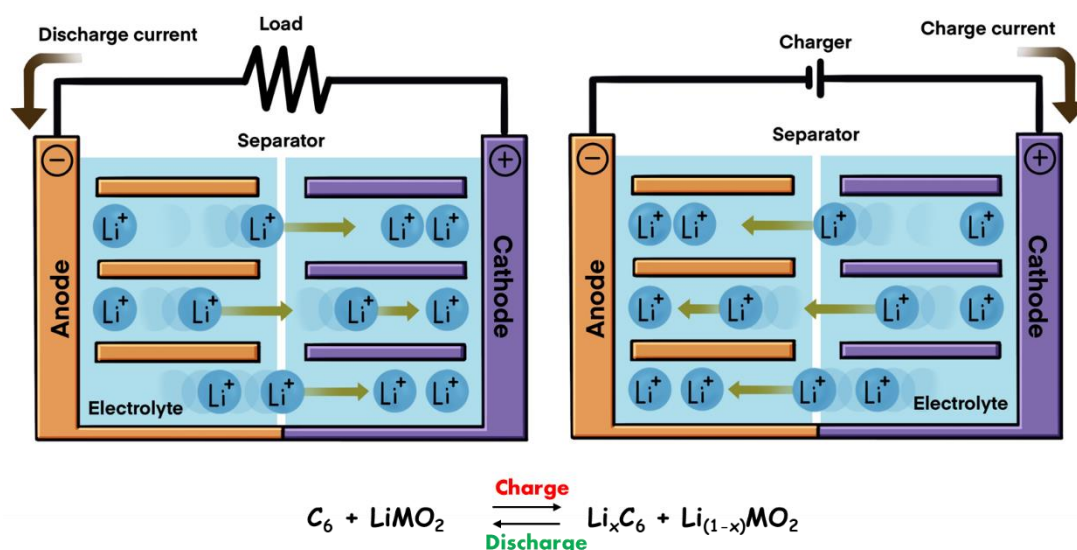
**Figure I.30:** Illustration of the basic components and operation principle of a Li- ion cell.

cathode (positive electrode) and an anode (negative electrode) through an electrolyte that contains lithium ions. In order to avoid direct contact between the electrodes, a separator, often a microporous polymer membrane, is used. The function of this separator is to enhance the transfer of $Li^+$ ions between the electrodes while inhibiting the movement of electrons. Aside from liquid electrolytes, researchers have also explored alternate forms such as polymer, gel, and ceramic electrolytes for their potential application in Li-ion batteries. The basic operational mechanism of a typical lithium-ion battery cell is illustrated in Figure I.30.[129]

LIBs are renowned for their high cell voltage, volumetric and gravimetric energy densities, as well as power density, making them indispensable energy sources in our day to day lives. However, lithium is a highly reactive element, and LIBs operate under varying voltages, temperatures, and environmental conditions, necessitating special attention to their safety concerns.

**I.1.5.2 Commercial applications and impact of Li Ion Battery**

Since their inception by Sony Ltd. in 1991, LIBs have found extensive application in consumer electronics and transportation due to their high energy density, voltage, and long cycle life. However, the safety of LIBs has remained a significant concern, given the potential for serious consequences in the event of accidents. Even small-scale incidents, such as explosions in cell phones, can garner substantial public attention, leading to significant financial losses and reputational damage.
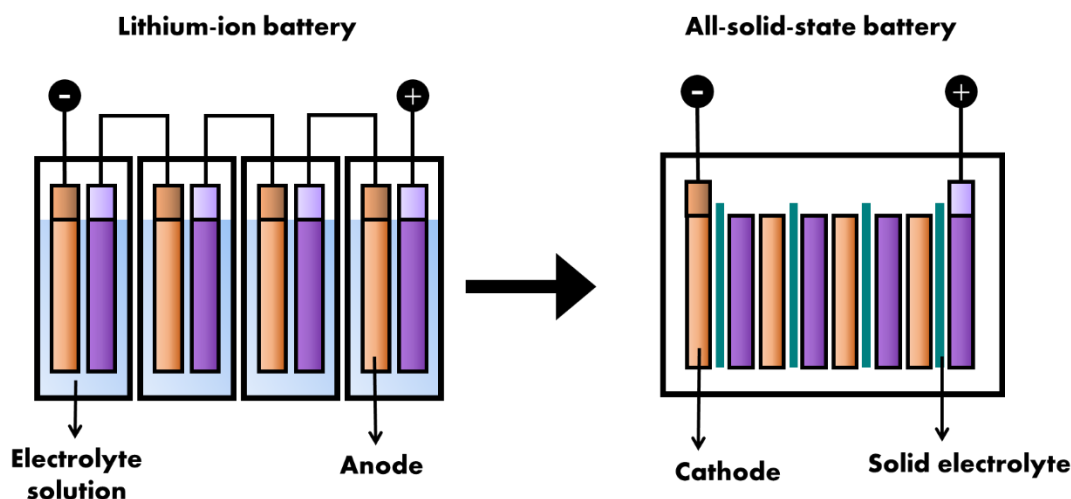
**Figure I.31:** Schematic showing enhancement in the flexibility and rigidity in All-solid-state battery.

In the case of electric vehicles (EVs), which rely on high-energy and power battery systems comprising numerous cells connected in series and parallel configurations, the safety considerations become even more crucial and complex. For instance, vehicles like the Tesla Model S, equipped with a 99 kWh battery pack, rely on thousands of cylindrical cells arranged in intricate patterns. The unique operating conditions of EVs expose battery systems to various challenges, including vibration, extreme temperatures, water exposure, and rapid charging, among others.

The potential triggers for failures in EVs encompass a range of factors such as collisions, foreign object intrusion, overcharging, over-discharging, water exposure, overheating, battery leakage, and electrical system malfunctions. To develop safer and more reliable LIB-based energy systems for EVs, it is imperative to thoroughly understand the safety issues associated with LIBs underlying these accidents.

**I.1.5.3 Solid state Li ion conducting electrolyte**

Liquid electrolytes are commonly used in traditional lithium-ion batteries, which are typically found in rigid forms such as button cells, cylinder cells, and pouch cells. In order to increase the flexibility of these batteries, it is possible to replace stiff components and metal casings with materials that are naturally flexible or incorporate them into flexible structures using soft supports. Thin lithium polymer batteries, such as those mentioned, substitute the liquid electrolyte with solid polymer electrolyte layers, resulting in enhanced physical size and flexibility (Figure I.31). At ambient temperature, these polymer electrolytes, which consist of lithium salts incorporated into different polymer hosts like polyvinylidene fluoride, can demonstrate ionic conductivities of $10^{-4}$ S cm$^{-1}$. Nevertheless, safety issues continue to exist as a result of the polymer electrolytes' low flammability.

Solid electrolytes are essential for the progress of solid-state batteries, which can be classified into three primary categories: inorganic solid electrolytes, solid polymer electrolytes, and thin-film solid electrolytes. Examples of inorganic solid electrolytes include garnets such as $Li_7La_3Zr_2O_{12}$, NASICON-type materials such as $LiZr_2(PO_4)_3$, sulfide-type materials such as $Li_2S$–$SiS_2$-based compounds, and perovskite-structured materials such as $Li_{3x}La_{2/3}TiO_3$. Among these materials, oxide-type materials exhibit good chemical stability, exceptional mechanical properties, and reasonable conductivities. However, they encounter difficulties in terms of flexibility and scalability. On the other hand, solid electrolytes of the sulphide type demonstrate notable conductivity, flexibility, and low resistance at grain boundaries. However, they are hindered by limited stability against oxidation and inadequate compatibility with electrodes. Solid polymer electrolytes, such as those utilising polyethylene oxides (PEOs), possess advantageous characteristics like non-toxicity, affordability, and high chemical stability. Nevertheless, their ionic conductivity is lower in comparison to inorganic solid electrolytes, which presents a hurdle for practical application. Thin-film solid electrolytes have become favourable options for thin-film batteries due to their superior characteristics such as increased energy density, flexibility in application design, and compactness in comparison to traditional lithium-ion batteries.[130]

Covalent organic frameworks (COFs) are meticulously crafted from organic building blocks to form crystalline porous materials with tailored channels or functional groups.[103, 131-137] Their tunability, design flexibility, and diverse functionalities make them highly attractive for energy conversion and storage applications, particularly in lithium-ion batteries.[138, 139]

Unlike conventional polymer electrolytes, COFs hold a significant intrinsic free volume due to their rigid and periodic crystalline frameworks, facilitating rapid Li$^+$ diffusion.[108,139,141] Moreover, their inherent porosity offers numerous ionic-conducting pathways and the ability to host guest molecules, enhancing Li$^+$ conduction acceleration[140-143] Additionally, COF materials exhibit exceptional thermal

stability, maintaining structural integrity even at temperatures reaching 300 °C, which supports stable $Li^+$ conduction under extreme conditions.[144, 145]

The process of forming organic building blocks into COFs creates a regular pattern within the framework. This is often compared to the ordered structure of graphene sheets that have been doped with heteroatoms. The robust covalent bonds present in COFs enhance their exceptional thermal and chemical durability. COFs possess a crystalline structure that allows for the clear understanding of their structural characteristics and properties. This makes them notable for their one-dimensional channels, capacity to withstand electrochemical processes, and ease of modification.[146]

### I.1.5.4 Previous reports

COF-based materials have been extensively studied for diverse applications over the past decade, with ion conduction emerging as a promising area of focus. The tunable nature of COF's one-dimensional channels and their inherent phase stability make them promising candidates for applications in fuel cells and solid-state ion batteries. (Figure I.32) While their potential advantages over polymer-based solid-state electrolytes are recognized, further exploration is needed to fully uncover and harness these advantages.[128]

Zhang and co-workers developed a method of self-assembly to create three different thiophene-based imine-linked COFs. These crystalline organic frameworks (COFs) are capable of effectively hosting large quantities of lithium ionic liquids, leading to rapid conductivity of $Li^+$ ions (reaching up to $2.60 \times$
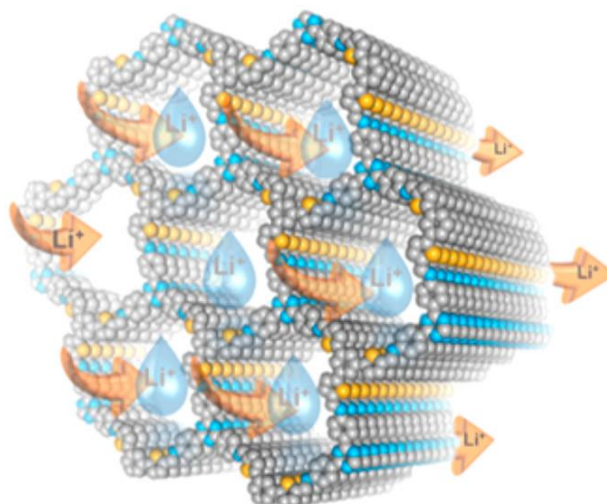


**Figure I.32:** Illustration of COF's one-dimensional pathways showing fast ion conductive/transport in the solid state.

$10^{-3}$ S cm$^{-1}$, one of the highest values observed for doped COFs). The combination of ionic liquids with COFs produces a composite electrolyte that effectively resolves the issue of low thermal stability found in conventional liquid electrolytes. In addition, these composite electrolytes showed consistent cycling performance in a solid-state LiFePO$_4$–Li complete cell. They displayed an impressive initial discharge

specific capacity of 140.8 mAh/g at a temperature of 100 °C. The stability of the IL@COF composite electrolytes was notably higher than that of electrolytes built from poly(ethylene oxide) (PEO). This study demonstrates the potential of using doping strategies to develop solid electrolytes based on COFs (covalent organic frameworks) with high ionic conductivity. These highly thermostable COF-based electrolytes show promise for use in solid-state lithium-ion batteries that operate at very high temperatures. (Figure I.33)
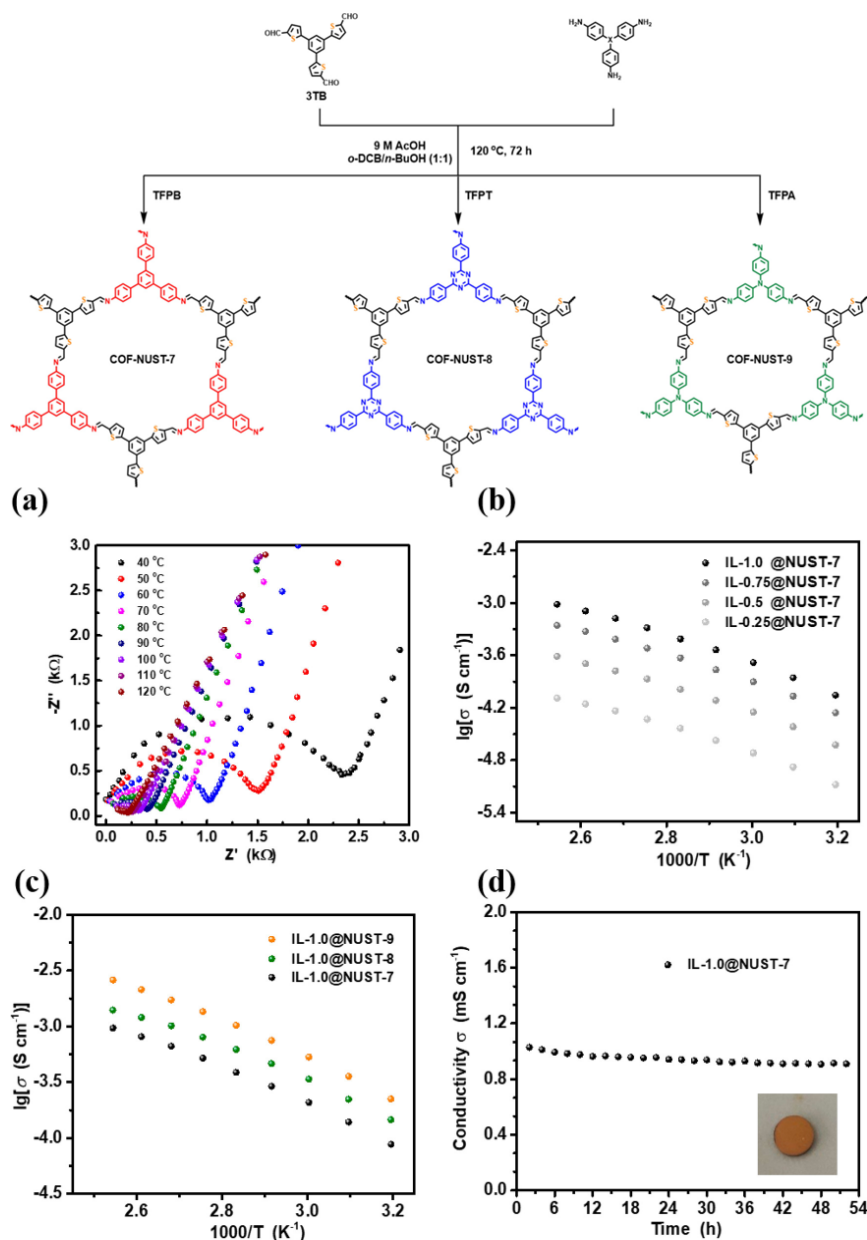


**Figure I.33:** Scheme synthesis of COF-NUST-7, COF-NUST-8, and COF-NUST-9. (a) Nyquist plots of IL-1.0@NUST-7 at different temperatures. Temperature-dependent Li+ conductivities of (b) IL@NUST-7 with various (IL+LiTFSI))/COF-NUST-7 powders ratios and (c) IL-1.0@NUST-7, IL-1.0@NUST-8, and IL-1.0@NUST-9. (d) Long-period conductivity test of IL-1.0@NUST-7 property at high temperature 120 °C.

Li and co-workers have developed a new solvent-free, single Li-ion conducting COF, representing a notable breakthrough in the field. The COF, known as lithium sulfonated COF (TpPa-SO₃Li), is specifically designed to have distinct ion channels, a high concentration of Li-ions, and anion groups that are covalently attached. The theoretical elucidation of the directional conduction of Li-ions through the axially stacked pores of TpPa-SO3Li, in conjunction with the participation of oxygen atoms from keto groups, has been accomplished. The distinctive arrangement of the structure, along with the lack of mobile anions and solvents, gives TpPa-SO3Li remarkable ion conduction capabilities ($\sigma = 2.7 \times 10^-$
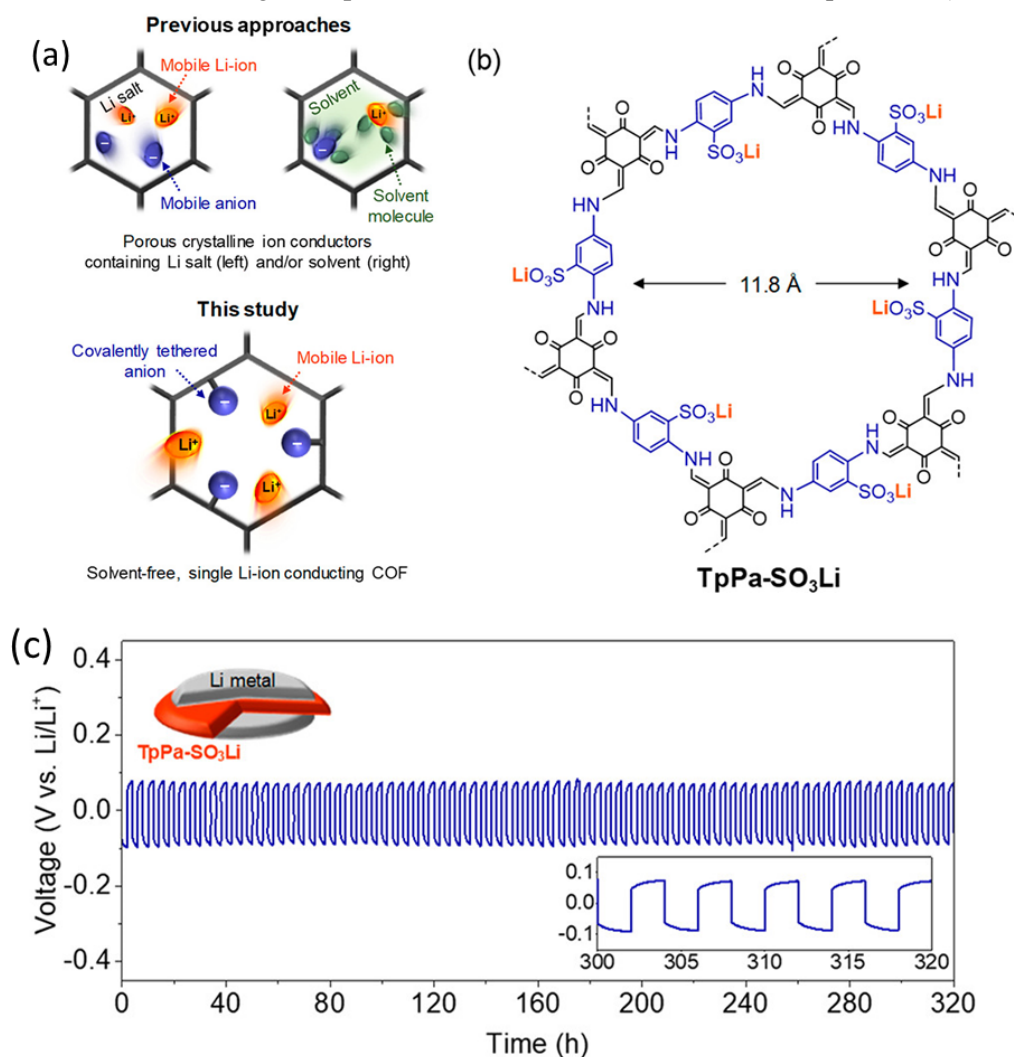


**Figure I.34:** (a) Conceptual illustrations of ion transport phenomena in the porous crystalline ion conductors: previous approaches (top) and this study (bottom). (b) Chemical structure of lithium sulfonated COF (TpPa-SO3Li). (c) Galvanostatic Li plating |stripping profile of Li |Li containing cell TpPa-SO₃Li.

$^5$ S cm$^{-1}$, tLi+ = 0.9 at ambient temperature, and Ea = 0.18 eV). These features notably enable the stable cycling of Li plating/stripping on Li metal electrodes. This innovative research introduces a novel electrolyte strategy for advanced batteries of the future, specifically all-solid-state and Li metal batteries, which demand exceptional solid-state single-ion conductors with superior performance.[143] (Figure I.34)

A novel strategy was developed by Manthiram and co-workers[147] for high-performance solid-state electrolytes (SSEs) in foldable lithium batteries. Where they discovered a new liquid electrolyte (DMA@LiTFSI) that polymerizes upon lithium salt addition. This in-situ polymerizable solution was encapsulated within a lithium covalent organic framework (COF), where it interacted with the COF
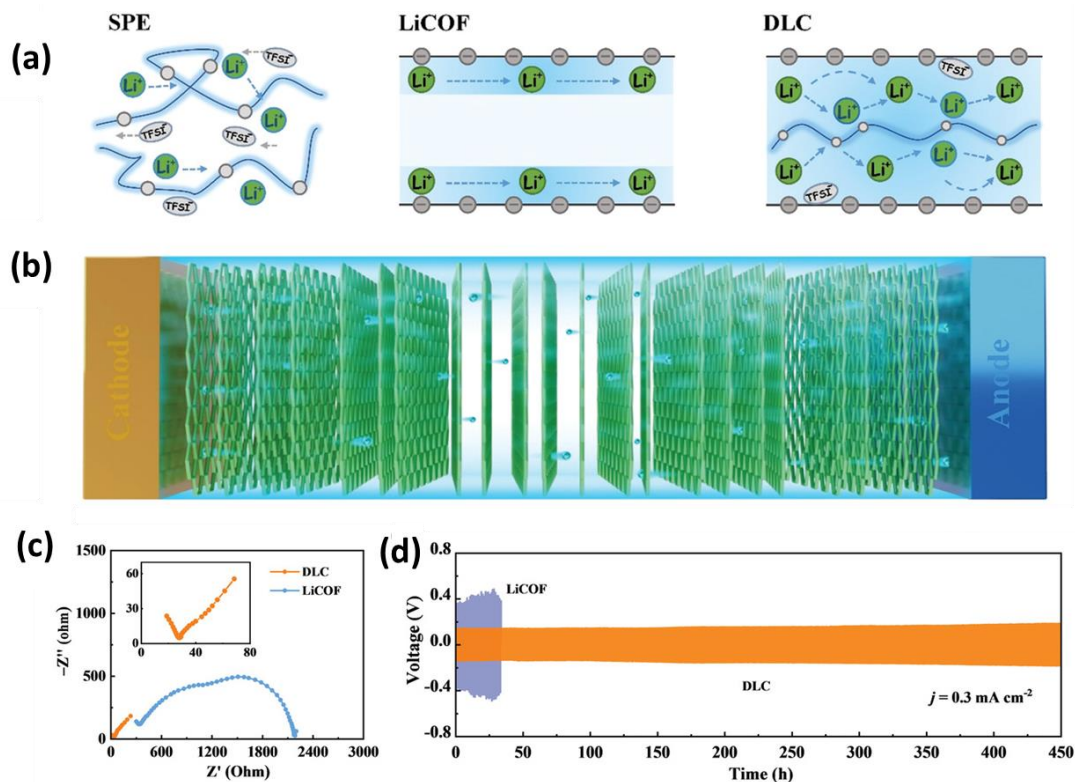


**Figure I.35:** (a) Illustration of the Li$^+$-transport mode in conventional SPE, pristine LiCOF, and DLC. (b) Illustration of an SSB with the proposed DLC electrolyte. (c) EIS of SS|SSE|SS symmetric cells. (d) Li|SSE|Li symmetric cell cyclability.

structure to improve lithium ion (Li$^+$) mobility. The resulting DMA@LiTFSI-mediated COF (DLC) exhibited exceptional Li$^+$ conductivity ($1.7 \times 10^{-4}$ S cm$^{-1}$) and transformability into a highly flexible film, aiding the fabrication of a foldable solid-state battery with good performance (120 mAh g$^{-1}$ at RT) even under folding tests. This work presents a new class of SSEs with superior Li$^+$ transport, processability, and mechanical flexibility, overcoming limitations of traditional electrolytes. . (Figure I.35)

## I.1.6 References

1.  A. S. Permana, R. Perera and S. Kumar, *Energy Policy*, 2008, **36**, 4287-4297.
2.  P. P. Edwards, V. L. Kuznetsov, W. I. David and N. P. Brandon, *Energy policy*, 2008, **36**, 4356-4362.
3.  D. W. Kang, M. Kang, H. Yun, H. Park and C. S. Hong, *Adv. Funct. Mater.*, 2021, **31**, 2100083.
4.  Y. Xiang, J. Li, J. Lei, D. Liu, Z. Xie, D. Qu, K. Li, T. Deng and H. Tang, *ChemSusChem*, 2016, **9**, 3023-3039.
5.  Y. Jiang and J. Liu, *Energy & Environmental Materials*, 2019, **2**, 30-37.
6.  R. G. Taylor, C. G. Bezzu, M. Carta, K. J. Msayib, J. Walker, R. Short, B. M. Kariuki and N. B. McKeown, *Chemistry–A European Journal*, 2016, **22**, 2466-2472.
7.  Y. Jiao, F. Stillinger and S. Torquato, *Physical review letters*, 2008, **100**, 245504.
8.  S. Krause, V. Bon, I. Senkovska, D. M. Többens, D. Wallacher, R. S. Pillai, G. Maurin and S. Kaskel, *Nat. Commun.*, 2018, **9**, 1573.
9.  Z. Li, X. Feng, Y. Zou, Y. Zhang, H. Xia, X. Liu and Y. Mu, *Chemical Communications*, 2014, **50**, 13825-13828.
10. Z. Li, Y. Zhi, X. Feng, X. Ding, Y. Zou, X. Liu and Y. Mu, *Chemistry–A European Journal*, 2015, **21**, 12079-12084.
11. L. Stegbauer, M. W. Hahn, A. Jentys, G. k. Savasci, C. Ochsenfeld, J. A. Lercher and B. V. Lotsch, *Chem. Mater.*, 2015, **27**, 7874-7881.
12. M. Dogru and T. Bein, *Chemical communications*, 2014, **50**, 5531-5546.
13. K. Yuan, C. Liu, J. Han, G. Yu, J. Wang, H. Duan, Z. Wang and X. Jian, *RSC advances*, 2016, **6**, 12009-12020.
14. K. Wang, H. Huang, D. Liu, C. Wang, J. Li and C. Zhong, *Environmental science & technology*, 2016, **50**, 4869-4876.
15. T. Ben, C. Pei, D. Zhang, J. Xu, F. Deng, X. Jing and S. Qiu, *Energy Environ. Sci.*, 2011, **4**, 3991-3999.
16. S. Singh Dhankhar, N. Sharma, S. Kumar, T. Dhilip Kumar and C. Nagaraja, *Chemistry–A European Journal*, 2017, **23**, 16204-16212.
17. B. Li, Y. Zhang, R. Krishna, K. Yao, Y. Han, Z. Wu, D. Ma, Z. Shi, T. Pham and B. Space, *J. Am. Chem. Soc.*, 2014, **136**, 8654-8660.
18. T. Hasell, M. Miklitz, A. Stephenson, M. A. Little, S. Y. Chong, R. Clowes, L. Chen, D. Holden, G. A. Tribello and K. E. Jelfs, *J. Am. Chem. Soc.*, 2016, **138**, 1653-1659.
19. S. S. Dhankhar and C. Nagaraja, *New Journal of Chemistry*, 2019, **43**, 2163-2170.
20. M. Gupta, N. Chatterjee, D. De, R. Saha, P. K. Chattaraj, C. L. Oliver and P. K. Bharadwaj, *Inorganic Chemistry*, 2020, **59**, 1810-1822.
21. Z.-A. Qiao, S.-H. Chai, K. Nelson, Z. Bi, J. Chen, S. M. Mahurin, X. Zhu and S. Dai, *Nat. Commun.*, 2014, **5**, 3705.
22. Q. Song, S. Jiang, T. Hasell, M. Liu, S. Sun, A. K. Cheetham, E. Sivaniah and A. I. Cooper, *Adv. Mater.*, 2016, **28**, 2629-2637.
23. Q. Fang, S. Gu, J. Zheng, Z. Zhuang, S. Qiu and Y. Yan, *Angewandte Chemie*, 2014, **126**, 2922-2926.
24. H. Xu, J. Gao and D. Jiang, *Nature chemistry*, 2015, **7**, 905-912.
25. M. Giménez-Marqués, A. Santiago-Portillo, S. Navalón, M. Álvaro, V. Briois, F. Nouar, H. Garcia and C. Serre, *J. Mater. Chem. A*, 2019, **7**, 20285-20292.
26. K. Iwase, T. Yoshioka, S. Nakanishi, K. Hashimoto and K. Kamiya, *Angew. Chem. Int. Ed.*, 2015, **54**, 11068-11072.
27. P. Thomas, C. Pei, B. Roy, S. Ghosh, S. Das, A. Banerjee, T. Ben, S. Qiu and S. Roy, *J. Mater. Chem. A*, 2015, **3**, 1431-1441.
28. Q. Wang and K. Domen, *Chemical Reviews*, 2019, **120**, 919-985.
29. H. Furukawa and O. M. Yaghi, *J. Am. Chem. Soc.*, 2009, **131**, 8875-8883.
30. Y. Zhi, Z. Yao, W. Jiang, H. Xia, Z. Shi, Y. Mu and X. Liu, *ACS applied materials & interfaces*, 2019, **11**, 37578-37585.
31. Z. Xie, C. Wang, K. E. deKrafft and W. Lin, *J. Am. Chem. Soc.*, 2011, **133**, 2056-2059.

32. J.-X. Jiang, Y. Li, X. Wu, J. Xiao, D. J. Adams and A. I. Cooper, *Macromolecules*, 2013, **46**, 8779-8783.
33. L. Pan, M.-Y. Xu, L.-J. Feng, Q. Chen, Y.-J. He and B.-H. Han, *Polymer Chemistry*, 2016, **7**, 2299-2307.
34. L. Chen, Y. Honsho, S. Seki and D. Jiang, *J. Am. Chem. Soc.*, 2010, **132**, 6742-6748.
35. K. V. Rao, R. Haldar, T. K. Maji and S. J. George, *Physical Chemistry Chemical Physics*, 2016, **18**, 156-163.
36. S. Dalapati, E. Jin, M. Addicoat, T. Heine and D. Jiang, *J. Am. Chem. Soc.*, 2016, **138**, 5797-5800.
37. Y. Hong, J. W. Lam and B. Z. Tang, *Chemical communications*, 2009, 4332-4353.
38. V. S. Vyas and R. Rathore, *Chemical communications*, 2010, **46**, 1065-1067.
39. X. Liu, Y. Xu and D. Jiang, *J. Am. Chem. Soc.*, 2012, **134**, 8738-8741.
40. S. Dalapati, S. Jin, J. Gao, Y. Xu, A. Nagai and D. Jiang, *J. Am. Chem. Soc.*, 2013, **135**, 17310-17313.
41. Z. Xiang and D. Cao, *Macromolecular rapid communications*, 2012, **33**, 1184-1190.
42. F. Xu, X. Chen, Z. Tang, D. Wu, R. Fu and D. Jiang, *Chemical communications*, 2014, **50**, 4788-4790.
43. Y. Kou, Y. Xu, Z. Guo and D. Jiang, *Angewandte Chemie*, 2011, **123**, 8912-8916.
44. J.-S. M. Lee, T.-H. Wu, B. M. Alston, M. E. Briggs, T. Hasell, C.-C. Hu and A. I. Cooper, *J. Mater. Chem. A*, 2016, **4**, 7665-7673.
45. F. Xu, H. Xu, X. Chen, D. Wu, Y. Wu, H. Liu, C. Gu, R. Fu and D. Jiang, *Angewandte Chemie*, 2015, **127**, 6918-6922.
46. C. R. DeBlase, K. E. Silberstein, T.-T. Truong, H. D. Abruña and W. R. Dichtel, *J. Am. Chem. Soc.*, 2013, **135**, 16821-16824.
47. C. R. Mulzer, L. Shen, R. P. Bisbey, J. R. McKone, N. Zhang, H. c. D. Abruña and W. R. Dichtel, *ACS central science*, 2016, **2**, 667-673.
48. S. Khatua, A. K. Bar, J. A. Sheikh, A. Clearfield and S. Konar, *Chemistry–A European Journal*, 2018, **24**, 872-880.
49. B. Guo, T. Ben, Z. Bi, G. M. Veith, X.-G. Sun, S. Qiu and S. Dai, *Chemical communications*, 2013, **49**, 4905-4907.
50. H. Xu, S. Tao and D. Jiang, *Nature materials*, 2016, **15**, 722-726.
51. H. Ma, B. Liu, B. Li, L. Zhang, Y.-G. Li, H.-Q. Tan, H.-Y. Zang and G. Zhu, *J. Am. Chem. Soc.*, 2016, **138**, 5897-5903.
52. Q. Fang, J. Wang, S. Gu, R. B. Kaspar, Z. Zhuang, J. Zheng, H. Guo, S. Qiu and Y. Yan, *J. Am. Chem. Soc.*, 2015, **137**, 8352-8355.
53. E. Derouane, J. C. Vedrine, R. R. Pinto, P. Borges, L. Costa, M. Lemos, F. Lemos and F. R. Ribeiro, *Catalysis Reviews*, 2013, **55**, 454-515.
54. L.-E. Sandoval-Díaz, J.-A. González-Amaya and C.-A. Trujillo, *Microporous and mesoporous materials*, 2015, **215**, 229-243.
55. A. Tuel, S. Moussa-Khouzami, Y. B. Taarit and C. Naccache, *Journal of molecular catalysis*, 1991, **68**, 45-52.
56. G. Wu, Y. Wang, L. Wang, W. Feng, H. Shi, Y. Lin, T. Zhang, X. Jin, S. Wang and X. Wu, *Chemical engineering journal*, 2013, **215**, 306-314.
57. H. Y. Luo, J. D. Lewis and Y. Román-Leshkov, *Annual review of chemical and biomolecular engineering*, 2016, **7**, 663-692.
58. R. Bai, Q. Sun, N. Wang, Y. Zou, G. Guo, S. Iborra, A. Corma and J. Yu, *Chem. Mater.*, 2016, **28**, 6455-6458.
59. H. Guo, G. Zhu, I. J. Hewitt and S. Qiu, *J. Am. Chem. Soc.*, 2009, **131**, 1646-1647.
60. S. Lv, K. Zhang, L. Zhu, D. Tang, R. Niessner and D. Knopp, *Analytical Chemistry*, 2019, **91**, 12055-12062.
61. A. Nuhnen, M. Klopotowski, H. B. T. Jeazet, S. Sorribas, B. Zornoza, C. Téllez, J. Coronas and C. Janiak, *Dalton Transactions*, 2020, **49**, 1822-1829.
62. S. Nandi, S. Collins, D. Chakraborty, D. Banerjee, P. K. Thallapally, T. K. Woo and R. Vaidhyanathan, *J. Am. Chem. Soc.*, 2017, **139**, 1734-1737.

63. A. Samanta, A. Zhao, G. K. Shimizu, P. Sarkar and R. Gupta, *Industrial & Engineering Chemistry Research*, 2012, **51**, 1438-1463.
64. S. Nandi, R. Maity, D. Chakraborty, H. Ballav and R. Vaidhyanathan, *Inorganic Chemistry*, 2018, **57**, 5267-5272.
65. J.-R. Li, R. J. Kuppler and H.-C. Zhou, *Chem Soc Rev*, 2009, **38**, 1477-1504.
66. S. Mollick, S. Mukherjee, D. Kim, Z. Qiao, A. V. Desai, R. Saha, Y. D. More, J. Jiang, M. S. Lah and S. K. Ghosh, *Angewandte Chemie*, 2019, **131**, 1053-1057.
67. S. Nandi, D. Chakraborty and R. Vaidhyanathan, *Chemical communications*, 2016, **52**, 7249-7252.
68. A. Karmakar, R. Illathvalappil, B. Anothumakkool, A. Sen, P. Samanta, A. V. Desai, S. Kurungot and S. K. Ghosh, *Angew. Chem. Int. Ed.*, 2016, **55**, 10667-10671.
69. R.-B. Lin, Y. He, P. Li, H. Wang, W. Zhou and B. Chen, *Chem Soc Rev*, 2019, **48**, 1362-1389.
70. N. Huang, S. Yuan, H. Drake, X. Yang, J. Pang, J. Qin, J. Li, Y. Zhang, Q. Wang and D. Jiang, *J. Am. Chem. Soc.*, 2017, **139**, 18590-18597.
71. A. P. Katsoulidis and M. G. Kanatzidis, *Chem. Mater.*, 2011, **23**, 1818-1824.
72. , International Union of Pure and Applied Chemistry (IUPAC), 3.0.1 edn., 2019, DOI: doi:10.1351/goldbook.V06624.
73. K. W. Shah, S.-X. Wang, D. X. Y. Soo and J. Xu, *Polymers*, 2019, **11**, 1839.
74. D. Chakraborty, S. Nandi, R. Kushwaha, D. Kaleeswaran and R. Vaidhyanathan, *Materials Research Bulletin*, 2022, **146**, 111614.
75. H. Li, L. Ma, C. Han, Z. Wang, Z. Liu, Z. Tang and C. Zhi, *Nano Energy*, 2019, **62**, 550-587.
76. Y. Li and H. Dai, *Chem Soc Rev*, 2014, **43**, 5257-5275.
77. J. Fu, D. U. Lee, F. M. Hassan, L. Yang, Z. Bai, M. G. Park and Z. Chen, *Adv. Mater.*, 2015, **27**, 5617-5622.
78. H. F. Wang, C. Tang and Q. Zhang, *Adv. Funct. Mater.*, 2018, **28**, 1803329.
79. Q. Wei, Y. Fu, G. Zhang and S. Sun, *Current Opinion in Electrochemistry*, 2017, **4**, 45-59.
80. Q. Liu, Z. Chang, Z. Li and X. Zhang, *Small Methods*, 2018, **2**, 1700231.
81. Y. Wang, Q. Cao, C. Guan and C. Cheng, *Small*, 2020, **16**, 2002902.
82. D. U. Lee, J. Y. Choi, K. Feng, H. W. Park and Z. Chen, *Adv. Energy Mater.*, 2014, **4**.
83. M. Prabu, K. Ketpang and S. Shanmugam, *Nanoscale*, 2014, **6**, 3173-3181.
84. M. Zeng, Y. Liu, F. Zhao, K. Nie, N. Han, X. Wang, W. Huang, X. Song, J. Zhong and Y. Li, *Adv. Funct. Mater.*, 2016, **26**, 4397-4404.
85. H. Cheng, M. L. Li, C. Y. Su, N. Li and Z. Q. Liu, *Adv. Funct. Mater.*, 2017, **27**, 1701833.
86. C. Y. Su, H. Cheng, W. Li, Z. Q. Liu, N. Li, Z. Hou, F. Q. Bai, H. X. Zhang and T. Y. Ma, *Adv. Energy Mater.*, 2017, **7**, 1602420.
87. L. Wei, H. E. Karahan, S. Zhai, H. Liu, X. Chen, Z. Zhou, Y. Lei, Z. Liu and Y. Chen, *Adv. Mater.*, 2017, **29**, 1701410.
88. H. Jiang, Y. Liu, W. Li and J. Li, *Small*, 2018, **14**, 1703739.
89. A. R. Mainar, O. Leonet, M. Bengoechea, I. Boyano, I. de Meatza, A. Kvasha, A. Guerfi and J. Alberto Blázquez, *Int. J. Energy Res.*, 2016, **40**, 1032-1049.
90. L. Xu, J. Liu, P. Chen, Z. Wang, D. Tang, X. Liu, F. Meng and X. Wei, *Cell Reports Physical Science*, 2020, **1**.
91. K. Wang, P. Pei, Z. Ma, H. Xu, P. Li and X. Wang, *J. Power Sources*, 2014, **271**, 65-75.
92. C. Chakkaravarthy, A. A. Waheed and H. Udupa, *J. Power Sources*, 1981, **6**, 203-228.
93. A. R. Mainar, E. Iruin, L. C. Colmenares, A. Kvasha, I. De Meatza, M. Bengoechea, O. Leonet, I. Boyano, Z. Zhang and J. A. Blazquez, *J. Energy Storage*, 2018, **15**, 304-328.
94. P. Chen, K. Zhang, D. Tang, W. Liu, F. Meng, Q. Huang and J. Liu, *Frontiers in Chemistry*, 2020, **8**, 372.
95. Q. Liu, R. Liu, C. He, C. Xia, W. Guo, Z.-L. Xu and B. Y. Xia, *escience*, 2022, **2**, 453-466.
96. W. Yao, Z. Zheng, J. Zhou, D. Liu, J. Song and Y. Zhu, *Polymers*, 2023, **15**, 4047.
97. Y. Wei, Y. Shi, Y. Chen, C. Xiao and S. Ding, *J. Mater. Chem. A*, 2021, **9**, 4415-4453.
98. W. Li, Y. Wang, R. Liu, W. Chen, H. Zhang and Z. Zhang, *ACS Sustain. Chem. Eng.*, 2023, **11**, 3732-3739.
99. M. Li, B. Liu, X. Fan, X. Liu, J. Liu, J. Ding, X. Han, Y. Deng, W. Hu and C. Zhong, *ACS applied materials & interfaces*, 2019, **11**, 28909-28917.

100. X. Wang and R. G. Lammertink, *Alkaline Anion Exchange Membranes for Fuel Cells: From Tailored Materials to Novel Applications*, 2024, 361-392.
101. M. T. Tsehaye, N. H. Choi, P. Fischer, J. Tübke, E. Planes, F. Alloin and C. Iojoiu, *ACS Appl. Energy Mater.*, 2022, **5**, 7069-7080.
102. P. Jhariat, A. K. U, A. Warrier, A. P. Sunda, S. Das, S. Sarfudeen, V. M. Dhavale and T. Panda, *ACS Applied Materials & Interfaces*, 2024.
103. A. P. Cote, A. I. Benin, N. W. Ockwig, M. O'Keeffe, A. J. Matzger and O. M. Yaghi, *science*, 2005, **310**, 1166-1170.
104. H. M. El-Kaderi, J. R. Hunt, J. L. Mendoza-Cortés, A. P. Côté, R. E. Taylor, M. O'Keeffe and O. M. Yaghi, *Science*, 2007, **316**, 268-272.
105. X. Feng, X. Ding and D. Jiang, *Chem Soc Rev*, 2012, **41**, 6010-6022.
106. D. Tian, H.-Z. Zhang, D.-S. Zhang, Z. Chang, J. Han, X.-P. Gao and X.-H. Bu, *RSC Advances*, 2014, **4**, 7506-7510.
107. S. K. Upadhyay, S. R. Pingali and B. S. Jursic, *Tetrahedron Letters*, 2010, **51**, 2215-2217.
108. S. Kandambeth, K. Dey and R. Banerjee, *J. Am. Chem. Soc.*, 2018, **141**, 1807-1822.
109. Q. Fang, Z. Zhuang, S. Gu, R. B. Kaspar, J. Zheng, J. Wang, S. Qiu and Y. Yan, *Nat. Commun.*, 2014, **5**, 4503.
110. L. Jiang, Y. Tian, T. Sun, Y. Zhu, H. Ren, X. Zou, Y. Ma, K. R. Meihaus, J. R. Long and G. Zhu, *J. Am. Chem. Soc.*, 2018, **140**, 15724-15730.
111. C. Zhang, S. Zhang, Y. Yan, F. Xia, A. Huang and Y. Xian, *ACS applied materials & interfaces*, 2017, **9**, 13415-13421.
112. W. Zhu, X. Wang, T. Li, R. Shen, S.-J. Hao, Y. Li, Q. Wang, Z. Li and Z.-G. Gu, *Polymer Chemistry*, 2018, **9**, 1430-1438.
113. X. Chen, Q. Dang, R. Sa, L. Li, L. Li, J. Bi, Z. Zhang, J. Long, Y. Yu and Z. Zou, *Chemical Science*, 2020, **11**, 6915-6922.
114. S. Royuela, E. Martínez-Periñán, M. P. Arrieta, J. I. Martínez, M. M. Ramos, F. Zamora, E. Lorenzo and J. L. Segura, *Chemical communications*, 2020, **56**, 1267-1270.
115. X. Zhu, S. An, Y. Liu, J. Hu, H. Liu, C. Tian, S. Dai, X. Yang, H. Wang and C. W. Abney, *AIChE Journal*, 2017, **63**, 3470-3478.
116. B. Ma, H. Guo, M. Wang, Q. Wang, W. Yang, Y. Wang and W. Yang, *Microchemical Journal*, 2020, **155**, 104776.
117. J. Lv, Y. X. Tan, J. Xie, R. Yang, M. Yu, S. Sun, M. D. Li, D. Yuan and Y. Wang, *Angewandte Chemie*, 2018, **130**, 12898-12902.
118. O. Rahmanian, M. Falsafin and M. Dinari, *Polymer International*, 2020, **69**, 712-718.
119. T. Wang, R. Xue, H. Chen, P. Shi, X. Lei, Y. Wei, H. Guo and W. Yang, *New Journal of Chemistry*, 2017, **41**, 14272-14278.
120. K. Liu, H. Qi, R. Dong, R. Shivhare, M. Addicoat, T. Zhang, H. Sahabudeen, T. Heine, S. Mannsfeld and U. Kaiser, *Nature chemistry*, 2019, **11**, 994-1000.
121. A. P. Cote, H. M. El-Kaderi, H. Furukawa, J. R. Hunt and O. M. Yaghi, *J. Am. Chem. Soc.*, 2007, **129**, 12914-12915.
122. J.-Y. Yue, Y.-P. Mo, S.-Y. Li, W.-L. Dong, T. Chen and D. Wang, *Chemical science*, 2017, **8**, 2169-2174.
123. T. S. Mathis, N. Kurra, X. Wang, D. Pinto, P. Simon and Y. Gogotsi, *Adv. Energy Mater.*, 2019, **9**, 1902007.
124. Z. Zha, L. Xu, Z. Wang, X. Li, Q. Pan, P. Hu and S. Lei, *ACS applied materials & interfaces*, 2015, **7**, 17837-17843.
125. J. Sun, A. Klechikov, C. Moise, M. Prodana, M. Enachescu and A. V. Talyzin, *Angewandte Chemie*, 2018, **130**, 1046-1050.
126. P. Wang, Q. Wu, L. Han, S. Wang, S. Fang, Z. Zhang and S. Sun, *Rsc advances*, 2015, **5**, 27290-27294.
127. C. Jain, R. Kushwaha, D. Rase, P. Shekhar, A. Shelke, D. Sonwani, T. G. Ajithkumar, C. P. Vinod and R. Vaidhyanathan, *J. Am. Chem. Soc.*, 2023, **146**, 487-499.
128. Z. Shan, M. Wu, Y. Du, B. Xu, B. He, X. Wu and G. Zhang, *Chem. Mater.*, 2021, **33**, 5058-5066.
129. D. Deng, *Energy Science & Engineering*, 2015, **3**, 385-418.

130. T. Kim, W. Song, D.-Y. Son, L. K. Ono and Y. Qi, *J. Mater. Chem. A*, 2019, **7**, 2942-2964.
131. R.-R. Liang, S.-Q. Xu, Q.-Y. Qi and X. Zhao, *J. Am. Chem. Soc.*, 2019, **142**, 70-74.
132. S.-Y. Ding, J. Gao, Q. Wang, Y. Zhang, W.-G. Song, C.-Y. Su and W. Wang, *J. Am. Chem. Soc.*, 2011, **133**, 19816-19822.
133. H. Li, J. Ding, X. Guan, F. Chen, C. Li, L. Zhu, M. Xue, D. Yuan, V. Valtchev and Y. Yan, *J. Am. Chem. Soc.*, 2020, **142**, 13334-13338.
134. B. Nath, W.-H. Li, J.-H. Huang, G.-E. Wang, Z.-h. Fu, M.-S. Yao and G. Xu, *CrystEngComm*, 2016, **18**, 4259-4263.
135. M. Dincă and J. R. Long, *Journal*, 2020, **120**, 8037-8038.
136. R. Tao, X. Shen, Y. Hu, K. Kang, Y. Zheng, S. Luo, S. Yang, W. Li, S. Lu and Y. Jin, *Small*, 2020, **16**, 1906005.
137. Z. Shan, X. Wu, B. Xu, Y.-l. Hong, M. Wu, Y. Wang, Y. Nishiyama, J. Zhu, S. Horike and S. Kitagawa, *J. Am. Chem. Soc.*, 2020, **142**, 21279-21284.
138. Y. Hu, N. Dunlap, S. Wan, S. Lu, S. Huang, I. Sellinger, M. Ortiz, Y. Jin, S.-h. Lee and W. Zhang, *J. Am. Chem. Soc.*, 2019, **141**, 7518-7525.
139. X. Li, Q. Hou, W. Huang, H.-S. Xu, X. Wang, W. Yu, R. Li, K. Zhang, L. Wang and Z. Chen, *ACS Energy Letters*, 2020, **5**, 3498-3506.
140. S. Horike, D. Umeyama and S. Kitagawa, *Accounts of chemical research*, 2013, **46**, 2376-2384.
141. Y. Zhang, J. Duan, D. Ma, P. Li, S. Li, H. Li, J. Zhou, X. Ma, X. Feng and B. Wang, *Angew. Chem. Int. Ed.*, 2017, **56**, 16313-16317.
142. Z. Guo, Y. Zhang, Y. Dong, J. Li, S. Li, P. Shao, X. Feng and B. Wang, *J. Am. Chem. Soc.*, 2019, **141**, 1923-1927.
143. K. Jeong, S. Park, G. Y. Jung, S. H. Kim, Y.-H. Lee, S. K. Kwak and S.-Y. Lee, *J. Am. Chem. Soc.*, 2019, **141**, 5880-5885.
144. G. Zhang, Y.-l. Hong, Y. Nishiyama, S. Bai, S. Kitagawa and S. Horike, *J. Am. Chem. Soc.*, 2018, **141**, 1227-1234.
145. Z. Xie, B. Wang, Z. Yang, X. Yang, X. Yu, G. Xing, Y. Zhang and L. Chen, *Angew. Chem. Int. Ed.*, 2019, **58**, 15742-15746.
146. X. Li and K. P. Loh, *ACS Materials Letters*, 2019, **1**, 327-335.

# Chapter 1

# Hydroxide ion–conducting viologen– bakelite organic frameworks for flexible solid-state zinc–air battery application

## 1.1. Introduction

Hydroxide ion-conducting materials are receiving substantial attention owing to their significance in green technologies like anion exchange membrane fuel cells (AEMFCs), Metal-air batteries and water electrolyzers.[1] [2] [3] Typically, hydroxide ions exhibit low conductivity compared to the protons due to their sluggish diffusion and higher mass.[4] Also, the proton-conducting materials are well established and commercialized for various energy applications.[5] [6] [7] In comparison, the hydroxide ion-conducting materials are still in the infancy stage. Hence, the rational design of hydroxide ion-conducting materials is beneficial and would pave the way for application specific charge-stroage devices.

The rapid increase in the energy requirement provides ample attention to the charge storage devices. [8] [9]  In order to manage the everlasting energy demand, it is necessary to develop efficient and cost-effective charge storage devices.[10] [11]  In this regard, Zinc-air batteries (ZABs) are getting wide attention due to their high energy density, low cost and safe nature and, have been used for many applications like hearing-aid devices, cameras, grid-scale energy storage, *etc*.[12] [13] [14] [15]  Development of high-performing ZABs requires the advancement of the electrodes and the separator.[16] [17] Along with the electrode kinetics, the hydroxide ion transport through the electrolyte largely determines the efficiency of ZABs.[18] The liquid-based electrolytes create complications in fabricating or handling the devices and achieving a long cycle life.[19] [20] In comparison, the solid-state electrolytes give less trouble in these regards and their leakage-proof framework offers superior safety features.[21] Therefore, developing ZAB with solid-state separators and concomitantly possessing improved performance and flexibility would benefit applications.[22] However, the key bottleneck associated with the hydroxide ion-conducting materials is their low ionic conductivity and poor stability under harsh chemical environments.[23] Several ion-conducting ($H^+$ or $OH^-$) materials with better conductivity have been reported in the literature in the pelletized state, but their practical potential as a thin and free-standing solid-state separator is not explored.[4] [24] [25] [26] [27] Hence, we developed a thin hydroxide ion-conducting solid-state separator-cum-electrolyte for ZAB from the cationic polymer by coating it on filter paper adopting a simple dip-coating strategy.

Various kinds of separators have been employed for ZABs to transport $OH^-$ ions and some porous separators provide satisfactory battery performance. [14] [28] A fundamental issue associated with the porous separators is the passage of zincate ions ($Zn(OH)_4^{2-}$) through the pores.[29] One can overcome this by integrating the porous separators with the hydroxide ion-conducting insoluble materials. This would block the pores, allow the passage of $OH^-$ ions, and restrict the movement of zincate ions.[30] Polymers are being intensely probed for their stability advantage,[31] and recently, amide polymers constructed from simple monomers (acyl chloride + melamine) were shown to possess strengths comparable to steel.[32] This inspired us to explore the potential of simple systems such as Bakelite and viologen for this task-specific application. Towards this approach, we have

synthesized triazine-resorcinol and viologen-based cationic polymeric organic frameworks (POFs) with enriched hydroxyl (−OH) groups.[33] These POFs can be obtained in a large scale via a one-pot synthesis using Bakelite chemistry: forming robust C−C bonds without any catalyst.[34] Such types of POFs are chemically robust, thermally stable and find use in a wide range of applications, including energy storage, gas storage, catalysis, and anion exchange.[35] [36] [37] [38] The viologen-based quaternary center is counterbalanced by the larger anion like Br⁻ which finds easy exchange with OH⁻ ions. Recently, our group reported a family of cationic POFs, amongst which IISERP-POF11 (**1**) performed excellently for the anion exchange.[38] Therefore, in the present chapter, hydroxide ion-exchanged IISERP-POF11, IISERP-POF11_OH (**1_OH**), was integrated with cellulose paper (IISERP-POF11_OH@Filter Paper, **1_OH@FP**) and employed as the solid-state separator-cum-electrolyte for Zinc-air battery applications. The integrated system displayed an improved performance for the ZAB and validated the suitability of employing **1_OH** for energy applications.

## 1.2. Results and discussion

### 1.2.1 Synthesis and bulk characterizations of as-made IISERP-POF11 (1) and hydroxide exchanged IISERP-POF11_OH (1_OH):
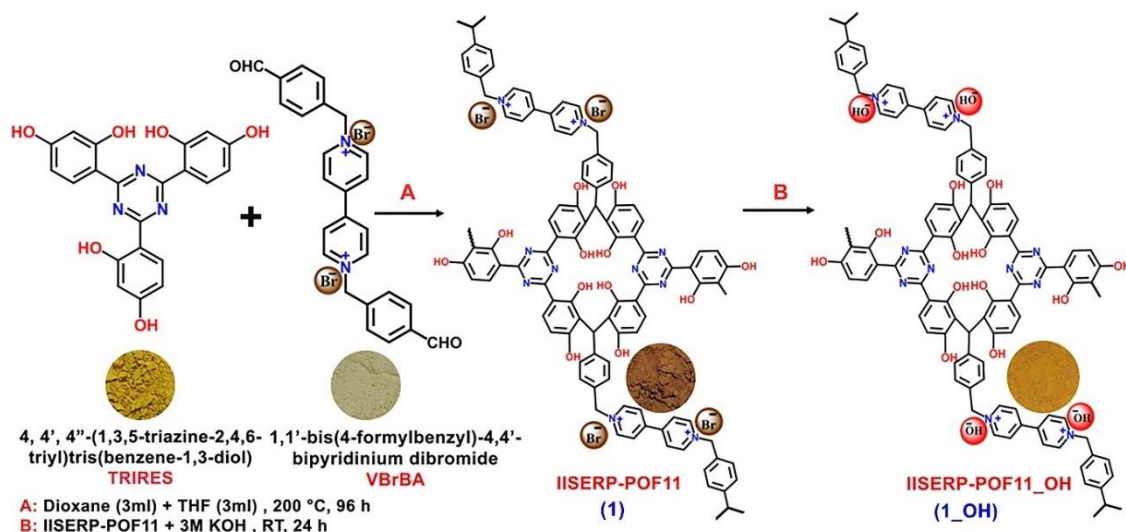


**Scheme 1.1:** Synthetic procedure of 1_OH. Insets show the photographic images of the corresponding compounds.

The synthesis of 1 from the monomers and its further conversion into 1_OH after the exchange of the Br⁻ with OH⁻ ions is illustrated in Scheme 1 (detailed synthesis procedure is provided in the Appendix). The formation of as-synthesized polymer was confirmed by the various characterization techniques such as NMR, FTIR, FESEM, HRTEM, TGA, and $N_2$ adsorption measurements. The ^{13}C cross-polarization (CP) magic angle spinning (MAS) solid state Nuclear Magnetic Resonance (NMR) indicates the presence of Bakelite type coupling between triazine-resorcinol and viologen-based bipyridinium aldehyde (Figure 1.1), along with some unsubstituted sites on the phloroglucinol rings led to the formation of a characteristic aliphatic
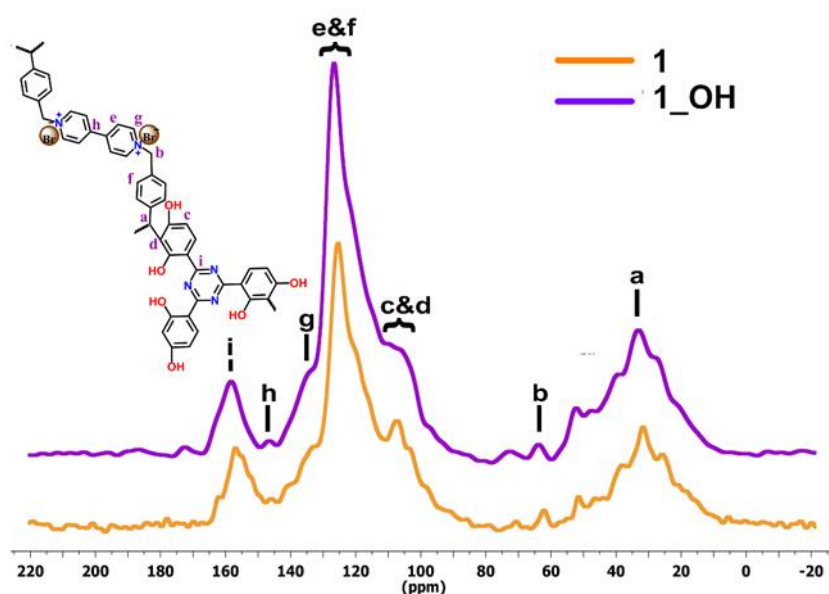


**Figure 1.1:** ^{13}C-CPMAS spectra of 1 and 1_OH.

C-C bond which was observed around 26 ppm (a).[39] [40] It was followed by the other characteristics peaks from aromatic groups like triazine around 172 ppm (i) and aromatic peak for viologen-based unit around 151 ppm (h). The aliphatic peaks for building blocks around 65 ppm (b) were intact. While this displays the polymerization taking place, to confirm the stability of the polymer powder, we recorded the IR and NMR spectrum of the material subjected to boiling in THF+DMF mixture, followed by a 24 h soak in 6 M KOH solution. All the characteristic peaks remain and are positioned at similar chemical shifts with matching intensity. This exceptional
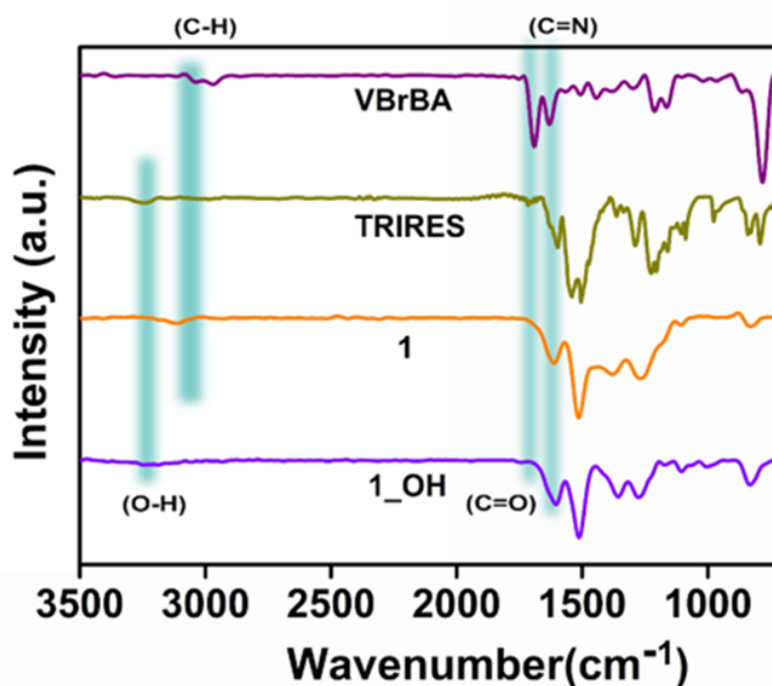


**Figure 1.2:** FTIR spectra of TRIRES, VBrBA, 1, and 1_OH.

chemical stability, and functional group integrity of the polymer especially towards harsh treatments is highly desirable for electrolyte applications (Figure A1.1). Subsequent to the anion exchange (Br$^-$ with OH$^-$ ions), a significant colour change from brown to yellow was observed and is represented with the photographic images in Scheme 1.1.

The Figure 1b shows the comparative IR spectrum of the monomers *i.e.*, 1,1'-bis(4-formylbenzyl)-4,4'-bipyridiniumdibromide (VBrBA), 4,4',4''-(1,3,5-triazine-2,4,6-triyl)tris(benzene-1,3-diol) (TRIRES),as-synthesized cationic polymer (1), its hydroxide exchanged form, 1_OH. The disappearance of the C=O (1690 cm$^{-1}$) from the monomer VBrBA with the polymerization confirms the C-C bond formation between the aldehyde and the phenolic moieties (Scheme 1.1). Also, the presence of C=N (1620 cm$^{-1}$) assures that the building blocks are intact in 1 and 1_OH (Figure 1.2).

The field emission scanning electron microscopy (FESEM) images of 1 indicate that the particles are connected or intergrown microspheres of different diameters ranging from 500 nm to 2 mm (Figure 1.3). It is confirmed from Figure 1.3 that there is no deformation in the shape of these microspheres after treating with 3 M KOH solution, i.e., on the formation of 1_OH. This indicates their textural
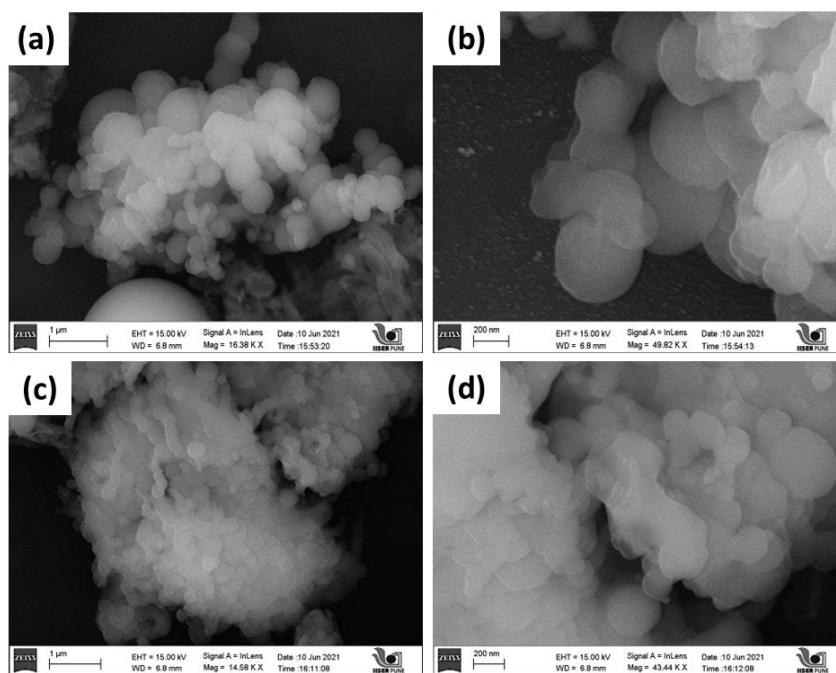
**Figure 1.3:** FESEM images of (a,b) 1 and (b,c) 1_OH.

stability under the harsh corrosive environment. Thus, 1_OH could be suited for operating under concentrated alkaline conditions.

In the Energy dispersive X-ray (EDX) analysis, the drop in the atomic percentage of Br$^-$ ions from 1.74 to 0.21% confirms the effective exchange of Br- ions with OH- to form 1_OH (Figure 1.4). The K$^+$ ion traces in 1_OH is negligible, which confirms that the hydroxide ions are counter-balanced by the cationic centers of the polymer.

The High-resolution transmission electron microscopy (HRTEM) images of 1 and 1_OH are displayed in Figure 1.5. The HRTEM showed that the spherical balls in 1_OH are connected incessantly, which could aid the ionic transport across grains and spheres. After OH$^-$ ion exchange, we noticed a slight



| Element | Weight% | Atomic% |
|---------|---------|---------|
| C K | 68.5 | 78.5 |
| N K | 10.7 | 10.5 |
| O K | 10.8 | 9.2 |
| Br L | 10.0 | **1.7** |
| Total | 100.00 | |

| Element | Weight% | Atomic% |
|---------|---------|---------|
| C K | 74.1 | 79.3 |
| N K | 6.7 | 6.2 |
| O K | 17.7 | 14.2 |
| Br L | 1.3 | **0.1** |
| K K | 0.2 | 0.2 |
| Total | 100.00 | |
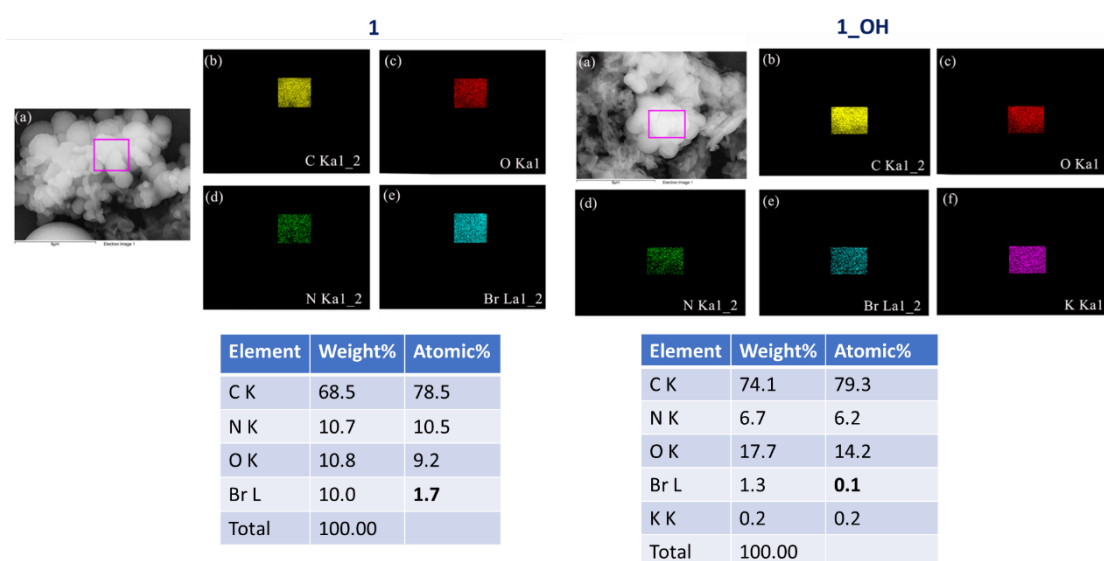
**Figure 1.4:** Elemental mapping and EDX analysis of 1 and 1_OH.

decrease in the surface diameter of 1_OH spheres and this could be due to more compacting from OH⁻ compared to Br⁻. However, the spherical morphology is still intact (Figure 1.5).
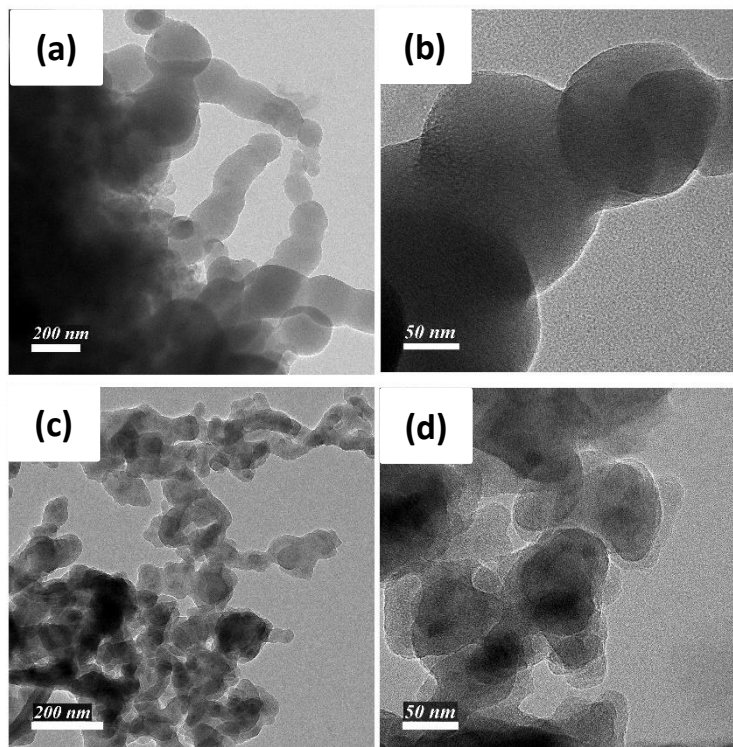


**Figure 1.5:** HRTEM images of (a, b) 1 and (c, d) 1_OH.

Thermogravimetric analysis in Figure 1.6 revealed that the framework 1 is stable up to 280 °C. We attribute this to the strong C-C bond formed between the monomers, resembling Bakelite. The cationic polymer treated with 3 M (1_OH) and 6 M KOH (1_6OH) display slightly different TGA profiles (Figure 1.6), but their thermal stabilities are comparable.
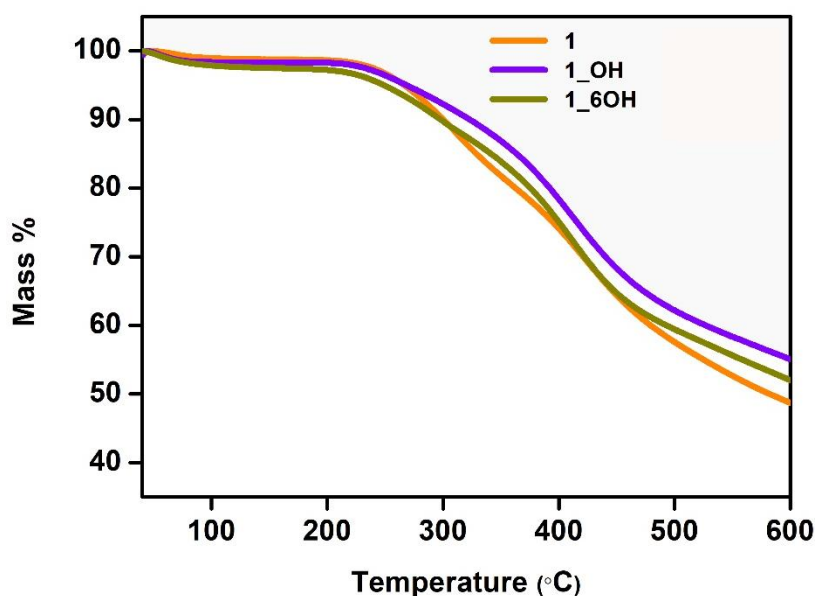


**Figure 1.6:** Comparative thermogravimetric analysis plot for 1, 1_OH and 1_6OH.

The contact angle measurements pointed at the surface of the as-made polymer powder, 1, being super-hydrophobic; however, the 1_OH prepared by anion exchange in an aqueous alkaline solution yielded



**(a)**

**(b)**
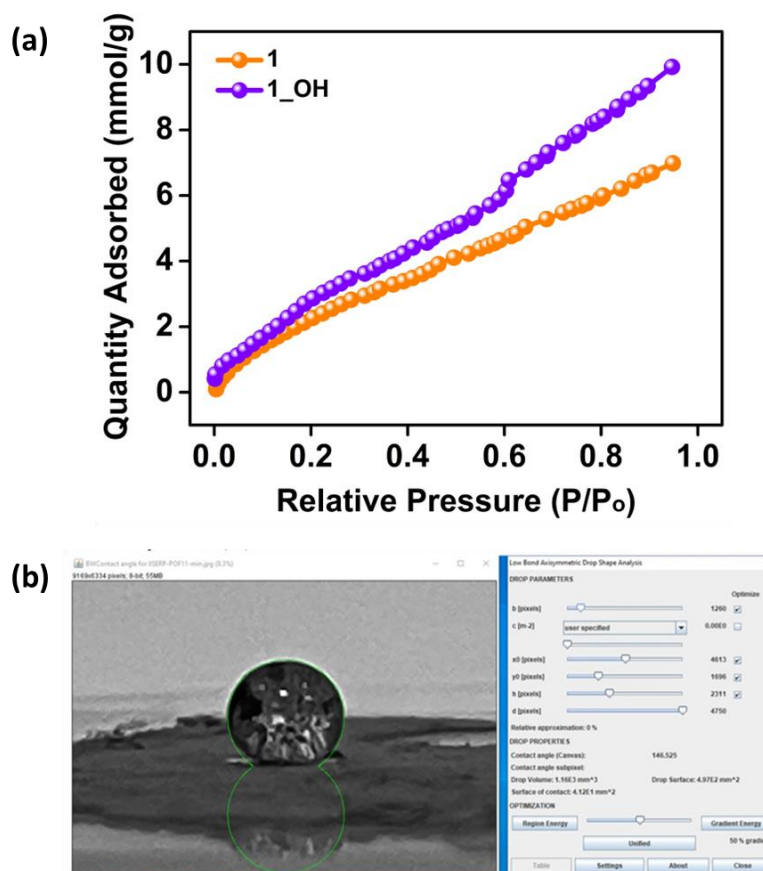
**Figure 1.7:** (a)Water adsorption isotherms of 1 and 1_OH. (b) Contact angle of the droplet of water sitting on the surface of the 1.

a final powder that was hydrophilic (Figures 1.7). This surface wettability is crucial for the material's interaction with electrolytes. We investigated the intrinsic porosity with water sorption isotherms. The water adsorption isotherms of 1 and 1_OH showed a very similar profile stating that there were no major changes to the pore environment or structure. The overall water capacity of the 1_OH is higher
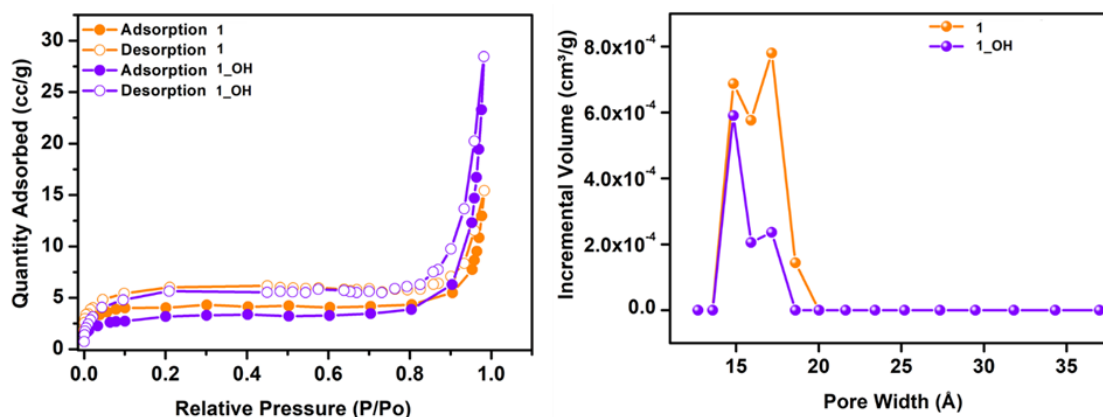


**Figure1.8:** Adsorption isotherms and plot of the pore width vs. incremental pore volume of 1 and 1_OH.

than 1, suggesting improved intrinsic wettability. Thus, the near super-hydrophobic (148° ± 3°) material with Br⁻ containing framework becomes much more hydrophilic when exchanged with OH⁻. Notably, there was no noticeable swelling of the polymer or significant change in density.

The density functional theory-based model fitted to the 77 K N$_2$ isotherm shows the majority of the pores being 15 to 18 Å in size, which are still intact after the ion exchange (Figure 1.8). However, the N$_2$ uptakes are nominal, which is expected as the pores are permanently occupied by the counter-balancing anions. Still, there is sufficient openness to support the transport of OH- ions; also, unlike the crystalline frameworks, these polymers can exhibit structural flexibility with changing humidity, opening up spaces for dynamic interactions between the framework atoms and the free hydroxide ions. This impacts the electrolyte's wetting and hydroxide ion transport characteristics (Figure 1.7).
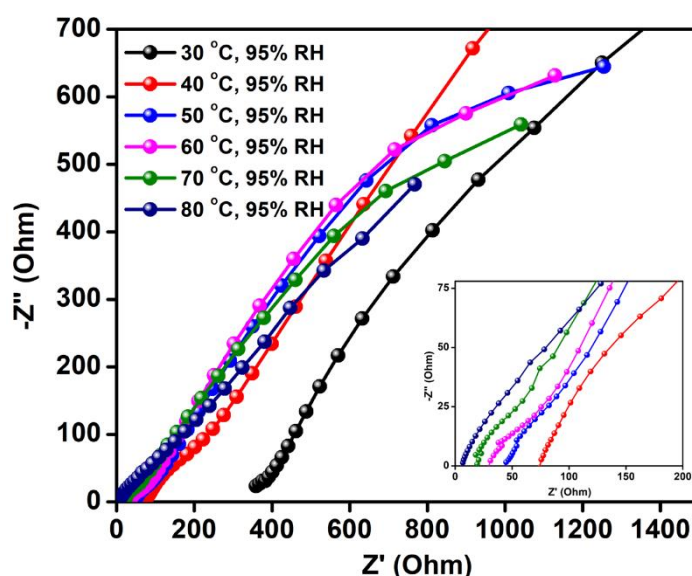


**Figure 1.9:** Nyquist plots from the temperature dependent conductivity measurements.

## 1.2.2 Electrochemical studies:

Electrochemical impedance analysis was performed in the frequency range of $10^6$ to 0.1 Hz with an AC amplitude of 10 mV using Solartron impedance analyzer. The impedance was recorded at variable temperatures from 30 °C to 80 °C with a constant relative humidity of 95 % and the data is presented as Figure 1.9. To evaluate the intrinsic conductivity of the 1_OH, the measurements were performed on a densely pressed pellet of the same. The equivalent circuit was employed for fitting all the Nyquist curves, using the Zview-4 software. At a constant relative humidity of 95 %, the OH⁻ ion conductivity value increases from 2.7 x $10^{-4}$ S/cm at 30 °C to 1.4 x $10^{-2}$ S/cm at 80 °C (Figure 1.9; Table A1.1, Appendix).

In order to check the humidity dependent conductivity of **1_OH**, we measured ac-impedance at 80 °C by varying the humidity (60% RH, 80% RH and 95% RH) (Figure 1.10). The conductivity values are 3.6 x $10^{-5}$, 3.8 x $10^{-4}$ and 1.4 x $10^{-2}$ S/cm at RH of 60%, 80% and 95%, respectively. The increase in
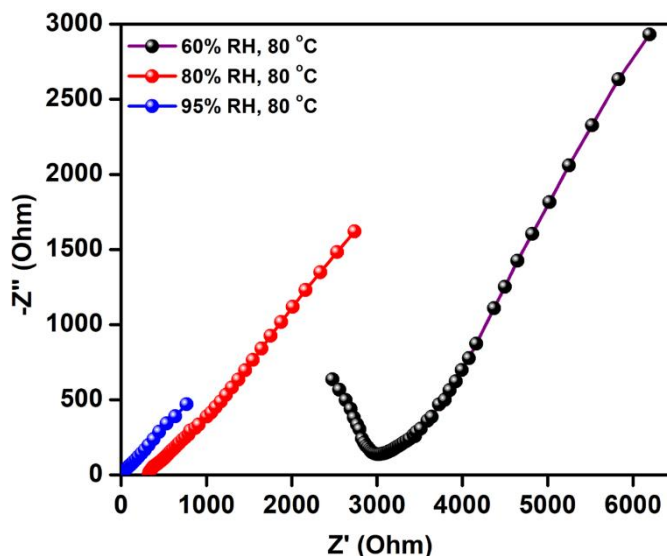
**Figure 1.10:** Humidity dependent Nyquist plots of 1_OH at 80 ℃.

hydroxide ion conductivity at 80 °C with increasing temperature suggests lowering of activation energy, while the increase in conductivity with increasing humidity suggests water could be playing a crucial role via hydrogen bonding.[41]

Fitting an Arrhenius equation to this temperature-dependent impedance data yields an activation energy of 0.52 eV (Figure 1.11) suggesting a mixed Grotthuss-Vehicular diffusion mechanism.[42] The observed activation energy is comparable to some of those reported for hydroxide ion in other nanoporous structures.[43]
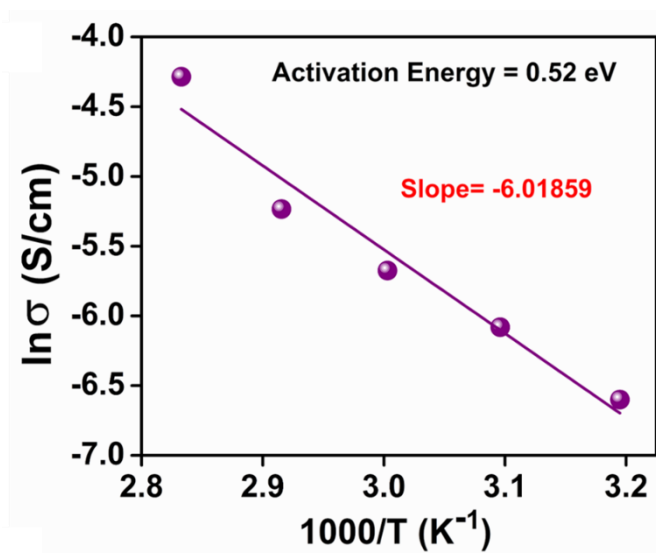


**Figure 1.11:** Arrhenius plot of 1_OH.

An equivalent circuit fit to the most promising Nyquist plots (80℃, 95% RH) reveals an ohmic resistance of 3.22 ohm (neat pellet) (Figure 1.12). In the fitted equivalent circuit, we confirmed the need for a CPE component, by measuring the CV of the 1_OH, which clearly indicated the capacitive behavior being present (Figure 1.12).

In our case, considering that the hydroxide is moving in channels lined with hydroxyl groups and triazine, both of which might provide some hydrogen bond assistance resulting in Grotthuss mechanism, at the same time, under the applied ac-potential, there could be sufficient force for a vehicular motion
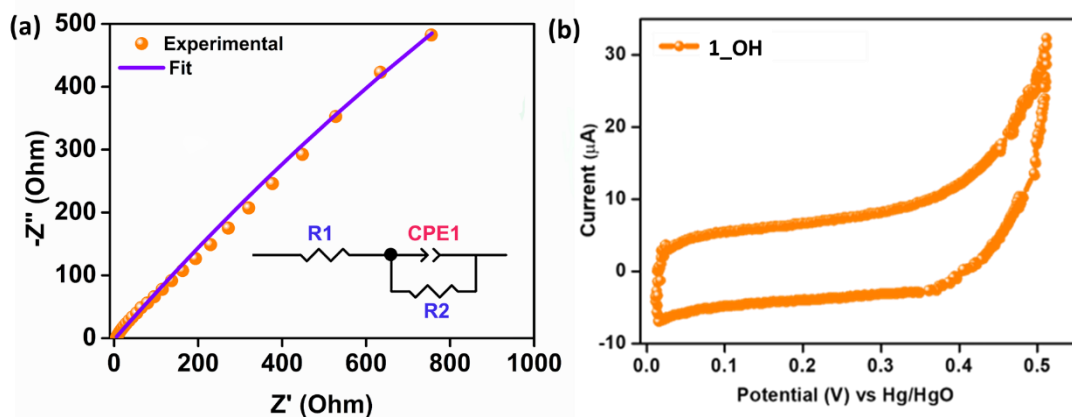


**Figure 1.12:** (a) An equivalent circuit fit to the Nyquist plot of 1_OH at 80 °C and 95% RH. (b) Cyclic voltammogram of 1 measured using a three-elctrode system in 1M KOH electrolyte with Hg/HgO as reference and Pt wire as counter electrode.

too. Due to the absence of OH$^-$ ions in the pristine polymer (1), it shows a poor ionic conductivity value of 7.39 x 10$^{-5}$ S/cm at 80 °C and 95% RH. This is expected as the Br$^-$ ions are heavier and will be even less effective for a hydrogen-bond assisted Grotthuss type movement.–Further, the comparison of the equivalent circuit fitted Nyquist plots of the 1 vs. 1_OH (Figure 1.13) suggests that the series resistance and charge-transfer resistance both are substantially higher for the 1 (R1= 352 Ω, R2=509 Ω) compared to the 1_OH (R1=3.22 Ω, R2=11.76 Ω). The large semi-circle in the low-frequency regime in the case of 1 suggests limited or restricted diffusion even in the same time-scale of measurements as employed for the 1_OH. Meanwhile 1_OH has a typical semi-infinite linear diffusion – that is, diffusion in one
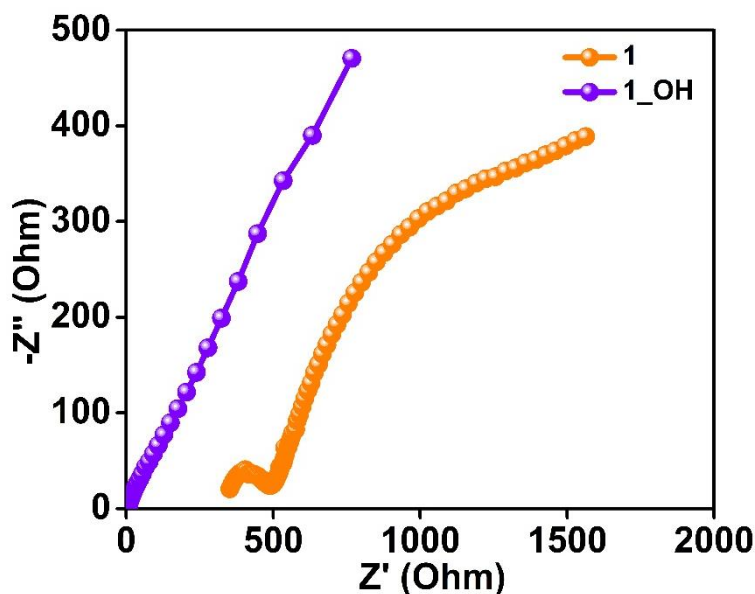


**Figure 1.13:** Comparison of the Nyquist plots of 1 containing Br$^-$ as the counter ion vs. 1_OH.

dimension which is only bounded by a large planar electrode on one side (45° angle with Z'-axis), a typical Warburg behavior.

A CPE-P value close to 0.5 for 1_OH pellet is suggestive of a pseudocapacitive behavior expected for the polymer with the porous structure. Remark: A transmission line model mimicking the Fickian diffusion, wherein the movement of ions through the pores is coupled to the movement of electrons through the pore walls, was not chosen. This is considering that the polymer does not have a crystalline structure with highly ordered pores and also the electronic conductivity in larger length scales is limited.[44]
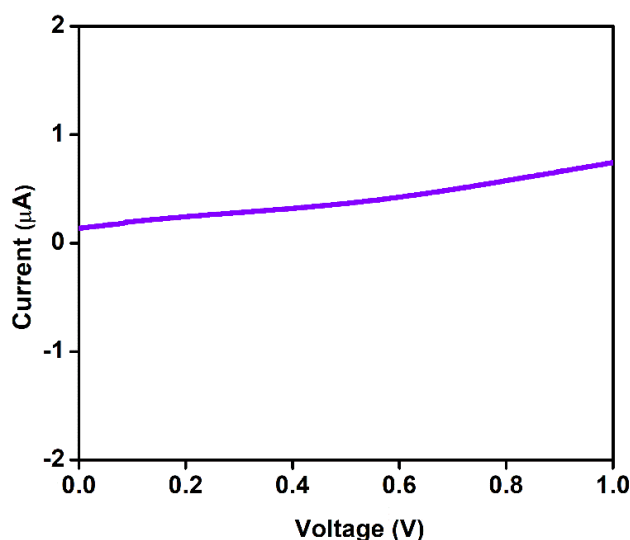


**Figure 1.14:** Linear sweep voltammogram (LSV) of 1_OH measured using a two-probe set-up.

The linear sweep voltammetry (LSV) was conducted to check the electronic conductivity of 1_OH in the potential window of 0 to 1.0 V with a scan rate of 10 mV/s (Figure 1.14). 1_OH shows negligible electronic conductivity which suggests that the observed conductivity is predominantly ionic arising from the OH⁻ ions.

To assess the ability of 1_OH in delivering a stable hydroxide-ion conductivity, we measured it at 80 °C and 95 % RH for 15 h. There is a build-up of a small charge transfer resistance over 15h, and notably, the 1_OH retains > 95% of its conductivity (Figure 1.15).

This hydroxide ion conductivity is reproducible across different batches of the sample (Figure 1.15 inset). To check the cyclic stability of **1_OH** for OH⁻ transport, the pellet was dried overnight at 100 °C in a vacuum oven, the impedance analysis was carried out for both the forward cycle (increasing the temperature from 30 to 80 °C at 95% RH) and the backward cycle (decreasing the temperature from 80 to 30 °C at 95% RH) (Figure 1.16).
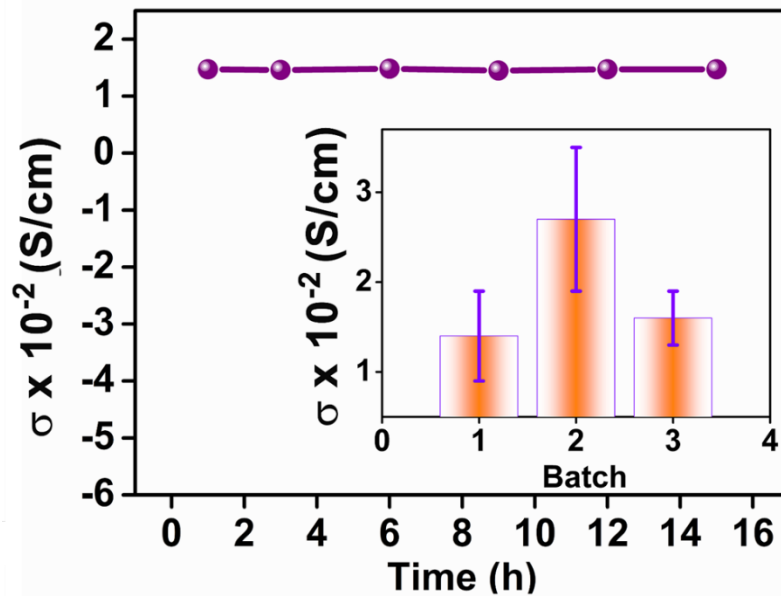
**Figure 1.15:** Conductivity of 1_OH at 80 °C and 95% RH recorded for 15 h, inset shows the conductivity is reproducible across different batches of the sample.

The conductivities remained the same during the cycling reflecting the electrochemical stability of the polymer and the shape/profile of the Nyquist plots remained alike suggesting that the pathway and the mechanism of conduction is unchanged. We calculated the diffusion coefficient for the hydroxide ions inside the cationic polymer framework using the Z' vs. $(\omega)^{-1/2}$ plot. The low-frequency spectrum of the impedance plot yielded the characteristic linear fits (Figure 1.16) from which the diffusion coefficients were estimated to be 2.9 x $10^{-5}$ cm$^2$/s at 80 °C with 95% RH. The diffusion coefficient increases systematically with increase in temperature (Figure 1.16b). The calculated diffusion coefficients match well with the theoretical values reported in the literature.[45] [46] However, we could not find any experimentally calculated diffusion coefficients for hydroxide ions inside a porous material, but for Cl$^-$ the diffusion coefficient is of the order of $10^{-8}$ cm$^2$/s. [47]
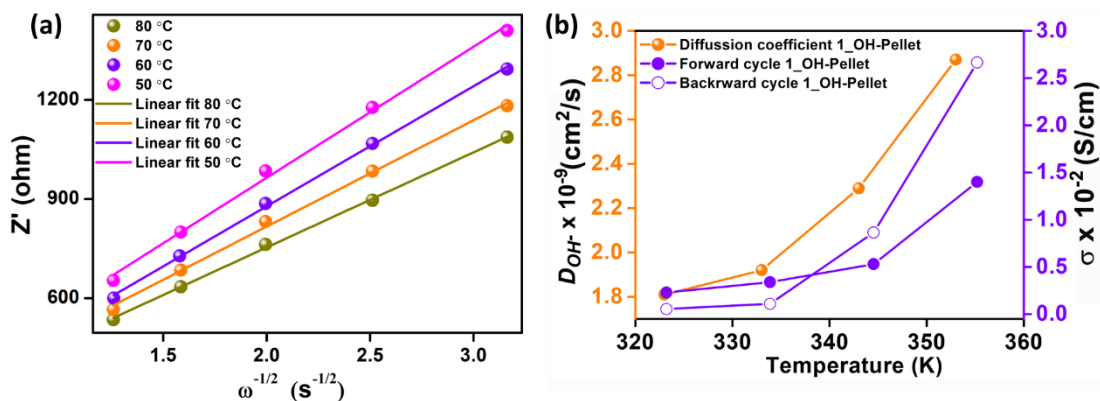


**Figure 1.16:** (a) A plot of the Z' versus $\omega^{-1/2}$ for 1_OH at 95% RH at different temperatures. (b) Hydroxide ion diffusion coefficient and forward-backward cycling plot for OH- conductivity of 1_OH at different temperatures and a constant relative humidity of 95%.

## 1.2.3 Conductivity characteristics of 1_OH coated on Filter Paper (1_OH@FP):

Encouraged by the appreciable hydroxide ion conductivity and stability exhibited by this viologen polymer, we set out to investigate its scope as a solid-state electrolyte in a Zinc-air battery. It is hugely advantageous to coat the polymer on a porous filter paper, which provides a bulk wettable microporous-macroporous separator-cum-electrolyte membrane. However, the composite needs to retain the high
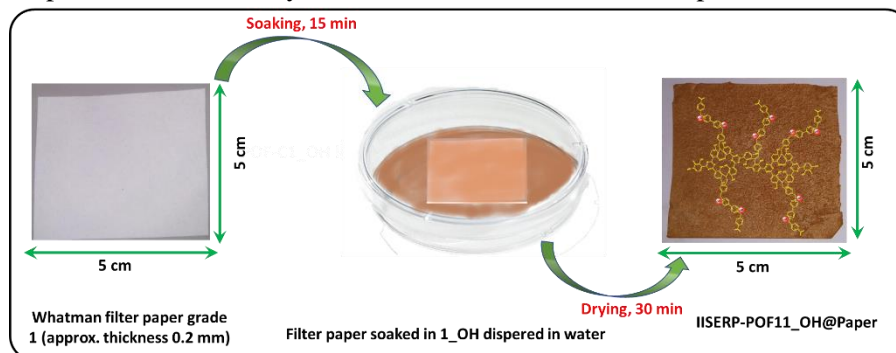


**Scheme 1.2:** Schematic of the preparation of thin, flexible OH⁻ ion conducting membrane.

levels of OH⁻ ion conductivity. To investigate this, the 1_OH was devised into a separator-cum-electrolyte by coating it on research-grade Whatman filter paper (1_OH@FP). Commonly available filter paper was chosen owing to its advantageous features such as low cost, lightweight, flexibility and easy accessibility.[48] The dip-coating method was used to deposit the polymer by soaking cellulose
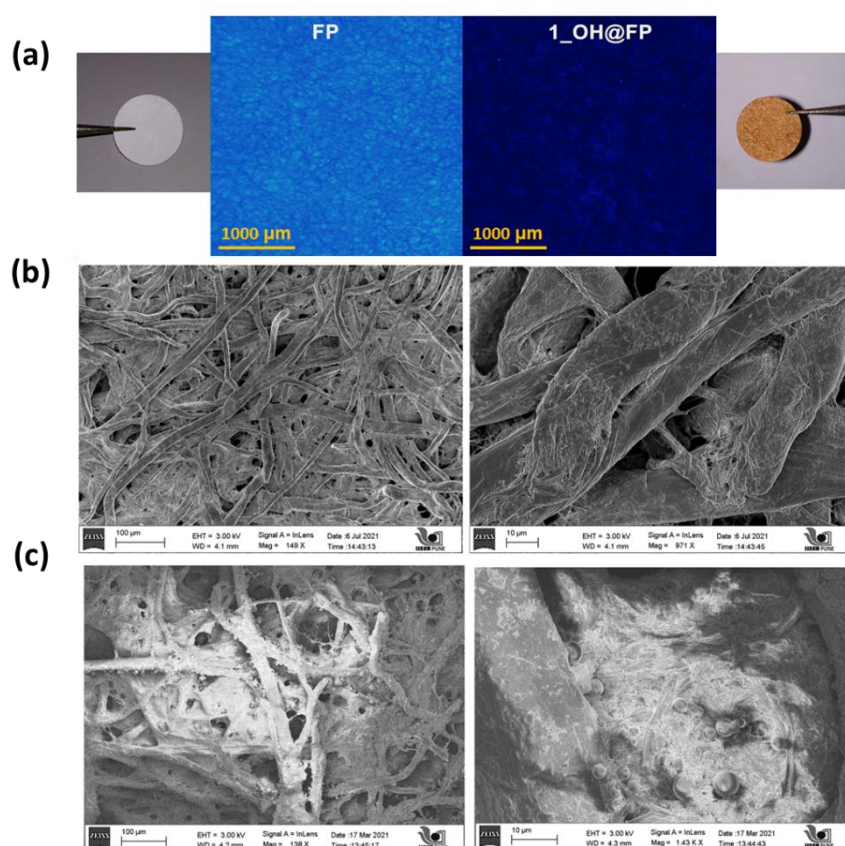


**Figure 1.17:** (a) Macro zoom fluorescence microscope images of neat filter paper and 1_OH@FP with side-on images showing the corresponding photographic images. FESEM image of (a) neat filter paper and (b) 1_OH@FP.

paper in a dispersed solution of 1_OH in water. The process is scalable and 25 cm$^2$ 1_OH@FP was prepared in a few hours.
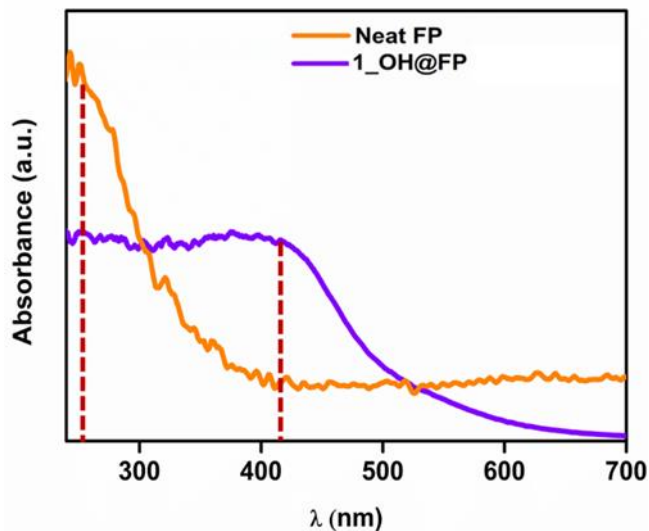


**Figure 1.18**: Comparison of the solid-state UV absorption spectra of neat FP vs. 1_OH@FP showing significant lowering of the absorbance intensity (@280 nm) of the FP upon coating with the polymer.

The fluorescence microscopy images illustrated in Figure 1.17a shows the loss of fluorescence of the FP upon loading with the polymer. Its uniform loading on paper is evident. Typically the filter paper has entangled cellulose fibers (Figure 1.17b) which are rich-in terminally placed binding groups, which are likely to be compatible with our hydroxyl-functionalized polymer backbone. From the FESEM images it is evident that the polymer composite buries extremely well into the cellulose matrix of the paper (Figure 1.17c; A.1.3, Appendix). This could be crucial to providing an intimate contact between the two entities in the composite. Even a strong thumb-pressure does not make the polymer particles lose its adhesion with the paper.

The solid-state UV-Vis absorption spectra of neat FP vs. 1_OH@FP showed lowering of the absorbance intensity (@280 nm) of the FP upon coating with the polymer (Figure 1.18), which is in agreement with the results from the fluorescence microscopy. These suggest the polymer directly contacting the electrolyte and the electrodes, while the paper is acting as a separator.

The hydroxide ion conductivity of 1_OH@FP was analyzed at 80 °C and 95 % RH and the Nyquist plot is presented as Figures 1.19. 1_OH@FP shows a OH$^-$ conductivity value of 4.5 x 10$^{-3}$ S/cm at 80 °C and 95 % RH (R1 = 10.42 and R2 = 18.22 Ω), which is quite comparable to the values obtained with the pellets at similar operating conditions. The same equivalent circuit fits extremely well. From the fitted data we observe the resistances of the 1_OH@FP is relatively higher, which is expected as more interfaces are generated and the paper is much less conductive. Notably the CPE value of the 1_OH (0.45) increases to 0.72 for the 1_OH@FP indicating the increase in double layer capacitive character.

Interestingly, the ion diffusion is noticeably improved when the material is coated on the FP (Figure 1.20). Comparing the Warburg tail of the 1_OH pellet versus the 1_OH@FP brings some noteworthy features. At lower frequencies, the diffusion tail of the 1_OH@FP starts to deviate more and more from making an angle of 45° with the x-axis, and this indicates deeper penetration of the ions into the material even at these low frequencies, which is expected as the active material is coated on a paper to form a much thinner electrolyte membrane compared to the pellet. This points at the advantage of making this paper-derived electrolyte-cum-separator units. Importantly, the overall conductivity still remains very much in acceptable regime for a hydroxide-ion conducting electrolyte. Thus, the 1_OH@FP provides an appropriate electrolyte material with micro-macroporous structure that still inhibits the direct zincate ion crossover through the separator, properties which are crucial for the battery performance.

### 1.2.4 1_OH@FP as solid-state electrolyte in ZAB:

The excellent ionic conductivity of 1_OH@FP fascinated us to use it for Zinc-air battery applications. For this, 1_OH@FP was employed as the solid-state separator-cum-electrolyte by sandwiching between the electrodes. Figure 1.21 depicts the schematic of the Zinc-air battery assembly with its components.



| | 1_OH-Pellet | 1_OH@FP |
|---|---|---|
| R1 | 3.22 | 10.42 |
| CPE-T | $5.6 \times 10^{-6}$ | $5.7 \times 10^{-6}$ |
| CPE-P | 0.45 | 0.72 |
| R2 | 11.76 | 18.22 |
| Wo-R | 965.7 | 1503 |
| Wo-T | 0.75 | 0.033 |
| Wo-P | 0.44 | 0.68 |
| Chi-Squared Value | $5.7 \times 10^{-3}$ | $3.1 \times 10^{-3}$ |
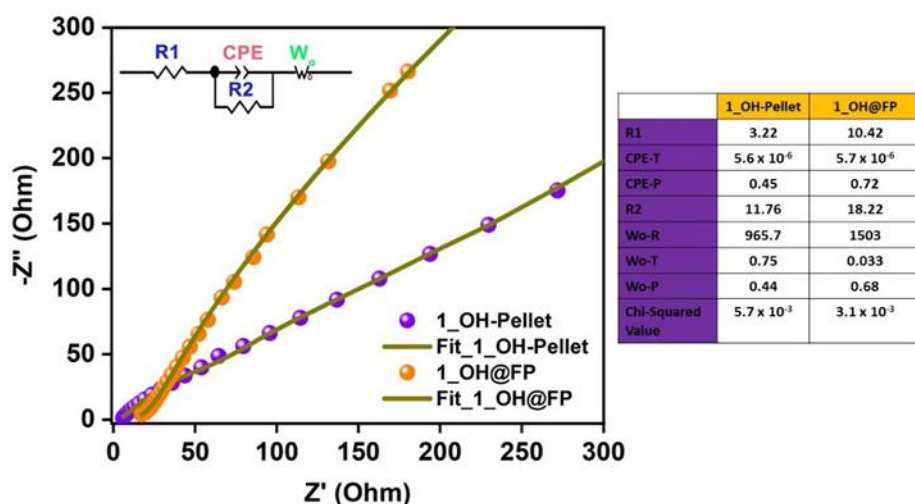
**Figure 1.19:** Comparative Nyquist plot of 1_OH and 1_OH@FP at 80 °C and 95% RH. Table shows the values for each fitting parameter.

During discharge, oxygen electrocatalytically reduces to form hydroxide ions at the cathode.[49] At the anode, zinc would oxidize to $Zn^{2+}$. The zinc ions would react with the hydroxide ions to form zincate ions and further to ZnO. To assess the performance of 1_OH@FP in ZAB, LSV was performed at a scan rate of 10 mV/sec and shown in Figure 1.22a. The polarization analysis presented in Figure 4c
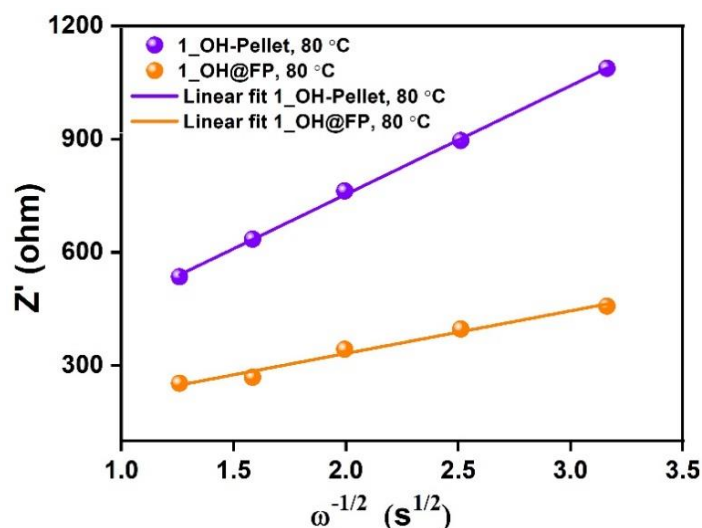
**Figure 1.20:** Comparative plots of the Z' versus $\omega-1/2$ for 1_OH and 1_OH@FP at 80 °C and 95% RH.

shows a maximum power density of 115 mW/cm$^2$ for 1_OH@FP based battery compared to 38 mW/cm$^2$ obtained for the neat filter paper-based counterpart. The resistances of the 1_OH@FP vs. neat
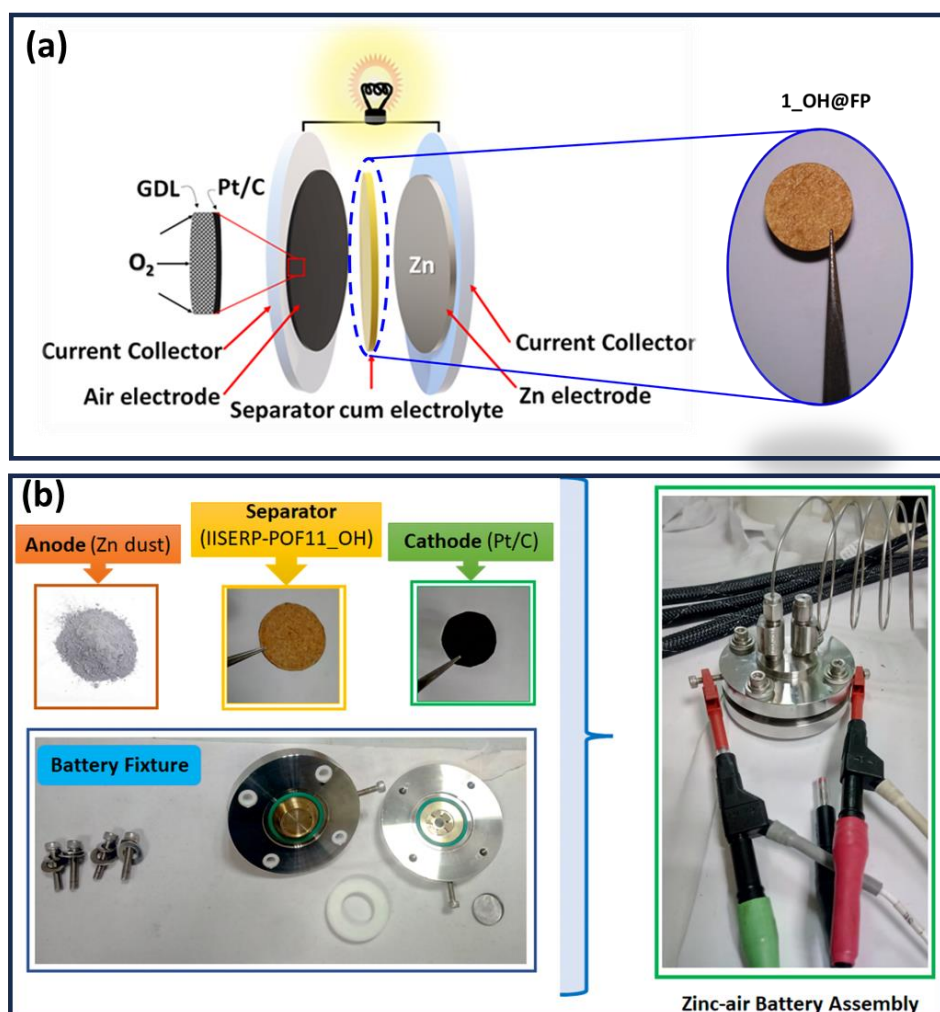


**Figure 1.21:** (a) The schematic of the ZAB with its components, (b) Photographic images of the ZAB assembly.

FP were determined from impedance analysis performed on their respective ZAB assemblies. The ohmic drop in 1_OH@FP is notably lower compared with neat filter paper (1.55 vs. 2.1 Ω ) (Figure 1.22a). Also, the resistance increases almost by 0.85 ohm during the use of the neat filter paper as electrolyte support in the battery which was run for about 2hrs. In contrast, the 1_OH@FP, maintains almost the same resistance even after 8hrs under comparable battery set-up. It is worth mentioning that even a difference of 0.55 Ω (between FP vs 1_OH@FP) hugely impacts the power density (Figure 1.22) as well as the specific capacity of the ZAB derived out of these electrolyte supports.

Accordingly, the 1_OH@FP containing battery exhibits a high specific capacitance of 435 mAh/g
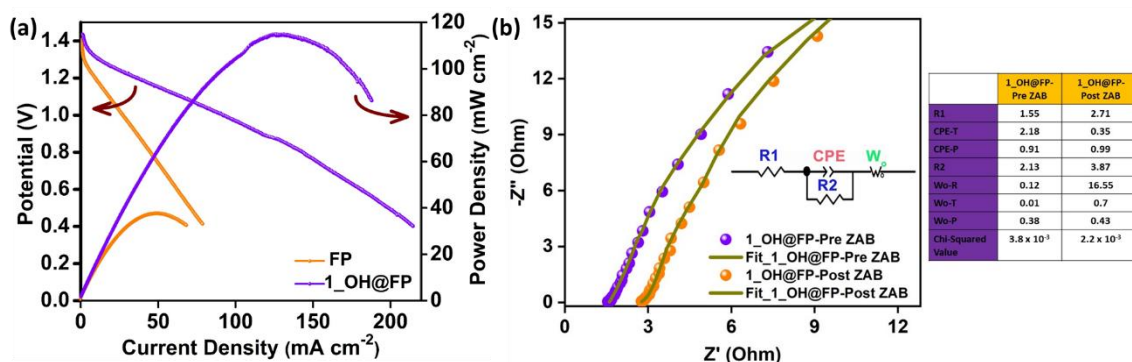


**Figure 1.22:** (a) Polarization plot of neat filter paper and 1_OH@FP based ZAB. (b) Comparison of the Nyquist plots for the 1_OH@FP measured in the zinc-air battery set-up. Table shows the values for each fitting parameter.

compared to 397 mAh/g obtained for the neat paper-based battery (Figure 1.23). Furthermore, the Figure 1.23 inset shows that the 1_OH@FP containing battery delivers four times more run time compared with FP based ZAB.

Flexible solid-state ZAB was fabricated to show the practical applicability of the as-prepared 1_OH@FP. The fabricated solid-state battery offers an OCV value of 1.44 V in an air atmosphere
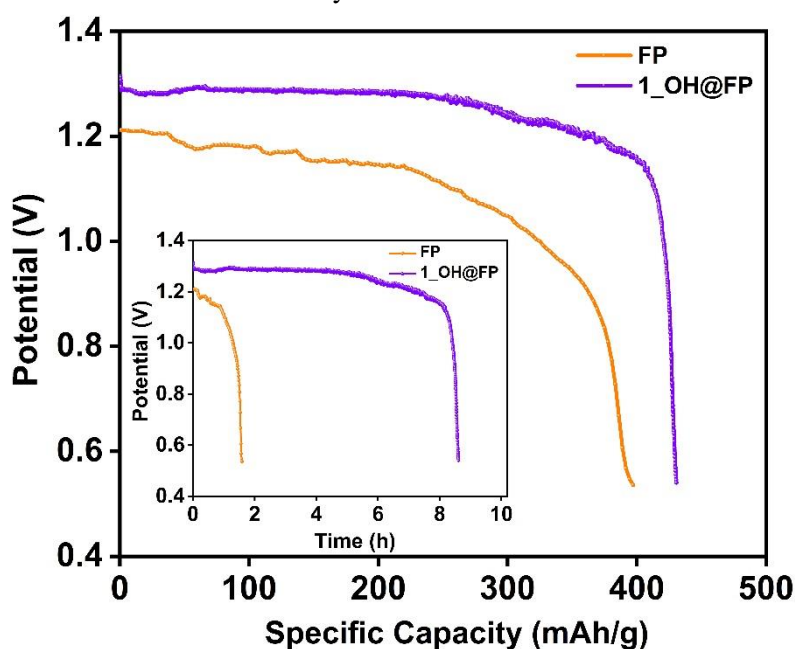


**Figure 1.23:** Comparative specific capacity of neat FP and 1_OH@FP based batteries; inset shows the durability of the ZAB over time.

(without purging any additional $O_2$ gas) (Figure 1.24a). Three flexible devices connected in series yielded an output of 4.22 V (Figure A.1.6, Appendix). The output voltage was stable to bending and twisting (Figure 1.24b) owing to the liquid-free nature of the 1_OH@FP. By combining the batteries in series, we could power three light-emitting diodes (LEDs) connected in parallel, resembling the traffic signal lights (Figure 1.24d). Overall, the results indicate the feasibility of employing 1_OH@FP as the hydroxide ion-conducting material for flexible batteries.
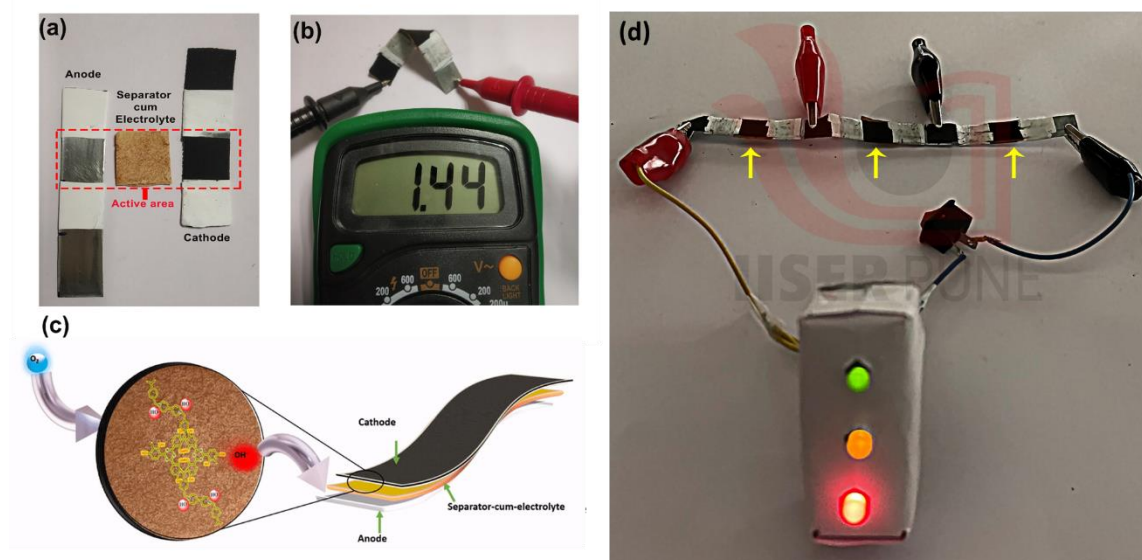


**Figure 1.24:** (a) Photographic images of the electrodes and the separator employed for the flexible battery. (b) Photograph showing constant OCV on bending of the solid-state ZAB. (c) Schematic of flexible solid-state ZAB. (d) Image of the flexible solid-state ZAB powering a demo traffic signal with yellow arrows indicating the air-breathing cathode.

## 1.2.5 Post ZAB usage stability analysis of 1_OH@FP:

The stability 1_OH@FP when employed as separator-cum-electrolyte- in the ZAB was investigated. The PXRD and IR analysis indicated that the polymer remains intact on the FP even after the complete discharge cycle (8h) (Figures 1.25). Then this composite electrolyte in the ZAB, 1_OH@FP, was subjected to high-frequency impedance analysis after a complete discharge cycle and compared with the neat FP's performance (Figure 1.22b, A1.6, Appendix). The resistance remains the same for the 1_OH@FP but increases for the neat FP; this is due to the relatively higher loss of KOH (aqueous solution) from the neat FP creating a passivation layer disfavoring the conduction. This problem is not observed in the case of the 1_OH@FP. Most likely due to the intrinsic tendency of the polymer to hold on to OH- species driven by its charge-balance requirements, and their pores trap water more efficiently (Figure 1.7a).
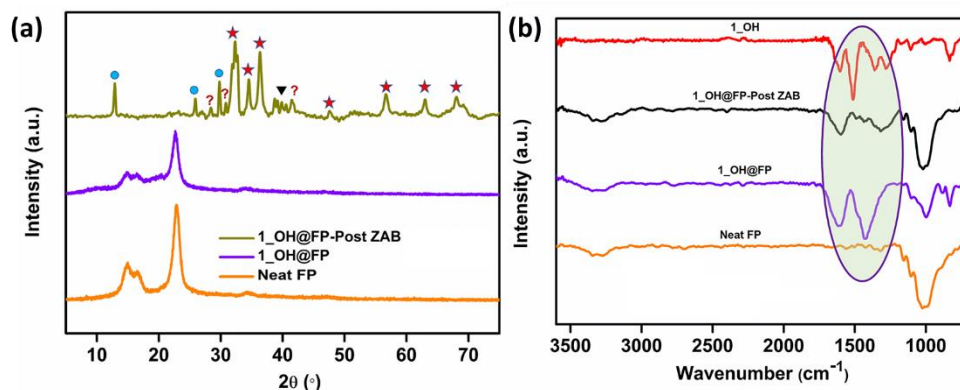
**Figure 1.25:** (a) Comparison of the PXRD patterns of the **FP**, **1_OH@FP** and the pyrolyzed product of the **1_OH@FP** (burnt at 600 °C under $N_2$). The inorganic species in this pyrolyzed sample includes ZnO (⭐), $K_2CO_3$ (●) and $Pt_3O_4$ (▼)(from cathode). (b) Comparison of the IR spectra showing the integration of the polymer (**1**) with the **FP** and the functionalities remain intact even after the ZAB measurements.
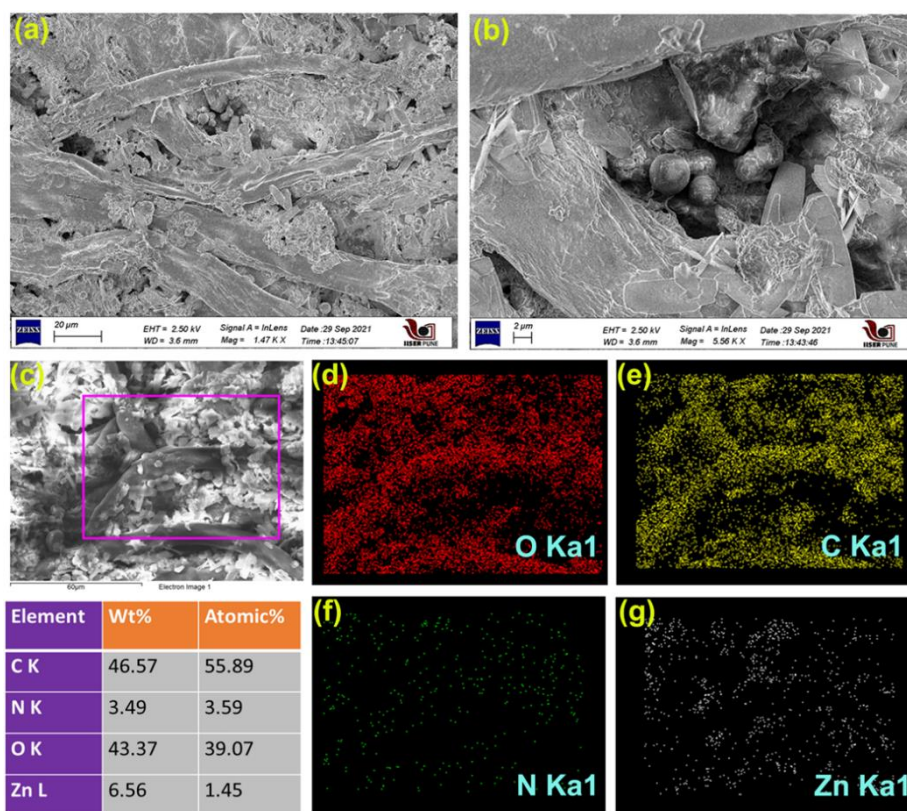


| Element | Wt% | Atomic% |
|---------|-------|---------|
| C K | 46.57 | 55.89 |
| N K | 3.49 | 3.59 |
| O K | 43.37 | 39.07 |
| Zn L | 6.56 | 1.45 |

**Figure 1.26:** The FESEM and EDAX images of the post-battery measurement electrolyte (1_OH@FP) showed the presence of a few additional components compared to the pristine 1_OH@FP.

Also, in the case of **1_OH@FP**, the conduction pathway and diffusion mechanism remain the same as seen from the equivalent circuit fits. The post-ZAB microscopy analysis of the **1_OH@FP** further confirms the homogeneous adherence of the active material on the FP (Figure 1.27).
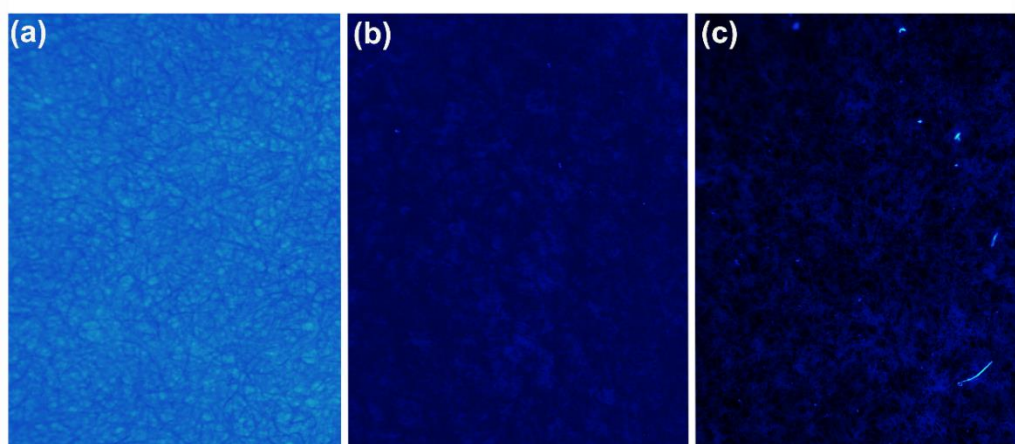
**Figure 1.27:** Comparison of the confocal microscopy images of the neat (a) FP, (b) 1_OH@FP and (c) post ZAB 1_OH@FP.

### 1.2.6 Push-pull electronics in the triazine-resorcinol-viologen framework portrayed by frontier orbitals:

To investigate the potential role of the cationic polymers in interacting with the hydroxide ion movement in this viologen functionalized spongy polymer, we looked at the potential/electron distribution within the polymer backbone. As a coherent step, we replaced the heteroatoms within the covalently linked modules and monitored the impact it brings to the HOMO-LUMO distribution. The local electronics is likely to be dictating the hydroxide-framework (heteroatom) interactions. For this, we developed a two-repeat unit polymer using the Random Copolymer module in the Materials Studio. This initial model was then geometry optimized using DMOL$^3$ package.

The geometry optimizations were performed for each of the individual configurations that were generated with and without heteroatoms. Important demarcation arises from the position of the HOMO and the LUMO. The **1_OH** with conjugated triazine-resorcinol core covalently linked to the viologen units have the HOMO residing on the resorcinol ring and the triazine nitrogen and to some extent on the hydroxyl groups that are located proximal to the viologen (Figure 1.28). While the LUMO resides mostly on the viologen rings. For the as-made polymer the HOMO-LUMO gap turns out to be 0.03 eV, but when the triazine rings are replaced with phenyl moieties, the all-carbon backbone does not demarcate much between the HOMO-LUMO levels leading to a gap of 0.002 eV.

This removes the push-pull characteristics within the framework backbone. This points at how crucial the triazine nitrogens are in setting up the push-pull characteristics between the triazine-resorcinol unit and the viologen rings. Remark: This is only for the small section of the polymer, and as the polymer grows into amorphous extended cross-linked structure there is bound to be breakdown of long-range conjugation assisted electronic transport and the overall bandgap will be much larger, typically in the

semiconducting regime,.[31] However, the redox active localized regions are sufficient to set-up a push-pull effect, which would govern the movement of the hydroxide ions.

## 1.2.7 Diffusion coefficient of hydroxide ions in the viologen polymer:

We resorted to MD simulations for garnering insights into the transport of hydroxide ions within the polymer framework. All structural dynamics were carried out using the Forcite module in the Materials Studio. An amorphous cell was constructed for a structure encompassing cross-linked chains. These
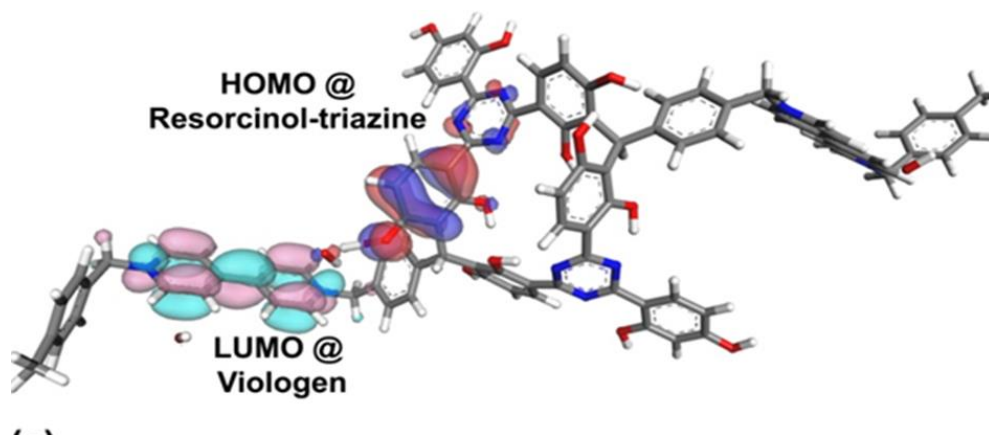


**Figure 1.28:** Computational modeling: (a) Frontier orbital locations within the polymer backbone. The resorcinol-triazine could set-up a push-pull with the e-deficient viologen units.

were filled with hydroxide ions in a 8:32 ratio per unit cell. A rigorous geometry optimization was performed until excellent convergence was achieved. The optimized structure was further equilibrated using an NPT ensemble and the average lattice parameters were employed to output structure. The migration of the hydroxide ions in the cationic framework was explored under the NVT conditions and the final trajectory was obtained from a 1ns microcanonical NVE dynamics with a large 50Å cut-off distance performed at 300K. The Mean Square Displacement (MSD) vs time plots were used to calculate the average diffusion coefficient for the hydroxide ions, which turned out to be $5.2 \times 10^{-6}$ $cm^2/s$. However, the computed diffusion coefficient is lower than the experimental one ($2.9 \times 10^{-5}$ $cm^2/s$), because the hydration was not considered in the MD simulations.[50] Importantly, the observed
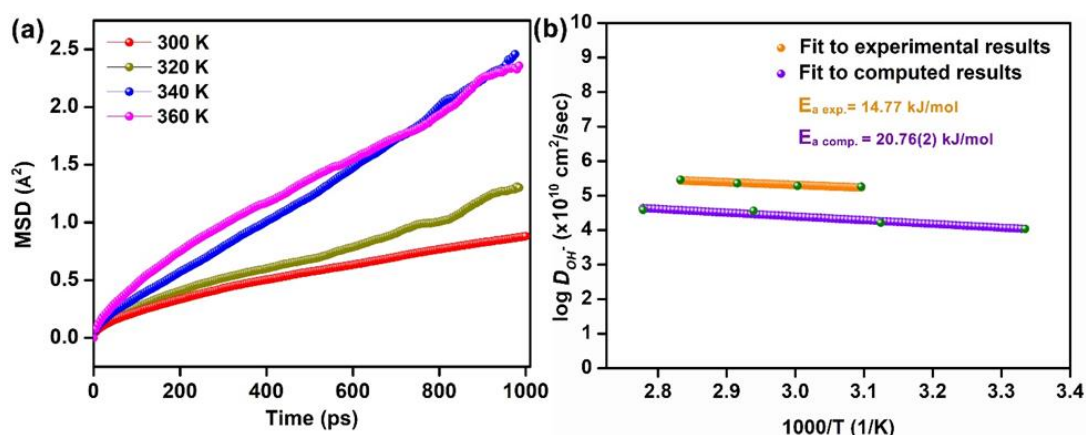


**Figure 1.29:** (a) Mean Square Displacement (MSD) vs. time plot calculated at variable temperature using MD simulations and the derived hydroxide ion self-diffusion coefficient. (b) Plot of log ($D_{OH^-}$) vs 1000/T from experimental and computational for **1_OH**. The data points were fitted to a straight line.

and calculated diffusion coefficients for the hydroxide ions compare extremely well with those available from the recent computational works.[51] [52] [53] From the fits to the MSD plots, we estimated the activation energy for the diffusion of the hydroxide ions in the cationic polymer framework to be 0.22 eV (21 kJ/mol, Figure 1.29), which is comparable to the experimental activation energy (0.153 eV) (14.77 kJ/mol) calculated using the Warburg Bode plot (Figure 1.29).[54]

### 1.2.8 Large energy barrier for Zinc-ion incorporation into the cationic polymer:

To estimate the energy barriers associated with the process of incorporation of the $Zn^{2+}$ ions into the polymer and its interaction with the $OH^-$ ion, we used the Nudged Elastic Band calculations. In the "reactant" model, the $Zn^{2+}$ ions were positioned relatively farther from the hydroxide ions present within the polymer's unit cell. Meanwhile, we configured the "product" to have the $Zn^{2+}$ ions at a bonding distance to the hydroxide ions (Figure 1.30). The framework atoms of the "reactant" and "product" were made indistinguishable to sequester only the effect of Zn-ion incorporation. Then a transition state confirmation for the bound state was performed using the climbing-image NEB method. We included multiple intermediate configurations between reactant-TS and TS-product to obtain a good extrapolation of the minimum energy path (MEP) and optimized under the NEB. The Ea for the $Zn^{2+}$ ions incorporation was calculated using as much as 7 intermediate configurations.

Most importantly, both the reactants and the product configurations showed stable structure, and the incorporation of the $Zn^{2+}$ ions go through an acceptable intermediate but with a significant energy barrier (2.11 eV). We observe that the energy barrier for incorporating zincate-ion into the polymer were even higher, and the zincate species goes through some unacceptable geometry deformations due to repulsive interactions with the polymer's framework atoms. This reveals the non-compatibility of the
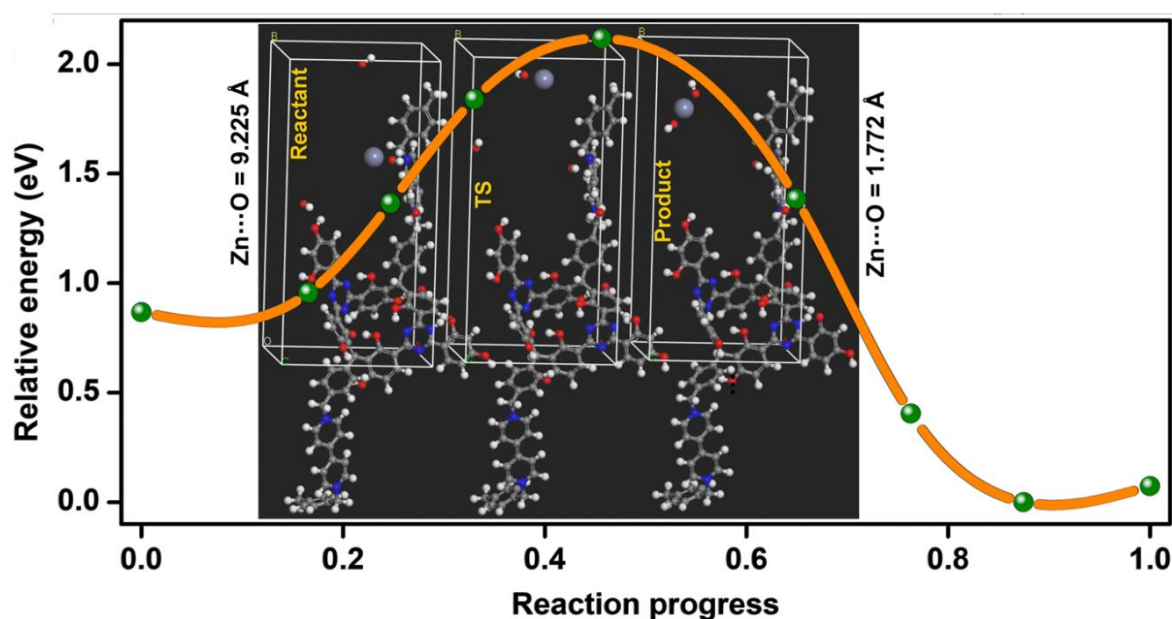


**Figure 1.30:** A representative minimum energy path (MEP) for the $Zn^{2+}$ ions movement within the hydroxyl-containing polymer assessed from NEB.

$Zn^{2+}$ ions and zincates in the polymer, a desirable feature in preventing zinc-dendrimer formation or cell short-circuiting.

**Table 1.1:** Comparison of the hydroxide ion conductivity of the 1_OH with releveant literature reports

| S. No. | Membrane | Electrolyte (Conc. of KOH) | Catalyst | Application | Maximum Power Density (in mW/cm²) | OH⁻ Conductivity ( in S/cm) | Reference |
|---|---|---|---|---|---|---|---|
| 1. | 25 μm polypropylene membrane, Celgard 5550 | 6 M | Pt/C | Zinc-air battery | 30 | - | J. Electrochem. Soc. 160, no. 9 (2013): F910 |
| 2. | Celgard® 3501 | 6 M | Pt/C | Zinc-air battery | 90 | $1.70 \times 10^{-2}$ | Molecules 26, no. 13 (2021): 4062 |
| 3. | Perfluorinated piperazinium | 2 M | Pt/C | Fuel Cell | 77 | $4.70 \times 10^{-2}$ | J. Mater. Chem. 21, no. 17 (2011): 6158-6160 |
| 4. | polymeric ionomer TPQPOH with a tris(2,4,6-trimethoxyphenyl) phosphonium | - | Pt/C | Fuel Cell | 138 | $2.70 \times 10^{-2}$ | Angewandte Chemie 121, no. 35 (2009): 6621-6624 |
| 5. | poly(vinyl alcohol) (PVA)/poly(acrylic acid) (PAA) | 32 wt% | - | Zinc-air battery | 50 | $1.42 \times 10^{-1}$ | J. Membr. Sci. 280, no. 1-2 (2006): 802-808 |
| 6. | semi-IPN MOF | 2 M | - | (Fuel cell) | 42.5 | $12 \times 10^{-2}$ | Energy & Fuels 2019, 33, 5749−5760 |
| 7. | KI–PVAA–GO GPE | 4 M KOH + 2 M KI | $CO_3O_4$ | Zinc-air battery | 78.6 | $1.55 \times 10^{-1}$ | Adv. Mater. 32, no. 22 (2020): 1908127. |
| 8. | polyacrylamide (PAM) based alkaline gel electrolyte (AGE) | 20 wt% | MnO2/NRGO-Urea | Zinc-air battery | 105.0 | $2.15 \times 10^{-1}$ | J. Power Sources 450 (2020): 227653 |

| 9. | IISERP-POF11_OH | 3 M | Pt/C | Zinc-air battery | 115 | 1.47 x 10$^{-2}$ | This Work |
|---|---|---|---|---|---|---|---|

## 1.3. Conclusions

This work describes a cationic polymer with counter-balancing hydroxide anions as a solid-state electrolyte for a Zinc-air battery. The uniqueness of the work is its simplicity and yet delivering high performance. We couple Bakelite and viologen chemistry to make this polymer which is exceptionally stable, easy to make, and affordable. The organic nature of this ion-conducting polymer (1.4 x 10$^{-2}$ S/cm at 80 °C and 95% RH) integrates it well with filter paper to yield an electrolyte requiring minimal KOH wetting. **1_OH@FP** delivers an excellent performance as separator-cum-electrolyte for Zinc-air battery with a power density of 115 mW/cm$^2$, three times more than the neat filter paper-based counterpart. The fabricated device easily withstands bending and twisting operations. Gradual and constant increment in OCV was observed for devices upon connecting them in series, enabling them to light up a power-demanding traffic signal for a long time. Computational modeling reveals the importance of heteroatoms in providing an electronic push-pull across the framework, which aids in transporting the hydroxide ions. At the same time, the MD simulations confirm the favorable diffusion of hydroxide ions and the high barrier for the undesirable penetration of Zn$^{2+}$ ions into the polymer. Thus our findings assert readily accessible C-C-linked cationic polymer's capacity as solid-state electrolytes for ZAB and any anion conducting membrane.

## 1.4 Acknowledgements

## 1.5 References

[1]     J. R. Varcoe, P. Atanassov, D. R. Dekel, A. M. Herring, M. A. Hickner, P. A. Kohl, A. R. Kucernak, W. E. Mustain, K. Nijmeijer, K. Scott, T. Xu, L. Zhuang, *Energy Environ. Sci.* **2014**, *7*, 3135-3191.

[2]    N. Chen, H. H. Wang, S. P. Kim, H. M. Kim, W. H. Lee, C. Hu, J. Y. Bae, E. S. Sim, Y.-C. Chung, J.-H. Jang, S. J. Yoo, Y. Zhuang, Y. M. Lee, *Nat. Commun.* **2021**, *12*, 2367.

[3]    D. R. Dekel, *J. Power Sources* **2018**, *375*, 158-169.

[4]    S. Tao, H. Xu, Q. Xu, Y. Hijikata, Q. Jiang, S. Irle, D. Jiang, *J. Am. Chem. Soc.* **2021**.

[5]    K.-D. Kreuer, *Chem. Mater.* **1996**, *8*, 610-641.

[6]    Y. Meng, J. Gao, Z. Zhao, J. Amoroso, J. Tong, K. S. Brinkman, *Journal of Materials Science* **2019**, *54*, 9291-9312.

[7]    L. Malavasi, C. A. J. Fisher, M. S. Islam, *Chem. Soc. Rev.* **2010**, *39*, 4370-4387.

[8]    S. S. Shinde, C.-H. Lee, A. Sami, D.-H. Kim, S.-U. Lee, J.-H. Lee, *ACS nano* **2017**, *11*, 347-357.

[9]    Z. Li, W. Niu, Z. Yang, N. Zaman, W. Samarakoon, M. Wang, A. Kara, M. Lucero, M. V. Vyas, H. Cao, H. Zhou, G. E. Sterbinsky, Z. Feng, Y. Du, Y. Yang, *Energy Environ. Sci.* **2020**, *13*, 884-895.

[10]   S. Haldar, D. Kaleeswaran, D. Rase, K. Roy, S. Ogale, R. Vaidhyanathan, *Nanoscale Horiz.* **2020**, *5*, 1264-1273.

[11]   R. Kushwaha, S. Haldar, P. Shekhar, A. Krishnan, J. Saha, P. Hui, C. P. Vinod, C. Subramaniam, R. Vaidhyanathan, *Adv. Energy Mater.* **2021**, *11*, 2003626.

[12]   J. Fu, R. Liang, G. Liu, A. Yu, Z. Bai, L. Yang, Z. Chen, *Adv. Mater.* **2019**, *31*, 1805230.

[13]   W. Sun, F. Wang, B. Zhang, M. Zhang, V. Küpers, X. Ji, C. Theile, P. Bieker, K. Xu, C. Wang, *Science* **2021**, *371*, 46-51.

[14]   Y. Li, H. Dai, *Chem. Soc. Rev.* **2014**, *43*, 5257-5275.

[15]   Q. Liu, Y. Wang, L. Dai, J. Yao, *Adv. Mater.* **2016**, *28*, 3000-3006.

[16]   M. Yu, Z. Wang, C. Hou, Z. Wang, C. Liang, C. Zhao, Y. Tong, X. Lu, S. Yang, *Adv. Mater.* **2017**, *29*, 1602868.

[17]   F. Cheng, J. Chen, *Chem. Soc. Rev.* **2012**, *41*, 2172-2192.

[18]   N. S. V. Narayanan, B. V. Ashokraj, S. Sampath, *J. Electrochem. Soc.* **2009**, *156*, A863.

[19]   A. R. Mainar, E. Iruin, L. C. Colmenares, A. Kvasha, I. De Meatza, M. Bengoechea, O. Leonet, I. Boyano, Z. Zhang, J. A. Blazquez, *J. Energy Storage* **2018**, *15*, 304-328.

[20]   P. Chen, K. Zhang, D. Tang, W. Liu, F. Meng, Q. Huang, J. Liu, *Front. Chem.* **2020**, *8*.

[21] H. Miao, B. Chen, S. Li, X. Wu, Q. Wang, C. Zhang, Z. Sun, H. Li, *J. Power Sources* **2020**, *450*, 227653.

[22] J. Park, M. Park, G. Nam, J.-s. Lee, J. Cho, *Adv. Mater.* **2015**, *27*, 1396-1401.

[23] D. Chen, M. A. Hickner, *ACS Appl. Mater. Interfaces* **2012**, *4*, 5775-5781.

[24] Y. A. Elabd, *Molecular Systems Design & Engineering* **2019**, *4*, 519-530.

[25] Z. Cao, H. Hu, M. Wu, K. Tang, T. Jiang, *J. Mater. Chem. A* **2019**, *7*, 17581-17593.

[26] J. Fu, J. Zhang, X. Song, H. Zarrin, X. Tian, J. Qiao, L. Rasen, K. Li, Z. Chen, *Energy Environ. Sci.* **2016**, *9*, 663-670.

[27] S. Nandi, V. M. Dhavale, S. Shalini, U. Werner-Zwanziger, H. Singh, S. Kurungot, R. Vaidhyanathan, *Adv. Mater. Interfaces* **2015**, *2*, 1500301.

[28] R. Illathvalappil, V. M. Dhavale, S. N. Bhange, S. Kurungot, *Nanoscale* **2017**, *9*, 9009-9017.

[29] M. T. Tsehaye, F. Alloin, C. Iojoiu, R. A. Tufa, D. Aili, P. Fischer, S. Velizarov, *J. Power Sources* **2020**, *475*, 228689.

[30] D. J. Arnot, M. B. Lim, N. S. Bell, N. B. Schorr, R. C. Hill, A. Meyer, Y.-T. Cheng, T. N. Lambert, *Adv. Energy Mater.* **2021**, *11*, 2101594.

[31] Y. Kim, M. Künzel, D. Steinle, X. Dong, G.-T. Kim, A. Varzi, S. Passerini, *Energy Environ. Sci.* **2022**, *15*, 2610-2618.

[32] Y. Zeng, P. Gordiichuk, T. Ichihara, G. Zhang, E. Sandoz-Rosado, E. D. Wetzel, J. Tresback, J. Yang, D. Kozawa, Z. Yang, *Nature* **2022**, *602*, 91-95.

[33] A. P. Katsoulidis, M. G. Kanatzidis, *Chem. Mater.* **2011**, *23*, 1818-1824.

[34] R. Paul, S. C. Shit, T. Fovanna, D. Ferri, B. Srinivasa Rao, G. T. K. K. Gunasooriya, D. Q. Dao, Q. V. Le, I. Shown, M. P. Sherburne, Q. T. Trinh, J. Mondal, *ACS Applied Materials & Interfaces* **2020**, *12*, 50550-50565.

[35] R. Dawson, E. Stöckel, J. R. Holst, D. J. Adams, A. I. Cooper, *Energy & Environmental Science* **2011**, *4*, 4239-4245.

[36] B. Li, R. Gong, W. Wang, X. Huang, W. Zhang, H. Li, C. Hu, B. Tan, *Macromolecules* **2011**, *44*, 2410-2414.

[37] S. Nandi, U. Werner-Zwanziger, R. Vaidhyanathan, *J. Mater. Chem. A* **2015**, *3*, 21116-21122.

[38] D. Chakraborty, S. Nandi, R. Kushwaha, D. Kaleeswaran, R. Vaidhyanathan, *Materials Research Bulletin* **2021**, 111614.

[39] D. Crespy, M. Bozonnet, M. Meier, *Angew. Chem. Int. Ed.* **2008**, *47*, 3322-3328.

[40]  E. Breitmaier, W. Voelter, *Carbon-13 NMR spectroscopy*, VCH Publishers Inc, United States, **1987**.

[41]  L. Feng, X. Zhang, C. Wang, X. Li, Y. Zhao, X. Xie, Y. Lv, *Int. J. Hydrog. Energy* **2016**, *41*, 16135-16141.

[42]  G. A. Ludueña, T. D. Kühne, D. Sebastiani, *Chem. Mater.* **2011**, *23*, 1424-1429.

[43]  D. W. Kang, M. Kang, H. Yun, H. Park, C. S. Hong, *Adv. Funct. Mater.* **2021**, *31*, 2100083.

[44]  U. Tröltzsch, O. Kanoun, *Electrochimica Acta* **2012**, *75*, 347-356.

[45]  J. Chen, P. Li, N. Zhang, S. Tang, *J. Mater. Chem. A* **2022**.

[46]  S. H. Lee, J. C. Rasaiah, *J. Chem. Phys.* **2013**, *139*, 124507.

[47]  R. Vedalakshmi, V. Saraswathy, H.-W. Song, N. Palaniswamy, *Corros. Sci.* **2009**, *51*, 1299-1307.

[48]  H. Zhang, B. Zhang, Y. Yang, D. Ye, R. Chen, Q. Liao, X. Zhu, *ChemComm* **2021**, *57*, 1258-1261.

[49]  Z.-L. Wang, D. Xu, J.-J. Xu, X.-B. Zhang, *Chem. Soc. Rev.* **2014**, *43*, 7746-7786.

[50]  V. Dubey, S. Daschakraborty, *J. Phys. Chem. B* **2022**, *126*, 2430-2440.

[51]  J. Chen, P. Li, N. Zhang, S. Tang, *J. Mater. Chem. A* **2022**, *10*, 7146-7154.

[52]  P. Prakash, A. Shylendran, B. Fall, M. J. Zdilla, S. L. Wunder, A. Venkatnathan, *J. Phys. Chem. C* **2022**, *126*, 4744-4750.

[53]  T. Zelovich, L. Vogt-Maranto, C. Simari, I. Nicotera, M. A. Hickner, S. J. Paddison, C. Bae, D. R. Dekel, M. E. Tuckerman, *Chem. Mater.* **2022**, *34*, 2133-2145.

[54]  P. Prakash, J. Aguirre, M. M. Van Vliet, P. R. Chinnam, D. A. Dikin, M. J. Zdilla, S. L. Wunder, A. Venkatnathan, *J. Mater. Chem. A* **2018**, *6*, 4394-4404.

## Appendix of chapter 1

**A1.1 Experimental Section**

**A1.1.1 Synthesis of 4-(bromomethyl)benzaldehyde**

The synthesis of the compound is based on a previous report.[147] A 500 mL flask was charged with 5 g of 4-(bromomethyl) benzonitrile (25.5 mmol) and vacuumed at ambient temperature for 2 h. About 140 mL Toluene was used to dissolve 4- (bromomethyl)benzonitrile, the obtained solution was then cooled to 0 °C and stirred under $N_2$ atmosphere for 8 h. 36.0 mL DIBAl-H (1 M in hexane) was added dropwise to the solution cautiously, immediately, the solution turned

yellow and becomes clear. After stirring for 2 h, the solution was added with 66 mL CHCl$_3$ and then added with 200 mL 10 % HCl solution. After stirring for one more hour, the organic phase was extracted from the mixture and washed with water twice. The solution was dried with Na$_2$SO$_4$ and further dried under a vacuum oven to obtain the pale-yellow clear oil. After cooling down to ambient temperature, the white solid was immediately observed after the addition of ice-cold hexane. The whole mixture was placed in the refrigerator (4 °C) overnight and then filtrated to obtained the white crystals with a yield of 84%. NMR results are in good agreement with the literature. $^1$H (400 MHz, CDCl$_3$) δ = 10.01 (s, 1H), 7.87 (d, J = 7.5 Hz, 2H), 7.56 (d, J = 7.5 Hz, 2H), 4.52 (s, 2H) ppm. $^{13}$C NMR (400 MHz, CDCl$_3$) δ = 191.25, 143.98, 135.86, 129.98, 129.41, 31.68 ppm.





$^1$H NMR of 4-(bromomethyl)benzaldehyde
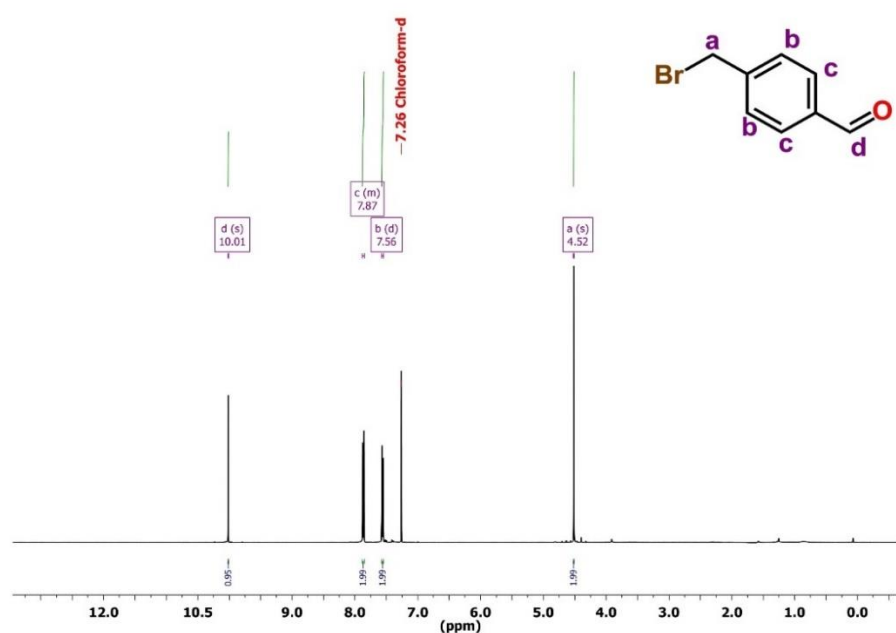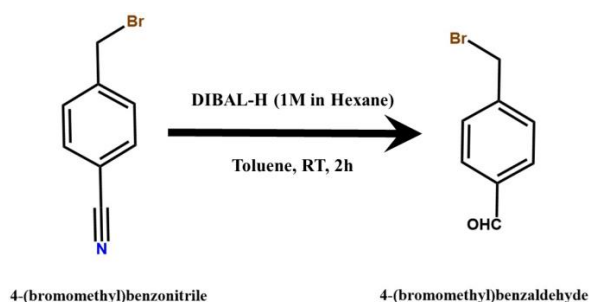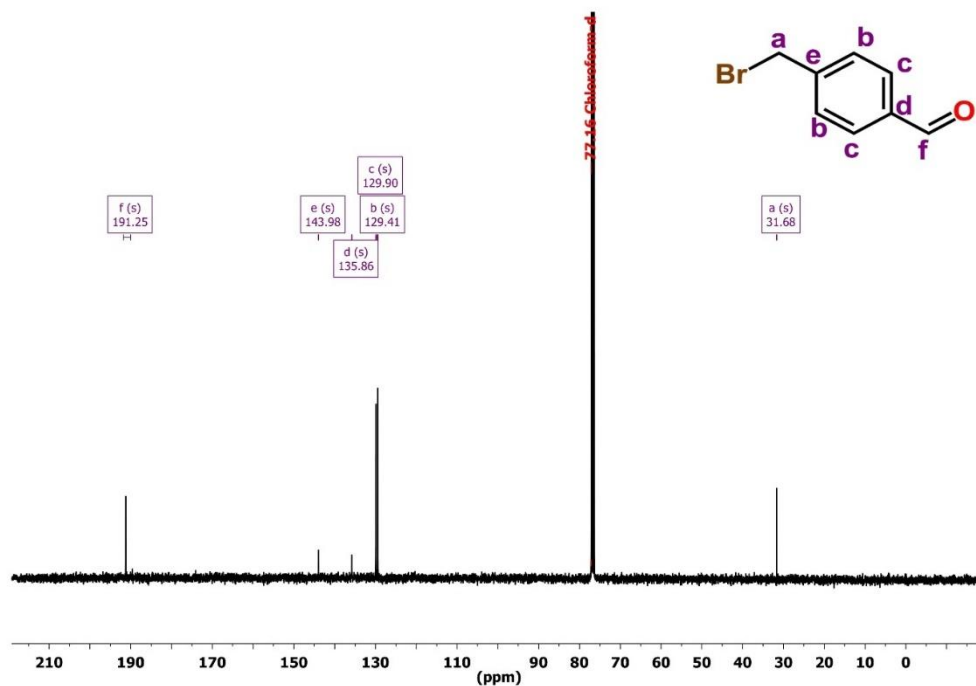
$^{13}$C NMR of 4-(bromomethyl)benzaldehyde

## A1.1.2 Synthesis of 1,1'-bis(4-formylbenzyl)-4,4'-bipyridiniumdibromide (VBrBA)

A solution of 0.39 g 4,4'-Bipyridine (2.50 mmol) and 1 g 4-(bromomethyl)-benzaldehyde (4.97 mmol) in 15 mL of acetonitrile was heated at 75 °C for 6 h. After cooling down to room temperature, the precipitate was filtered off, washed with acetonitrile and ether, and dried in an oven, and obtained the yield of nearly 1.30 g (94%) of a yellow powder.



1,1'-bis(4-formylbenzyl)-[4,4'-bipyridine]-1,1'-diium dibromide
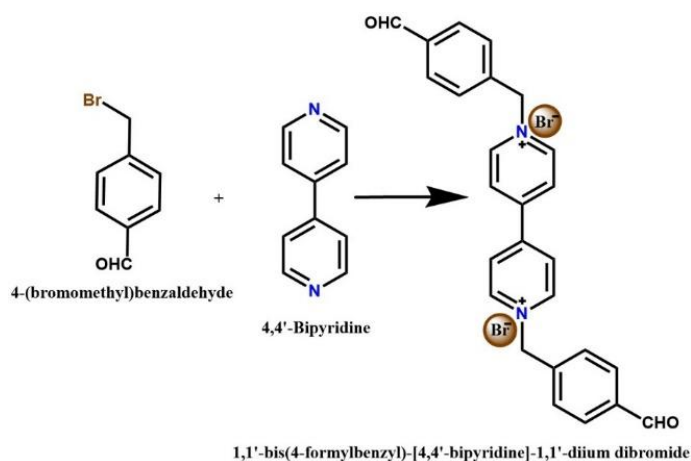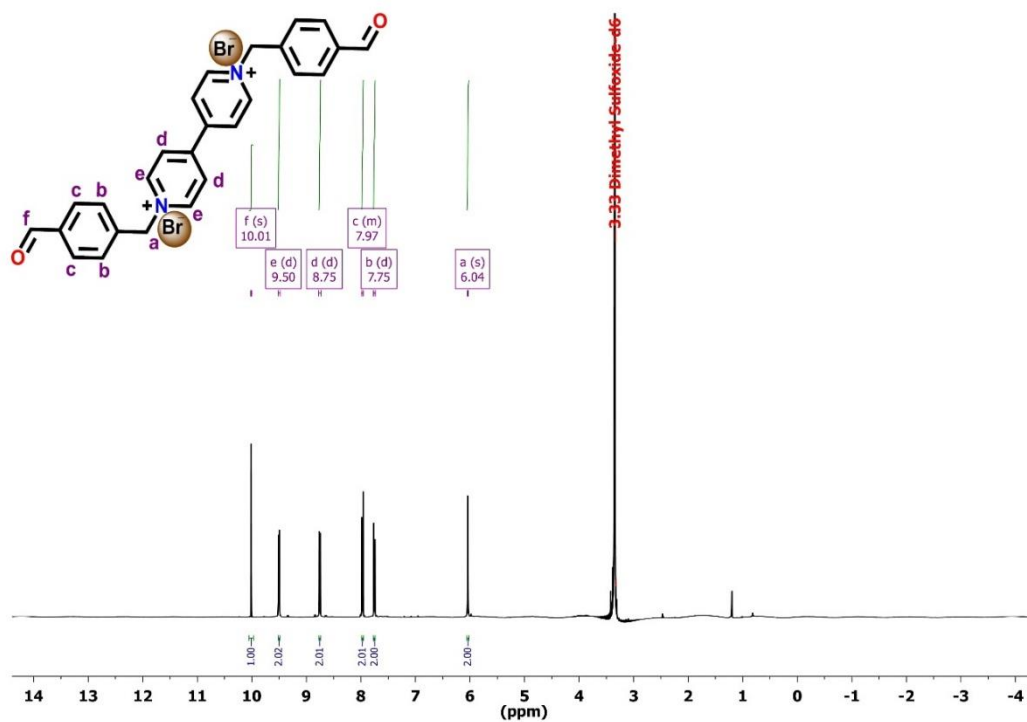
$^1$H NMR of 1,1'-bis(4-formylbenzyl)-4,4'-bipyridiniumdibromide
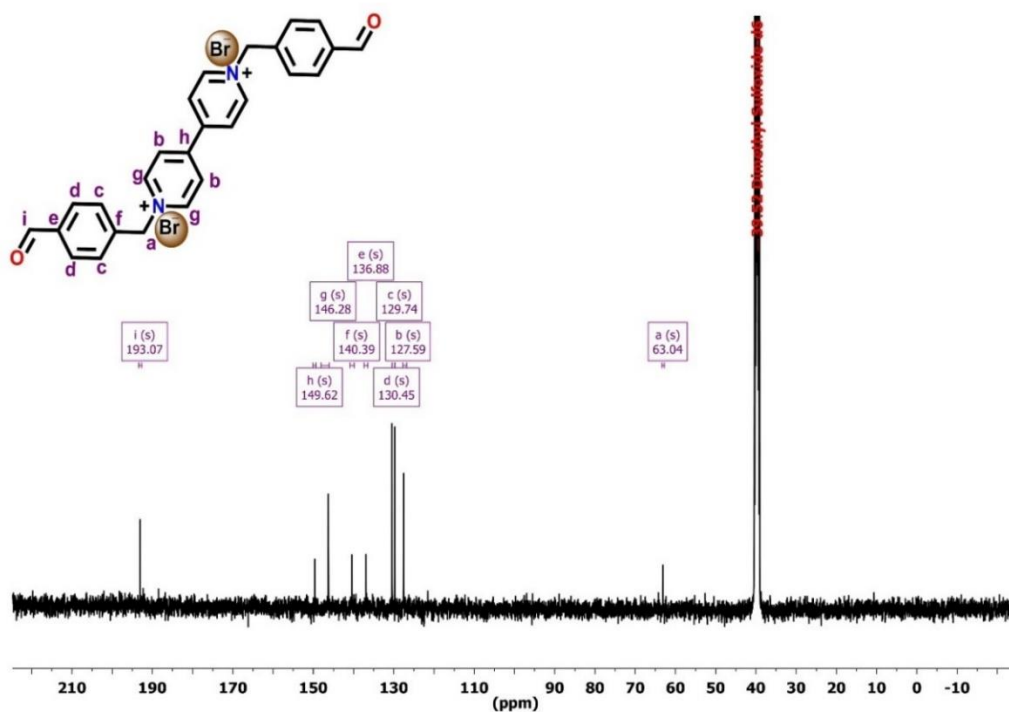


$^{13}$C NMR of 1,1'-bis(4-formylbenzyl)-4,4'-bipyridiniumdibromide

**A1.1.3 Synthesis of 4,4',4''-(1,3,5-triazine-2,4,6-triyl)tris(benzene-1,3-diol) (TRIRES)**

The synthesis of the compound is based on a previous report.[148] 2 g (10.8 mmol) of cyanuric chloride and 3.58 g (32.5 mmol) of resorcinol were dispersed in 100 mL of 1,2-dichloroethane. Contents were dissolved by heating at 75 °C, following this, the mixture was cooled to 0 °C. To this, about 4.35 g (32.5 mmol) anhydrous AlCl$_3$ was slowly added in 30 minutes. This mixture was refluxed for 36 h. The reaction mixture was cooled to room temperature and the solvent was removed using a rota-evaporator. The solid was then stirred in 100 mL of 10% HCl for 3 h and kept it for an additional 3 h. A yellow solid was precipitated, which was filtered under vacuum and washed with about 250 mL of diethyl ether to remove any unreacted starting materials. The product was dried in a vacuum oven. About 3.2 g (yield: 88%) of the product was obtained.



4,4',4''-(1,3,5-triazine-2,4,6-triyl)tris(benzene-1,3-diol)



HRMS of RMS data of 4,4',4''-(1,3,5-triazine-2,4,6-triyl)tris(benzene-1,3-diol) shows only a single intense peak of [M+H]+:406.10 . The exact molecular mass of bispyridine-s-tetrazine diamine (C$_{21}$H$_{15}$N$_3$O$_6$) is 405.37.

**A1.1.4 Synthesis of cationic polymer IISERP-POF11 (1)**

The polymer has been synthesized according to the optimized protocol by our group.[149] The solvothermal reaction between 0.2 mmol phenolic compound and 0.15 mmol viologen aldehyde

in a mixture of 3 mL THF and 3 mL 1,4- dioxane at 200 °C for 72 h yielded a brown-colored precipitate which was sequentially washed with DMF, THF, MeOH and finally acetone. The product was dried in the vacuum oven for 6 h and the obtained material was named hereafter as **1**. CHN analysis: **1**: C=80.71%, H=10.83%, N=8.46%.
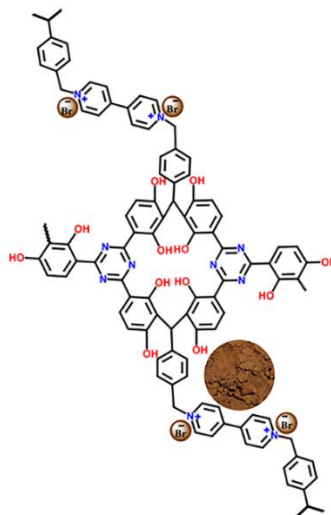


Schematic showing the structure of **1**. Inset showing the photographic image of the compound.

## A1.1.5 Anion exchange with IISERP-POF11 to form IISERP-POF11_OH (1_OH)

The as-made polymer **1** (100 mg) was dispersed in 10 mL of 3 M KOH and sonicated for 10 minutes. After sonication, the mixture was stirred for 24 h at room temperature for hydroxide ion (OH⁻) incorporation. Hydroxide ion exchanged polymer was filtered and washed with an ample amount of water to remove the excess KOH. The product was dried in a vacuum oven for 12 h at 80 °C and obtained a yield of 88 %. A significant colour change was observed after the exchange with the hydroxide ions to obtain **1_OH**. **1** was exchanged with 6 M KOH followed by the above procedure to obtain **1_6OH.**
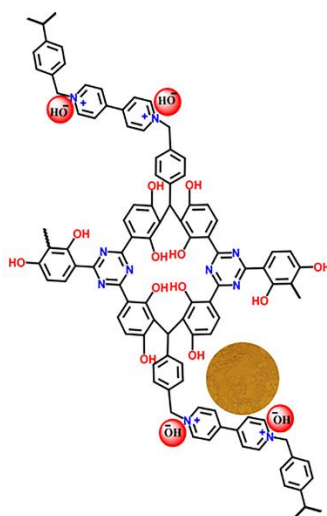
**1_OH** with inset showing the photographic image of the compound
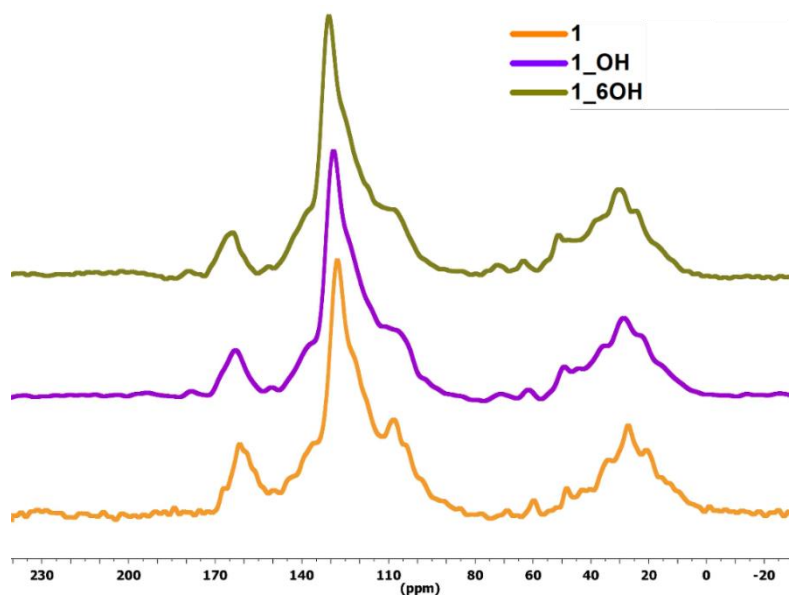


**Figure A.1.1:** Comparative Solid-state Cross-Polarization Magic Angle Spinning Carbon-13 Nuclear Magnetic Resonance ($^{13}$C CP-MAS NMR) spectra 1, 1_OH and 1_6OH.
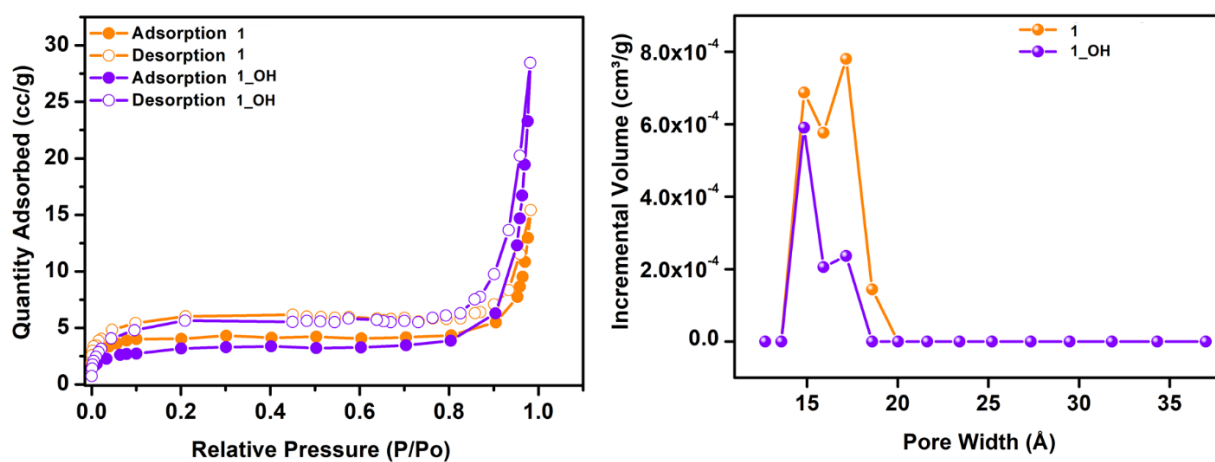


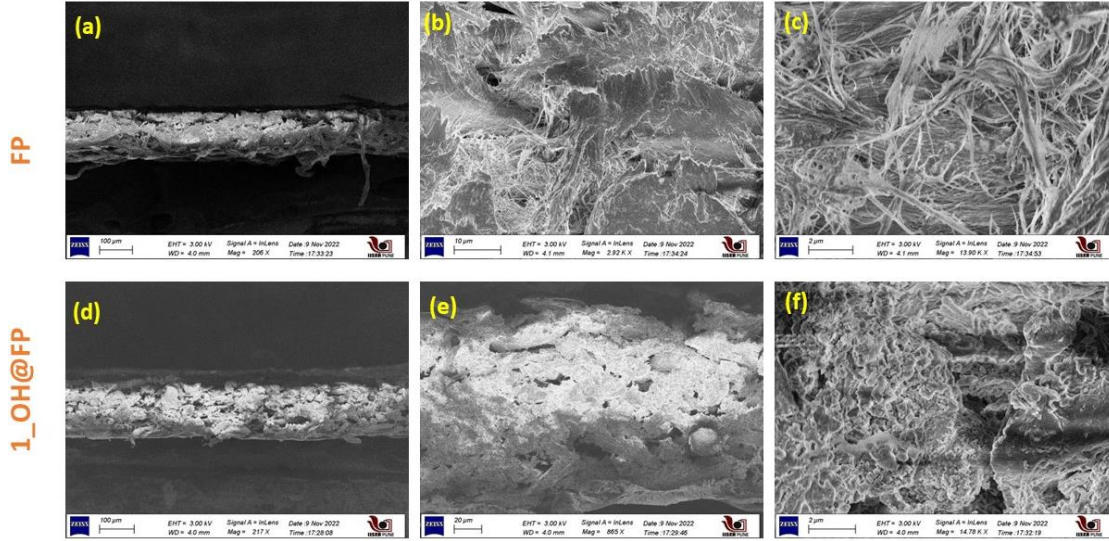**Figure A.1.2**: Adsorption isotherms and plot of the pore width vs. incremental pore volume of **1** and **1_OH**.

**Figure A.1.3:** Cross-sectional SEM images of (a-c) Neat FP and, (d-f) 1_OH@FP at different magnifications.

**A1.2 Hydroxide ion conductivity Analysis**

**A1.2.1 Temperature-dependent hydroxide ion conductivity analysis of 1_OH:**

The hydroxide ion conductivity (σ) of the 1_OH was investigated by the electrochemical impedance spectroscopy method from a frequency range of $1-10^6$ Hz using the Solartron Impedance Analyzer. For this, 1_OH was made into a pelletized form. The conductivity measurements were carried out three times on different pellet thicknesses (0.6 to 0.8 mm) and diameters of 10 mm to validate the consistency in the obtained results. Before each measurement, the sample was equilibrated at the particular temperature and humidity for 2 h throughout the experiment. The hydroxide ion conductivity of the pellet was measured from 30 to 80 °C in relative humidity (RH) of 95% and calculated using the following equation;

$$\sigma \ (\text{S cm}^{-1}) = \frac{l}{RA}$$

where *l* is the thickness of the pellet (cm), R is the resistance of the sample (Ω) obtained from the x-axis intercept, and A is the cross-sectional area of the pellet (cm$^2$). The humidity dependent OH$^-$ ion conductivity of 1_OH was also measured at 80 °C with variable relative humidity under similar conditions.

**A1.2.2 Activation energy calculation for 1_OH**

The activation energy was obtained using the Arrhenius equation where m is the slope of the plot between ln σ Vs 1000/T and the R is the gas constant with the value of 8.314 J/mol.

$$\ln\sigma = (-E_a/RT) + \ln A$$

**Table A1.1:** Hydroxide ion conductivity of 1_OH at variable temperatures and a constant relative humidity of 95%.

| Sr. No. | Humidity (%) | Temperature (°C) | Conductivity (S/cm) |
|---------|--------------|-------------------|---------------------|
| 1 | 95 | 30 | $2.7 \times 10^{-4}$ |
| 2 | 95 | 40 | $1.4 \times 10^{-3}$ |
| 3 | 95 | 50 | $2.3 \times 10^{-3}$ |
| 4 | 95 | 60 | $3.4 \times 10^{-3}$ |
| 5 | 95 | 70 | $5.3 \times 10^{-3}$ |
| 6 | 95 | 80 | $1.4 \times 10^{-2}$ |
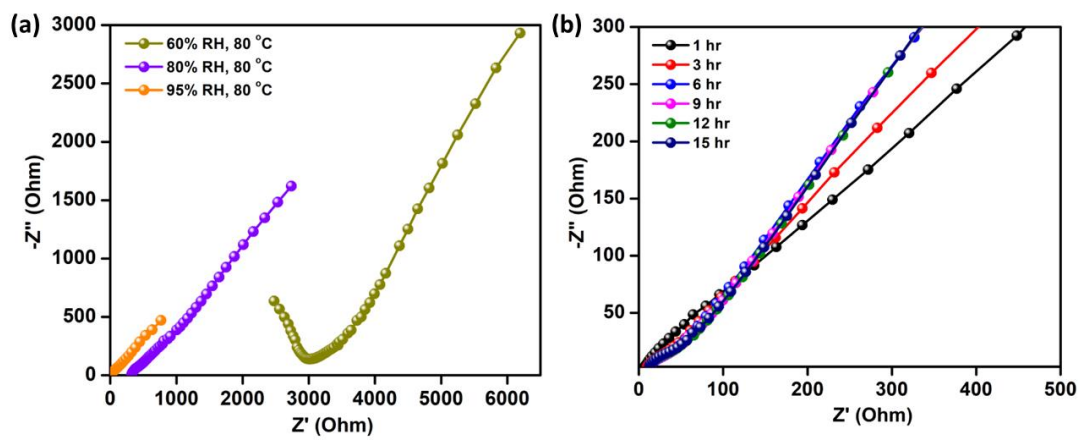


**Figure A.1.4:** (a) Humidity dependent Nyquist plots of **1_OH** at 80 °C. (b) **1_OH** impedance anlysis measured at 80 °C and 95 % RH for 15 h.



| | FP-Pre ZAB | FP-Post ZAB |
|---|------------|-------------|
| R1 | 2.104 | 2.942 |
| $W_o$- R | 0.323 | 1.494 |
| $W_o$- T | 0.032 | 0.170 |
| $W_o$- P | 0.443 | 0.408 |
| Chi-Squared Value | $5.5 \times 10^{-3}$ | $3.1 \times 10^{-3}$ |
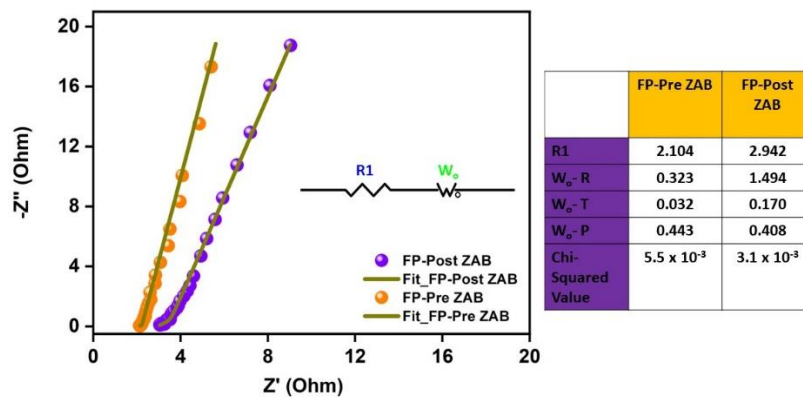
**Figure A.1.5**: Comparison of the Nyquist plots for the neat paper measured in the zinc-air battery set-up. Table shows the values for each fitting parameter.

## A1.3 Fabrication of flexible solid-state ZAB:

For the flexible solid-state Zinc-air battery, Zn foil with 0.25 mm thickness was employed as the anode, Pt/C coated carbon cloth was used as the air-breathing cathode and hydroxide ion conducting **1_OH@FP** as the solid-state separator-cum-electrolyte. During the fabrication of

the battery, **1_OH@FP** was wetted with 3 M KOH solution. The anode and cathode were separated with **1_OH@FP** and the sandwich is sealed. The backside of the cathode was kept it open for the passage of air and the battery was operated without providing any additional $O_2$ supply.
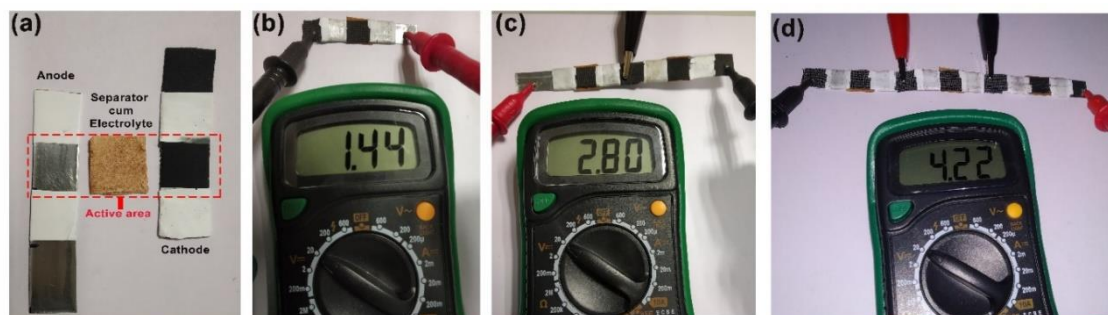


**Figure A.1.6:** (a) Photographic images of the electrodes and the separator employed for the flexible battery, (b) Photographic images of the single flexible battery, (c) Two flexible batteries connected in series and, (d) Combination of three devices in series.
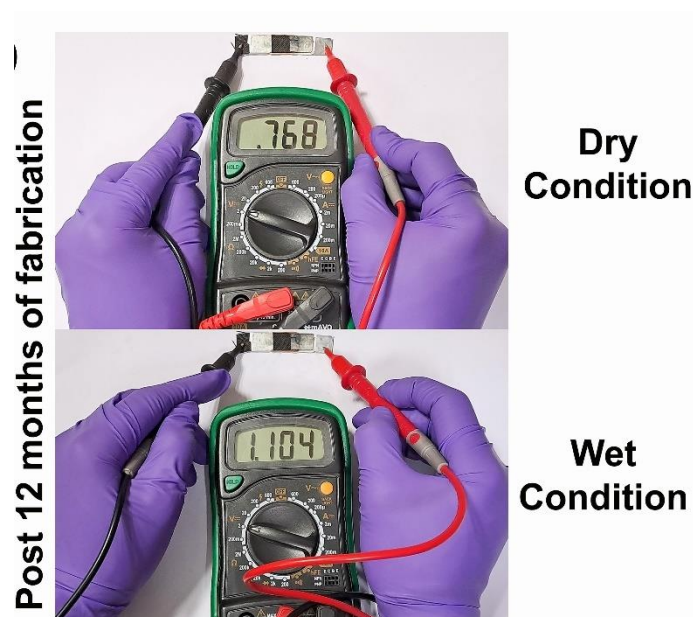


**Figure A.1.7:** OCV regeneration of solid-state ZAB after 10 months of fabrication on wetting with water.

## A1.4 Computational details:

The crystallographic modeling of the structure of the 1_OH and its DFT optimization was carried out using the DMOL$^3$ package embedded in the Materials Studio (Accelrys) V.8.0.[S4,S5] The initial structure of the polymer containing two triazine-triresorcinol units linked to two viologen units terminated with a tolyl ring was constructed using atomic manipulation. Four hydroxide ions were introduced to counter-balance the protonated viologen nitrogens. In the initial configuration, the hydroxides were positioned adjacent to the protonated nitrogen centers and were allowed to find their final atomic positions freely during the optimization. The optimized structure of this polymer's representative unit

and its frontier orbitals was calculated using the DMOL minimization routine. To calculate the frontier orbitals, we used the DMOL[3] module S6 with a high tolerance of $1 \times 10^{-6}$ for the SCF convergence and a global cut-off of 3.7 Å. UFF-based Lennard-Jones dispersion corrections were included in Energy, Force and Displacement calculations. All calculations are at 0 K and were spin-unrestricted, adopting the formal spin as the initial spin. The final configuration converged with acceptable geometries and bond parameters.

We created an amorphous cell consisting of four oligomeric chains and the charge-balancing hydroxide ions. The cell parameters, as well as the geometries, were optimized using the DMOL[3]. In the optimized configuration, the cross-linked chains packed efficiently and possessed ample spaces capable of accommodating the extra-framework hydroxide anions and with very few solvent-accessible voids. This is consistent with the experimental observations, which point to the material being non-porous to nitrogen gas but comprises some solvent molecules in the as-synthesized form.

Core elements were treated with all-electron pseudopotentials and the DNP basis set with a basis cut-off of 3.7 Å. For our dispersion corrections, we used Generalized Gradient Approximation (GGA) for calculating the exchange and the correlation energies and employed the Perdew-Wang 91 (PW91) functional.[S6] Density mixing was done using the Pulay scheme. The final configuration considered in the analysis converged well. We used this final optimized structure for the molecular dynamics simulations.

**A1.4.1 Molecular Dynamics Simulations (MD):**

The optimized amorphous cell containing four polymer chains was investigated using the Forcite Dynamics module embedded in the Accelrys Package. For the MD, the initial velocities were made Random. A 5 ns NPT MD simulation (1.0 fs time step, 300K) was used to generate were used to reach an equilibrium state. The COMPASS force field was employed, and the Coulumbic interactions were treated with Group-based summation methods with a considerable cut-off distance of 40 Å, considering the large unit-cell. We did not alter the charge group size. Nose-Hoover Thermostat was employed to control the temperature, while Berendsen barostat helped control the pressure. Energy tolerance of 5 x 105 kcal/mol was applied. Finally, a 5 ns NVE simulations (1.0 fs time step) were used to generate the low-energy trajectory from which we analyzed the radial distribution function (RDF). We used the COMPASS force field (V 2.8) for these simulations with the NVE ensemble and treated the Coulumbic interactions with Group-based summation methods. The electrostatic and van der Waals summation were calculated to a cut-off distance of 18.5 Å. Similar MD simulation parameters were employed for all the other temperatures used to calculate the activation energy from the slope of the MSD

# Chapter 2

# Design enhancement in hydroxide ion conductivity of viologen–bakelite organic frameworks for a flexible rechargeable zinc–air battery

## 2.1 Introduction

Rechargeable zinc-air batteries (RZABs), represents a promising candidate for the development of flexible energy storage solutions.[1-14] This potential is rooted in their uncomplicated architecture, capacity to be modelled into diverse shapes, environment friendly attributes, cost-effectiveness, and high energy and power density.[15-17] Traditionally, a battery having an alkaline electrolyte with a zinc anode has been desirable due to the inherent electrochemical reversibility and fast kinetics (low overpotential).[18, 19] But highly alkaline electrolytes cause zinc corrosion, shape changes, and dendrite growth, precipitation of insoluble carbonates, electrolyte evaporation, and hydrogen evolution – all of these contribute to performance decay.[20-22] Rendering the ZAB as solid-state battery solves many of these issues.[3, 4, 7, 10, 17, 23] A major obstacle to integrating flexible designs into ZABs is the lack of appropriate solid electrolytes that can conduct hydroxide ions (OH⁻) while being flexible. Alongside electrode kinetics, the efficient movement of hydroxide ions across the electrolyte significantly influences ZAB efficiency.[16, 24] Though there is a recent surge in the investigation of hydroxide-ion conducting polymers for energy storage, they are aimed mostly at supercapacitor electrolytes and fuel cell membranes,[25-32] to our knowledge, there is only one report on their utilization in ZAB,[33] but there is no evidence that these porous hydroxide-ion conducting polymer electrolytes can support a RZAB.

Polymeric membranes, which possess an inherent ability to facilitate OH⁻ ion conduction, are commonly referred to as anion exchange polymer electrolyte membranes (AEPEMs). These are distinguished by the presence of positively charged functional groups, such as quaternary nitrogen or imidazole groups, and some hydrogen-bonding moieties integrated into the polymer chain.[30, 34-36] These functional groups play a crucial role in creating interconnected nanochannels and ensuring the selective conduction of anions via optimal electrostatic interactions and they cooperate very well with water within these polymer networks.[37] However, their archetypal 1-D chain structure cannot avoid potential swelling and if they are electronically conductive it promotes Zn-dendrimer growth. High structural flexibility and porosity can promote undesired passage of zincate ions through their pores.[38, 39] These drawbacks underscore the need for alternative approaches in ZAB design and separator technology. Furthermore, considering that ZABs are designed to be cost-effective energy storage solutions, using expensive commercial AEPEM membranes is not an ideal approach. Consequently, there is a compelling need to engineer cost-effective AEPEMs.

Expanding further, among the polymer electrolytes and gel polymer electrolytes reported, poly(ethylene oxide) (PEO)[40, 41] or PVDF-based systems[42, 43], as well as their combinations with various zinc salts, are the most studied for ZAB.[44] The polymer electrolytes, such as PEO, due to their semicrystalline nature, show poor ionic conductivity. To attain high ionic conductivity

these polymers require the use of organic solvents such as propylene carbonate (PC), ethylene carbonate (EC), and dimethylsulfoxide (DMSO).[42, 43, 45] In spite having acceptable ionic conductivity, organic solvents such as PC, EC, and DMSO are inapplicable for open systems such as secondary zinc-air systems due to their volatility.[46] Nevertheless, PVA has proven to be an excellent choice for flexible electrolyte preparation due to its hydrophilic nature and film-forming capabilities.[35, 47-50] We decided to exploit these advantageous features of PVA by integrating it with a superior hydroxide ion conducting polymer in an aqueous system.

To this demand, robust C-C bonded cross-linked polymers capable of conducting hydroxide ions in humid environments became our target RZAB electrolyte material. Their amorphous nature and low electronic conductivity help minimize zinc-dendrite formation and their microporous structure should favour selective conduction of hydroxide ions, while the organic framework should aid them be a component of a flexible battery. They generally do not swell under aqueous conditions, hence as solid electrolyte they will adhere to the electrode while the electrode volume increases or reduces during charging and discharging, respectively.[51, 52] Thus, in this study, a thin hydroxide ion-conducting solid-state separator that pairs as an electrolyte for ZABs has been devised by combination of cationic polymer with PVA through a simple solution processing.

Inspired by the versatility of viologen chemistry[53, 54] earlier in chapter 1 we showed how the viologen-bakelite polymers can be manipulated to have stoichiometrically loaded mobile hydroxide ions to render them as superior quasi-solid electrolyte for primary zinc-air battery.[32, 33] Following this, with the rapidly surging interest in secondary or rechargeable batteries we realized the paramount need for demonstrating the potential of this hydroxide ion conducting cationic polymer in a more challenging secondary zinc air battery where its compatibility demands increase.[55-57] Specifically, a hydroxide ion-exchanged POF were integrated with PVA to form a solid-state separator-cum-electrolyte for zinc-air battery applications. Also, realizing that the monomeric building unit of these polymers can be tuned to have systematically increased number of hydroxide ions per unit, we successfully verified that this stoichiometric controlled can be translated to enhanced hydroxide ion conductivity. Our demonstration of high-power density and running life for this viologen-bakelite electrolyte based RZAB devised opens-up numerous possibilities.

## 2.2 Results and discussion

### 2.2.1 Synthesis and characterisation of IISERP-POF12 (2) and IISERP-POF13 (3)

The synthesis of two novel polymers, IISERP-POF12 (**2**) and IISERP-POF13 (**3**), from the monomers and its further conversion into **2_OH** and **3_OH** after the exchange of the Br- with OH⁻ ions illustrated in Scheme 1. The details for synthesizing the catalyst are presented in the Experimental Section of the Appendix. Briefly, the solvothermal reaction between 0.2 mmol phenolic compound and 0.2 (for 2)-0.15 (for 3) mmol viologen aldehyde in a mixture of 3 mL THF and 3 mL 1,4- dioxane at 200 °C for 72 h yielded the polymer as a brown-colored precipitate which was sequentially washed with DMF, THF, MeOH and finally acetone (Scheme 2.1). This powder was insoluble even in boiling DMF, so a Soxhlet wash was performed to remove unwanted oligomers, but none were observed. This as-made halogenated polymers 2 or 3 (100 mg) were converted to hydroxide-ion based polymer by exchanging the extra-framework guest halide ions for hydroxide ions using a KOH solution.  A yield of ~85-89 % was achieved for both the polymers. Note: We called our earlier hydroxide-ion conducting polymer from this family as 1_OH in chapter 1.[33]
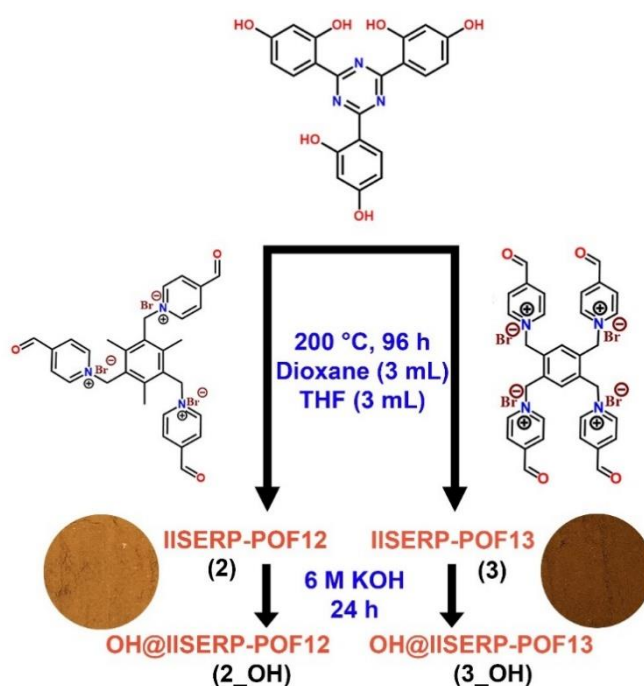


**Scheme 2.1:** Synthetic procedure of 2_OH and 3_OH. Insets show the photographic images of the compound 2 and 3.

There is evidence of Bakelite-type coupling between triazine-resorcinol and viologen-based bipyridinium aldehyde according to $^{13}C$ cross-polarisation (CP) magic angle spinning (MAS) solid-state nuclear magnetic resonance (NMR) (Figure 1a and 1b). The coupling between aldehyde and unsubstituted sites on the phloroglucinol rings led to a distinctive aliphatic peak for C-C at 29 and 28 ppm for 2 and 3, respectively.  It is followed by the other characteristic peaks from aromatic groups like triazine, around 195 ppm for 2 and 191 ppm for 3, and the

aromatic peaks for a viologen-based unit, around 142 ppm and 143 ppm for 2 and 3, respectively. The aliphatic peaks for building blocks around 69 ppm and 61 ppm were intact on forming 2 and 3 (Figure 2.1).[58, 59]
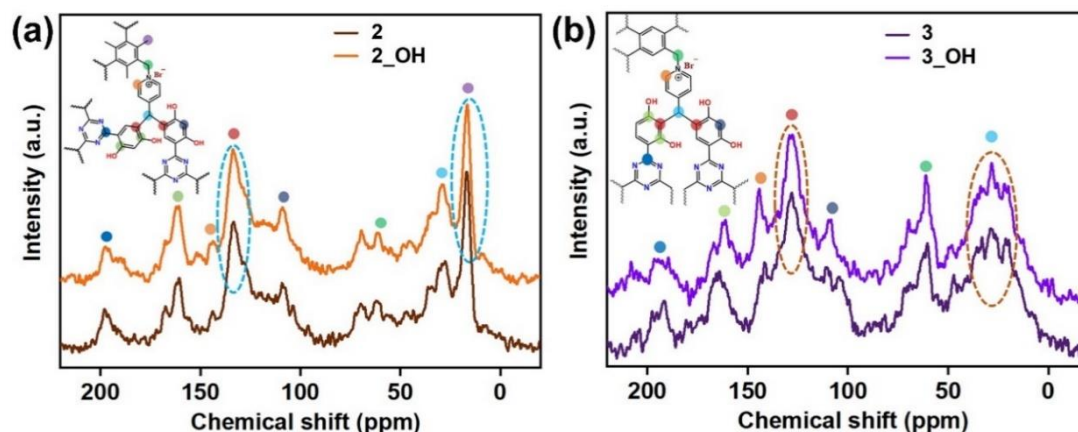


**Figure 2.1:** (a) $^{13}$C-CPMAS spectra of 2 and 2_OH. (b) 3 and 3_OH.

While this shows that polymerization is occurring, we recorded the NMR spectra of the material after boiling it in a THF + DMF mixture and then soaking it over 24 hours in a 6 M KOH solution to exchange the Br$^-$ with OH$^-$ ions. The characteristic peaks were still equally intense and situated at similar chemical shifts. For electrolyte applications, the polymer's exceptional chemical stability and functional group integrity, especially when subjected to harsh treatments, are highly desirable (Figure 2.1a and 2.1b). Figures 1c and 1d show the comparative FTIR spectrum of the aldehyde monomers, i.e., tri and tetra aldehyde, as-synthesized cationic polymers (2 and 3), its hydroxide exchanged form, 2_OH and 3_OH. The increase in intensity for C-H (2890 cm$^{-1}$) makes it clear that the C-C bond between the phenolic and aldehyde moieties has formed,

as evidenced by the elimination of the C=O (1690 cm$^{-1}$) from the monomers with polymerization. Additionally, the C=N (1620 cm$^{-1}$) ensures the integrity of the building blocks in 2, 2_OH, 3, and 3_OH, respectively (Figure 2.2a and 2.2b). These are highly cross-linked
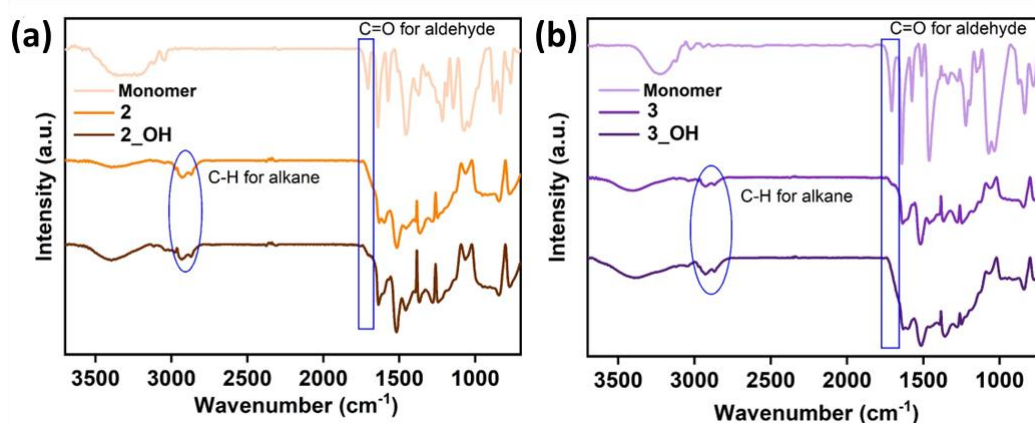


**Figure 2.2:** (a) FTIR spectra of Aldehyde monomers, 2, and 2_OH. (b) 3, and 3_OH.

high molecular weight polymers and insoluble in boiling solvents (glycol, DMF, DMSO); hence, we could not use methods such as Gel Permeation Chromatography in our characterizations.

Field emission scanning electron microscopy (FESEM) images of 2 and 3 (Figure 2.3 and 2.5) show that the polymer particles are agglomerated or intergrown microspheres with sizes ranging from 1 µm to 20 µm (Figure 2.3 and 2.5). Figures 2.4 and 2.6 show that even after treatment of 2 and 3 with a 6 M KOH solution to make 2_OH and 3_OH, respectively, there is no deformation in the shape of these microspheres. This shows that their texture remained stable in the corrosive environment. Thus, 2_OH and 3_OH seem well suited for operating under highly concentrated alkaline conditions necessitated by ZABs.
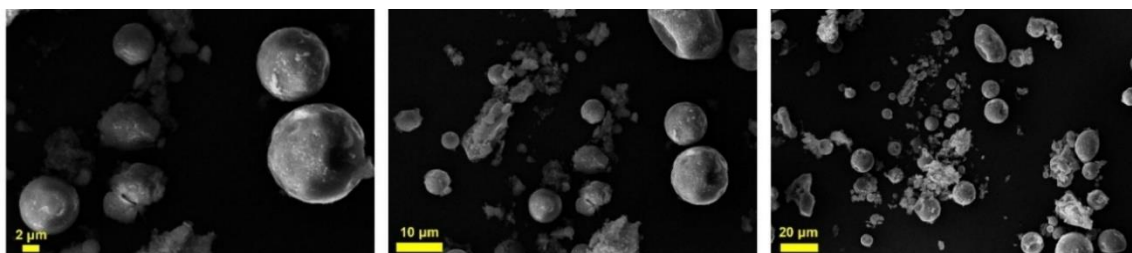


**Figure 2.3:** FESEM images of 2 at different magnifications.
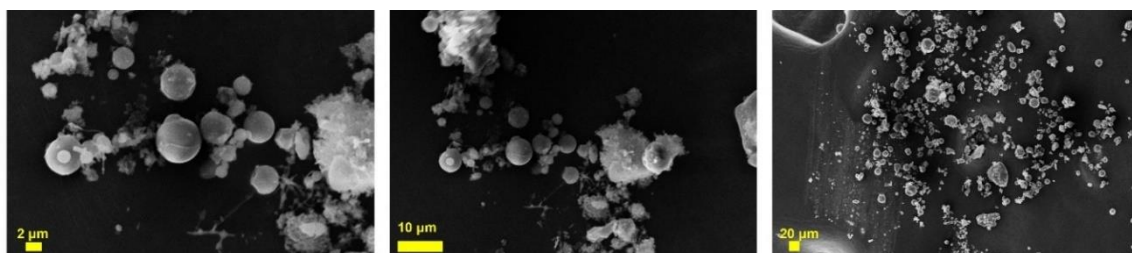


**Figure 2.4:** FESEM images of 2_OH at different magnifications.
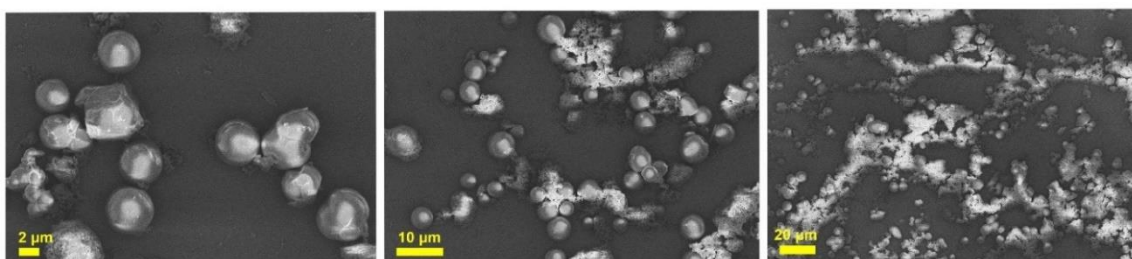


**Figure 2.5:** FESEM images of 3 at different magnifications.
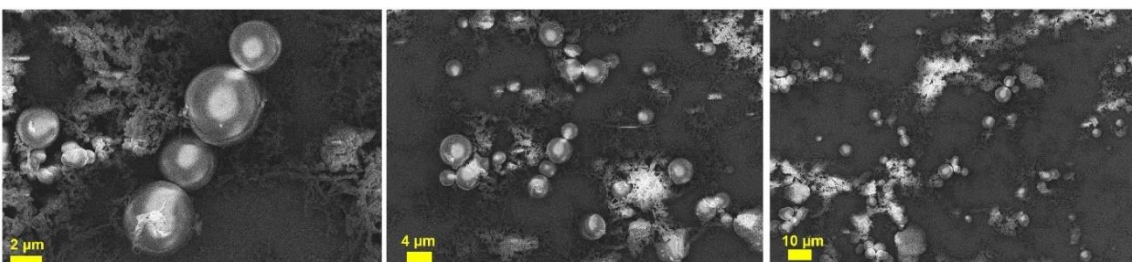


**Figure 2.6:** FESEM images of 3_OH at different magnifications.

The Energy dispersive X-ray (EDX) analysis shows the systematic increment in the atomic percentage of Br$^-$ ions from 1[33] to 3. It shows the presence of excess Br$^-$ ions available for the exchange with OH$^-$ ions (Figure 2.7). Also, the colour difference in 2 (brown) and 3 (dark brown) echoes the presence of a higher amount of Br$^-$ ions (Scheme 2.1).

**IISERP-POF13**
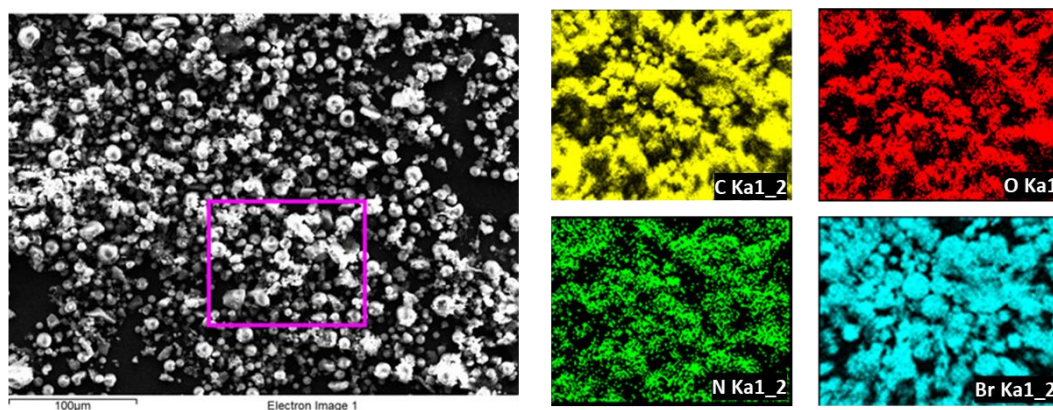


| IISERP-POF11 | | |
|---|---|---|
| Element | Weight% | Atomic% |
| C K | 68.2 | 76.9 |
| N K | 6.2 | 6.0 |
| O K | 18.8 | 16.0 |
| Br L | 6.8 | 1.1 |
| Totals | 100.00 | |

| IISERP-POF12 | | |
|---|---|---|
| Element | Weight% | Atomic% |
| C K | 69.1 | 78.8 |
| N K | 5.5 | 5.3 |
| O K | 16.9 | 14.5 |
| Br L | 8.5 | 1.5 |
| Totals | 100.00 | |

| IISERP-POF13 | | |
|---|---|---|
| Element | Weight% | Atomic% |
| C K | 64.7 | 77.7 |
| N K | 2.2 | 2.2 |
| O K | 19.6 | 17.6 |
| Br L | 13.5 | 2.5 |
| Totals | 100.00 | |

**Figure 2.7:** FESEM-EDX elemental mapping of 1, 2 and 3.

The High-resolution transmission electron microscopy (HRTEM) images unveiled that the spherical ball in 2 and 3 (Figure 2.8) are connected continuously, which could support the ionic transport across grains and spheres. We noticed no changes in the surface diameter of 2_OH and 3_OH spheres during OH- ion exchange, further demonstrating the chemical stability of the polymers (Figure 2.8). However, the elemental mapping of 2 and 3 (Figure 2.8) reveals the presence of Br- ions, which significantly lowered when exchanged with OH-. The presence of K$^+$ traces demonstrates that the exchange in 2_OH and 3_OH was successful (Figure S7 and S9, ESI).
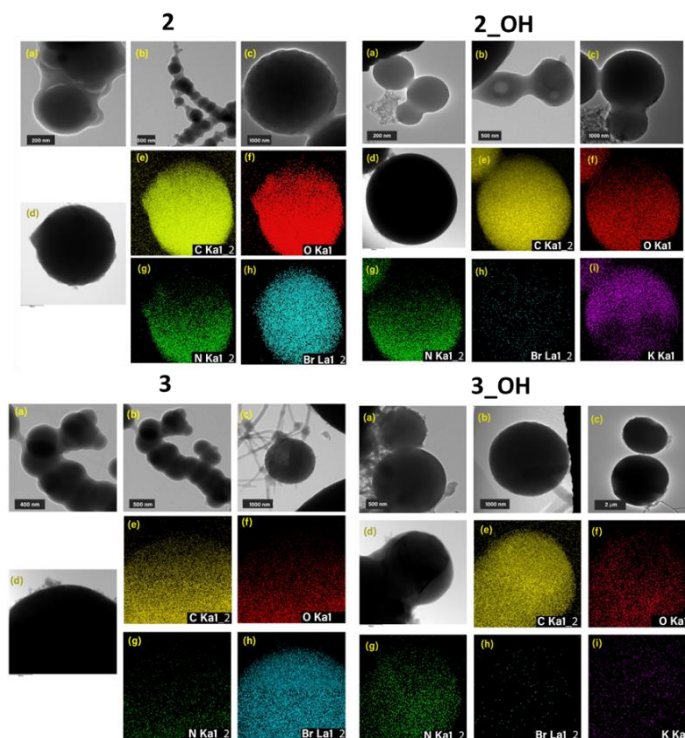
**Figure 2.8 :** HRTEM images of 2,3,2_OH and 3_OH at different magnifications.

Thermogravimetric analysis displayed that the frameworks 2 and 3 are stable up to 280 °C. We associate this with the strong C-C bond between the monomers, resembling Bakelite (Figure 2.9). The cationic polymers treated with 6 M KOH, 2_OH and 3_OH display similar TGA profiles (Figure S10, ESI), which exhibit no effect of harsh alkaline conditions on their thermal stabilities.
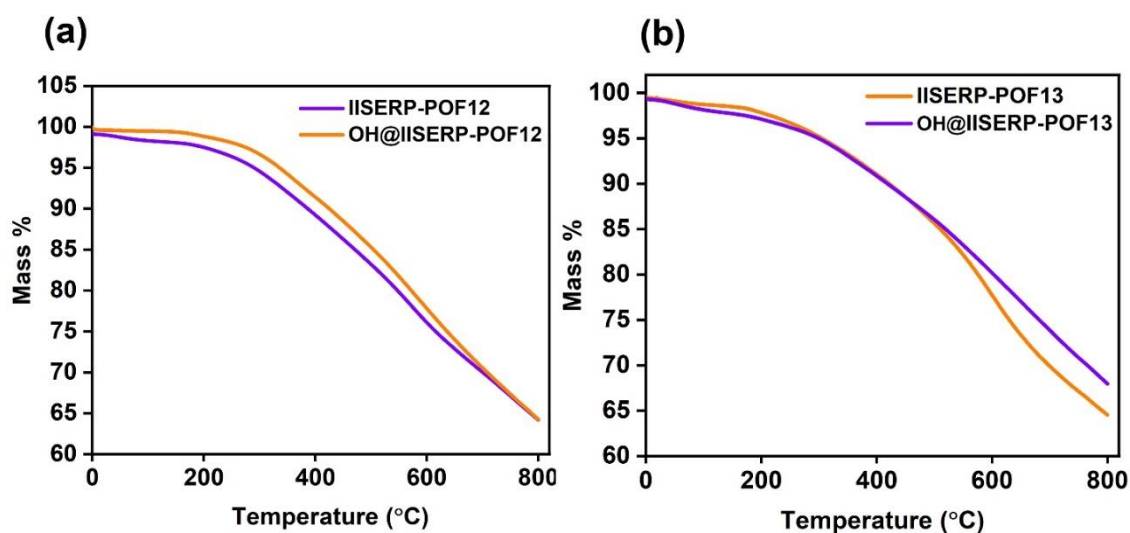


**Figure 2.9:** (a) Comparative thermogravimetric analysis plot for 2, 2_OH and (b) 3, 3_OH.

The contact angle measurements on the surface of the freshly synthesized halogen-containing polymer powders, labelled as 2 and 3, indicated a super-hydrophobic nature (Figure 2.10a and 2.10b at left). However, the 2_OH and 3_OH prepared by exchanging the halogen for hydroxide ions in an aqueous alkaline medium resulted in hydrophilic powders (Figure 2.10a and 2.10b at right). This change in surface wettability positively influences the materials' interaction with electrolytes.
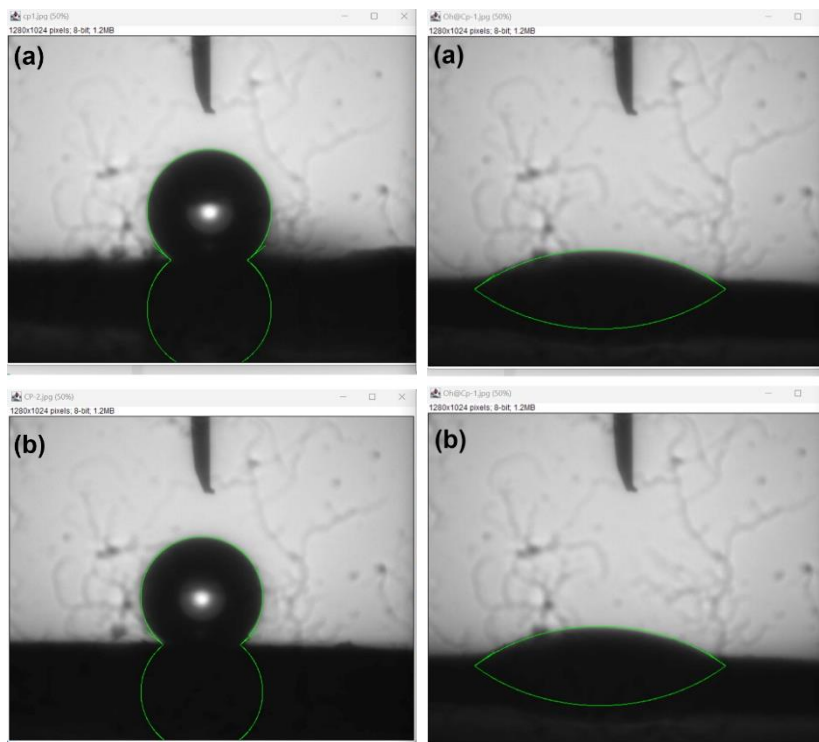


**Figure 2.10**: (a) Contact angle of the droplet of water sitting on the surface of the (a) 2 and (b) 3 [Left] and (a) 2_OH and (b) 3_OH [Right].

We investigated molecular porosity using water sorption isotherms. The water adsorption isotherms for 2, 3, 2_OH, and 3_OH were almost identical, indicating that the pore environment and structure had not undergone significant changes; however, the 2_OH and 3_OH have higher water capacity than the 2 and 3, demonstrating improved intrinsic wettability. Thus, materials with $Br^-$ containing frameworks are nearly super-hydrophobic (140° ± 3°) and become significantly hydrophilic when the bromides are replaced by $OH^-$ ions (Figure 2.11a). Notably, neither a significant change in density nor a detectable swelling of the polymer occurred (Figure 2.11b-f).
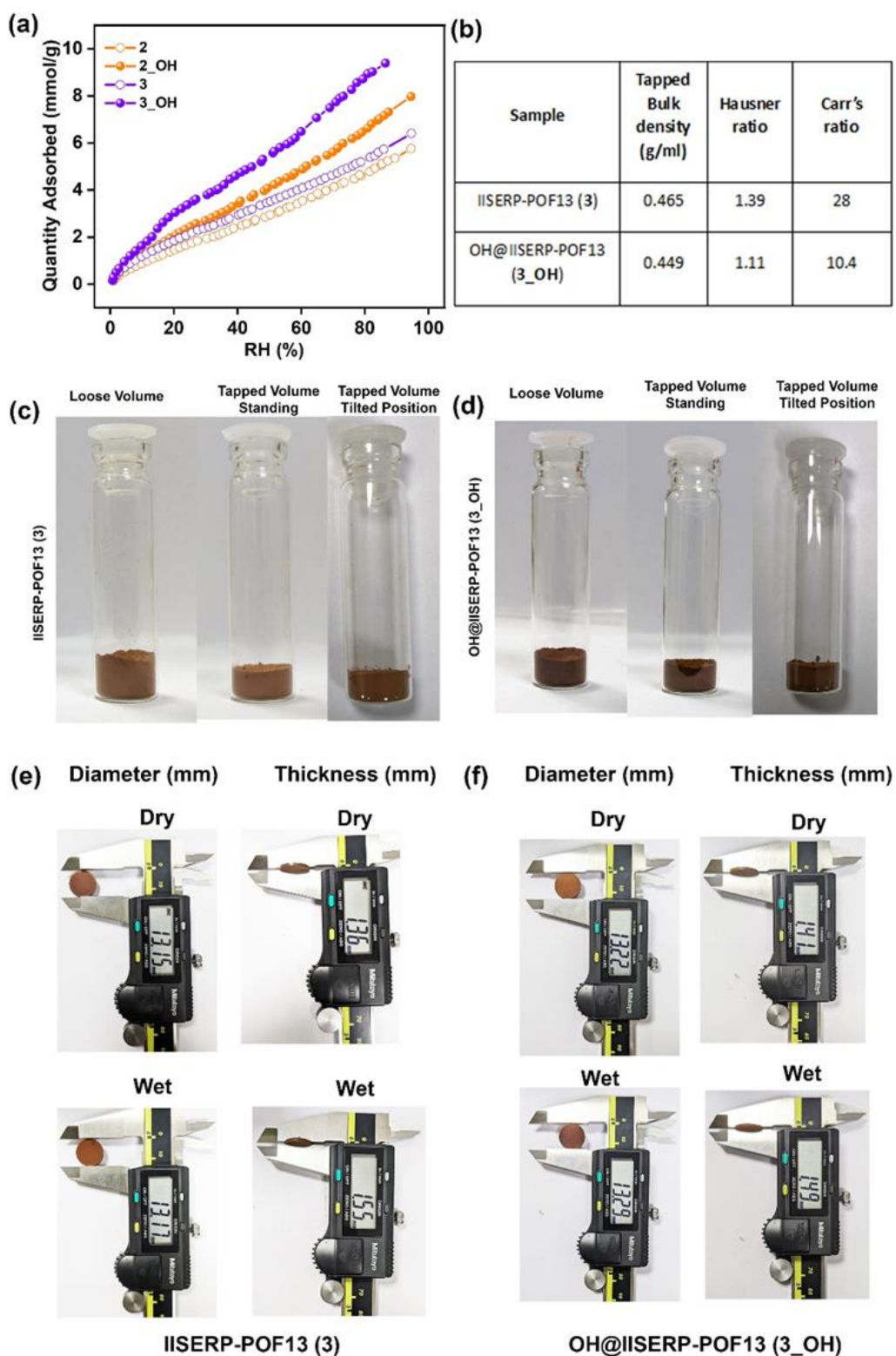
**Figure 2.11:** (a) Comparative water adsorption isotherms of 2, 3, 2_OH and  3_OH (b) Density calculations using tapping method  Photograph showing the volume change of (c) 3 and (d) 3_OH at different stages. Photograph showing the parameters of (e) 3 and (f ) 3_OH before and after humidity exposer.

## 2.2.2 Electrochemical studies

Electrochemical impedance analysis was performed in the $10^6$ to 0.1 Hz frequency range with an AC amplitude of 10 mV using Solartron impedance analyser. The densely pressed pellet of the 2, 3, 2_OH and 3_OH were employed to evaluate the intrinsic conductivity measurements of polymers. The impedance was recorded at variable temperatures (30 °C to 80 °C) and relative humidity (30% to 95 %) (Figure 2.12 and A2.1 to A2.3). As synthesized polymers, 2 and 3 displayed extremely low $Br^-$ ion-mediated ionic conductivity values (Figure 2.1). It is expected as the $Br^-$ ions are heavier and will be even less effective for a hydrogen-bond-assisted Grotthuss-type movement. The conductivity significantly increased after exchange with hydroxide ions, and the highest values were achieved for a range of temperatures at a constant relative humidity of 95%. The $OH^-$ ion conductivity value increases from $7.30 \times 10^{-4}$ S cm$^{-1}$ (30 °C) to $1.53 \times 10^{-2}$ S cm$^{-1}$ (80 °C) and $2.96 \times 10^{-3}$ S cm$^{-1}$ (30 °C) to $4.88 \times 10^{-2}$ S cm$^{-1}$ (80 °C) for 2_OH and 3_OH respectively (Figure 212c and 2.12a-b; Table A2.1, Appendix).
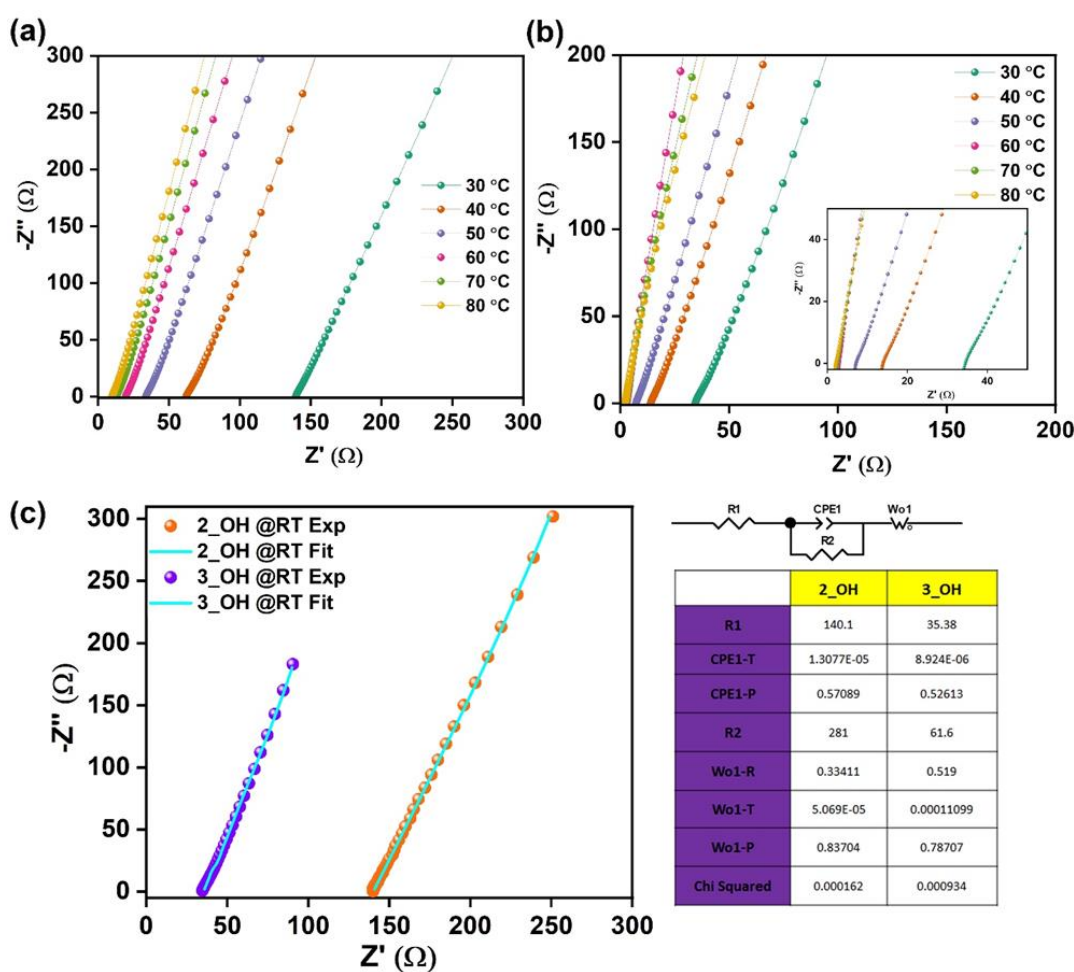


**Figure 2.12:** Temperature dependent Nyquist plots of (a) 2_OH, (b) 3_OH impedance analysis measured at 95 % RH (c) Circuit fits for 2_OH and 3_OH impedance analysis measured at 80 °C and 95 % RH.

The equivalent circuit was fitted for all the Nyquist curves using the Zview-4 software. The comparison of the most promising Nyquist plots (30 °C, 95% RH) of the 2_OH vs. 3_OH (Figure 2.12c) suggests that the series resistance and charge-transfer resistance both are substantially higher for the 2_OH (R1 = 140.1 Ω, R2 = 281.3 Ω) compared to the 3_OH (R1 = 35.4 Ω, R2 = 61.6 Ω). However, both 2_OH and 3_OH exhibit typical semi-infinite linear diffusion, or diffusion in one dimension that is only constrained by a substantial planar electrode on one side (at a 45° angle to the Z'-axis). By measuring the CV of the 2_OH and 3_OH, which showed that the capacitive behaviour was present in the fitted equivalent circuit, we confirmed the need for a CPE component (Figure 2.13).
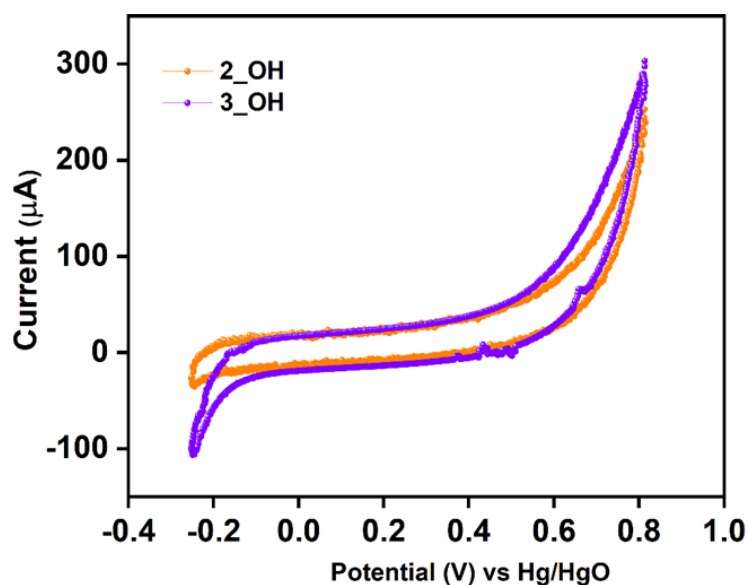


**Figure 2.13:** Cyclic voltammogram of 2_OH and 3_OH measured using a three-electrode system in 1M KOH electrolyte with Hg/HgO as reference and Pt wire as counter electrode.

A pseudocapacitive behaviour anticipated for the polymer with the porous structure is shown by a CPE-P value close to 0.5 for both pellets. In our scenario, hydroxide ions move through pathways created by the presence of hydroxyl groups and triazine. These pathways can potentially facilitate the formation of hydrogen bonds, contributing to the Grotthuss mechanism. However, concurrently applying an AC potential can generate sufficient force to induce vehicular motion. Furthermore, we investigated ac-impedance by varying the temperature (30 °C to 80 °C) to examine the humidity-dependent conductivity of 2_OH and 3_OH (Figure A2.1-A2.3, Apendix).

Comparative heatmaps of 2_OH and 3_OH show that polymers' conductivities range from $10^{-8}$ S cm$^{-1}$ (30% RH at 30 °C) to $10^{-2}$ S cm$^{-1}$ (95% RH at 80 °C). Up to 80% RH, a steady rise in conductivity values was seen as the temperature was elevated, but after that, both polymers exhibited a sudden increase in conductivity (the area changes from green to yellowish orange)

(Figure 2.14). Particularly, 3_OH has a higher conductivity value than 2_OH even at lower temperatures, especially above 80% RH (the wider area covered by the red-coloured zone). Increasing hydroxide ion conductivity with increasing temperature implies lowering the activation energy. In contrast, increased conductivity with increasing humidity means water could play a crucial role via hydrogen bonding. This takes into account the fact that the polymer lacks a crystalline structure with well-organized pores and that its electronic conductivity is constrained at longer-length scales.[60]
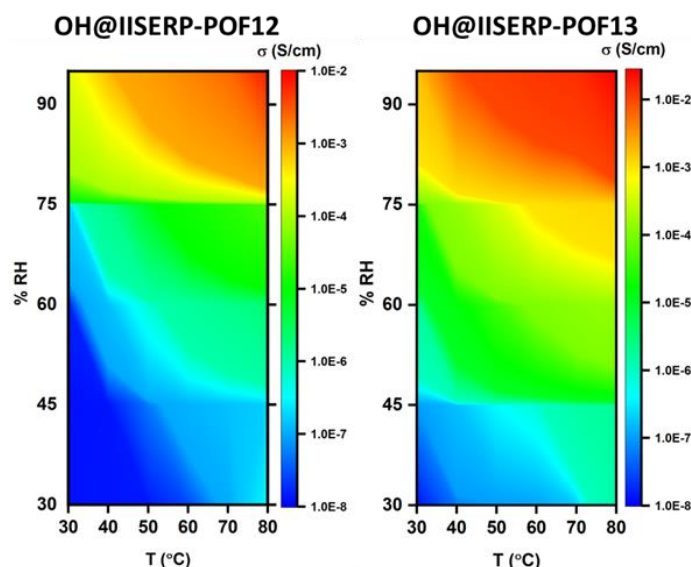


**Figure 2.14:** Heatmaps of 2_OH and 3_OH showing improvement in the conductivity on systematic increase in temperature and relative humidity.

To examine the electronic conductivity of 2_OH and 3_OH, linear sweep voltammetry (LSV) was used at a scan rate of 10 mV s$^{-1}$ in the potential window of −1 to 1 V (Figure 2.15). The conductivity observed in 2_OH and 3_OH is primarily ionic, likely due to the OH$^-$ ions, as evidenced by its minimal electronic conductivity.
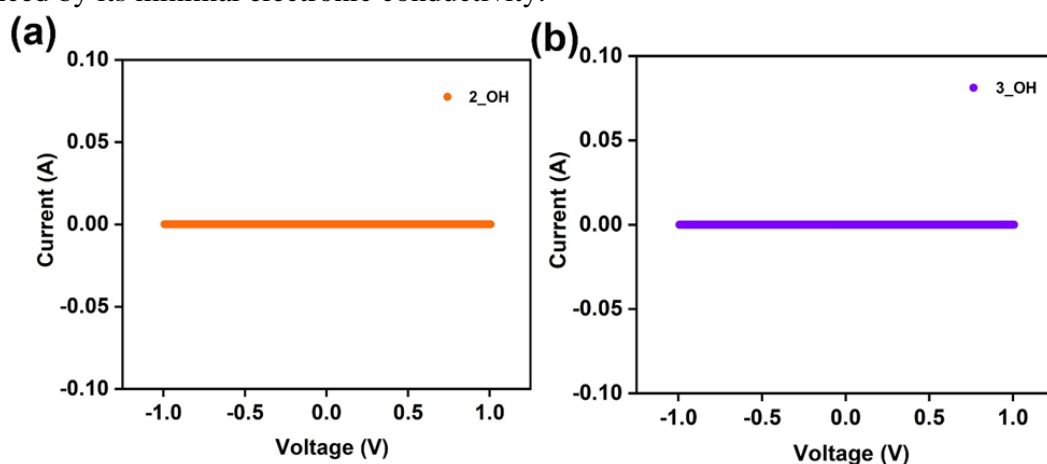


**Figure 2.15:** I-V curve of 2_OH and 3_OH measured using a two-probe set-up.

An activation energy of 0.49 eV and 0.45 eV for 2_OH and 3_OH are obtained when an Arrhenius equation is fitted to the temperature-dependent impedance data (Figure 2.16a-b),

which points to a Grotthuss diffusion process.[61] The reported activation energy for hydroxide ions in various nano-porous materials are comparable to the observed activation energies.[62]
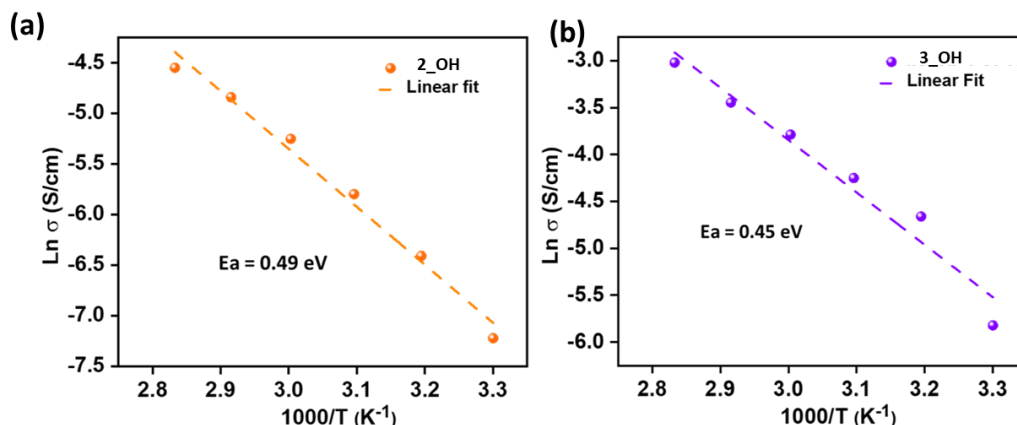


**Figure 2.16:** Construction of Arrhenius plots to investigate the comparable activation energy of (a) 2_OH and (b) 3 _OH.

It must be noted that when comparing our results to those of chapter 1, the polymers show a gradual increase in hydroxide ion conductivity from 1_OH[33] to 3_OH (Figure 2.17, Table A2.1, Appendix). It was anticipated, given the systematic increment in intrinsic hydroxide ion concentration. The activation energy obtained from 1_OH to 3_OH almost same since the structural environments of the polymers remain similar across all three cases. Using the Z' vs. $\omega^{-1/2}$ plot, we computed the diffusion coefficient for the hydroxide ions inside the cationic polymer framework.
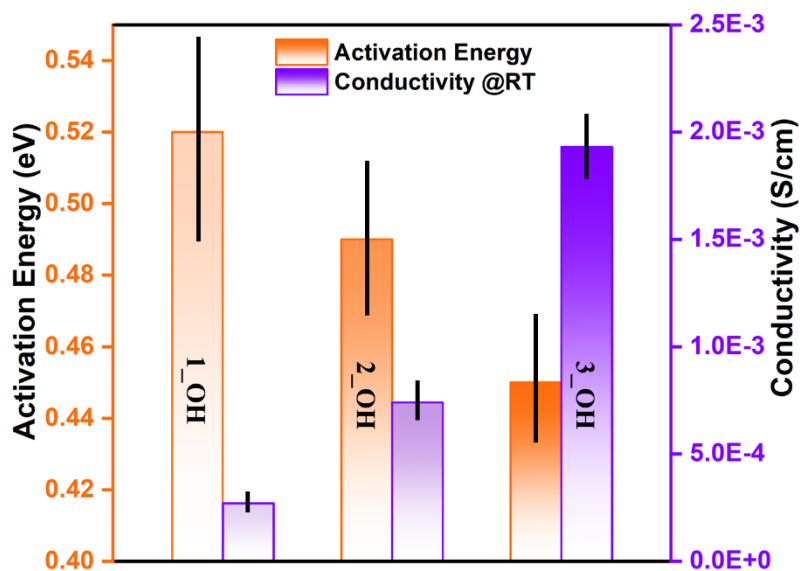


**Figure 2.17:** Systematic increment in the OH- ion conduction on increasing the no. of hydroxide ions in each polymer.

The impedance plot's low-frequency spectrum produced the distinctive linear fits (Figure 2.18), from which the diffusion coefficients at 80 °C and 95% relative humidity were calculated to be $3.61 \times 10^{-5}$ cm$^2$ s$^{-1}$ (2_OH) and $3.71 \times 10^{-5}$ cm$^2$ s$^{-1}$ (3_OH). As the temperature rose, the diffusion coefficient increased systematically. The calculated diffusion coefficients at 80 °C and 95% relative humidity agreed well with the values published in the earlier publication $2.9 \times 10^{-5}$ cm$^2$ s$^{-1}$ (1_OH).
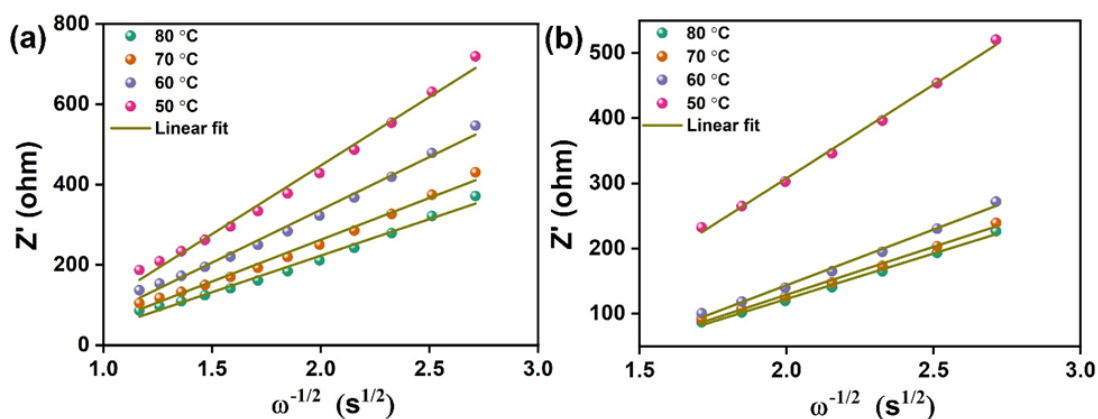


**Figure 2.18:** A plot of the Z' versus ω−1/2 for (a) 2_OH and (b) 3_OH at 95% RH at different temperatures.

The best-performing polymer, 3_OH, was tested for temperature-dependent cycling stability in an 8-hour cycle ranging between 30 °C and 60 °C at 95% relative humidity (Figure 2.19a). The cycling demonstrated excellent conductivity retention, varying the temperature between 30 °C and 60 °C. We also measured conductivity for various batches of 3_OH, and the results are in the same order (Figure 2.19b inset-top). Additionally, for more than 50 hours, the time-dependent conductivity stability demonstrated outstanding stability up to 95% (Figure 2.19b inset-bottom).
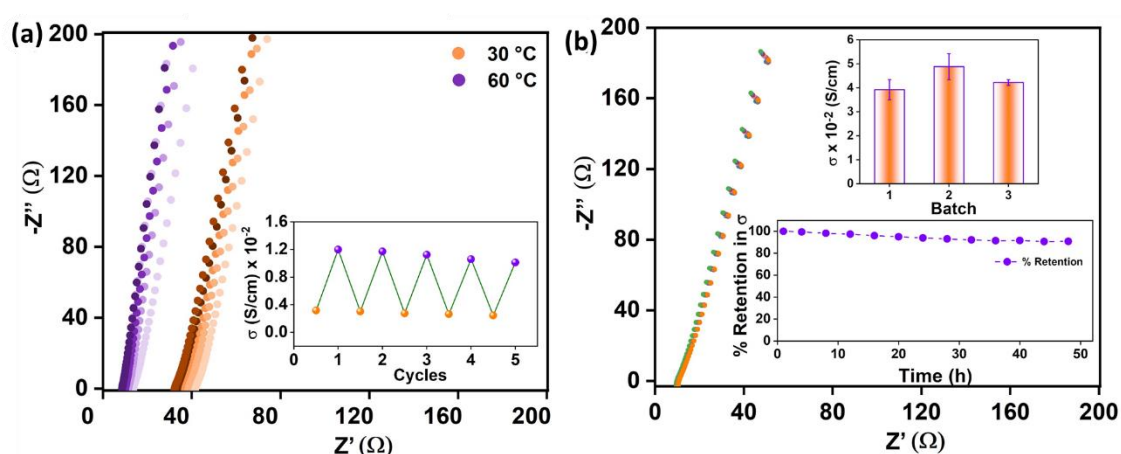


**Figure 2.19:** A plot of the Z' versus ω−1/2 for (a) 2_OH and (b) 3_OH at 95% RH at different temperatures.

On post-impedance characterization, the polymers 2_OH and 3_OH showed excellent chemical and structural integrity. The SS-NMR demonstrates retention of all peaks from the pristine

polymers (Figure 2.20), and the surface morphology is also intact in the FESEM images (Figure A2.5, A2.6, Appendix).
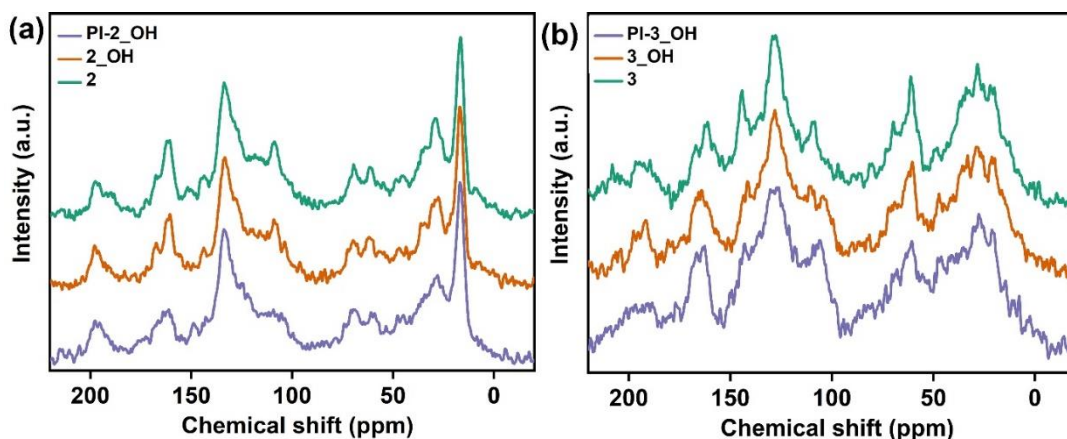


**Figure 2.20:** Comparative Solid-state Cross-Polarization Magic Angle Spinning Carbon-13 Nuclear Magnetic Resonance ($^{13}$C CP-MAS NMR) spectra 2, 2_OH, PI-2_OH and 3, 3_OH, PI-3_OH.

The remarkable robust nature of the polymers makes them apt candidates for charge storage applications in harsh alkaline conditions like zinc-air batteries. So, we explored the potential of exceptional hydroxide ion conducting viologen polymer 3_OH as a solid-state electrolyte in a zinc-air battery application. A thin, flexible, and stable membrane is developed by blending 3_OH and polyvinyl alcohol (PVA) in a 1:1 ratio (3_OH@PVA), as shown in Figure 2.21. Photographs shown in red circles are images of the membrane at different stages. According to
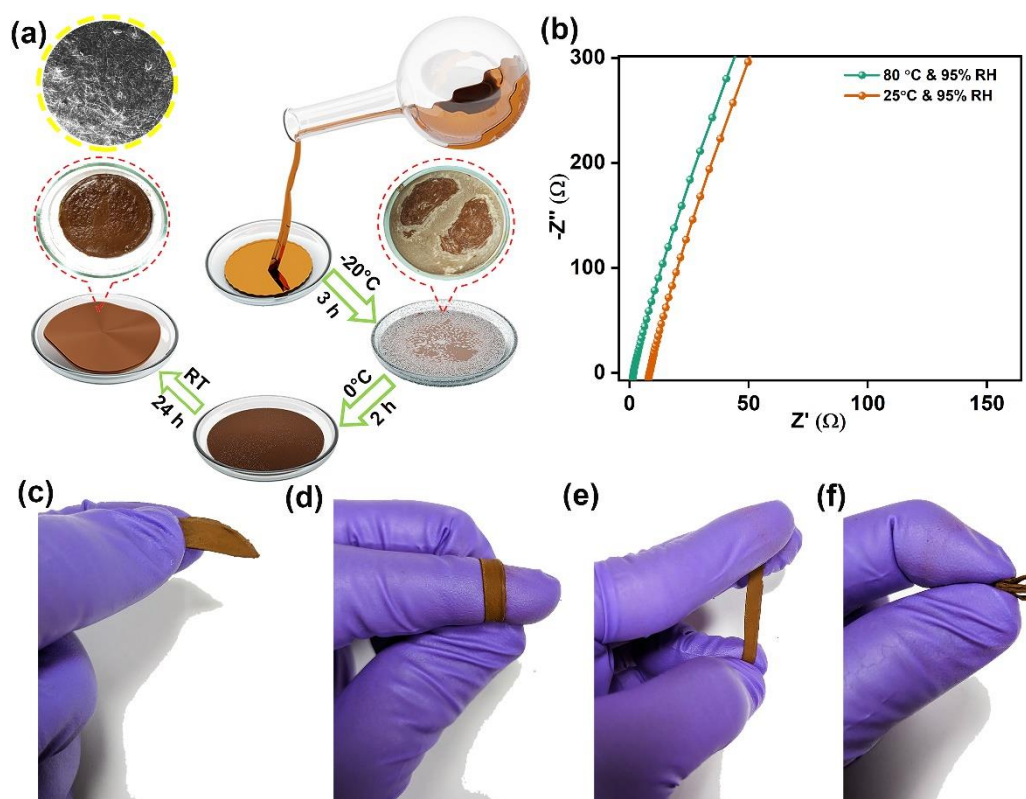


**Figure 2.21:** (a) Schematic of the preparation of thin, flexible OH- ion conducting membrane; (b) Comparison of the Nyquist plots for the 3_OH@PVA at various temperatures and 95% humidity; (c-f) Digital photograph of the synthesized membrane and their flexibility at different angles.

the FESEM images (Figure 2.21, highlighted in a yellow ring, and Figure 2.22a), membranes with a uniform surface would considerably assist in creating an interface between an electrode and an electrolyte.

The ultra-thin membrane, which has a thickness of just 277 μm, is seen in the cross-sectional FESEM images. It contains uniformly distributed polymer spheres, which assist in speeding up ion transport via a shorter path (Figure 2.22d to 2.22e). The analysis of AFM images and amplitude roughness parameters indicates that the electrolyte membrane exhibits satisfactory flatness. The consistent mean surface roughness (Sa) values, ranging from 177 nm to 268 nm across different samples, demonstrate that the membrane maintains a consistent level of flatness. (Figure A2.7: Table A2.2). Measurements of the membrane's conductivity revealed a significantly promising hydroxide ion conductivity of $4.78 \times 10^{-3}$ S cm$^{-1}$ at room temperature
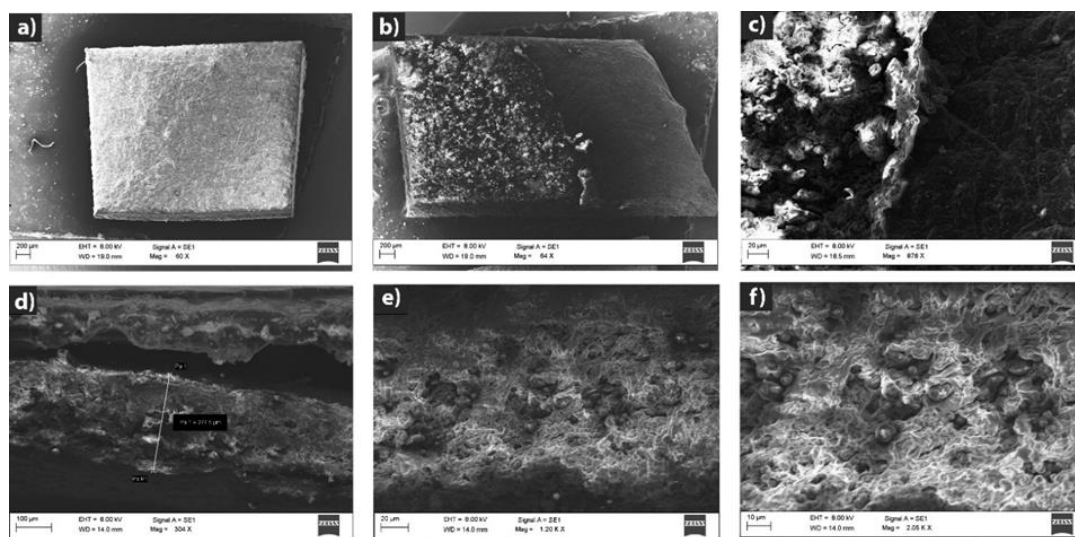


**Figure 2.22:** FESEM images of 3_OH@PVA membrane at different magnifications.

(25 °C) in the presence of 95% humidity. The conductivity increased when the temperature was changed from room temperature to 80 °C, reaching a maximum of $2.53 \times 10^{-2}$ S cm$^{-1}$ (Figure 2.21b). Along with superior ionic conductivity, the membrane exhibits excellent flexibility on bending, stretching and crumbling (Figure 2.21c-f).

### 2.2.3 Quasi solid state electrolyte in ZAB

To assess the suitability of 3_OH@PVA used as a quasi-solid-state electrolyte for rechargeable zinc-air battery (ZAB) applications, a conventional ZAB cell was assembled (Figure 2.23 ). In this cell configuration, 3_OH@PVA served as the quasi-solid-state electrolyte, while Pt/C-RuO$_2$ was employed as the air-cathode, and the anode consisted of zinc paste (comprising Zn powder mixed with a solution of 3 M KOH and 0.2M Zn (OAc)$_2$. As depicted in Figure 2.23, the ZAB

configuration includes the use of an ORR catalyst-coated gas carbon diffusion layer (GDL) as the cathode, zinc powder as the anode, and 3_OH@PVA as the electrolyte.
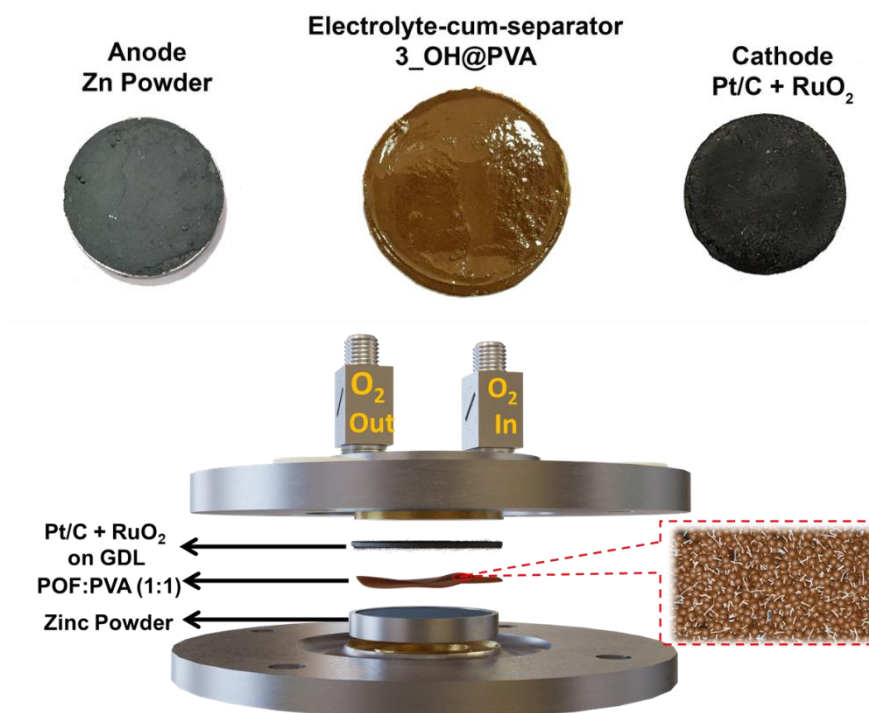


**Figure 2.23:** Photographic images of the ZAB assembly. The process of creating, evaluating performance, and demonstrating the zinc-air battery (ZAB). A schematic illustration depicting the fabrication of the ZAB, where the cathode catalyst loading is set at 1.0 mg/cm², the anode employs zinc powder, and the separator consists of a 3_OH@PVA.

During ZAB operation, oxygen diffuses through the porous air cathode and undergoes reduction to form hydroxide ions (OH⁻), which subsequently migrate toward the anode through the
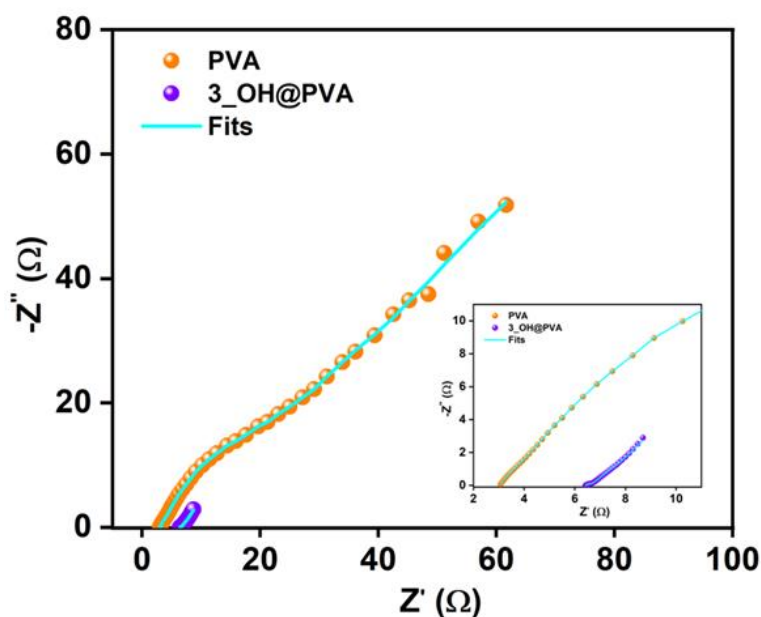


**Figure 2.24:** Nyquist plots from electrochemical impedance spectroscopy (EIS) analysis recorded for RZAB cells at the open-circuit voltage (OCV) condition, along with the corresponding equivalent circuit model fit.

electrolyte, facilitating the oxidation of zinc into its hydroxide and oxide forms. The electrons released during the zinc oxidation process flow through the external circuit, thereby establishing the flow of electric current. The open circuit voltage (OCV) condition of the cell was subjected to electrochemical impedance spectroscopy (EIS) analysis. The comparative Nyquist plot for PVA-based and 3_OH@PVA -based membrane along with the fit of an equivalent circuit model, is illustrated in Figure 2.24.

The system's performance is comparable to previously reported ZAB systems in the literature (refer to Table 2.1). The comparative analysis of steady-state cell polarization (Figure 2.25) reveals maximum power densities ($P_{max}$) of 72 mW cm$^{-2}$ and 158 mW cm$^{-2}$ for ZABs utilizing PVA and 3_OH@PVA as membranes, respectively. Notably, the 3_OH@PVA based cell when compared to the PVA-based counterpart, the former gradually improves its performance,
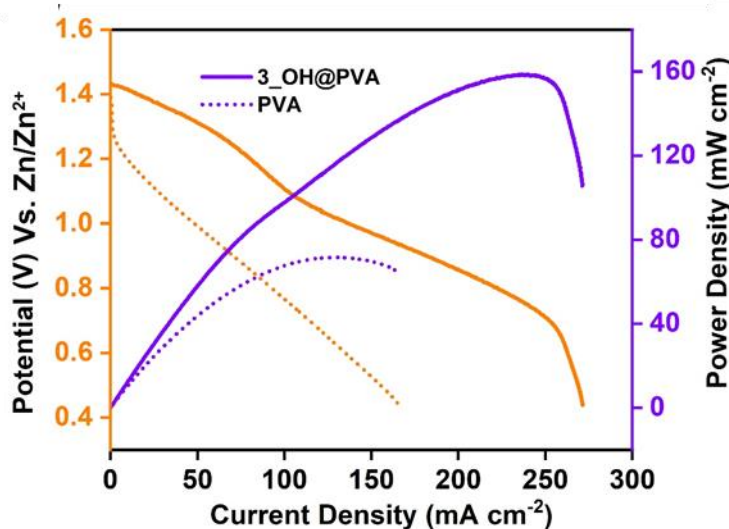


**Figure 2.25:** Polarization plots were generated for the ZABs produced using Pt/C +RuO$_2$ as the air electrodes, illustrating their electrochemical performance.

ultimately outperforming the latter. This improvement can be attributed to the intrinsic advantages of 3_OH@PVA membranes, particularly in terms of mass transport facilitated by the membrane and electrolytes interface formation. Furthermore, the superior performance of the 3_OH@PVA membrane can be directly attributed to the improved ionic conductivity of the membrane and the enhanced contact achieved at the electrode-electrolytes interface. To determine the specific capacities of the prepared ZAB cell, the discharge process was carried out to a voltage of 1.38 V at a current density of 10 mA cm$^{-2}$.

Moreover, the galvanostatic discharge curve, captured at a current density of 10 mA cm$^{-2}$ (Figure 2.26), provides evidence of durability of ZAB system. It is noteworthy that the discharge duration for ZABs utilizing 3_OH@PVA and PVA as membrane is approximately 22 hours and 8 hours (Figure 2.26 inset), respectively. The observed voltage decrease within the plateau

region over the course of operation is likely attributable to side reactions occurring at the surface of the zinc powder, as indicated in prior studies. The calculated specific capacity, as illustrated in Figure 2.26, for the constructed zinc-air battery (ZAB) utilizing 3_OH@PVA-membrane as the separator cum electrolyte, amounts to approximately 742 mAh/$g_{Zn}$. In comparison, the ZAB system employing PVA as the separator cum electrolyte exhibits a specific capacity of around 579 mAh/$g_{Zn}$. The failure of the RZAB (PVA-KOH) systems after 8 hours, can be attributed to the rapid drying of the commercial and PVA-KOH membranes within the semi-open ZAB system configured for air-breathing. This drying phenomenon is a consequence of the inferior electrolyte retention characteristics exhibited by PVA-KOH membrane.
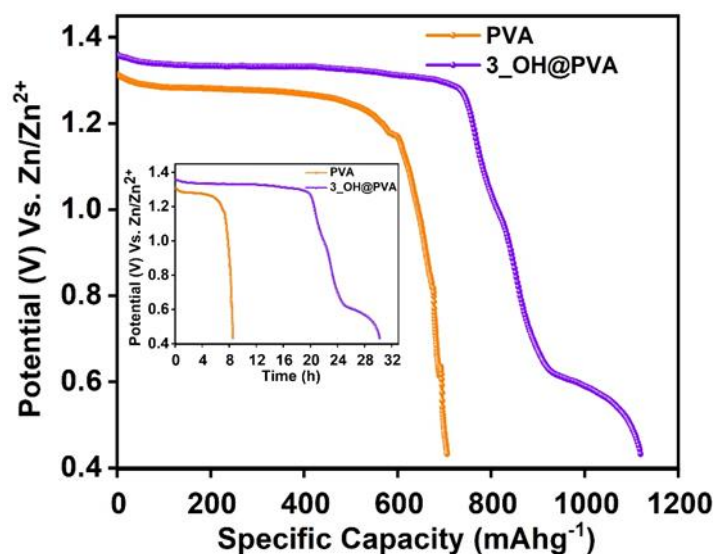


**Figure 2.26:** Galvanostatic discharge capacities of the fabricated ZABs, normalized by the consumed amount of zinc during the discharging process.

Furthermore, Figure 2.27 displays the galvanostatic charge-discharge curves recorded for cells operating at 10 mA cm$^{-2}$. The zinc-air battery (ZAB) fabrication using 3_OH@PVA revealed a
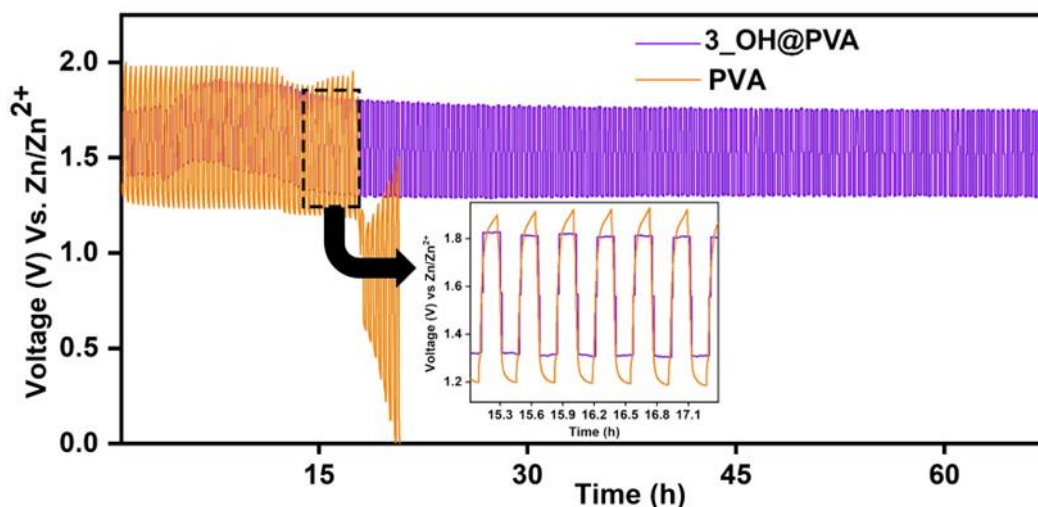


**Figure 2.27:** Long-term galvanostatic charge-discharge profiles of the ZABs employing Pt/C +RuO2 as the cathode catalysts, monitored until the complete consumption of the anodic zinc powder

lower voltage difference (0.55 V) between charging and discharging compared to the PVA-KOH (0.72 V). Over 67 hours of continuous charge-discharge cycles, the 3_OH@PVA membrane-based cell showed a nominal increase of 0.02 V in the voltage difference.

In contrast, the PVA-KOH -based system exhibited a rapid increase to 0.67 V within just 17 hours, leading to termination of the test. Additionally, the inset image (Figure 2.27 the magnified charge-discharge profile between 14 to 18 hours shows the symmetric plateau nature of the 3_OH@PVA membrane based RZAB, while the PVA-KOH cell displayed asymmetric behaviour. This difference reveals the better interface formation and water uptake capacity of 3_OH@PVA compared to PVA-KOH which helps to run for long time charge-discharge device.

In response to the growing interest in portable and flexible electronic devices, we designed and demonstrated a flexible and rechargeable zinc-air battery (F-RZAB) with a surface area of 2 x 2 cm². This innovative system utilized a catalyst-coated carbon cloth as the cathode, 3_OH@PVA -based membrane as the electrolyte, and a polished 0.10 mm thick zinc foil as the anode (Figure 2.28a). A flexible solid-state ZAB was developed to demonstrate the practical usability of the as-prepared 3_OH@PVA (Figure 5a; more information is provided in the supporting info. Section, resulting in a combined voltage of 1.386 V, as measured using a multimeter device (Figure 5b). Without additional $O_2$ gas purging, the constructed solid-state battery delivers an OCV value of 1.38 V (Figure 2.28b) in an air atmosphere. The maximum power density is 79 mW/cm$^2$, according to the polarisation study shown in Figure 2.28c.
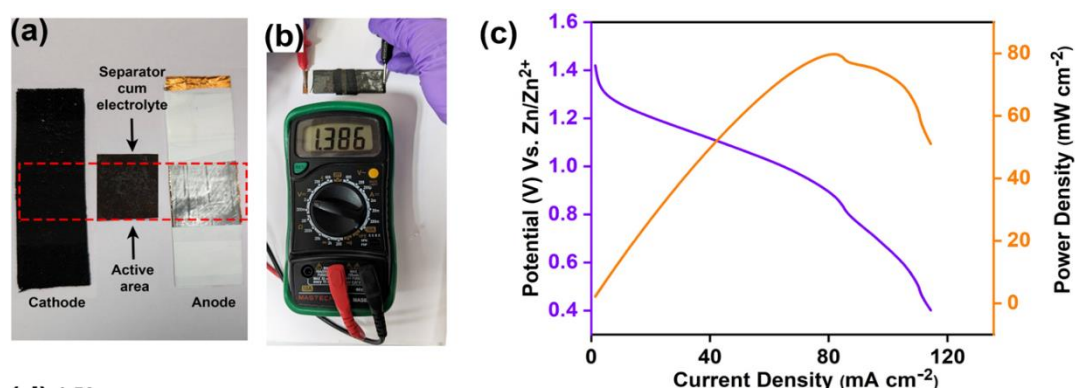


**Figure 2.28:** (a) Components of the F-RZABs showing cathode, anode and electrolyte; (b) Digital photograph of F-RZAB and the multimeter device respectively; c) Recording of the current (I)-voltage (V) Polarization plot for F-RZAB.

The output voltage was stable on bending the device at different angles (Figure 2.29b-c) owing to the liquid-free nature of **3_OH@PVA**. The device's flexibility was assessed by monitoring its open-circuit voltage (OCV) at various bending angles (0°, 90°, and 180°). Remarkably, the system maintained a consistent OCV of approximately 1.40 V across these different bending angles (Figure 2.29a). Figure 5e-g shows the digital photograph of the flexible device in various angles.
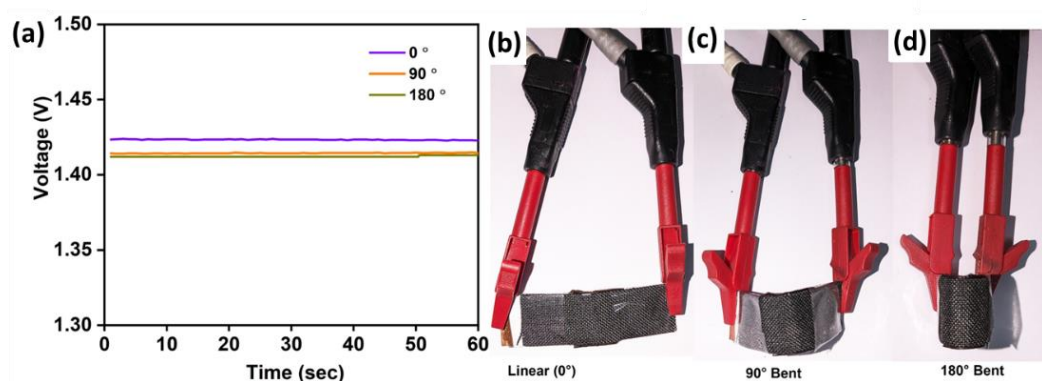
**Figure 2.29:** (a) Comparative OCV acquired at different bending angles, illustrating the device's flexibility; (b-d) Digital photograph of the flexible device in various angles (0 º, 90 º, and 180º).

**Table 2.1: Comparison of the RZAB of the 3_OH with releveant literature reports.**

| Sr. No. | Bifunctional catalysts | Hydrogel/Solid-state electrolyte | Current density (mA cm-2) | Power density (mW cm-2) | Cycle life (h) | Reference |
|---|---|---|---|---|---|---|
| 1 | FeNi SAs/NC | PVA–KOH | 1 | 52.12 | 45 | Adv. Energy Mater.2021, 11, 2101242 |
| 2 | Pt/C+RuO2 | PVA–KOH | 1 | 45.25 | 20 | Adv. Energy Mater.2021, 11, 2101242 |
| 3 | FeCo/Se-CNT | PVA-KOH-Zn(Ac)2 | 5 | 37.5 | 70 | NanoLett.2021, 21, 2255−2264 |
| 4 | CS-NFO@PNC | PVA–KOH–Zn(CH3COO)2 | 5 | - | 40 | Appl. Catal. B-environ 2022, 300, 120752 |
| 5 | Fe,Mn/N-C | PVA–KOH | 5 | 160.8 | 81 | NATURE COMMUNICATIONS \| (2021) 12:1734 \| https://doi.org/10.1038/s41467-021-21919-5 |
| 6 | Co/ZnCo2O4@NC-CNTs | PVA-KOH-Zn(Ac)2 | 5 | 151 | 20 | Nano Energy Volume 82, April 2021, 105710 |
| 7 | Fe1Co1-CNF | PVA-18M | 2 | - | 3.5 | Nano Energy |

| | | KOH-0.02M Zn(OAc)2 | | | | Volume 87, September 2021, 106147 |
|---|---|---|---|---|---|---|
| 8 | FeP/Fe2O3@NPCA | PVA-KOH-Zn(Ac)2 | 5 | 35.5 | 8.3 | Adv.Mater.2020, 32, 2002292 |
| 9 | NiCo2S4@g -C3N4 -CNT | PVA -10M KOH | 3 | - | 14 | Adv.Mater.2019, 31, 1808281 |
| 10 | 1nm CoO x | PVA-4M KOH -0.2M Zn(Ac)2 | 6 | 300 | 10 | Adv.Mater.2019, 31, 1807468 |
| 11 | Pt/C+RuO2 | PVA-4M KOH -0.2M Zn(Ac)2 | 6 | 225 | 10 | Adv.Mater.2019, 31, 1807468 |
| 12 | Co -NiO | PVA -KOH | 2 | 50 | 6 | Applied Catalysis B: Environmental 2019, 250, 71 |
| 13 | Co 3 O 4@CC | PVA -2M KOH | 2 | - | 10 | Adv. Energy Mater.2017, 7, 1700779 |
| 14 | Co 4N/CNW/CC | PVA -9M KOH | 0.5 | - | 15 | Journal of the American Chemical Society 2016, 138, 10226 |
| 15 | V2O3/MnS | PVA–KOH | 2 | 72 | 18 | Small2022, 18, 2104411 |
| 16 | CoMn2O4/NCNFs | PVA–KOH–ZnO | 1 | 39.3 | 5 | J. Mater. Chem. A, 2019, 7, 24868–24876 |
| **17** | **Pt/C+RuO2** | **3_OH@PVA** | **5** | **158** | **67** | **This work** |

### 2.2.4 Post battery characterizations

### 2.2.5

When used as a separator-cum-electrolyte in the ZAB, the stability of **3_OH@PVA** was examined. According to PXRD analysis, there were no ZnO characteristic peaks on the cathode side, suggesting that dendrite growth during battery measurements did not cause membrane tearing. (Figure A2.4, Appendix)

It was observed that the neat PVA membrane displayed a few tiny fractures while measuring the battery (Figure A2.8b-d, Appendix). In contrast, the membrane in the case of **3_OH@PVA** is stable and undamaged, with uniformly distributed spherical polymer particles (Figure A2.9e-f, Appendix), just like the membrane initially applied (Figure 2.22). Additionally, the thickness of **3_OH@PVA** dropped from 277 μm to 177 μm (Figure A2.9, Appendix) on post-battery characterization, which may be attributed to pressure applied during battery packing.

## 2.3 Conclusions

A new strategy for the POF -based membrane has been developed, involving controlled polymerization initiated from a pre-admitted and infiltrated precursor. This POF-based membrane shows robust OH$^-$ ion conductivity of $2.53 \times 10^{-2}$ S cm$^{-1}$, as well as its attributes high electrolyte uptake, and retention capacity. The rechargeable ZAB assembled through POF-based membrane in Quasi-solid-state and flexible device applications shows favourable enhancements in the performance of RZABs. The performance evaluation of the rechargeable zinc-air battery (RZAB) using POF-membrane in conjunction with the Pt/C-RuO$_2$ catalyst-coated air-cathode revealed a peak power density of 158 mW cm$^{-2}$ at a current density of 246 mA cm$^{-2}$ and a specific capacity of 742 mAh g$^{-1}$. This was accompanied by promising charging/discharging characteristics. To validate the flexibility of the system, the POF-membrane was integrated with a thin Zn foil as the anode and a Pt/C-RuO$_2$ catalyst-coated carbon cloth featuring the cathode. F-RZAB delivered an OCV value of 1.38 V in an air atmosphere and the maximum power density is 79 mW/cm$^2$. Remarkably, the system maintained a consistent OCV of approximately 1.40 V across these different bending angles. Beyond the realm of metal-air batteries, the outcomes of this study and the strategies employed hold promise as effective practical solutions that can offer technological benefits in various other electrochemical systems, enhancing performance in both quasi-solid-state and flexible configurations.

## 2.4 Acknowledgements

## 2.5 References

1.  J.-N. Liu, C.-X. Zhao, J. Wang, D. Ren, B.-Q. Li and Q. Zhang, *Energy Environ. Sci.*, 2022, **15**, 4542-4553.

2.  T. Zhang, Y. Tang, S. Guo, X. Cao, A. Pan, G. Fang, J. Zhou and S. Liang, *Energy Environ. Sci.*, 2020, **13**, 4625-4665.

3.  Q. Wang, S. Kaushik, X. Xiao and Q. Xu, *Chem Soc Rev*, 2023.

4.  P. Tan, B. Chen, H. Xu, H. Zhang, W. Cai, M. Ni, M. Liu and Z. Shao, *Energy Environ. Sci.*, 2017, **10**, 2056-2080.

5.  R. Kushwaha, C. Jain, P. Shekhar, D. Rase, R. Illathvalappil, D. Mekan, A. Camellus, C. P. Vinod and R. Vaidhyanathan, *Adv. Energy Mater.*, 2023, **13**, 2301049.

6.  J. S. Lee, S. Tai Kim, R. Cao, N. S. Choi, M. Liu, K. T. Lee and J. Cho, *Adv. Energy Mater.*, 2011, **1**, 34-50.

7.  P. Zhang, Z. Chen, N. Shang, K. Wang, Y. Zuo, M. Wei, H. Wang, D. Zhong and P. Pei, *Mater. Chem. Front.*, 2023.

8.  J. Fu, Z. P. Cano, M. G. Park, A. Yu, M. Fowler and Z. Chen, *Adv. Mater.*, 2017, **29**, 1604685.

9.  S. S. Shinde, N. K. Wagh, C. H. Lee, D. H. Kim, S. H. Kim, H. D. Um, S. U. Lee and J. H. Lee, *Adv. Mater.*, 2023, **35**, 2303509.

10. Z. Farmani, M. A. Sedghamiz and M. R. Rahimpour, *Zinc Batteries: Basics, Developments, and Applications*, 2020, 187-213.

11. A. M. Asiri and R. Boddula, *Zinc batteries: basics, developments, and applications*, John Wiley & Sons, 2020.

12. X. W. Lv, Z. Wang, Z. Lai, Y. Liu, T. Ma, J. Geng and Z. Y. Yuan, *Small*, 2023, 2306396.

13. S. Peng, *Zinc-Air Batteries: Fundamentals, Key Materials and Application*, Springer Nature, 2023.

14. N. Manna, S. K. Singh, M. Kurian, A. Torris and S. Kurungot, *ACS Appl. Energy Mater.*, 2022, **5**, 8756-8768.

15. Q. Liu, R. Liu, C. He, C. Xia, W. Guo, Z.-L. Xu and B. Y. Xia, *escience*, 2022, **2**, 453-466.

16. A. R. Mainar, E. Iruin, L. C. Colmenares, A. Kvasha, I. De Meatza, M. Bengoechea, O. Leonet, I. Boyano, Z. Zhang and J. A. Blazquez, *J. Energy Storage*, 2018, **15**, 304-328.

17. M. Xu, D. Ivey, Z. Xie and W. Qu, *J. Power Sources*, 2015, **283**, 358-371.

18. C. Chakkaravarthy, A. A. Waheed and H. Udupa, *J. Power Sources*, 1981, **6**, 203-228.

19. R. Gilliam, J. Graydon, D. Kirk and S. Thorpe, *Int. J. Hydrog. Energy*, 2007, **32**, 359-364.

20. X. Liu, X. Fan, B. Liu, J. Ding, Y. Deng, X. Han, C. Zhong and W. Hu, *Adv. Mater.*, 2021, **33**, 2006461.

21. A. R. Mainar, O. Leonet, M. Bengoechea, I. Boyano, I. de Meatza, A. Kvasha, A. Guerfi and J. Alberto Blázquez, *Int. J. Energy Res.*, 2016, **40**, 1032-1049.

22. V. Verma, R. M. Chan, L. Jia Yang, S. Kumar, S. Sattayaporn, R. Chua, Y. Cai, P. Kidkhunthod, W. Manalastas Jr and M. Srinivasan, *Chem. Mater.*, 2021, **33**, 1330-1340.

23. Y. Wei, Y. Shi, Y. Chen, C. Xiao and S. Ding, *J. Mater. Chem. A*, 2021, **9**, 4415-4453.

24. X. Cai, L. Lai, J. Lin and Z. Shen, *Mater. Horiz.*, 2017, **4**, 945-976.

25. J. Li, J. Qiao and K. Lian, *Sustain. Energy Fuels*, 2017, **1**, 1580-1587.

26. C. Choi, K. Robert, G. Whang, P. Roussel, C. Lethien and B. Dunn, *Joule*, 2021, **5**, 2466-2478.

27. J. Li, J. Qiao and K. Lian, *Energy Stor. Mater.*, 2020, **24**, 6-21.

28. O. D. Thomas, K. J. Soo, T. J. Peckham, M. P. Kulkarni and S. Holdcroft, *J. Am. Chem. Soc.*, 2012, **134**, 10753-10756.

29. W.-H. Lee, A. D. Mohanty and C. Bae, *ACS Macro Lett.*, 2015, **4**, 453-457.

30. F. Wang, D. Wang and Y. Nagao, *ChemSusChem*, 2021, **14**, 2694-2697.

31. J. Fan, S. Willdorf-Cohen, E. M. Schibli, Z. Paula, W. Li, T. J. Skalski, A. T. Sergeenko, A. Hohenadel, B. J. Frisken and E. Magliocca, *Nat. Commun.*, 2019, **10**, 2306.

32. F. Liu, H.-J. Chung and J. A. Elliott, *ACS Appl. Energy Mater.*, 2018, **1**, 1489-1495.

33. D. Rase, R. Illathvalappil, H. D. Singh, P. Shekhar, L. S. Leo, D. Chakraborty, S. Haldar, A. Shelke, T. G. Ajithkumar and R. Vaidhyanathan, *Nanoscale Horiz.*, 2023, **8**, 224-234.

34. R. Chen, X. Xu, S. Peng, J. Chen, D. Yu, C. Xiao, Y. Li, Y. Chen, X. Hu and M. Liu, *ACS Sustain. Chem. Eng.*, 2020, **8**, 11501-11511.

35. X. Zhong, Z. Zheng, J. Xu, X. Xiao, C. Sun, M. Zhang, J. Ma, B. Xu, K. Yu and X. Zhang, *Adv. Mater.*, 2023, **35**, 2209980.

36. M. Kurian, V. Vijayakumar, N. Manna, F. Kanheerampockil, S. Bhat and S. Kurungot, *J. Mater. Chem. A*, 2023, **11**, 14776-14787.

37. A. D. Easley, K. Mohanty and J. L. Lutkenhaus, *J. Mater. Chem. A*, 2023, **11**, 8783-8790.

38. M. T. Tsehaye, F. Alloin, C. Iojoiu, R. A. Tufa, D. Aili, P. Fischer and S. Velizarov, *J. Power Sources*, 2020, **475**, 228689.

39. R. K. Sankaralingam, S. Seshadri, J. Sunarso, A. I. Bhatt and A. Kapoor, *Mater. Today: Proc.*, 2022, **64**, 1649-1654.

40. W. Hagan, R. Latham, R. Linford and S. Vickers, *Solid State Ion.*, 1994, **70**, 666-669.

41. J. Fauvarque, S. Guinot, N. Bouzir, E. Salmon and J. Penneau, *Electrochim. Acta*, 1995, **40**, 2449-2453.

42. G. G. Kumar and S. Sampath, *Solid State Ion.*, 2003, **160**, 289-300.

43. G. G. Kumar and S. Sampath, *Polymer*, 2004, **45**, 2889-2895.

44. S. Ikeda, Y. Mori, Y. Furuhashi and H. Masuda, *Solid State Ion.*, 1999, **121**, 329-333.

45. A. Lewandowski and I. Majchrzak, *J. New Mater. Electrochem. Syst.*, 2001, **4**, 135-142.

46. H. Ye and J. J. Xu, *J. Power Sources*, 2007, **165**, 500-508.

47. Z.-X. Lin, Y.-T. Lu, C.-Y. Lai and C.-C. Hu, *J. New Mater. Electrochem. Syst.*, 2021, **168**, 100531.

48. E. García-Gaitán, D. Frattini, I. Ruiz de Larramendi, M. Martínez-Ibáñez, D. González, M. Armand and N. Ortiz-Vitoriano, *Batter. Supercaps*, 2023, **6**, e202200570.

49. X. Fan, R. Zhang, S. Sui, X. Liu, J. Liu, C. Shi, N. Zhao, C. Zhong and W. Hu, *Angew. Chem. Int. Ed.*, 2023, **62**, e202302640.

50. X. Fan, H. Wang, X. Liu, J. Liu, N. Zhao, C. Zhong, W. Hu and J. Lu, *Adv. Mater.*, 2023, **35**, 2209290.

51. G. Zhang, X. Cai, C. Li, J. Yao, W. Liu, C. Qiao, G. Li, Q. Wang and J. Han, *ACS Appl. Polym. Mater.*, 2023, **5**, 3622-3631.

52. S. K. Yadav, D. Deckenbach and J. J. Schneider, *Batteries*, 2022, **8**, 244.

53. Y. Zhang, Y.-P. Deng, J. Wang, Y. Jiang, G. Cui, L. Shui, A. Yu, X. Wang and Z. Chen, *Energy Stor. Mater.*, 2021, **35**, 538-549.

54. H. Dou, M. Xu, Y. Zheng, Z. Li, G. Wen, Z. Zhang, L. Yang, Q. Ma, A. Yu and D. Luo, *Adv. Mater.*, 2022, **34**, 2110585.

55. M. Kathiresan, B. Ambrose, N. Angulakshmi, D. E. Mathew, D. Sujatha and A. M. Stephan, *J. Mater. Chem. A*, 2021, **9**, 27215-27233.

56. H. Nishide, *Green Chem.*, 2022, **24**, 4650-4679.

57. P. Gu, M. Zheng, Q. Zhao, X. Xiao, H. Xue and H. Pang, *J. Mater. Chem. A*, 2017, **5**, 7651-7666.

58. D. Crespy, M. Bozonnet and M. Meier, *Angew. Chem. Int. Ed.*, 2008, **47**, 3322-3328.

59. S. Haldar, D. Rase, P. Shekhar, C. Jain, C. P. Vinod, E. Zhang, L. Shupletsov, S. Kaskel and R. Vaidhyanathan, *Adv. Energy Mater.*, 2022, **12**, 2200754.

60. U. Tröltzsch and O. Kanoun, *Electrochim. Acta*, 2012, **75**, 347-356.

61. G. A. Luduena, T. D. Kühne and D. Sebastiani, *Chem. Mater.*, 2011, **23**, 1424-1429.

62. D. W. Kang, M. Kang, H. Yun, H. Park and C. S. Hong, *Adv. Funct. Mater.*, 2021, **31**, 2100083.

## Appendix for chapter 2

**A2.1 Solid-state ZAB demonstration:**

**A2.1.1 Preparation of the Gel Electrolytes:**

To prepare the mixture, 100 mg of 3_OH powder was dispersed in 2 ml of water and stirred at 90°C for 1 hour until a uniform distribution of the polymer was achieved. Subsequently, 100 mg of PVA was introduced into the same solution, and the mixture was heated for 3 hours to ensure a homogeneous blend of POF (3_OH) and PVA. As soon as the PVA had completely dissolved in the water, the solution was poured into a petri dish and promptly subjected to a cooling process. The cooling procedure involved two stages: initially at -20 °C for 3 hours, followed by a subsequent stage at 0 °C for 2 hours. After this cooling process, the resultant membrane solidified. The solidified membrane was then air-dried at room temperature, resulting in the formation of a flexible membrane. This flexible membrane was subsequently employed as a combined separator and electrolyte within the context of a Zinc air battery application.

**A2.1.2 Assembly and test of solid-state ZAB device:**

The construction of the solid-state rechargeable zinc-air battery (ZAB) involved the following components: zinc powder as the anode, a gas diffusion layer (GDL) coated with Pt/C +RuO$_2$ as the air-cathode, and a PVA/KOH gel serving as the electrolyte. This assembly was set up within an electrochemical ZAB device arrangement provided by MTI Corporation. To prepare the catalyst slurry, Pt/C +RuO$_2$ was mixed with a 1:4 ratio mixture of isopropyl alcohol and water, followed by an hour of sonication. Subsequently, 10 wt% Fumion solution was added to the resulting dispersion, and the mixture underwent an additional hour of sonication. Once the dispersion was fully achieved, the catalyst slurry was applied to a gas diffusion layer (GDL) and allowed to dry at 60°C for 12 hours, resulting in a catalyst loading of 1.0 mg cm$^{-2}$ (with an electrode area of 1.0 cm$^2$). For the evaluation of the ZAB setup using a multichannel CH instrumrnt was employed under room temperature conditions. The analysis of the ZAB involved steady-state polarization conducted at a scan rate of 5 mV/s. Additionally, polarization analysis and electrochemical impedance spectroscopy (EIS) studies were performed at a constant voltage of 1.0 V with a 20 mV amplitude. Galvanostatic discharge and discharge-charge cycling tests (consisting of 15 minutes of discharge followed by 15 minutes of charge) were carried out using a CH- potentiostat.

**A2.1.3 Fabrication of flexible solid-state ZAB:**

For the flexible solid-state Zinc-air battery, Zn foil with 0.25 mm thickness was employed as the anode, Pt/C + RuO$_2$ coated carbon cloth was used as the air-breathing cathode and hydroxide ion conducting 3_OH@PVA as the solid-state separator-cum-electrolyte. During the fabrication of the battery,

3_OH@PVA was wetted with 300 µm 3 M KOH solution. The anode and cathode were separated with 3_OH@PVA and the sandwich is sealed. The backside of the cathode was kept it open for the passage of air and the battery was operated without providing any additional $O_2$ supply.

**A2.1.4 Electrochemical Measurements:**

The linear sweep voltammetry and the constant current charge-discharge measurements were performed using the AMETEK Battery analyzer using VERSA STUDIO (Version 2.52) software.

**A2.1.5 Impedance measurements:**

The Solartron SI 1260 IMPEDANCE/GAIN-PHASE ANALYZER model was used to carry out the impedance measurement. The impedance spectra were recorded by applying a range of frequencies from 1 MHz to 0.1 Hz with an amplitude of 10 mV. Moreover, ESPEC SH-222 Bench-top Type Temperature & Humidity Chamber was used to maintain the temperature and humidity while measurement. Impedance data fitting was done using Z-view software.

**A2.2 Synthesis of Polymers**

**A2.2.1 Synthesis of 1,3,5-tris(bromomethyl)-2,4,6-trimethylbenzene**

To a mixture of mesitylene (6.0 g, 50 mmol), paraformaldehyde (6.0 g, 200 mmol) and 30 mL of glacial acetic acid was added 40 mL of 33% HBr in acetic acid. The reaction mixture was kept at 110 °C for 12 hours. After cooling down to room temperature, the reaction mixture was poured into ice water. The products precipitated out, were filtered off, washed several times with distilled water to make it acid free. The compound was dried over P2O5 giving dirty yellow solid. Yield ~ 92%;–^{1}H NMR (400 MHz, CDCl$_3$) δ 4.59 (s, 1H), 2.48 (s, 1H). ^{13}C NMR (101 MHz, CDCl$_3$) δ 137.74 (s), 133.09 (s), 29.74 (s), 15.24 (s).

$^1$H NMR of 1,3,5-tris(bromomethyl)-2,4,6-trimethylbenzene
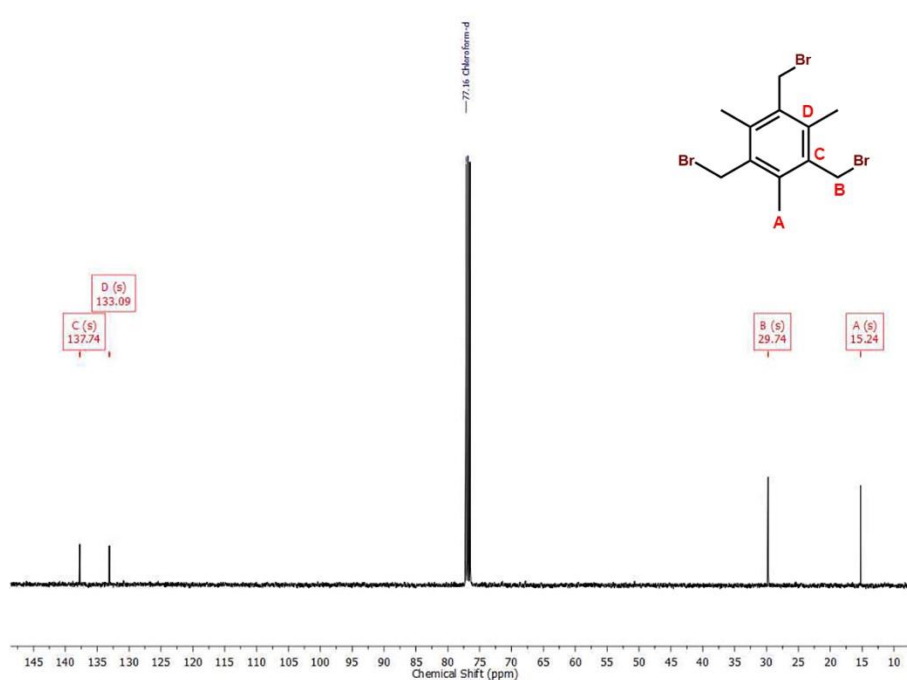


$^{13}$C NMR of 1,3,5-tris(bromomethyl)-2,4,6-trimethylbenzene

## A2.2.2 Synthesis of Aldehyde Monomers

Typically, **1,3,5-tris(bromomethyl)-2,4,6-trimethylbenzene** (398 mg, 1 mmol) or 1,2,4,5-Tetrakis(bromomethyl)benzene (450 mg, 1 mmol) and 4-Pyridinecarboxaldehyde (642-856 mg, 6-8 mmol) were added in acetonitrile (40 mL) and the reaction mixture was refluxed overnight at 85 °C. The resulting precipitate was filtered off and washed with acetone. to give the pure products.
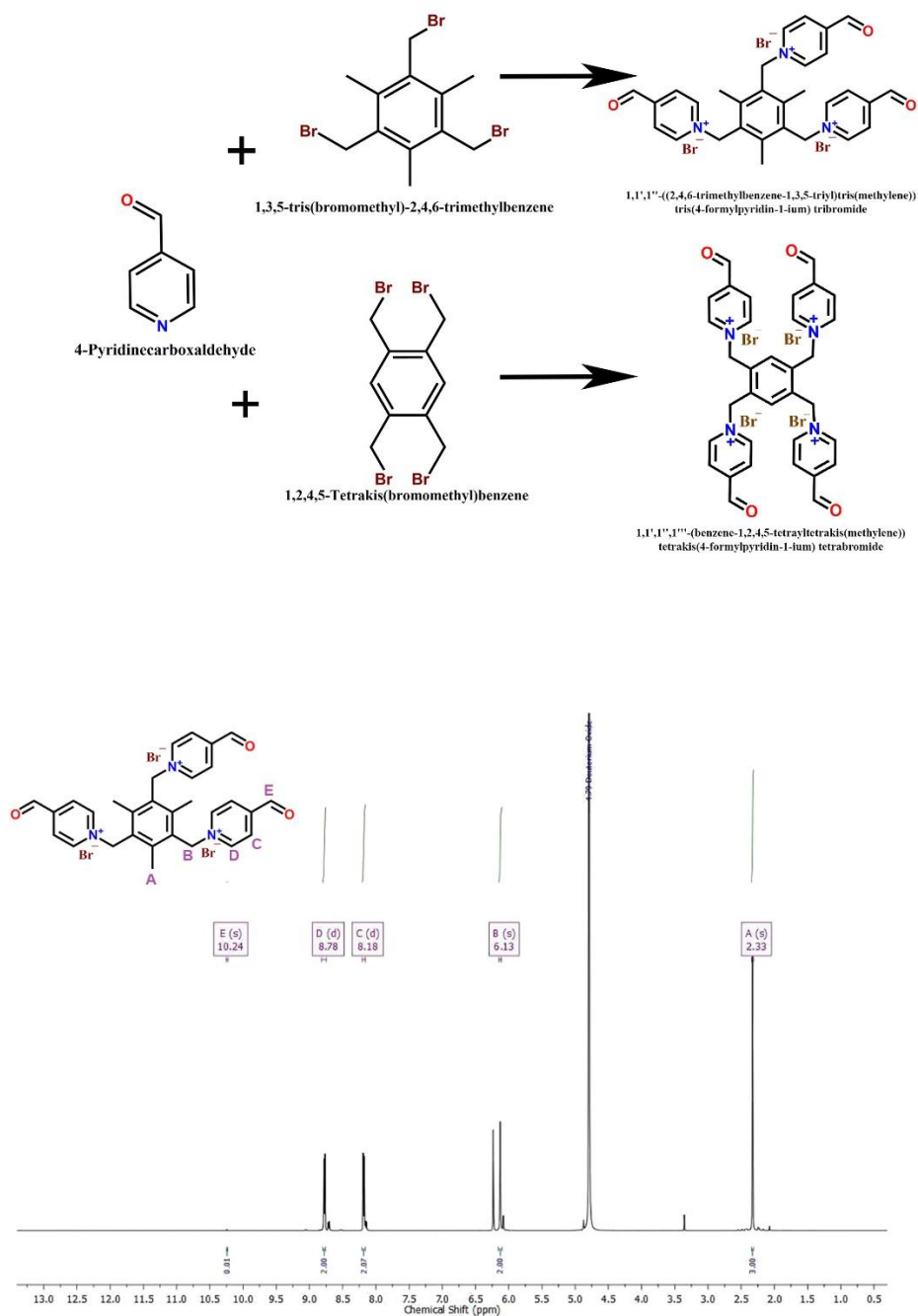
$^1$H NMR of 1,1',1''-((2,4,6-trimethylbenzene-1,3,5-triyl)tris(methylene))tris(4-formylpyridin-1-ium) tribromide

$^1$H NMR (400 MHz, D2O) δ 10.24 (s, 1H), 8.78 (d, J = 6.8 Hz, 1H), 8.18 (d, J = 6.6 Hz, 1H), 6.13 (s, 1H), 2.33 (s, 1H).
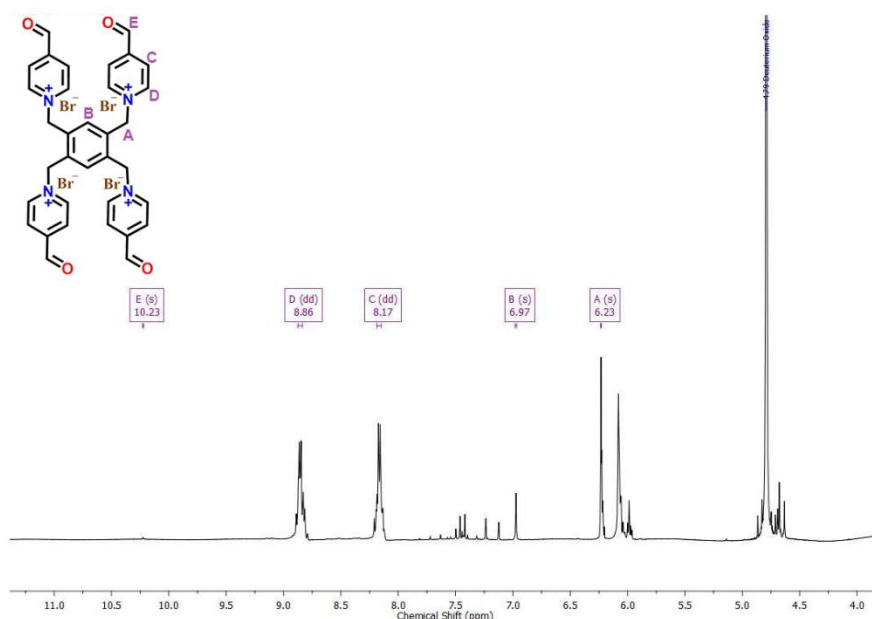
$^1$H NMR of 1,1',1'',1'''-(benzene-1,2,4,5-tetrayltetrakis(methylene))tetrakis(4-formylpyridin-1-ium) tetrabromide

1H NMR (400 MHz, D2O) δ 10.23 (s, 1H), 8.86 (dd, J = 6.4, 3.4 Hz, 3H), 8.17 (dd, J = 10.3, 4.0 Hz, 3H), 6.97 (s, 1H), 6.23 (s, 1H).

**A2.2.3 Synthesis of 4,4',4''-(1,3,5-triazine-2,4,6-triyl)tris(benzene-1,3-diol) (TRIRES)**

The synthesis of the compound is based on a previous report in chapter 1.[S2] 2 g (10.8 mmol) of cyanuric chloride and 3.58 g (32.5 mmol) of resorcinol were dispersed in 100 mL of 1,2-dichloroethane. Contents were dissolved by heating at 75 °C, following this, the mixture was cooled to 0 °C. To this, about 4.35 g (32.5 mmol) anhydrous $AlCl_3$ was slowly added in 30 minutes. This mixture was refluxed for 36 h. The reaction mixture was cooled to room temperature and the solvent was removed using a rota-evaporator. The solid was then stirred in 100 mL of 10% HCl for 3 h and kept it for an additional 3 h. A yellow solid was precipitated, which was filtered under vacuum and washed with about 250 mL of diethyl ether to remove any unreacted starting materials. The product was dried in a vacuum oven. About 3.2 g (yield: 88%) of the product was obtained.



**4,4',4''-(1,3,5-triazine-2,4,6-triyl)tris(benzene-1,3-diol)**

**A2.2.4 Synthesis of cationic polymer IISERP-POF12 (2) and IISERP-POF13 (3)**

The polymer has been synthesized according to the optimized protocol by our group.[S3] The solvothermal reaction between 0.2 mmol phenolic compound and 0.2 (for **2**)-.15 (for **3**) mmol viologen aldehyde in a mixture of 3 mL THF and 3 mL 1,4- dioxane at 200 °C for 72 h yielded a brown-colored precipitate which was sequentially washed with DMF, THF, MeOH and finally acetone. The product was dried in the vacuum oven for 6 h and the obtained material was named hereafter as **2** and **3**. A significant colour difference was observed in compound 2 and 3.

**A2.2.5 Anion exchange with IISERP-POF12 (2) and IISERP-POF13 (3) to form IISERP-POF12_OH (2_OH) and IISERP-POF13_OH (3_OH)**

The as-made polymer **2** or **3** (100 mg) was dispersed in 10 mL of 6 M KOH and sonicated for 10 minutes. After sonication, the mixture was stirred for 24 h at room temperature for hydroxide ion (OH⁻) incorporation. Hydroxide ion exchanged polymer was filtered and washed with an ample amount of water to remove the excess KOH. The product was dried in a vacuum oven for 12 h at 80 °C and obtained a yield of 89 %.

**A2.3 Density Calculation**

Density calculations were performed using an indirect method involving the mass and volume of the material. The volume calculation proceeded as follows: a fixed mass of the POF was filled in vials, marked, discharged, and then refilled with water up to the mark to determine the corresponding volume. It is acknowledged that the air trapped in the interparticle voids was not accounted for. To minimize this error, samples were meticulously prepared. All materials were thoroughly ground in a mortar and pestle before being sonicated to fine dispersive powders. After centrifugation, they were carefully filled into the vials to settle homogeneously. Each density calculation was performed three times to obtain a statistical average.

For the estimation of tap (bulk) densities, the samples underwent washing with methanol and acetone, followed by drying at 80 °C overnight to eliminate any solvent contributions. Subsequently, they were finely ground in a mortar and pestle to achieve a clump-free, free-flowing powder. A known weight of the powder was then transferred to the tap-density device, and the initial volume was recorded. The powder was subjected to 500 taps, and the final volume was recorded.

Note: The sample vial, post-tapping in a tilted position, demonstrates that the POF has settled tightly at the bottom without spilling out when tilted to 90 degrees.

Observation: Slight change in the tapped bulk densities of the samples 3 and 3_OH is observed.

**A2.4 Swelling study:**

A pellet comprising 200 mg of POF sample was pressed, and parameters such as diameter and thickness were measured both in the dry state and under wet conditions. In the wet condition, the pellet was exposed to 95% relative humidity (RH) for 24 hours.

Observation: Minimal increase in both diameter and thickness is observed on exposing the 3 and 3_OH to 95 % RH for 24 hours.

**A2.5 Hydroxide ion conductivity Analysis**

**A2.5.1 Temperature-dependent hydroxide ion conductivity analysis of 2_OH and 3_OH :**

The hydroxide ion conductivity ($\sigma$) of the **2, 3, 2_OH and 3_OH** were investigated by the electrochemical impedance spectroscopy method from a frequency range of $1-10^6$ Hz using the Solartron Impedance Analyzer. For this, **2_OH and 3_OH** were made into a pelletized form. The conductivity measurements were carried out three times on different pellet thicknesses (0.6 to 0.8 mm) and diameters of 10 mm to validate the consistency in the obtained results. Before each measurement, the sample was equilibrated at the particular temperature and humidity for 2 h throughout the experiment. The hydroxide ion conductivity of the pellet was measured from 25 to 80 °C in relative humidity (RH) of 95% and calculated using the following equation;

$$\sigma \ (\text{S cm}^{-1}) = \frac{l}{RA}$$

where $l$ is the thickness of the pellet (cm), R is the resistance of the sample ($\Omega$) obtained from the x-axis intercept, and A is the cross-sectional area of the pellet (cm$^2$). The humidity dependent OH$^-$ ion conductivity of **2_OH and 3_OH** were also measured at 80 °C with variable relative humidity under similar conditions.

**A2.5.2 Activation energy calculation for 2_OH and 3_OH**

The activation energy was obtained using the Arrhenius equation where m is the slope of the plot between ln $\sigma$ Vs 1000/T and the R is the gas constant with the value of 8.314 J/mol.

$$\ln\sigma = (-E_a/RT) + \ln A$$
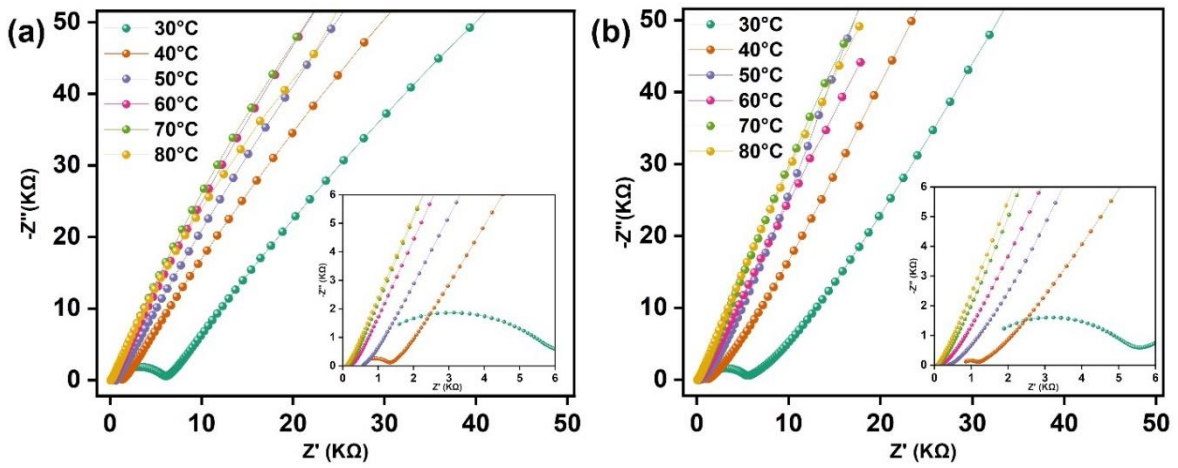
**Figure A2.1**: Temperature dependent Nyquist plots of (a) **2**, (b) **3** impedance analysis measured at 95 % RH .
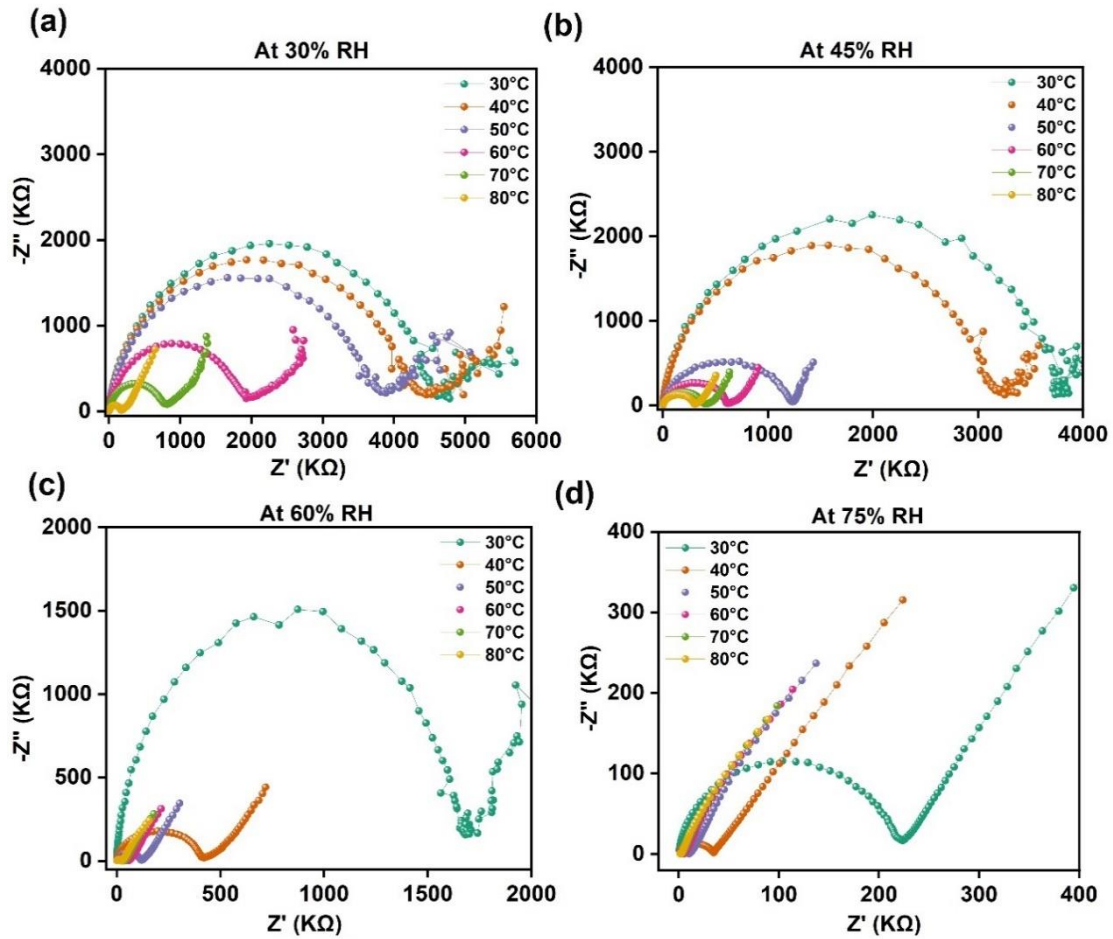


**Figure A2.2**: Temperature dependent Nyquist plots of **2_OH** impedance anlysis measured at (a) 30% (b) 45% (c) 60% (d) 75 % RH .
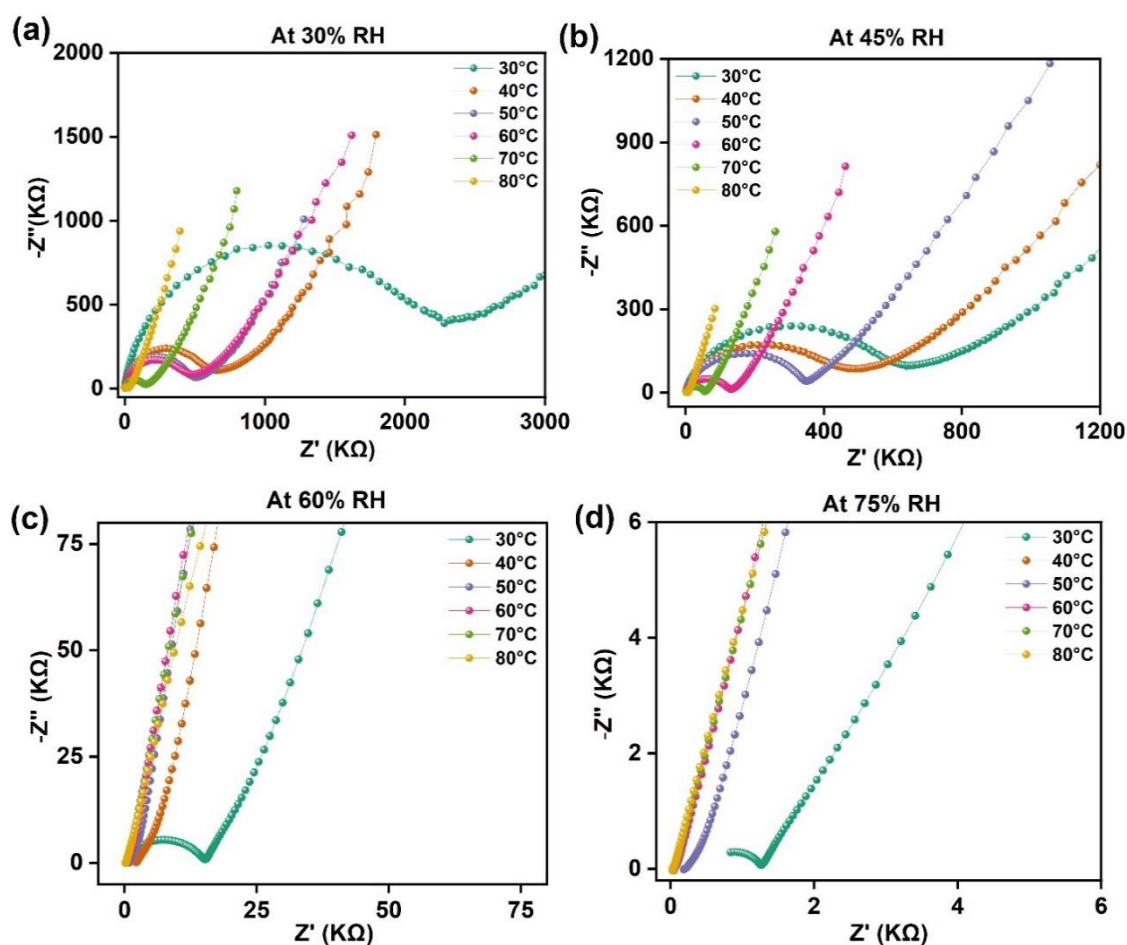
**Figure A2.3**: Temperature dependent Nyquist plots of 3_**OH** impedance anlysis measured at (a) 30% (b) 45% (c) 60% (d) 75 % RH.

**Table A2.1:** Comparative hydroxide ion conductivity of **1_OH** at variable temperatures and a constant relative humidity of 95%.

| Sr. No. | Relative Humidity (%) | Temperature (°C) | Conductivity (S/cm) 1_OH* | Conductivity (S/cm) 2_OH | Conductivity (S/cm) 3_OH |
|---|---|---|---|---|---|
| 1 | 95 | 30 | 2.70E-04 | 7.30E-04 | 2.96E-03 |
| 2 | 95 | 40 | 1.40E-03 | 1.65E-03 | 9.45E-03 |
| 3 | 95 | 50 | 2.30E-03 | 3.03E-03 | 1.43E-02 |
| 4 | 95 | 60 | 3.40E-03 | 5.23E-03 | 2.00E-02 |
| 5 | 95 | 70 | 5.30E-03 | 7.89E-03 | 2.43E-02 |
| 6 | 95 | 80 | 1.40E-02 | 1.53E-02 | 4.88E-02 |

## A2.6 Post ZAB measurement sample characterizations
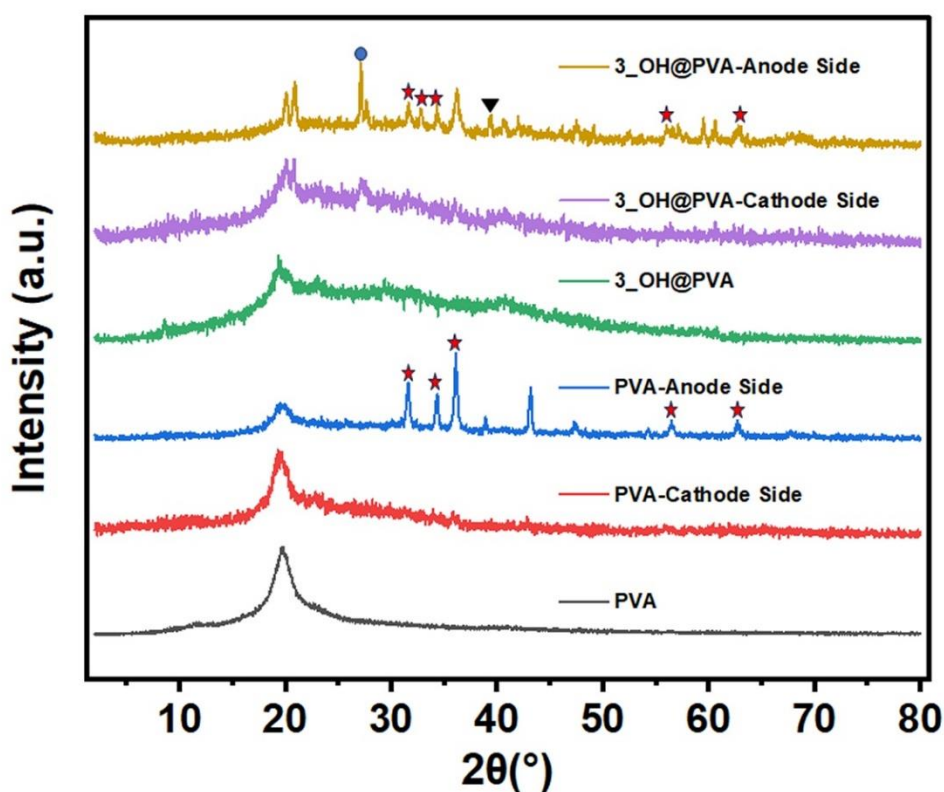


**Figure A2.4**: Comparison of the PXRD patterns of the **PVA**, **3_OH@PVA**. The inorganic species in this pyrolyzed sample includes ZnO(★), $K_2CO_3$ (●)and $Pt_3O_4$ (▼)(from cathode).
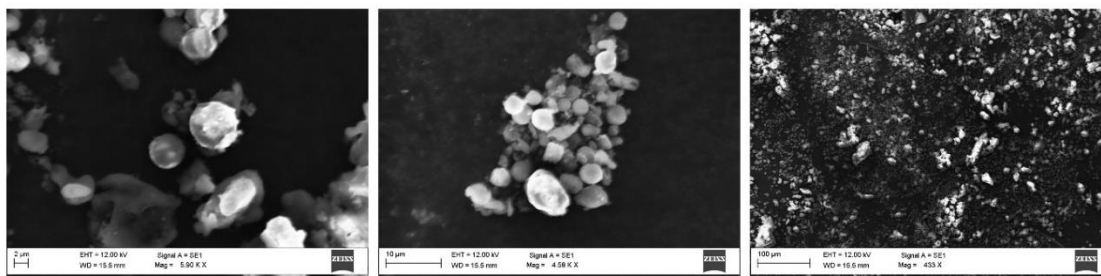


**Fig. A2.5:** Post impedance Field Emission-Scanning Electron Microscopy (FESEM) images of 2_OH at different magnifications.
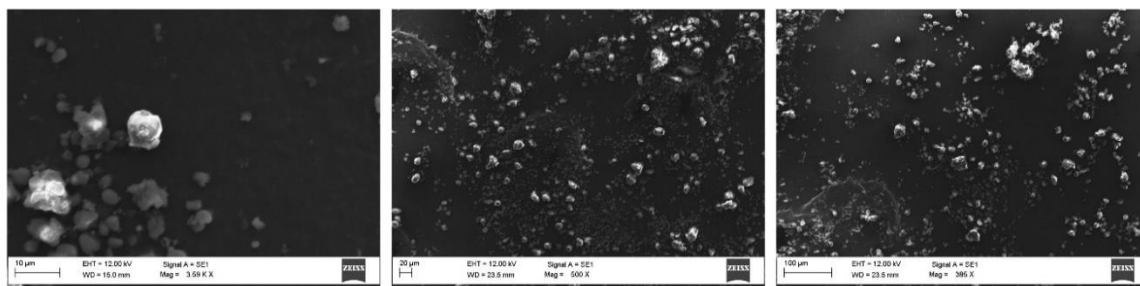


**Fig. A2.6:** Post impedance Field Emission-Scanning Electron Microscopy (FESEM) images of 3_OH at different magnifications.

**A2.7 Amplitude Roughness Parameters (Flatness Index)**

Based on the provided AFM images and amplitude roughness parameters, it is evident that the flatness of the electrolyte membrane is well within the desired range. The Mean Surface Roughness (Sa) values, ranging from 177 nm to 268 nm across different samples, demonstrating that the membrane maintains a consistent level of flatness.

Examining the Root Mean Square Height of the surface (Sq), the values range from 223 nm to 350 nm, further corroborating the findings regarding surface roughness. Despite slight variations between samples, the Sq values remain within reasonable limits, confirming the uniformity of the membrane surface.

In conclusion, the analysis of the amplitude roughness parameters and AFM images indicates that the electrolyte membrane exhibits satisfactory flatness characteristics. The consistent Sa values, along with the Sq, Sku, Sp, and Sz parameters, confirm the uniformity and stability of the membrane surface. These findings suggest that the membrane is well-suited for applications where flatness is crucial factor.

**Figure A2.7:** Atomic Force Microscopy (AFM) images of 3_OH@PVA membrane scanned at different sample area.
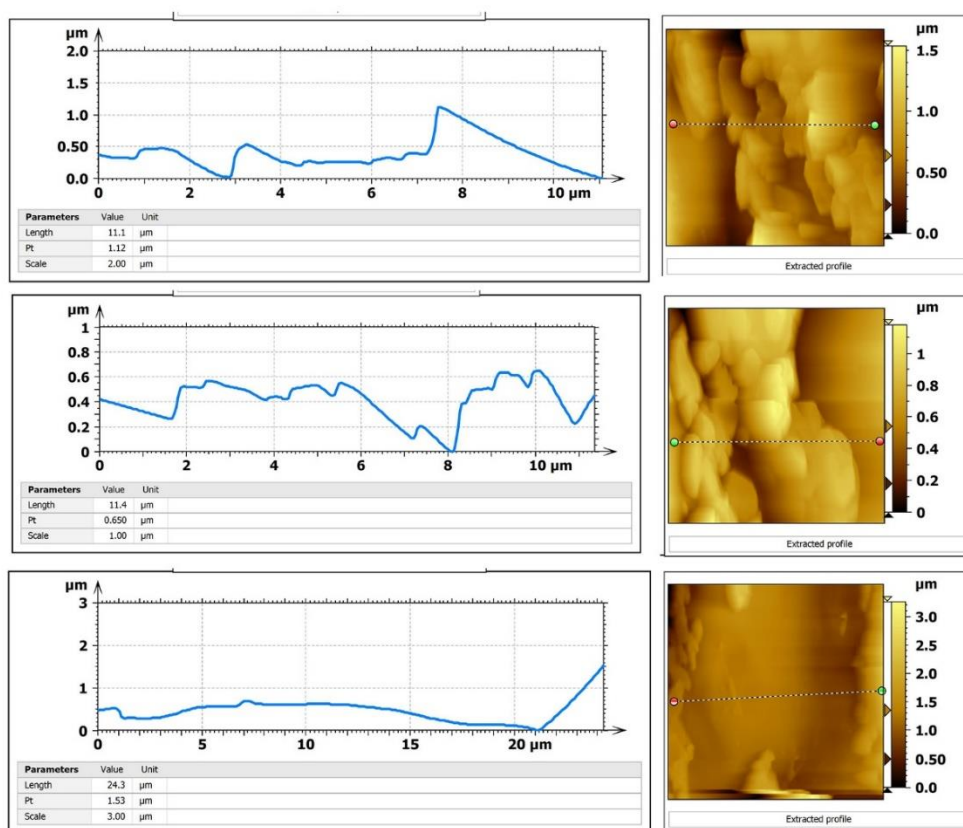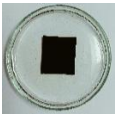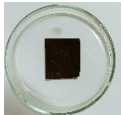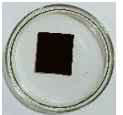


**Table A2.2**: Amplitude Roughness Parameters of different samples.
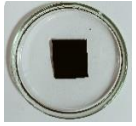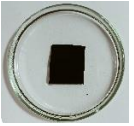
| Amplitude Roughness Parameters | Sample-1 | Sample-2 | Sample-3 |
|---|---|---|---|
| **Sa (Mean Surface Roughness)** | 177 nm | 167 nm | 268 nm |
| **Sq (Root mean square height of the surface)** | 223 nm | 205 nm | 350 nm |
| **Sku (Kurtosis (fourth statistical moment, qualifying the flatness of the height distribution). Width of the height distribution.** | 2.26 | 2.62 | 2.16 |
| **Sp (Height of highest peak)** | 903 nm | 556 nm | 990 nm |
| **Sz (Defined as the average of the five highest local maximums plus the average of the five lowest local minimums.)** | 1.54 µm | 1.19 µm | 1.97 µm |

## A2.8 Alkaline durability test

The durability test involved immersing the membrane in the solution for 12 hours, and the change in thickness was measured at each stage. Minimal change in membrane thickness was observed, indicating excellent alkali stability. No wear or tear was observed on the membrane throughout the test.

**Table A2.3**: The membrane thickness measurements before dipping, after dipping, and upon drying.

| KOH Conc. | Membrane Thickness (mm) | | |
|---|---|---|---|
| | **Before Dipping** | **After Dipping** | **On Drying** |
| **2M** | 0.34  | 0.38  | 0.37  |
| **4M** | 0.37  | 0.39  | 0.38  |

| | 0.38 | 0.42 | 0.41 |
|---|---|---|---|
| **6M** |  |  |  |

These results demonstrate the membrane's ability to maintain its integrity and thickness even after exposure to high concentrations of KOH solution for an extended period.
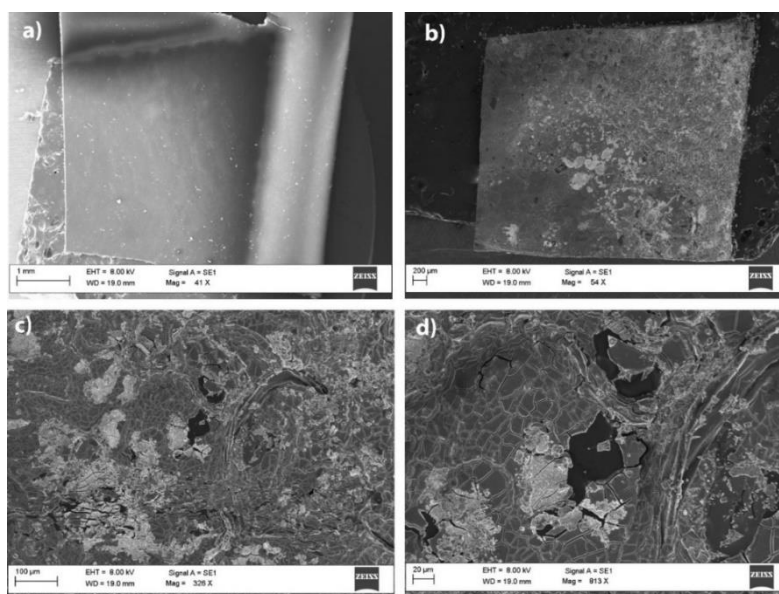


**Figure A2.8**: FESEM images of **PVA** membrane (a) Pre battery measurements (b) Post battery measurements at different magnifications.
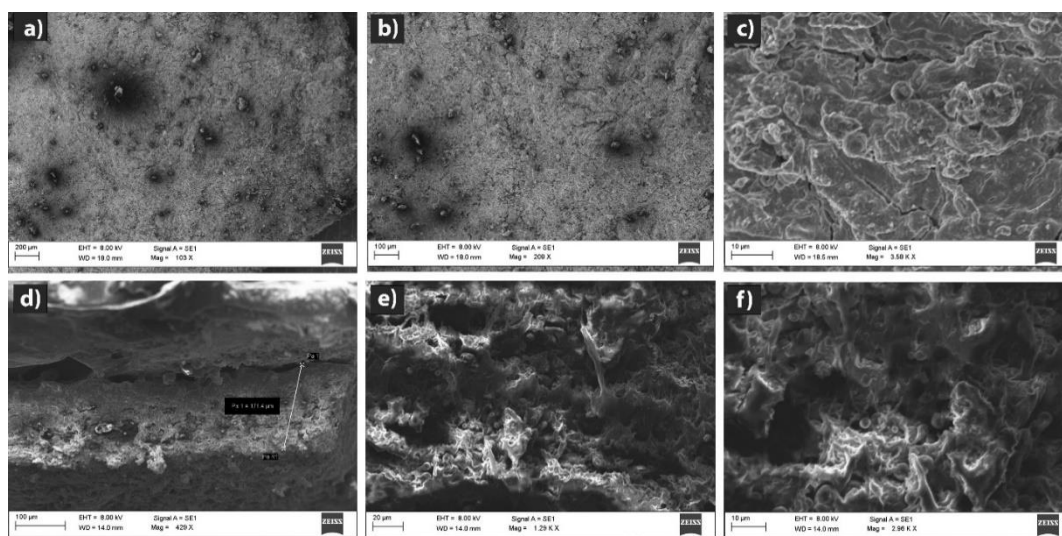


**Figure A2.9:** The FESEM images of the post-battery measurement electrolyte (**3_OH@PVA**) showed lowering in thickness compared to the **3_OH@PVA** pre battery measurements.

# Chapter 3

# Incorporating Conducting Polypyrrole into a Polyimide COF to Device Carbon-free Ultra-High Energy Supercapacitor

## 3.1. Introduction

Nano-porous crystalline COFs provide ample surface area to store charged ions through electrostatic interactions.[1] [2] [3] [4] [5] Also, its pore surface engineering with heteroatoms and redox-functionalities offers many active sites in its nanopores for reversible electrochemical interactions.[6] [7] The combination of these two features, along with the high mobility of charged ions within accessible pores of the COFs, undoubtedly enhances the performance of COF-derived electrodes for storing the charge under applied voltage (both in batteries and capacitors).[8] [9] [10] [11] [12] In comparison to the heteroatom-doped carbonaceous materials, the COF offers better atomic-level manipulation to develop the framework structure with desired redox-moieties and tunable pore dimension. [13] [14] [15] Especially the properly engineered one-dimensional nano-channel of two-dimensional COFs induces the facile guest-ions interactions with its hetero-structures.[16] [17] That enhances the electrical energy storage property of Graphite resembling 2D-COFs. However, the ability of COFs to hit record-level charge storage or their theoretical limit is restricted by their non- or poorly-conducting polymeric network, unlike Graphite materials. Considering also the molecular defects (ring slippage, stacking faults)[2] the COF is expected to have low conductivity, hence does not amply support charge transport. Consequently, the COF's redox centres do not get sufficient electron supply for electrochemical activation unless a heterogeneous mixture with conducting carbon particles is employed.[18] Also, the performance of the fabricated storage devices is completely limited due to the interface boundary between carbon particles and the relatively bigger COF particles.[19] [20] Sometimes profound interference of carbon leads to overestimating the overall performance of energy devices.[21] Moreover, the COF exhibits poor electrochemical stability when the window is expanded to higher voltages. If the COF can be made intrinsically redox-active, it could carry an excellent gravimetric advantage as the electrode. Imparting redox sites (e.g., heteroatoms) in a COF skeleton is a direct approach to improve electronics assisted ionic mobility [10], but there are only a limited number of heteroatoms one can introduce. As an alternative, we incorporate heteroatom-rich guests into the COF pores to improve electronic conductivity and this could set up the necessary driving force for the ions to interact under an applied current. With heteroatoms decorating both the host framework and the non-volatile guest units, superior charge storage is guaranteed.

To constitute the effectiveness of this approach, we have chosen a polyimide COF which is not completely conjugated and the push-pull effects are also not as prominent as in some of the earlier reported COFs.[22] This limits the pseudo-activity of the COF only in a

narrow voltage window, which in turn restricts the energy density of the capacitor. However, it is a relatively stable cyclic imide bond as compared to typical linear -C=N- bonded COFs, and this stability is required for the growth of the polymeric guests within their pores without losing much of the long-range order.[23] Polypyrrole represents the first systematically investigated conducting organic polymer.[24] [25] Polypyrrole in an acidic medium can exist in the oxidized form that carries protonated rings balanced by counter anions and this generates unpaired spins, polarons type of charge carrying species.[26] Under an applied voltage, even the reduced/neutral centres in the polypyrrole chains can be polarized. The charge carriers can be delocalized over the entire chain more effectively to accomplish higher conductivity. Typically, the polypyrrole chains can grow as less conducting globular structure or a highly conducting fibrous nanostructure, and this is controlled by using surfactants.[26] [27] Interestingly, growing them inside a COF with uniform 1-D pores can confine their growth into nanofibers. The heteroatom-lined pores of the COF hosting such conductive polypyrrole chains could create the synergy required to make the composite sufficiently conductive. In one example, the growth of the PEDOT:PSS merely on the surface of the COFs improves the conductivity of the COF; still, the conducting polymer suppresses the overall ion capacitance of COFs.[28] [29] The synergy of the redox reactions of the conducting agent and the COFs redox centres was not obvious. A detailed analysis of the heterojunction of these interfaces is arduous to investigate. In an alternate example, a radical-induced redox response of the COF leads to high capacitance, but the conductivity issues were still looming. Recently we used redox modulator in the electrolyte to gain a drastic enhancement of the pseudocapacitive behavior, but in some cases, it leads to poor cycling stability.[30] [31] [32] [33]

The heteroatoms containing redox active functional groups (pyridine, imide, carbonyls) in the polyimide linked COF become active sites for storing $H^+$ ions in an acidic electrolyte and this storage is mainly confined to a positive potential window (with respect to Ag/AgCl reference electrode) typically between 0 to 1 V.[21] Expanding the window to higher potential stores more $H^+$ ions, but this challenges the COF stability, especially for the widely-studied and easily accessed imine-based COFs. On a positive note, the large micro-mesopores of COFs allow the diffusion and storage of larger counter anions along with the cations.[30] [34] [35] [36] Now, if the effective storage of the bulky counter anions can be coupled with cations in this wide-potential window -1 V to +1 V of operation, one can readily realize higher energy density.[37] A recent work by Chen and co-workers reported the co-storage of $Li^+$ and $ClO_4^-$ ions in a viologen containing cationic framework to gain good LIB characteristics.[35] Similarly, we showed how

capacitatively stored $H^+$ can accommodate further $I_3^-$ units to gain enhanced charges per unit area or mass in a psuedocapacitor.[30]
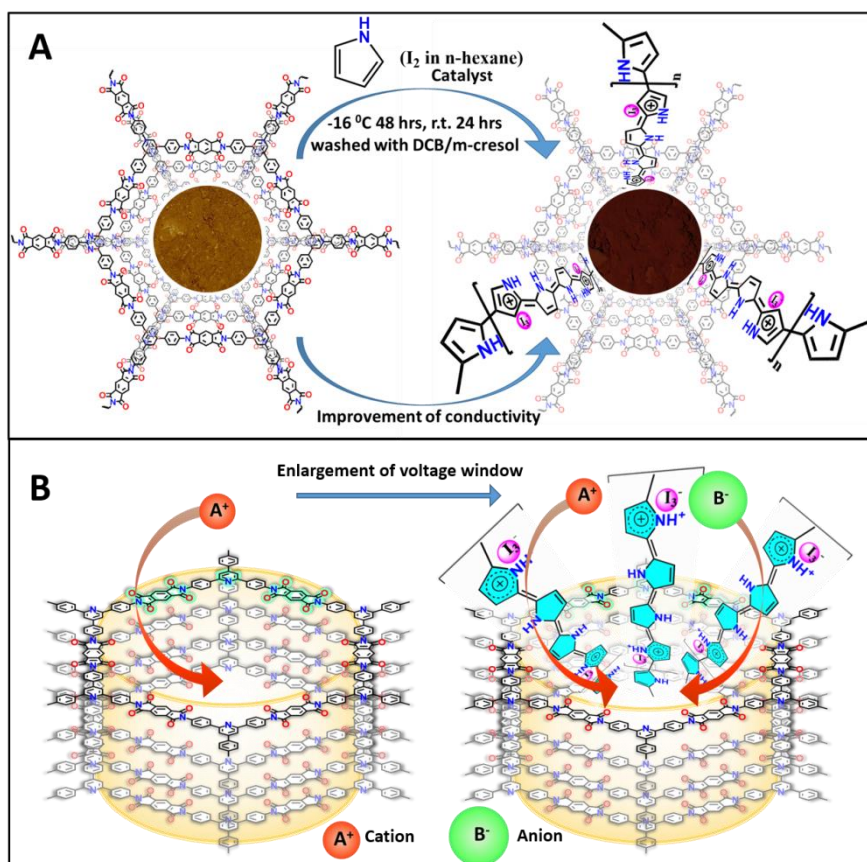


**Scheme 3.1:** (A) A schematic illustration of the incorporation of polypyrrole (Ppy) within the polyimide-linked COF. (B) The columnar channel of IISERP-COF30 is favored to interact with cationic and anionic centres. The green and cyano highlighted portions ar

But it is worth mentioning that both these systems employ CNT and conducting carbon for realizing practical activity. A carbon-free COF-based system showing superior charge storage will certainly boost the rank of COF as a charge storage material. Our present chapter showcases the drastic enhancement of the conductivity (from $10^{-7}$ to $10^{-3}$ S/cm) of a novel 2D-polyimide bridged COF by very controlled growth of the unbranched polypyrrole in the presence of the 1-D nanopores of the COFs (Scheme 3.1).[38] [39] This system substantially amplifies the voltage window for the synergic redox reactions of polyimide and polypyrrole units present in the structure. This certainly enhances the accumulation of more protons and sulfate ions per unit cell of the COFs under the applied voltage. Hence, we do see the huge proliferation of the specific capacitance and power densities when we configured conducting carbon-free three-electrode (1983 mF/g at 1 A/g) and two electrode solid-state capacitors (358 mF/cm$^2$ at 1 mA/cm$^2$). But the compromise with electrolytic stability of COF in aqueous acid-based electrolyte in higher voltage discards the possibilities to magnify energy densities of the all-solid-state capacitors derived from this polypyrrole loaded COF. One would expect the use

of the *bulkier organic electrolyte* would be detrimental owing to its slow diffusion and redox kinetics. Surprisingly, here, we still derive excellent specific capacitance (275 mF/cm$^2$ at 1 mA/cm$^2$) yielding a massive energy density (145 mWh//cm$^2$) by reaching a wider voltage window (from 0 V to 2.5 V). Therefore, a proper balance between the energy densities and power densities (1370 mW/cm$^2$) lifts the position of the Ppy@2D-COF in the Ragone plot as a superlative capacitor. These are achieved without combining with any metal oxide or sulphide-based asymmetric supercapacitor.[40] Thus, our symmetrical Ppy@COF-derived capacitors in organic ionic-gel electrolyte can be considered as a suitable alternative of the hybrid capacitor.

## 3.2. Results and Discussion

### 3.2.1. Synthesis and structure modelling of IISERP-COF30 (COF) and Ppy@IISERP-COF30 (Ppy@COF)

IISERP-COF30, is a novel 3+2 polyimide-framework prepared by solvothermal reaction between a 3-connecting pyridinyl triamine (4,4',4''-(pyridine-2,4,6-triyl)trianiline) and a linear dianhydride (1H,3H-benzo[1,2-c:4,5-c']difuran-1,3,5,7-tetraone), grows as fluffy yellowish powder (Figure 3.2).
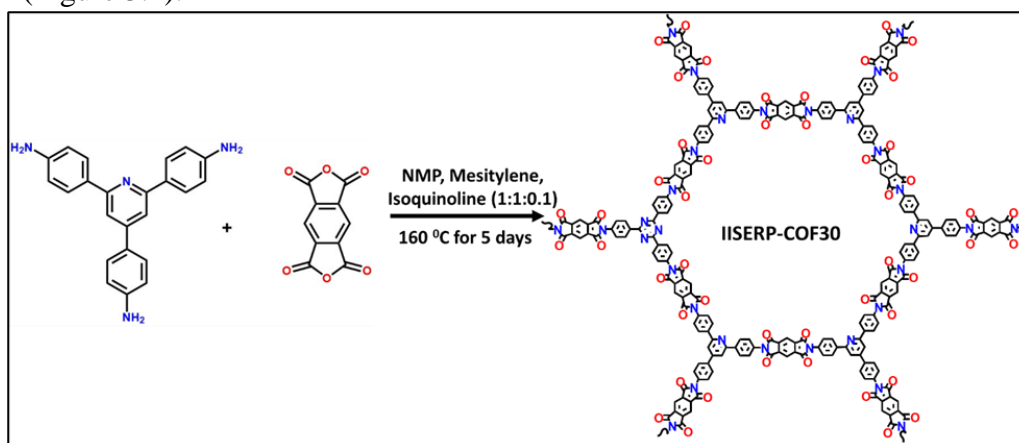


**Scheme 3.2:** A schematic illustration of the COF synthesis.

From a Pawley refinement, the structure of this COF was modelled in the P-6 space group. In this 2D structure of the COF, the hexagonal layers are connected in an eclipsed arrangement by π-stacking of polyimide units, pyridine and benzene rings. We optimized the geometry of the 2D hexagonal model using periodic Tight Binding Density Functional Theory (DFTB) to obtain the lowest energy configuration (Figure 3.1A and B). This full cell and motion group relaxed optimization finally resulted in a solution in the C222 space group (Figure 3.1A). From a comparison of the simulated PXRD with the experimental PXRD it was seen that the relative

intensities of the eclipsed model result in a better representative of the sample compared to the staggered ones (Figure S4, Supporting Information). The 3D propagation of the COF illustrates the uniform 1-D channels along the C-axis (dimension = 33.1 Å, not factoring in the van der Waal radii) (Figure 3.1B).
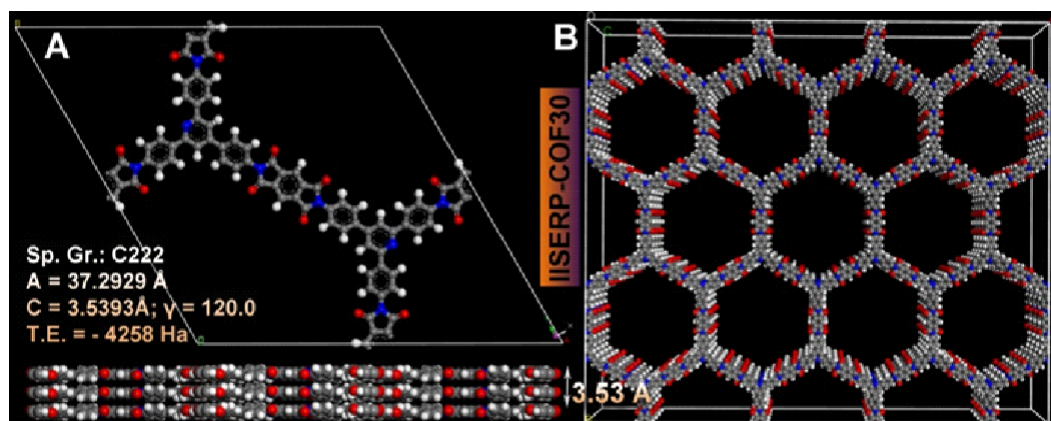


**Figure 3.1:** (A) The unit-cell of the COF structure refined using Pawley methods. (Below) AAA... stacking of the π-stacked layers of COF. (B) A perspective view of the COF showing its 1D nanochannels.

The pore size estimation (27 Å) by model-independent Barrett-Joyner-Halenda (BJH) model extracted from fitting the $N_2$ 77 K adsorption isotherm confirms the presence of eclipsed configuration of the synthesized COF (Figure 3.2B). This COF generates homogeneous micropores having a pore volume of 0.645 cc/g and a total surface area of 657 $m^2$/g which was estimated from a Brunauer-Emmett-Teller (BET) fit (Figure 3.2A).
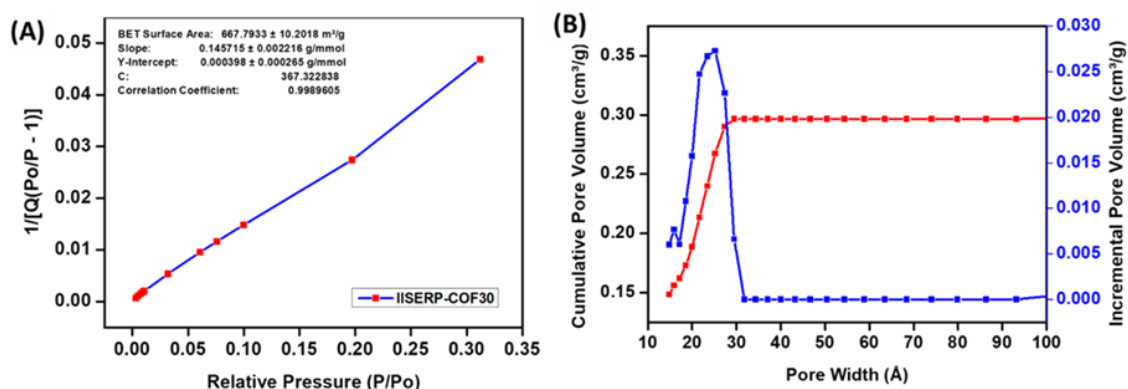


**Figure 3.2:** (A) Brunauer-Emmett-Teller (BET) fit and the goodness fit of N2 adsorption data. (B) Non-local density functional theory (NLDFT) pore width fit obtained using microporous Carbon at 77K model (pore-size: 27.2 Å).

Since the polyimide linkages in the framework do not possess the electronic conjugation, the growth of the unbranched polypyrrole was attempted inside the 1-D nanochannel of the COF to enhance the electronic conductivity. COF as a host material is expected to restrain its branching growth (See appendix information for the synthesis and characterization of neat Ppy, Figures A3.3-A3.5, Appendix). The templated synthesis of this conducting form of polypyrrole in the COF was carried out at a very low temperature (-16 °C) in hexane to slow

down the kinetics of the polymerization and to avoid the scope of branching (Scheme 3.3). The catalyst of the reaction, iodine ($I_2$) also nullifies the positive charge generated on the protonated-polypyrrole surface in form of tri-iodide ions. This polypyrrole embedded COF was washed out thoroughly with dichlorobenzene: m-cresol (1:1) mixture to offload the polymer which was grown only on the surface of the COF flakes.
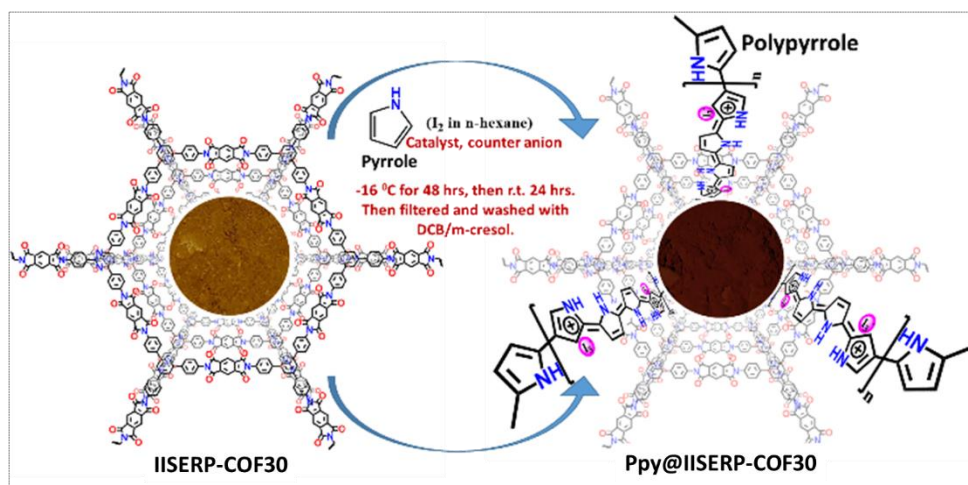


**Scheme 3.3:** A schematic illustration of the incorporation of polypyrrole (Ppy) within the polyimide-linked COF.

The loading of the polypyrrole chains into the pores of the COF results in the contraction of the unit cell of the COF along the *ab*-plane. This makes the (110) peak shift to a higher angle. The refined structure of the Ppy@COF shows that the topology is unchanged, though the space group symmetry is lowered, and the b-axis length is noticeably decreased (Figure 3.4).
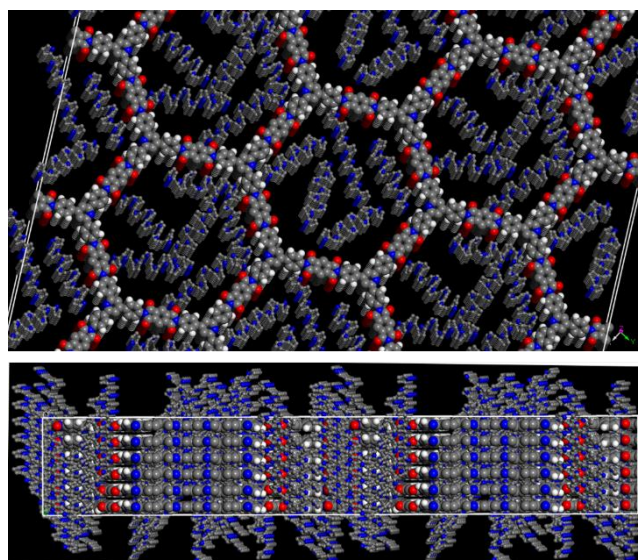


**Figure 3.3:** Snapshot of the structure of the Polypyrrole loaded COF (Ppy@COF). Note the Ppy chains can jet out of the pores and such configuration makes it difficult to differentiate if the chains are sitting within the pore or outside on the surface, however solvent wash cleans up surface

Importantly, this accommodates the polypyrrole chains well, does not compromise the stability of the imide-bonds in the framework, and yields an acceptable low-energy structure. In particular, significant lattice contraction happens along the *0k0* direction, as evidenced by (020) reflection. More details on the COF's structure solution and the Ppy@COF's structure modelling can be found in the Figures 3.4A-D.

## 2.2. Characterization of Ppy@COF
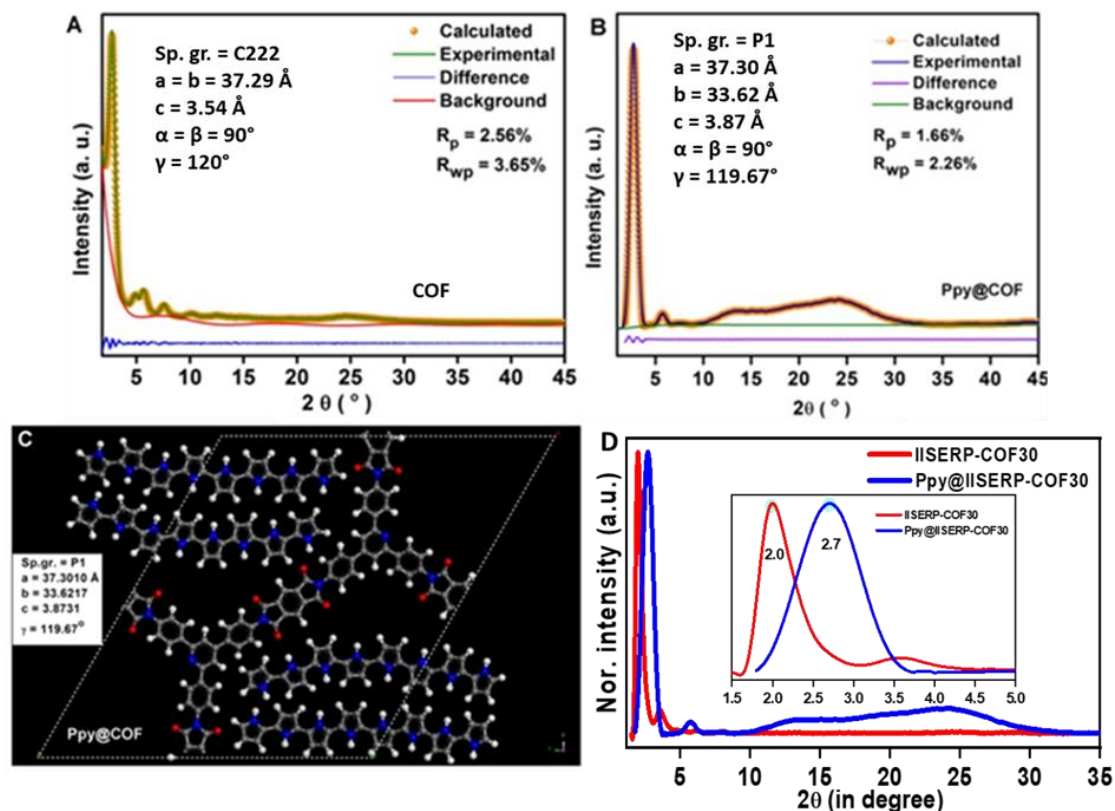


**Figure 3.4:** (A) The Pawley refinement fit of the COF and (B) Ppy@COF. (C) The refined structure of Ppy@COF shows acceptable bond parameters, connectivities, and a lattice contraction along the 0k0 direction. This arises from the free rotation of the C-C bond attached to the core of the triamine unit forming the COF. This leads to layer buckling while the polyimide linkers remain rigid and planar. (D) The comparison of the PXRD data of COF and Ppy@COF.

The growth of the polypyrrole (Ppy) chains inside the framework structure did not completely annihilate the crystallinity of the polyimide COF (Figure 3.4D). However, a 75 % loss of porosity was estimated (P/P$_0$ = 0.8, Figure 3.5), which infers that the pore filling happened due to the growth of the Ppy inside the nanochannel of the COF.
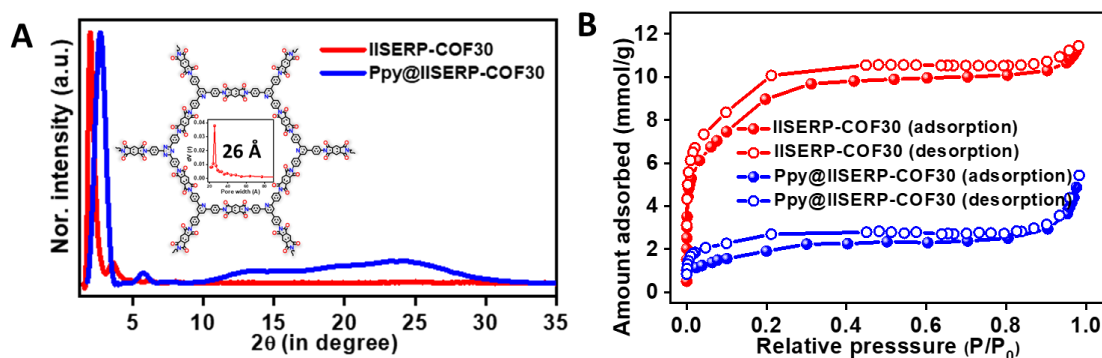
**Figure 3.5:** (A) PXRD of the COF and Ppy@COF. Lattice contraction upon inclusion of Ppy is seen from 2θ shifts. (B) 77K Nitrogen sorption isotherms of the COF and Ppy@COF.

The bulk purity of the polyimide-framework and the PPy embedded form of it was established from the [13]C Solid-state Nuclear Magnetic Resonance (^{13}C-SSNMR) (Figure 3.6) and the Fourier Transform Infrared spectroscopy (FTIR) of the soxhlet extracted samples (Figure 3.7). ^{13}C-NMR (500 MHz) spectrum shows the sharp signal of imide carbon at 165 ppm and a relatively broader signal of pyridine carbon at 153 ppm. The Ppy loading caused no significant change in ^{13}C-SSNMR since its carbon signals merged with those appearing due to the aromatic
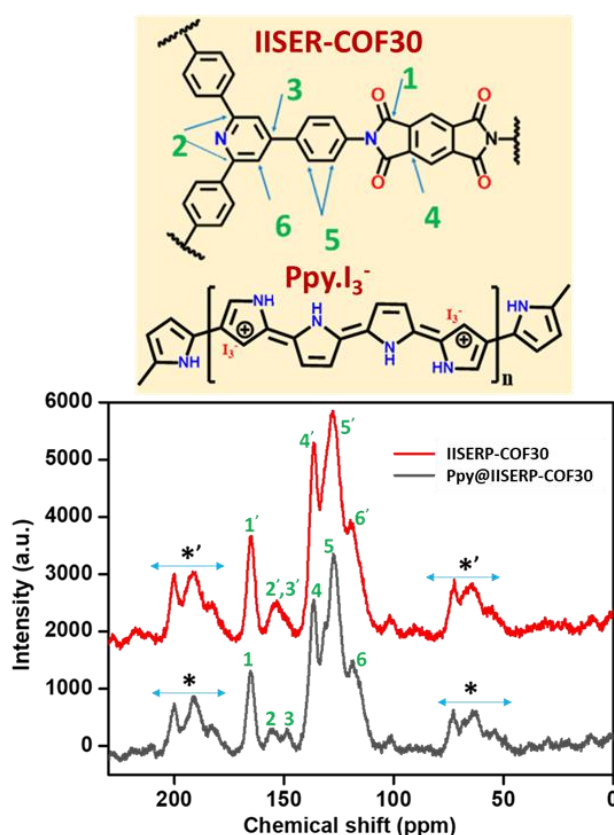


**Figure 3.6:** ^{13}C Solid-state NMR signals before and after the Ppy incorporation in COF.

region of the COF. That indirectly implies the amount of Ppy loading is not too high and the framework structure and the chemical integrity was retained even after the polymer loading. The same has been also confirmed from the Infra-red (IR) stretching frequencies of the functional groups of the COFs (-C=O group of imide linking at 1750 cm$^{-1}$, -C-C bond at 1502 cm$^{-1}$, -C-N bond of imide linking at 1353 cm$^{-1}$) before and after the Ppy loading. In addition, for the Ppy@COF few new peaks for the stretching and vibrations, new bonds were observed at 3611 cm$^{-1}$, 3732 cm$^{-1}$, 3860 cm$^{-1}$. That matches pretty well with the IR spectrum of freshly prepared individual polypyrrole polymer.
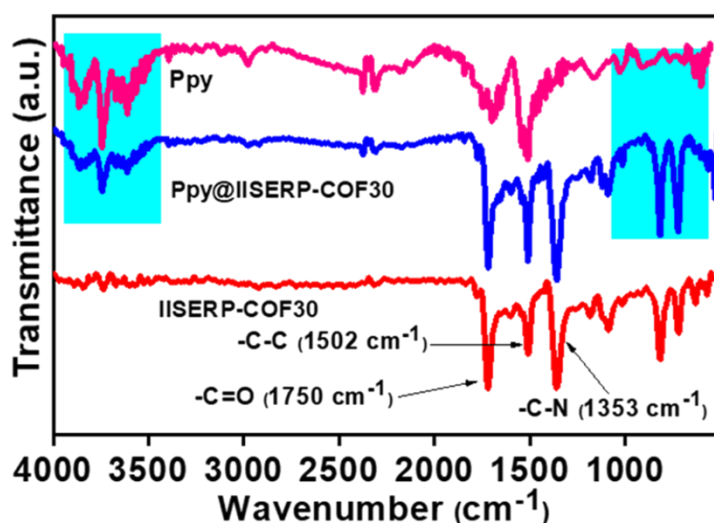


**Figure 3.7:** Fourier Transform Infra-red (FTIR) spectra of Ppy, COF and Ppy@COF. This confirms the existence of the characteristic's peaks (cyano highlighted) of Ppy in COF.

We obtained a quantitative estimate of the polypyrrole loading using the Thermogravimetric Analysis (TGA). The TGA measured between 25 to 800 °C exhibits a weight loss (~28 %) that sets in at a relatively low temperature of 230 °C and continues till 400 °C. In contrast, the neat polyimide COF, does not have any low-temperature weight loss other than the solvent loss and starts to degrade above 400 °C (Figure 3.8). This would mean that in Ppy@COF, the Ppy chains are not remaining merely as a heterogeneous mixture with the COF, this fact, coupled with the drop in porosity upon Ppy loading, suggests that the Ppy chains are lodged well into the pores of the COF.
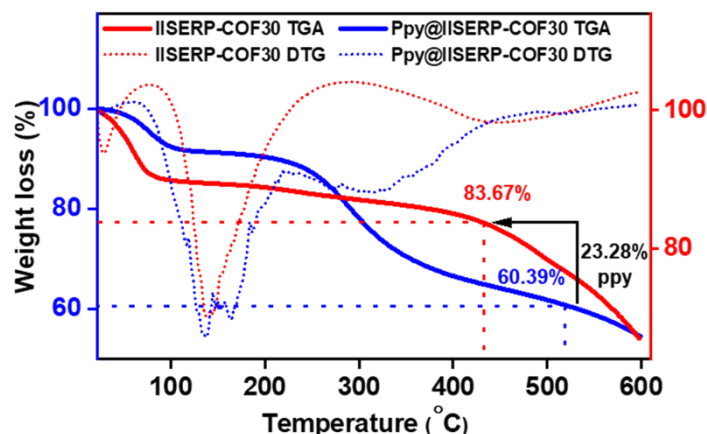
**Figure 3.8:** TGA and DTG plots of the COF and Ppy@COF.

Under the Field Emission Scanning Electron Microscope (FESEM) the COF particles appeared as spherical spheres of different diameters (from 500 nm to 3 μM). These microspheres are comprised of many tiny flakes of the COFs which are nicely oriented to each other to give rise to the hierarchical porous bed on the spheres (Figure 3.9). While a slight deformation of the shape of these microspheres was observed after the polypyrrole inclusion. The Ppy@COF had strands of polypyrrole nanofibers jetting out of the COF substrate, which approves what is expected from the modelled Ppy@COF structure (Figure 3.9). This confirms the growth of this polymer did not only occur on the surface of the COF flakes. These images were recorded from a sample that had been thoroughly washed with different solvents. The small amounts of iodine added during the polypyrrole synthesis in the presence of COF are expected to form $I^-$ or $I_3^-$ species, which will counter-balance the cationic oxidized sites in the Ppy chains.[41] [42]
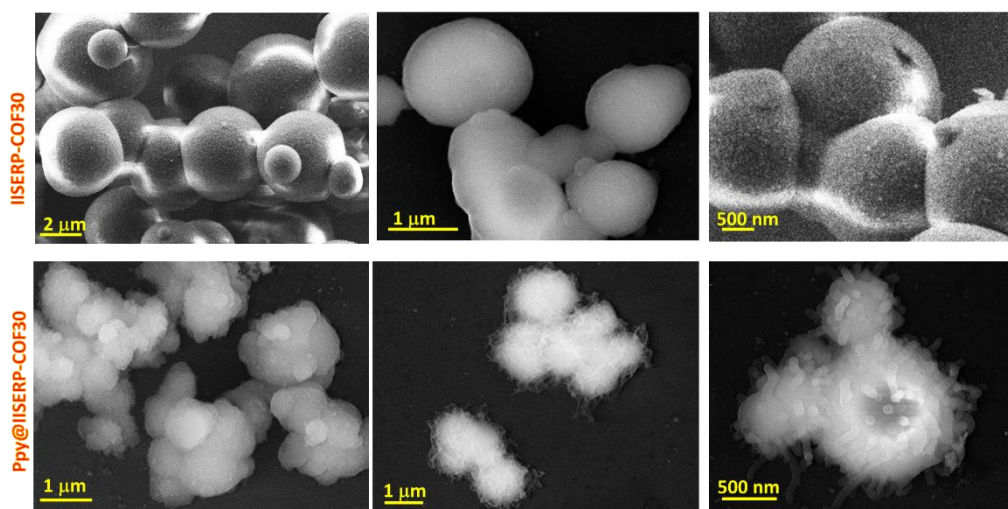


**Figure 3.9:** (FESEM) images of COF showing the spherical shapes of the COF particles. (FESEM) images of Ppy@COF showing the deformed spherical shapes of the COF particles. Closer look finds out the jetting out polypyrrole threads on the surface of those deformed COF sphere

The Energy Dispersive X-Ray Analysis (EDX) and the elemental mapping of the Ppy@COF reveals uniformly dispersed iodine species (Figure 3.10). This iodide can also be present in polyiodide ($I_3^-$) form, an energetically stabler species.[41] [42] [43]
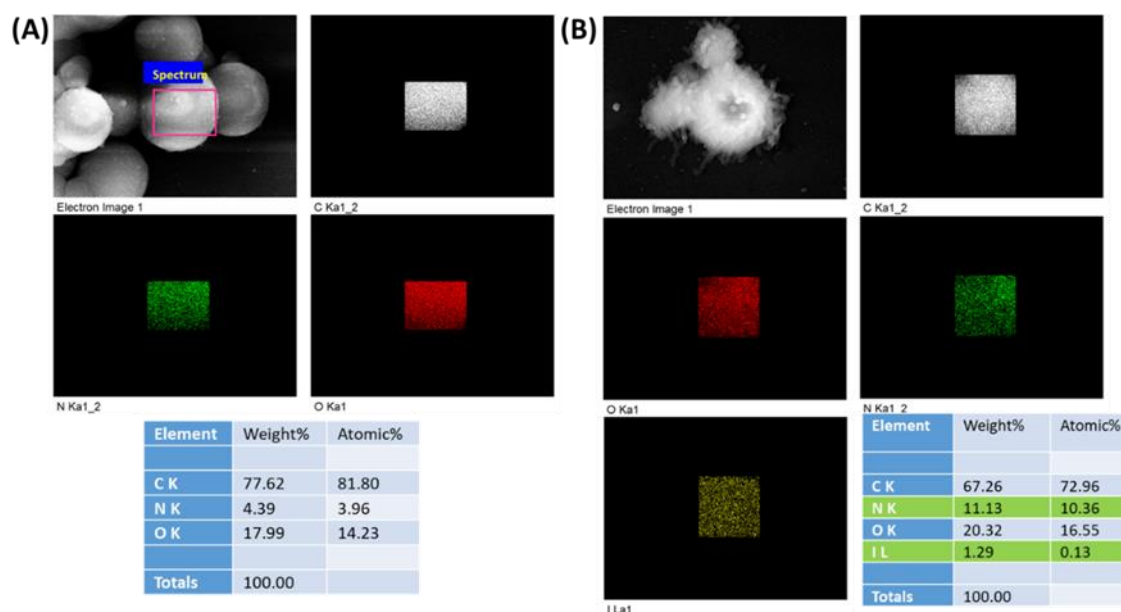


**Figure 3.10:** Energy Dispersive X-ray (EDX) analysis of SEM images of (A) COF and (B) Ppy@COF.

We confirmed the presence of $I_3^-$ and its ionic type interaction with pyrrole nitrogen from X-ray photoelectron spectroscopy (XPS) analysis. All the iodide (I 3d) XPS spectra display the peaks (618.6 eV) with binding energy corresponding to the I-I bond of $I_3^-$ species. If $I^-$ was the sole counter anion, peaks for I-I would have been absent. Also, a noticeable shoulder for terminal $I^-$ (of $I_3^-$) interaction with (protonated nitrogen) $NH^+$ of polypyrrole (619.8 eV) is seen. The binding energy difference between two spin states of iodine (I $3d_{5/2}$ and I $3d_{3/2}$) remained constant (11.5 eV) even when the polypyrrole was grown in the presence of the COF host. Figures S17 to S20 show the C 1s, N 1s, O 1s and I 3d spectra of the neat COF, Ppy@COF, and freshly prepared Ppy. The appearance of a C 1s shoulder at 288.5 eV along with C-N binding energy at 286.5 eV in the neat Ppy and Ppy@COF is most likely due to the interaction of the polypyrrole nitrogen with $I_3^-$ (Figure 3.11). Though it overlaps with the C=O peaks from the COF, it is much more prominent.[44] The ionic character of this interaction explains the higher C-N binding energy than expected.[45] This corroborates well with the binding energy trends displayed by the N 1s spectra of Ppy and Ppy@COF (Figure A3.6-A3.7, Appendix). Specifically, the peak due to the pyrrolic nitrogen centered at 400 eV for the Ppy and Ppy@COF has higher binding energy than neutral pyrrole due to interaction with $I_3^-$.[46]
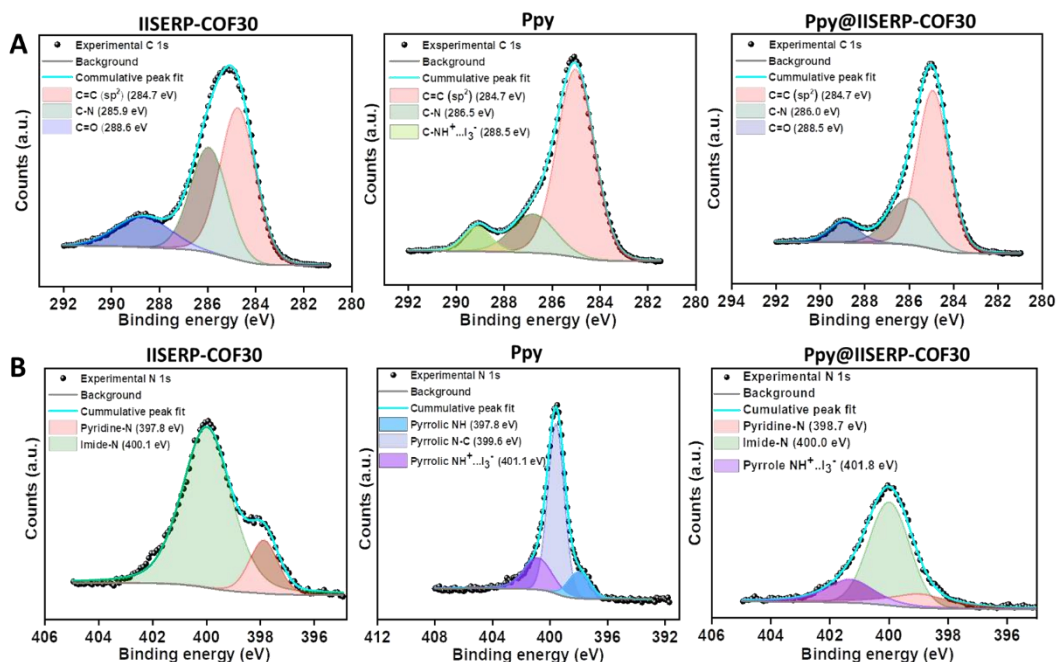
**Figure 3.11:** The comparison of (A) C 1s and (B) N 1s XPS of Ppy@COF with Ppy and as made COF.

The ultra-high magnification of the High-resolution Transmission Electron Microscopy (HRTEM) enabled us to perceive further the growth of this conducting polymer on the tiny flakes of the COF (Figures 3.12A-3.13A). The majority of the HRTEM images bring out two features: (i) thin layers of the COF showing up as flakes, and (ii) in some regions, the COF wrap-up into spherical balls (Figures 3.12A-B). The size of these balls varies from microns (2 µm) to nanometres (20 nm) range (Figure 3.12A-B). This is in agreement with some of the earlier reports.[47]
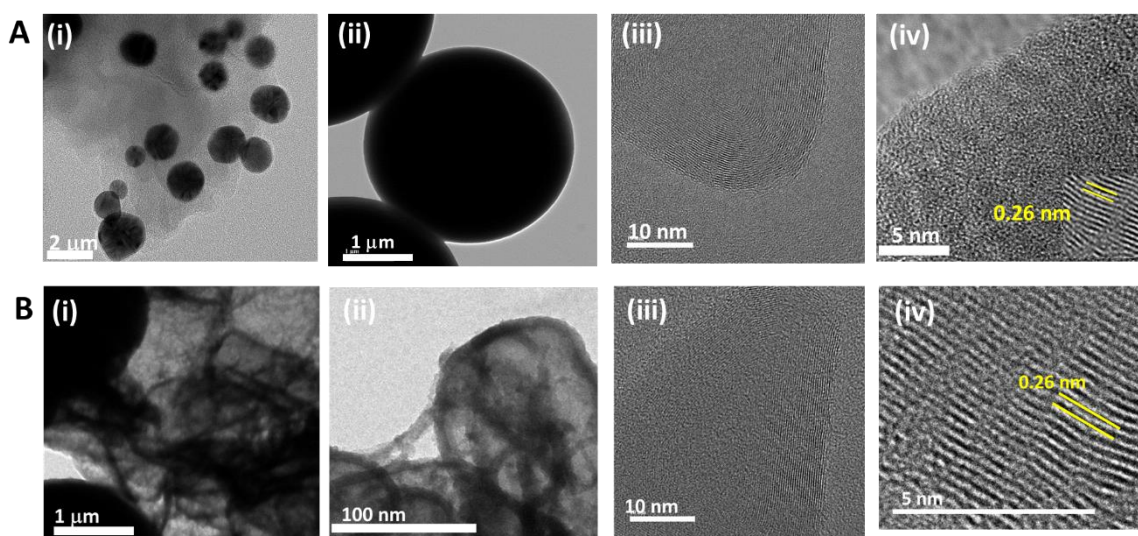


**Figure 3.12:** HRTEM images of (A) as made COF (B) Ppy@COF.

For imaging the layers and pores, the beam was focused on a transparent thin spherical particle of the COF (Figure 3.13A(i)and A3.8, Appendix).[47] From a view along the [110] direction, we can see the interlayer spacing with high order, which is consistent with earlier reports.[48] These thinner flakes, when viewed along the [001] direction, display the hexagonal pores arising from the COF-layer oriented on the *ab*-plane and their sizes (approx. two pores in 5 nm) agree well with what is expected (Figure A3.9, Appendix). The lattice fringes are visibly seen throughout the sphere, ensuring the high crystallinity of the COF (Figure 3.13A(i)). The cross-sectional view of the COF crystallites drop-casted on the TEM grid revealed an interlayer distance of 0.31 nm (Figure 3.13A(ii)). It corroborates well with the layer separation distances determined from the energy-geometry optimized structure and the experimentally obtained reflections in the PXRD pattern (Figures 3.4A-B). Furthermore, we probe sonicated the ethanolic suspension of the COF to break up the spheres into COF flakes. We noticed that the flakes were still large enough in lateral length and did not disintegrate into nanosheets or sub-nanometer particles. From these flakes, lattice fringes were observed; their spacings corresponded to the COF's inter-layer distances. Also, the flakes exhibited ordered hexagonal pores under the HRTEM as expected (Figure A3.10, Appendix).[48] [49]
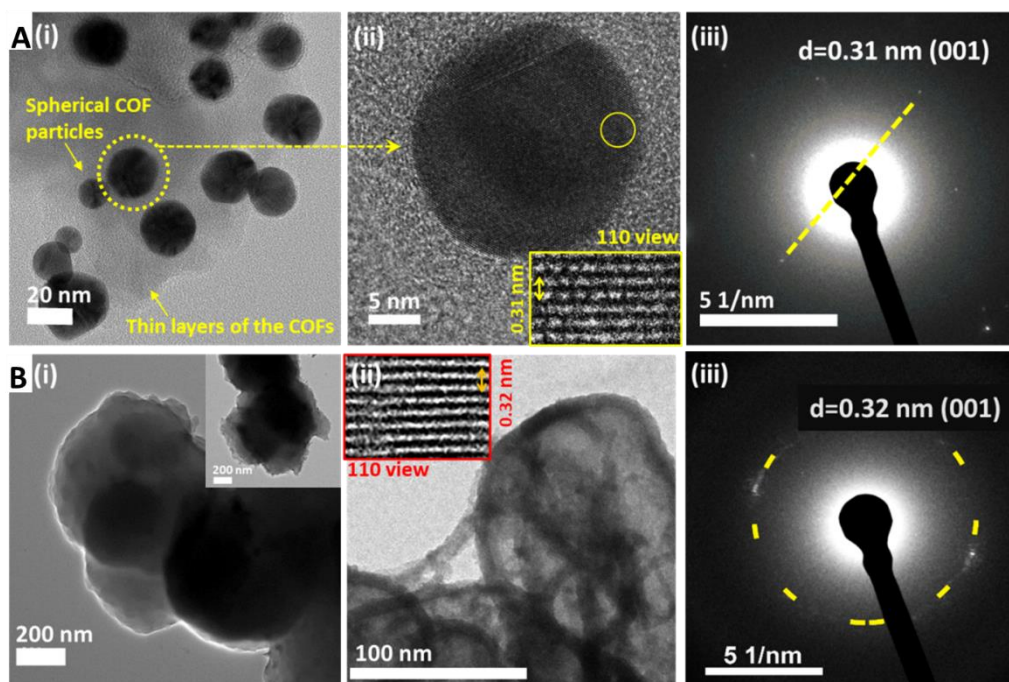


**Figure 3.13:** (A) (i). TEM image of the COF showing thin layers and wrapped-up flakes forming spherical balls. (ii). A transparent spherical particle shows the interlayer stacking of the COF (inset). (iii). SAED patterns of the COF observed for higher angle diffraction of the [00l] planes. (B) TEM images of the PPy@COF showing (i). The spherical particles made up of agglomerated flakes. (ii). Interlayer spacing of the COF and some polypyrrole threads on the COF-flakes. (iii). SAED patterns from higher angle [00l] planes reveals its lowered crystallinity compared to COF.

Distinct SAED patterns of COFs (at 5 nm⁻¹ scale bar) showed the presence of diffraction of [*00l*] planes at a higher angle (Figure 3.13A (iii)). But the lower angle reflections are merged in the smaller diameter range of the SAED, closer to the bright center of the direct TEM beam. There is a uniform lowering of crystallinity as the COF is transformed to Ppy@COF- indicated by the well-defined reflections of the COF lowering to polycrystalline rings. Furthermore, the minuscule threads of the polymer were preferably visible through the transparent thin flakes of the COF at the edges of each microsphere (Figure 3.13B(i) and 3.13B(ii) and Figure A3.11**,** Appendix). These Ppy fibres get more exposed in the TEM images only after prolong sonication which also segregates the Ppy@COF-spheres into nanoflakes.



| C K | 88 |
| N K | 3.2 |
| O K | 8.6 |
| I L | 0.2 |
|  |  |
| Totals | 100.00 |
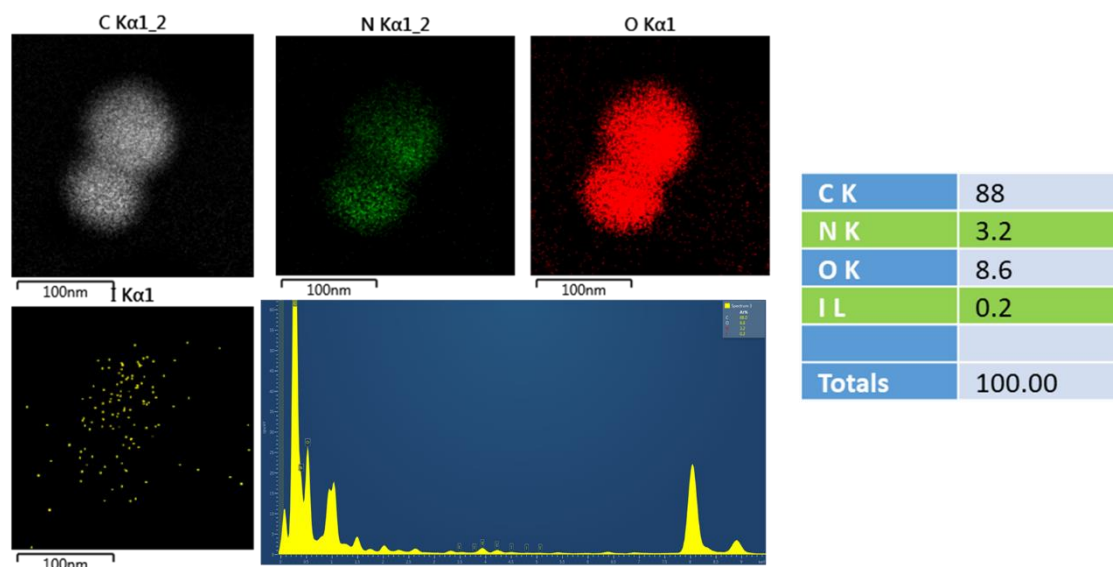
**Figure 3.14:** TEM-EDX reports of Ppy@COF.

Imaging in higher magnification required high electron volt, which scorched the pure organic backbone of the Ppy@COF, releasing the Ppy potentially from the pores of the COF. These images of the Ppy@COF are markedly different from that of the neat COF, polymer chains can be observed as dark streaks on the COF flakes, but it is not easy to identify if they are in the pore (Figure A3.11 and A3.12, Appendix). The TEM-EDAX identifies Iodine species associated with the Ppy, which, as expected, was not observed for the neat COF. This further confirms the integration of PPy with the COF (Figure 3.14).

### 3.2.3. Functionalization and electrical conductivity in Ppy@COF

We quantify the synergetic conductivity gain achieved by combining Ppy with COF by calculating the optical and electrochemical bandgaps. The electrochemical bandgap extracted from CV corroborates well with the optical bandgap obtained from the spectroscopic measurement for this polymeric system. The peaks in the CV plots from the organic electrolyte systems characterize all the possible redox-active functional groups. We correlate the extreme oxidized form (O2 and O2, Op1) and extreme reduced form (R3) of the system with the HOMO and LUMO levels (Figure 3.15A-C).[10] [50] The onset oxidation and reduction potentials (with respect to normalized hydrogen electrode, see SI) of the COF and the Ppy@COF can be related to the frontier orbitals (Table 3.1). The cyclic voltammetry in an inert atmosphere using a non-aqueous electrolyte system signposts the HOMO and LUMO energy levels (3.80 eV and 5.96 eV) and the corresponding bandgap (2.16 eV) of the COF. The elevation of the HOMO energy level (3.92 eV) and reduction of the LUMO energy level (5.48 eV) lowers the effective bandgap (1.56 eV) in the case of Ppy@COF, which suggests the possibility of better electron hustle (Figure 3.15A, Table 3.1).
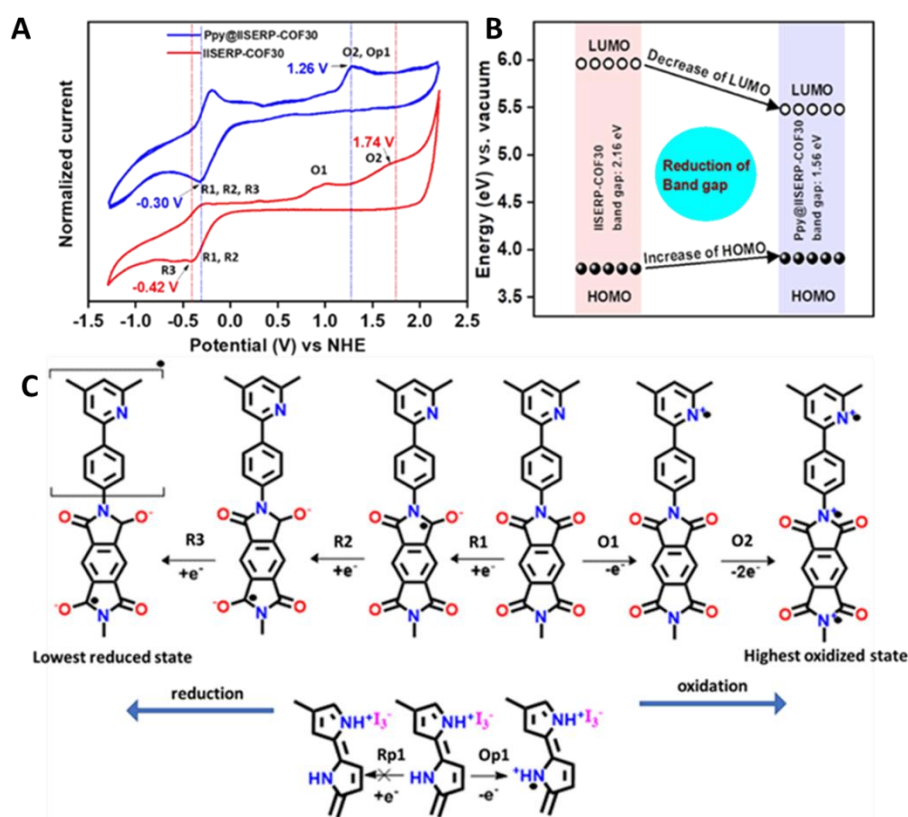


**Figure 3.15:** A schematic illustration of the different plausible redox species generated by the COF and the Ppy under the applied potential. (R1/O1, R2/O2, R3/O3, Op1 show the possible redox active interactions). The extreme oxidized and reduced state can be considered HOMO and LUMO.

Independently, we compared the UV-Visible absorption spectra of Ppy, COF and Ppy@COF. The comparison indicates an additional broad shoulder at around 600 nm in Ppy@COF, which is dark-colored compared to neat COF. The bandgap calculated using the 'Tauc plot' suggests that incorporating Ppy into the COF lowers the bandgap from 2.25 to 1.58 eV. This, in principle, should enhance the electronic conductivity (Figures 3.16A-3.16B).
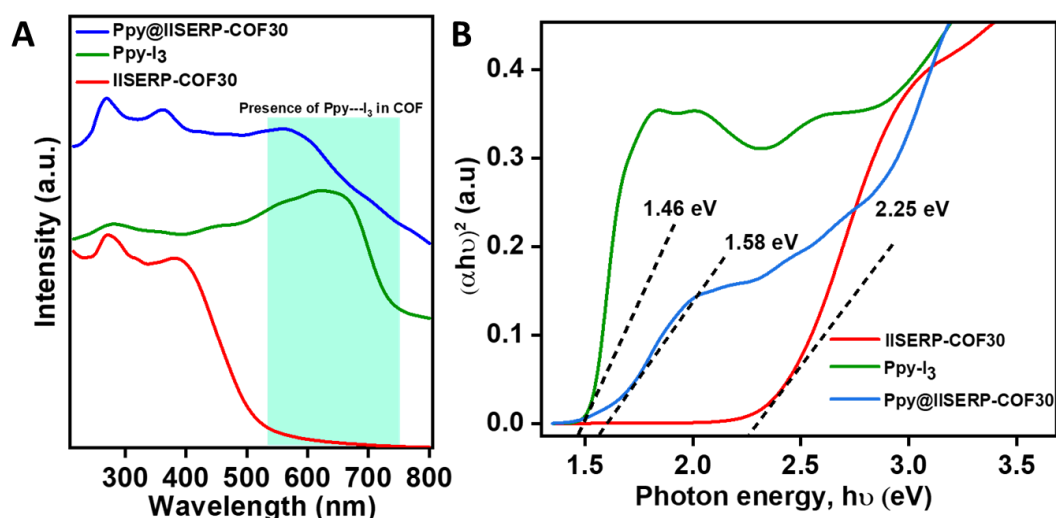


**Figure 3.16:** (A) The UV-visible spectra of COF, Ppy and Ppy@COF. (B) The Tauc plot extracted from UV-visible spectra showing the optical band gaps.

**Table 3.1:** Band gap calculation.

| COFs | $E_{Ox}$ vs SCE | $E_{Ox}$ vs. NHE | $E_{HOMO}$ (eV) | $E_{Red}$ vs. SCE | $E_{Red}$ vs. NHE | $E_{LUMO}$ (eV) | $E_g$ from CV (eV) | $E_g$ from Tauc plot (eV) |
|---|---|---|---|---|---|---|---|---|
| IISERP-COF30 | 1.05 | 1.74 | 5.96 | -1.11 | -0.42 | 3.80 | 2.16 | 2.25 |
| Ppy@COF | 0.57 | 1.26 | 5.48 | -1.00 | -0.31 | 3.91 | 1.56 | 1.58 |

We monitored the electron conductivity of the Ppy@COF with the help of I-V measurements and high-frequency impedance analysis (Figure 3.17; Figure A The non-defective and densely packed pellets were prepared from the solvent-free COF powder and the Ppy@COF. They were connected to a switchable voltage source, and the current outputs with the gradual deployment of the voltage were plotted. The I-V plots display the linearity and elevated slope for the Ppy@COF (Figure 3.17A), revealing a conductivity of the order of $10^{-3}$ S/cm. In comparison,
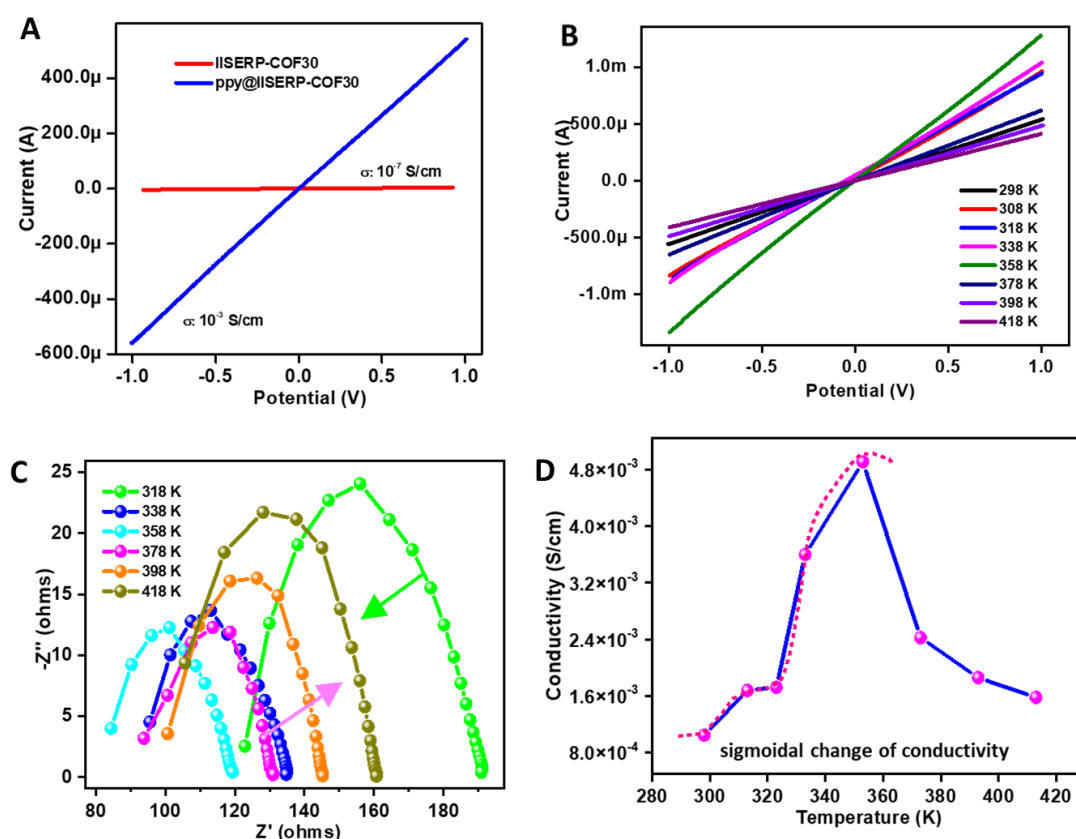
**Figure 3.17:** (A) Comparative I–V plots of the COF and Ppy@COF obtained from a four-probe conductivity set-up. (B) I–V plots of the Ppy@COF showing the increase in electronic conductivity with rise in temperature and decrease after 100 °C (373 K). (C) Nyquist plots from AC-Impedance measurements for Ppy@COF at different temperatures; the trend is similar to the I-V measurements. (D) The conductivity of Ppy@COF vs. temperature plot, a sigmoidal behaviour is seen.

the bare COF exhibits high resistivity with a shallow slope in the I-V plot. Also, the gradual elevation of the temperature increases the slopes of the I-V curves up to 358 K for the Ppy@COF (Figure 3.17B), indicating improvement of the conductivity. However, a significant drop of the conductivity beyond 358 K signifies the disruption of the electronic conjugation pathway, probably due to distortion of the framework. This observation was corroborated well in variable temperature high-frequency impedance analysis (Figure 3.17C). The diameter of the semicircles in the impedance plots, which indicates the resistance faced by the electron while traveling through the Ppy@COF, gradually decreases up to 378 K. But beyond this point, it starts to enlarge, generating a sigmoidal pattern like a perfect semiconductor (Figure 3.17D).[51] This temperature-driven conductivity boost is rare in any COFs reported so far, indirectly expresses the advantage of integrating Ppy with the COF.

### 3.2.4. Capacitance of COF and PPy@COF under acidic liquid electrolyte and their potential storage mechanisms

The facile electron propagation through the polymeric structure and the presence of redox-sensitive units in the backbone of the Ppy@COF makes it an apt candidate for storing charged particles under applied potential. Even without Ppy insertion, the activated COF offers multiple redox activities, evidenced by three-electrode cyclic voltammetry (CV) performed using 1 M $H_2SO_4$ electrolyte (Figure 3.18A and 3.184B). The polarized electron density on the COF surface attracts the $H^+$ ions under a positive bias of the implemented voltage (0 to 0.9 V). The COF's e-rich framework constituted by polyimide skeleton and pyridine centers undergoes stepwise reduction-oxidation in this positive potential window (vs. Ag/AgCl).[9] [52] [53] [54] We have assigned the redox peaks to activity at specific functional groups in the material by comparing them with closely related model systems that contain only the functional group(s) of interest.Importantly, to further strengthen the peak assignments, we studied the Ppy@COF under non-aqueous electrolytes to minimize the effects of a highly polarizing water medium and hydrogen evolution (Please see the calculations in appendix information). This redox trend in non-aqueous state CVs corroborates nicely with the observation under acidic electrolyte. Here in the case of Ppy@COF, the more electron-deficient center, imide's carbonyl reduces earlier in CV (at 0.67 V; R1) and gets neutralized by the $H^+$.[55] But the second stage of electrochemical reduction of another imide carbonyl group requires a more substantial potential
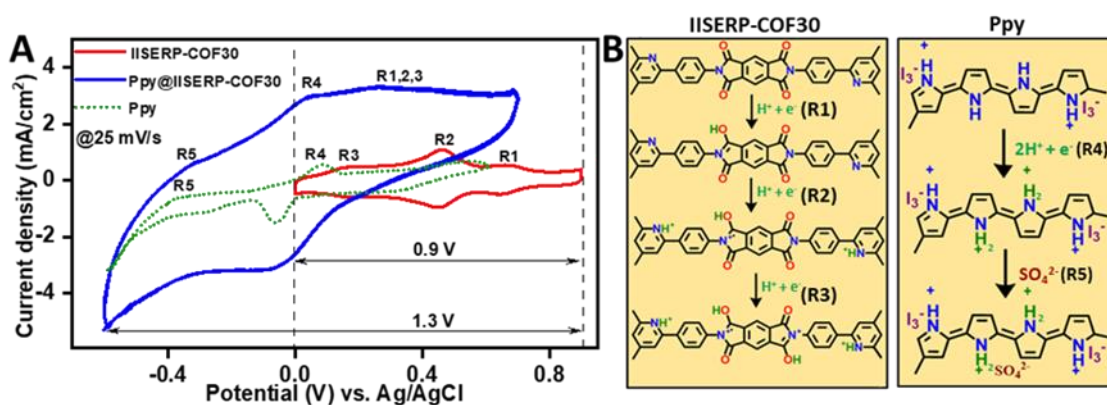


**Figure 3.18:** (A) Comparative CV plots of the of COF and Ppy@COF measured using these as working electrode employing 1 M H2SO4 as electrolyte in a three-electrode assembly at 25 mV s−1 scan rate with a 2 mg loading of the composite, Toray carbon paper as current collector of the working electrode. (B) Schematic of the electrochemical redox reactions of COF and conducting polymer (polypyrrole) in acid electrolyte.

(at 0.16 V; R3), followed by protonation. Meanwhile, the redox potential of pyridine nitrogen lies in between (at 0.46 V; R2).[9] The $SO_4^{2-}$ ions adsorb on the protonated COF's surface to counterbalance the overall charge, which constructs the Helmholtz double layer in the positive potential region. But the absence of any strong anion accepting functionality (e.g., cationic centers) in the parent COF structure certainly restricts the pseudo-activity of the COF only in a narrow potential window from 0-0.9 V (Figure 3.18A). This limits the energy density of the

capacitor (Figure 3.18A). Incorporation of conducting polypyrrole into the COF can help expand this potential window to yield higher energy and power density in a carbon-free system (Scheme 1).[37] As seen from figures 3.18A and S3.13, in the CV of polypyrrole, there are two major redox actions: (i) A two proton interaction that gives rise to a relatively larger current at lower potential (at 0.05 V; R4); (ii) The protonated polypyrrole chain under an acidic medium, induces the interaction of the $SO_4^{2-}$ with polypyrrole in the negative potential region. But this occurs over a wide potential window (R5: 0 to -0.6 V - implies withdrawing the electron density from the COF derived working electrode, Figure 3.18A, Appendix), hence the current density corresponding to this concerted inclusion of $SO_4^{2-}$ ions (at -0.42 V; R5) appears low. [56] Now, in PPy@COF, when the protonated Ppy-$I_3^-$ polymer threads are lodged in the COF, they translate this redox activity into the composite and thereby help expand the operating potential window from 0 to -0.6 V ( Figure 4A; S31**,** Supporting Information).[56] The similarity in CV peaks in Ppy@COF confirms the presence of these additional redox reactions (R4 and R5) in the composite as well as in polypyrrole (Figure 3.19A). Since the protonation of the COF and the interaction of $SO_4^{2-}$ ions with polypyrrole are very spontaneous processes and concerted, the distinct partitioning of the potential window is quite impossible.
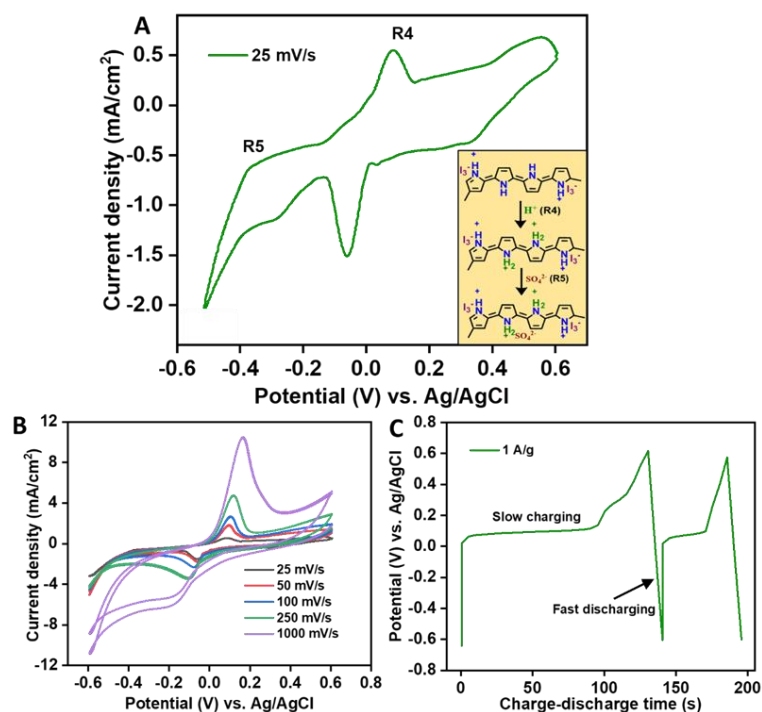


**Figure 3.19:** (A) The CV data of polypyrrole in $H_2SO_4$ electrolyte. (Inset) The redox reactivity of polypyrrole. (B) The CVs in $H_2SO_4$ electrolyte at different scan rates. (C) The Galvanostatic charge-discharge profile of polypyrrole at 1 A/g.

Lucratively, the intrinsic conductivity of the Ppy@COF enables the fabrication of a carbon-free electrode for charge storage which sees off the problems associated with inhomogeneous mixing of the COF with conducting agent. For the Ppy@COF, we observed a massive enhancement of the current output in a three-electrode CV measurement in an aqueous acid electrolyte system compared to the carbon mixed COF-electrode (Figure 3.18). The gradual augmentation of the peak current density with the increase of the scan rate indicates the proper capacitive type charge storage mechanism and facile mass transfer on the COF and Ppy@COF derived electrodes (Figure 3.20A; A3.13, Appendix). Meanwhile, the slope value of near 'one' from a fit to the logarithmic plot demonstrates the better pseudo activity on the surface of the Ppy@COF than non-conducting COF following the 'power law' (Figure 3.20B). The galvanostatic charge-discharge measurements at the positive potential window produce only 267 mF/g specific capacitance for the parent COF. The combination of the positive and negative potential window for Ppy@COF shows nearly 8 times enhancement of the specific capacitance (1983 mF/g) at the identical current density (1 A/g) (Figure 3.20C; Figure A3.14, Appendix).
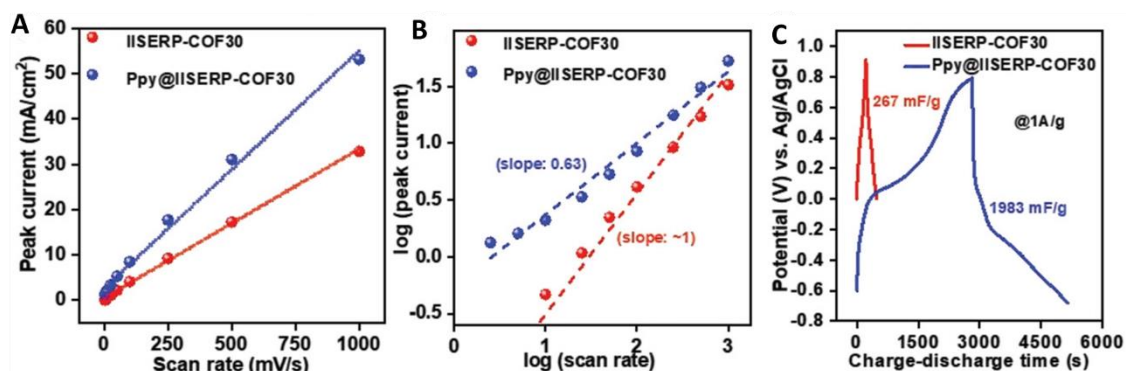


**Figure 3.20:** (A-B) Plot of the peak current vs. scan rate (250 mV to 1000 mV) displaying their linear relationship and plot of the log (Ipa) vs. log (scan rate) following the Power law. E. Charge-discharge curves of COF and Ppy@COF in the acid electrolyte.

Realizing that these redox modifications could be imprinted on the post-cycled PPy@COF, we analyzed a sample run for 2000 cycles using XPS. When we compared the XPS spectra of as-made Ppy@COF with the fully charged one, we observed a noticeable shift of the binding energy in C 1s, N 1s and O 1s spectra (Figure 3.21; Figure 3.15 and 3.16, Appendix). The carbonyl group's binding energy in O1s (532.3 eV) spectra increases to 535.5 eV due to –C=O---H$^+$ type ionic interactions. We anticipated similar ionic interactions induced changes in the binding energy for pyridine and pyrrole nitrogen centers. The C 1s spectra show an apparent increase in the binding energy after protonation of the pyridine and pyrrole nitrogen (from 286.0 to 287.7). While the strong interactions at the pyridine and pyrrole nitrogen cause

noticeable shifts in binding energy, the N 1s peaks shift from 398.7 to 400.7 eV and 401.8 to 405.9 eV, respectively.[45] Interestingly we observed good intensities for the O 1s (at 532.2 eV) and S 2p (at 168.9 and 170.9 eV) peaks in the XPS, arising from the sulfate ($SO_4^{2-}$) ions.[57] These observations sufficiently justify our proposed mechanism: *dual ion interaction to amplify the redox activity window*.

### 3.2.5. Solid-state capacitor derived from COF and Ppy@COF using acidic-gel electrolyte
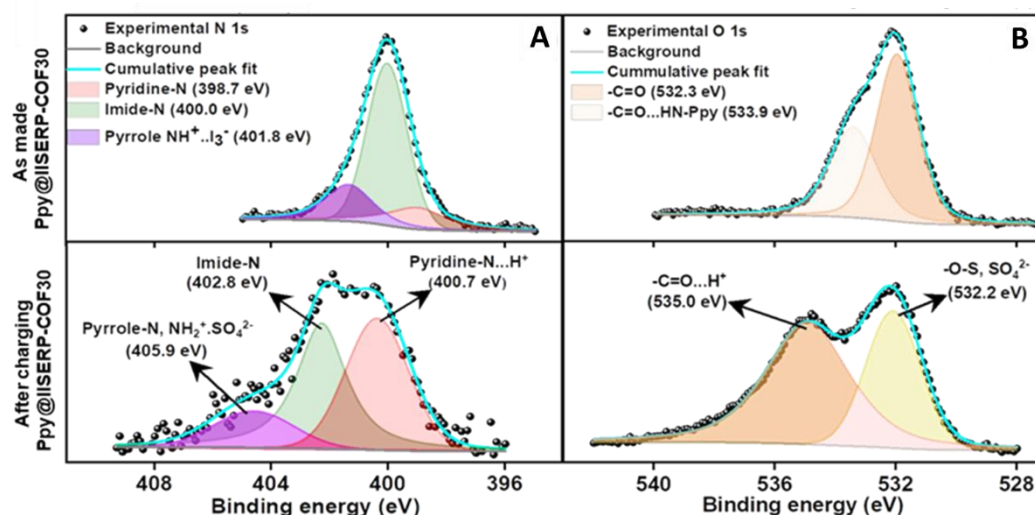


**Figure 3.21:** The XPS data analysis (A) N 1S and (B) O 1s nuclei before and after charging of Ppy@COF.

Though three-electrode systems help in the determination of the mechanistic pathway of the charge storage in the presence of plenty of the electrolyte, the practical applicability of the capacitor in electronic devices is only possible in two electrodes assemblies made out of two identical storage materials (Figure 3.22A). In that case, the liquid electrolyte is not a good choice since it dries fast after a few cycles. Hence we employed sulfuric acid trapped in a gelatin matrix of Polyvinyl-alcohol as gel-electrolyte between the two Ppy@COF electrodes unglued by the Celgard separator. Advantageously, the all-organic framework of the COF and Ppy@COF blends well with the carbon cloth imparting sufficient flexibility upon mechanical bending (Figure 3.22A). The polypyrrole chains ensure the facile electronic transport through the backbone of the COF, which aids in the electrochemical activation of the redox-active polyimide and pyridine centres for further interaction with the $H^+$ ions. Consequently, the CV of Ppy@COF at 25 mV/s swift rates delivers almost 3.5 times higher current density than the neat COF for an equal amount of the material loading on the carbon cloth (Figure 3.22B; Figure A3.17, Appendix).

The practical advantage is further marked by the prolonged charge-discharge time of Ppy@COF based capacitor in the galvanostatic charge-discharge measurement (Figure 3.22C, Figure A3.18, Appendix). The charge-discharge curves point that 3.5 times more charge can be stored by the Ppy@COF and provide the stored charge over 3.5 times longer duration when connected to an equal amount of current load.
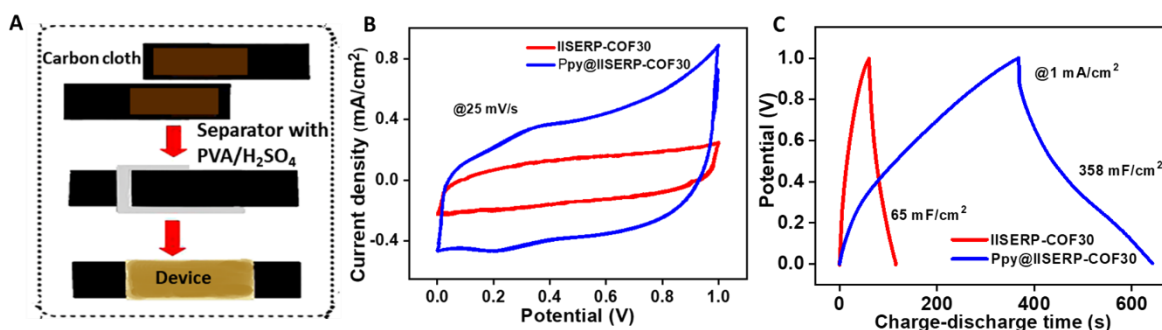


**Figure 3.22:** (A) Photographs of the COF and Ppy@COF-derived electrodes, the procedure for solid-state device fabrication. (B) CV plots of the COF and Ppy@COF measured for the solid-state devices (geometrical surface area = 1 cm$^2$) using a 1 M PVA-H$_2$SO$_4$ electrolyte at 25 mV s$^{-1}$ scan rate with a 10 mg total loading. (C) Galvanostatic charge–discharge curves of the COF and Ppy@COF measured for the solid-state devices made using 1 M PVA-H$_2$SO$_4$ as electrolyte at 1 mA/cm$^2$.

Interestingly, the solid-state device's CV profiles (at 25 mV/s) showed no deformation or current loss upon bending, illustrating the utility of this simple hand-made device in flexible electronics (Figure 3.23A). We witnessed a negligible deviation of the overall capacitance while bending this solid-state capacitor from 0° to 180° (Figure 3.22B). Though the specific capacitance of the device, 358 mF/cm$^2$ at 1 mA/cm$^2$, gradually reduces with the current density enhancement, it retains 115 mF/cm$^2$ of capacitance even at 10 mA/cm$^2$, which is remarkable (Figure 3.22C).
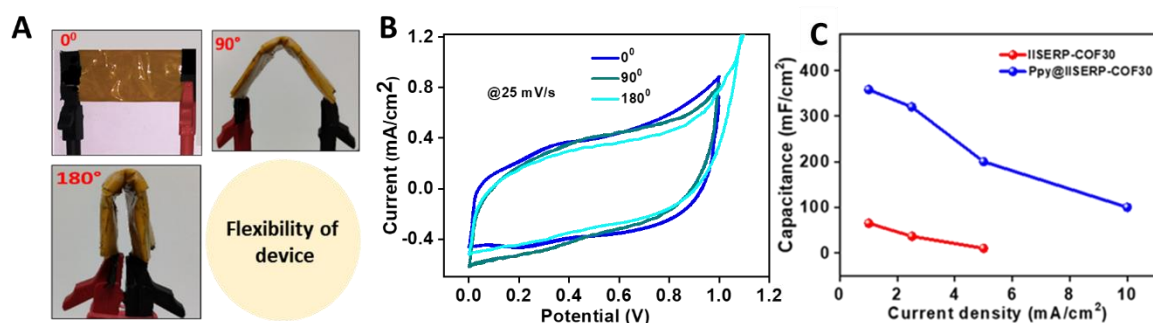


**Figure 3.23:** (A) Images of flexible device and (B) CV curves at different bending angles (0°,90° and 180°). (C) Comparative plot showing the variation in capacitance at different current densities for COF and Ppy@COF.

This highly flexible Ppy@COF capacitor supply 82% of its initial capacitance after 6000 continuous charge-discharge cycles (Figure 3.24A). The specific capacitance observed for Ppy@COF at 1 mA/cm$^2$ achieved without mixing with any conducting carbon is among some best performing COF-derived solid-state capacitors (Figure 3.24B).
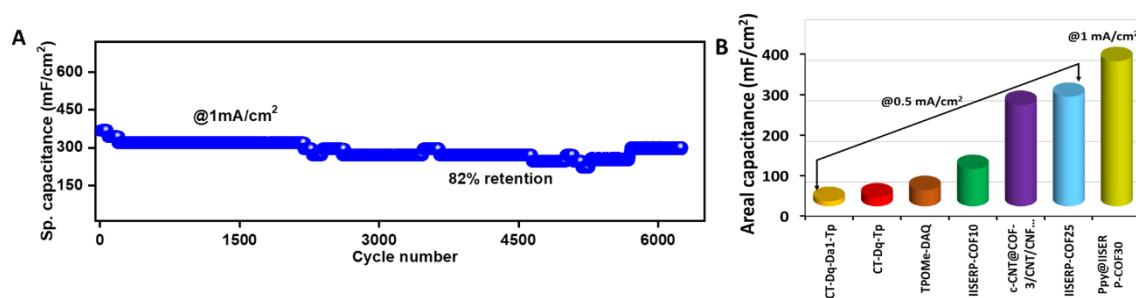
**Figure 3.24: (A)** Cyclic stability of the Ppy@COF-derived solid-state device measured over 6000 cycles. **(B)** A up-to-date comparison of the areal capacitances of some high performing COF based solid-state capacitors.

### 3.2.6. Capacitance of PPy@COF in organic electrolyte based devices

In the aqueous acid electrolyte described so far, the specific capacitance was recorded only in the narrow voltage window from 0 to 1V due to its limited electrochemical stability (water oxidation).[58] [59] Since the voltage window needs to be enhanced to obtain higher energy density, we lean on the organic electrolytes to access a more sweeping voltage regime. A similar kind of pseudo redox behavior is expected when the organic cations interact with the electron clouds of the pyridine, polyimide and pyrrole moieties. At the same time, the counter anions can neutralize positive charges. A glass microfiber separator was amply soaked with the tetraethylammonium tetrafluoroborate (1M $NEt_4^+BF_4^-$ in acetonitrile) (Type I, organic electrolyte) and 1-Ethyl-3-methylimidazolium tetrafluoroborate (Type II, organic ionic-liquid electrolyte) ($EMIMBF_4$,). It was sandwiched between the two Ppy@COF-derived electrodes coated on Cu current collectors. We hosted this sandwich assembly on a Swagelok cell in a glove box (Figure 3.25).
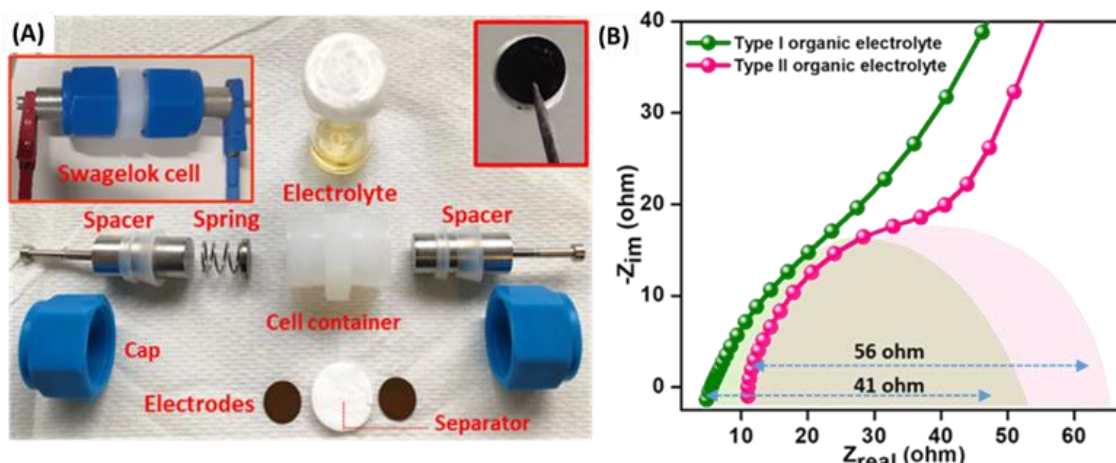


**Figure 3.25:** (A) A Swagelok-cell construction for capacitance measurements of Ppy@COF using organic electrolytes. (B) AC-Impedance spectra measured on the COF containing Swagelok-cells using two different bulky organic-electrolytes.

The lower charge transfer resistance and lower series resistance in the case of Type I all-organic-capacitor are explained by the low viscosity as well as the better wetting ability of the $NEt_4^+BF_4^-$ electrolyte in comparison to $EMIMBF_4$ (Figure 3.26).[60] [61] [62]

However, the superior electrochemical stability of the $EMIMBF_4$ illustrates the better
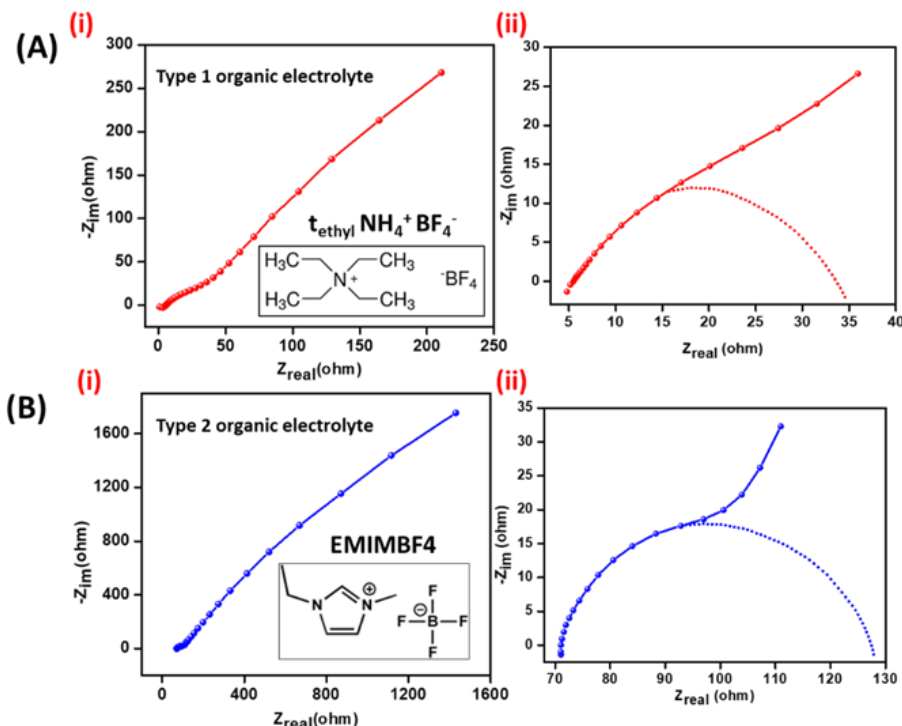


**Figure 3.26:** Complete Impedance plot along with extreme low frequency data for (A) 1M tetraethyl $NH_4^+BF_4^-$ gel electrolyte. (B) $EMIMBF4$ gel-electrolyte.

applicability of this ionic liquid electrolyte even up to 2.5 V (Figure 3.27; Figure A3.19 Appendix). Though the former electrolyte system with less bulky counter ions delivers higher power density (4509 $mW/cm^2$) within a smaller voltage window of 0 to 1.8 V, the ionic gel electrolyte maintains a proper balance between the energy densities (145 $mWh/cm^2$) and power densities (1370 $mW/cm^2$) (Table 3.2; Figures 3.20 and 3.21, Appendix). The CV at 25 mV/s displays profound redox interactions in organic electrolyte systems. Notably, a comparison of the CV of the capacitor in the $H_2SO_4$ (aqueous) vs. the organic electrolytes displays the prominent redox activity of the latter, and the EDLC behavior characterized by the rectangular shape is missing. To obtain a proper rectangular CV with mild redox peaks, the electron transfer associated with redox reactions and the mass transfer associated with charge neutralization between the cations and the anions should be occurring with comparable ease. In the case of organic electrolytes, the mass transfer limits the electron transfer due to the bulky nature of the

cations. This makes the pseudo redox peak dominate the EDLC type storage mechanism. However, these redox reactions are fully reversible.
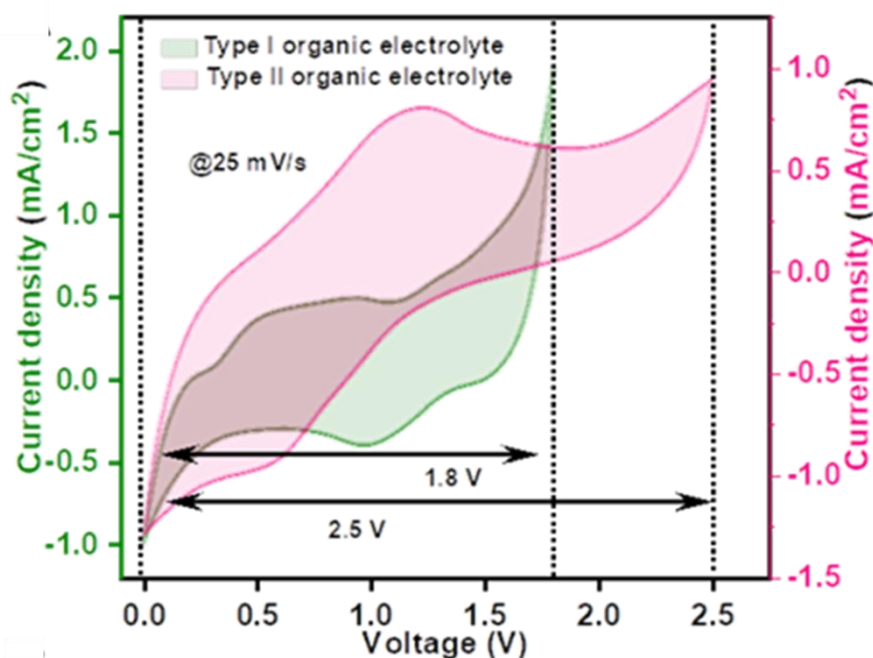


**Figure 3.27:** A comparative CV plot at 25 mV/s showing the enlargement of voltage window when organic ionic-liquid electrolyte was used

The galvanostatic charge-discharge curve displays an asymmetric profile, especially in the case of ionic liquid electrolytes, indicating faster discharge of Ppy@COF (Figure 3.28; Figure A3.20, Appendix). Unlike the liquid acid and gel electrolyte, for the organic liquid electrolyte (EMIMBF$_4$), there is a deformation of the charge-discharge plot at a low current density (Figure A3.21, Appendix). This is expected from this relatively large-sized organic electrolyte due to sluggish diffusion kinetics. Both charging and discharging happen within a more extended voltage region (charging window: 2 to 2.5 V; discharging window: 2.5 to 0.8 V) rather than at a fixed potential. The oxidation and reduction potential of the Ppy@COF loaded electrodes shift far apart and result in a large over-potential (nearly 1.05 V) system.[63] Consequently, the device fabricated with organic electrolytes tends to self-discharge at low current densities without a well-defined redox reaction until it reaches 1 V. This deformation of the charge-discharge curve is much less pronounced at high current densities. Only the electrolytic surface charge storage becomes a predominant factor at higher current densities. Meanwhile, the less viscous organic electrolyte (1 M NEt$_4^+$BF$_4^-$, in acetonitrile) shows less deformation of the GCD profile and 1.7 times higher specific capacitance than the ionic gel electrolyte (Figure 3.20A, Appendix ).
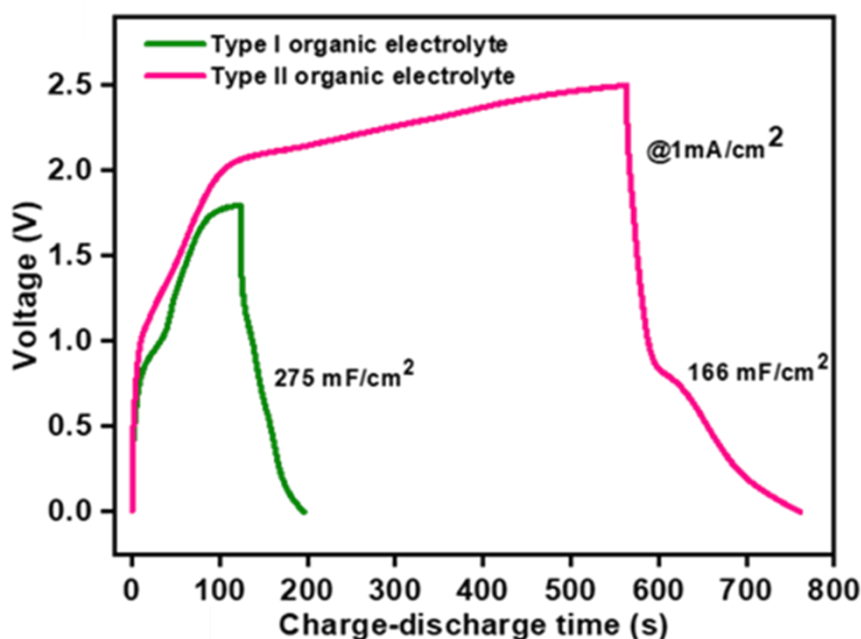
**Figure 3.28:** The Galvanostatic charge-discharge plots of Ppy@COF at 1mA/cm$^2$ using two different type of organic electrolytes.

However, the more extensive voltage stability and more than 98% retention of the capacitance even after 2800 cycles of charge-discharge undoubtedly make the ionic-gel the best-performing capacitor system with ultra-high energy densities (Figure 3.29A). In the 'Ragone' plot, the energy density and power density of all other COF and MOF-derived capacitors are confined in a particular region due to their limited voltage barrier, while the Ppy@COF shines with its high energy and high power output in variable current densities (Figure 3.29B).[4] [64]
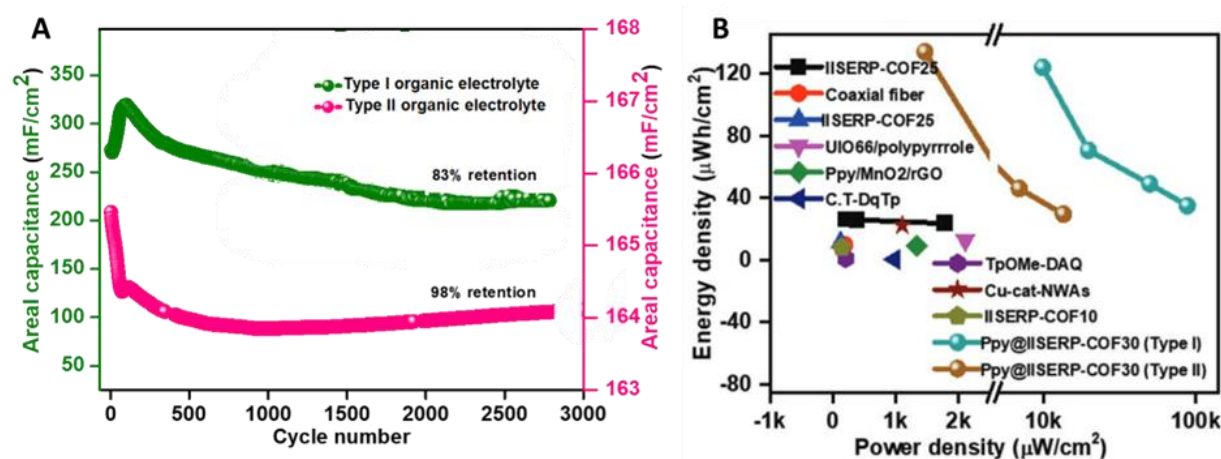


**Figure 3.29:** (A) The cycle stability of the Ppy@COF derived organic-capacitors. (B) A Ragone plots of some high performing capacitors indicating the high energy density and high-power density of Ppy@COF.

We carried out detailed characterizations of the post 2000 cycled sample, the outcomes supported the stability of the Ppy@COF as a charge storage material (Figures 3.30).
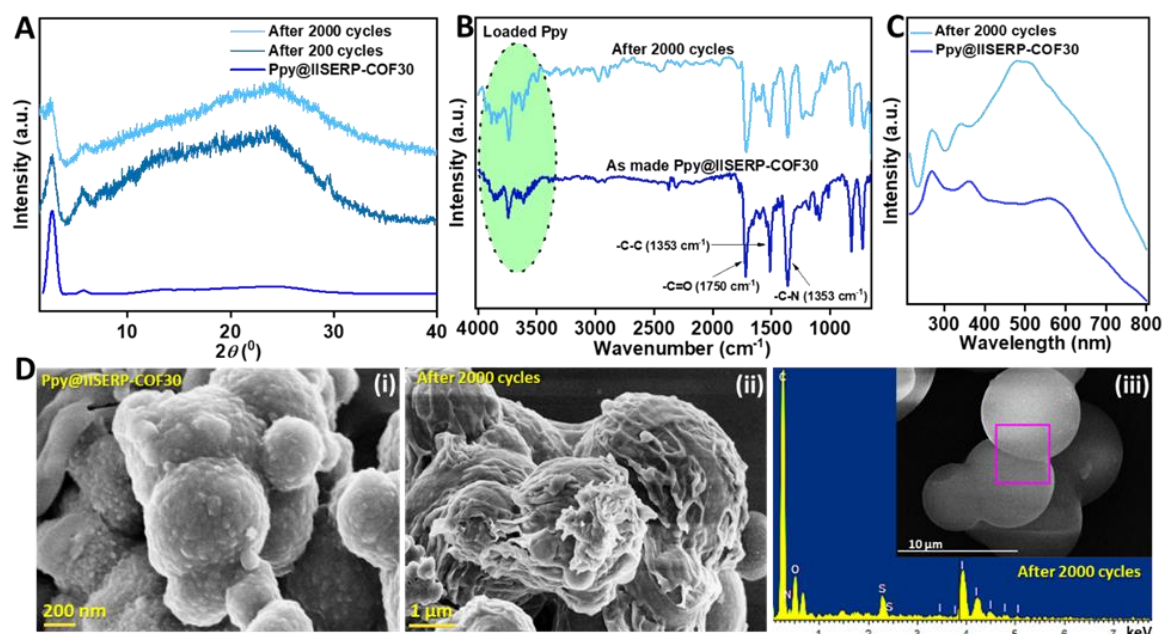


**Figure 3.30:** (A) Comparison of PXRD of Ppy@COF before and after galvanostatic charge-discharge cycling. (B) FT-IR spectra of Ppy@COF before and after cycling. (C) The UV-Visible spectra of of Ppy@COF before and after cycling. (D) (i) and (ii) The FE-SEM images of Ppy@COF before and after cycling. (iii) The EDX analysis data of Ppy@COF after cycling.

## Table 3.2. Device-performance of COF and Ppy@COF in different electrolytes

| Aqueous gel-electrolyte (potential window 0–1 V) | | |
|---|---|---|
| Energy density (in $\mu Wh\ cm^{-2}$) @1 mA cm$^{-2}$ | IISERP-COF30 (sp. capacitance 65 mF cm$^{-2}$) | 5 |
| | Ppy@IISERP-COF30 (sp. capacitance 358 mF cm$^{-2}$) | 50 |
| Power density (in $\mu W\ cm^{-2}$) @1 mA cm$^{-2}$ | IISERP-COF30 (sp. capacitance 65 mF cm$^{-2}$) | 316 |
| | Ppy@IISERP-COF30 (sp. capacitance 358 mF cm$^{-2}$) | 561 |
| Organic-electrolyte: Type I (potential window 0–1.8 V) | | |
| Energy density (in $\mu Wh\ cm^{-2}$) @1 mA cm$^2$ | Ppy@IISERP-COF30 (sp. capacitance 275 mF cm$^{-2}$) | 124 |
| Power density (in $\mu W\ cm^{-2}$) @1 mA cm$^{-2}$ | Ppy@IISERP-COF30 (sp. capacitance 275 mF cm$^{-2}$) | 4509 |
| Organic–ionic–liquid-electrolyte: Type II (potential window 0–2.5 V) | | |
| Energy density (in $\mu Wh\ cm^{-2}$) @1 mA cm$^{-2}$ | Ppy@IISERP-COF30 (sp. capacitance 166 mF cm$^{-2}$) | 145 |
| Power density (in $\mu W\ cm^{-2}$) @1 mA cm$^{-2}$ | Ppy@IISERP-COF30 (sp. capacitance 166 mF cm$^{-2}$) | 1370 |

### 3.2.7. Electronic energy level of the COF modules and their contributions

We had ascertained the lowering of the bandgap with the incorporation of PPy into the COF through electrochemical measurements. To further understand the exact electronic energy levels around each of the modules of the COF and their resulting bandgaps, we resorted to computational modeling. The aim was to verify if the calculated HOMO-LUMO energies and gaps follow the trend observed from electrochemically established gaps.[52][53] For this, a model of the polypyrrole dimer, chain, and the chains lodged into the COF was considered. The Ppy@COF was modeled by constructing 1-D polypyrrole chains with eight repeat units; this is a sterically appropriate fit given the dimensions of the COF pores (Figure 7). They were lodged into the COF following a GCMC method employing the simulated annealing algorithm. The optimized structure of the Ppy@COF displayed uniform loading of 4 chains per unit cell of the COF and the chains arranged in and out of the COF plane, which suggestively resembles the images observed from the SEM (Figure 3.9). The optimized structure of the Ppy@COF had relative energy higher than the empty COF (See computational details in the SI).

### 3.2.8. A modular/molecular viewpoint

Electronic energy levels (HOMO-LUMO) calculated using the DMOL yielded truly insightful elucidations.[65] For the neat COF, the LUMOs were centred around the non-aromatic five-membered rings of the imide-units. In comparison, the HOMO levels room around the e-rich aromatic rings and the pyridyl rings (Figure 3.13A-3.13C). Now, this sets up push-pull electronics in the backbone; however, the conjugation does break at the five-membered ring containing imide bonds, which could substantially lower the bulk conductivity of the COF. Thus the COF, by design, is not electronically conducting. Now, a look into the HOMO-LUMO levels of the Ppy@COF shows that the LUMO levels remain precisely at the COF centres, but the e-rich HOMO reside at the polymer chains confined within the COF pores (Figure 3.31D). Thus considering the electron distribution of both the COF and the Ppy@COF, it is evident that the polymer adds more electrons to the overall composite system. While the low-lying LUMO levels of the COF can accept electrons from both the HOMO of the COF and potentially from the HOMO of the polymer. Consequently, the polymer potentially increases the delocalized electrons in the system and sets up a relatively superior acceptor-donor pathway. This reflects in the drastic enhancement of electronic conductivity upon loading the polypyrrole as observed from the two-probe conductivity measurements ($10^{-7}$ S/cm (neat COF) vs. $10^{-3}$ S/cm Ppy@COF).
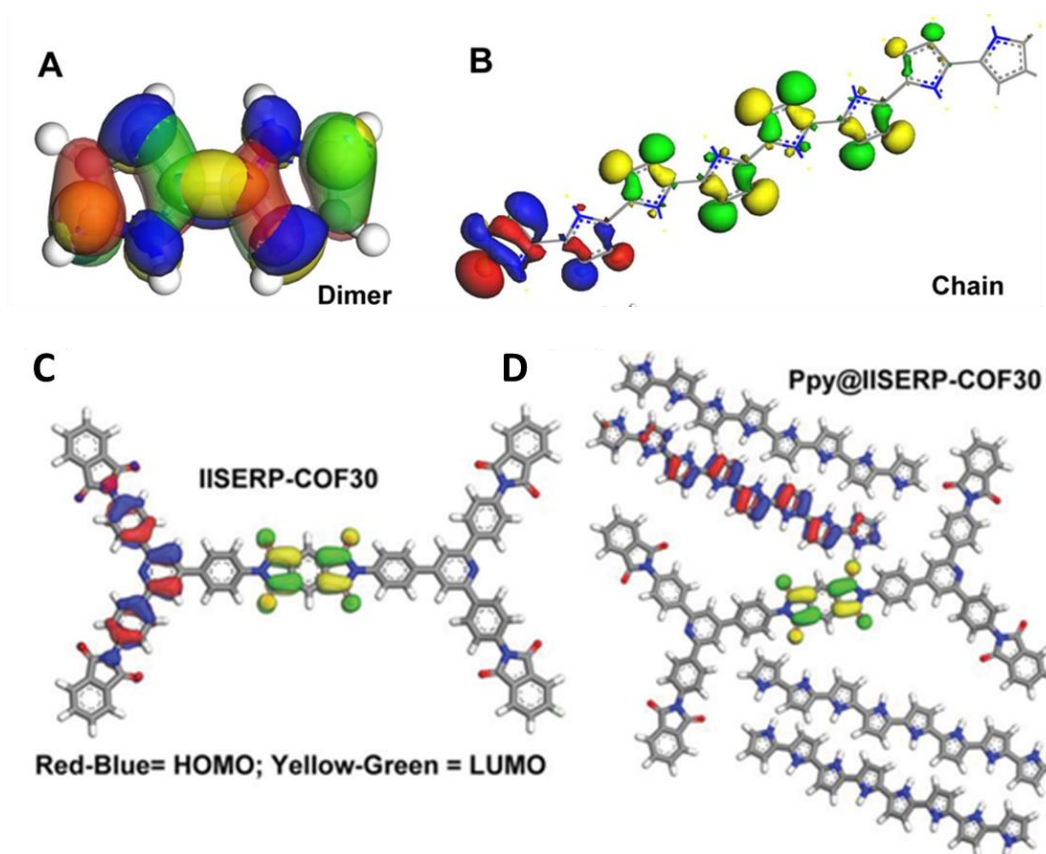
**Figure 3.31:** (A-B) Frontier orbitals calculated for the Pyrrole dimer and chain. The HOMO-LUMO positions calculated from the DMOL3 matches well with the trend expected from the electro negativity (push-pull) of the different functionalities that are linked together in the molecule, these are consistent with the previous reports. [ The observed HOMO-LUMO gaps agree very well with the literature values. The Frontier orbitals for the COF and Ppy@COF specis: (C) IISERP-COF30. (D) Ppy@COF with each polypyrrole being 8-units long.

Notably, the bandgap calculated from the cyclic voltammetry (CV) via a Tauc plot for the COF and the Ppy@COF matches well with the computationally observed bandgap lowering. In fact, electron-assisted through-space charge transfer is known in donor-acceptor assemblies, even in rod-like polymer structures and also in D-A pairs confined in MOF pores.[38] [39] [66] [67] Typically, the through-space transfer is associated with strongly π-stacked systems, and this can happen in the poly@COF when large chains of the polymer are considered for their potential π-interactions with the COF backbone. However, experimental and computational proof of such interactions would require a more specific and detailed computational study.

### 3.2.9. A polymer perspective

Further, the absolute HOMO-LUMO energies, as well as the gaps, were considered for understanding the energy level changes with the inclusion of the Ppy into the COF. It was evident that the HOMO-LUMO separation for the COF decreased substantially upon loading the polymer (COF: 1.66 eV; Ppy@COF: 0.98 eV). Meanwhile, when the absolute values of the HOMO and the LUMO were engaged to see how they compared between the COF and the

Ppy@COF, the HOMO showed a difference of 1.81 eV and the LUMO displayed a difference of 1.14 eV. This trend is opposite to that observed from the experimentally observed changes in the HOMO-LUMO (Figure 3A). To get a more appropriate picture, considering the periodic polymeric structure of the COF and the Ppy@COF, we calculated the bandgaps for a 3 x 3 x 3 supercell using the tight-binding DFT (DFTB) package (Supporting Information). Interestingly, the DOS plots revealed a significant electron population around the Fermi level for the Ppy@COF compared to the COF. The bandgap was 2.38 eV for the COF, which decreased to 1.41 eV upon the inclusion of the polymer (Figure 3.32). This agrees with the bandgap calculated from the CV measurements (COF: 2.16 eV; Ppy@COF: 1.57 eV).

Remark: Such a low bandgap of the Ppy@COF should make it relatively conductive, but the experimental bulk conductivity is still not as large. This is attributable to the low-level pyrrole loading (not all the pores fill-up) and also the intrinsic defects in the COF.[2] Further, to verify the electrochemical stability of the modeled structures of COF and the Ppy@COF under an applied potential, we optimized their geometries under an external electric field of 0.1 eV/Å/e/UC. Stable structures with acceptable van der Waals distances and bond lengths were obtained for both. No appreciable lengthening of bond lengths was observed compared to ground state structures optimized without any external field.[30] [68] [69] [70] However, their total energies under external field was higher compared to their structures without an external applied potential, as would be expected (Energy of the optimized structure of IISERP-COF30:
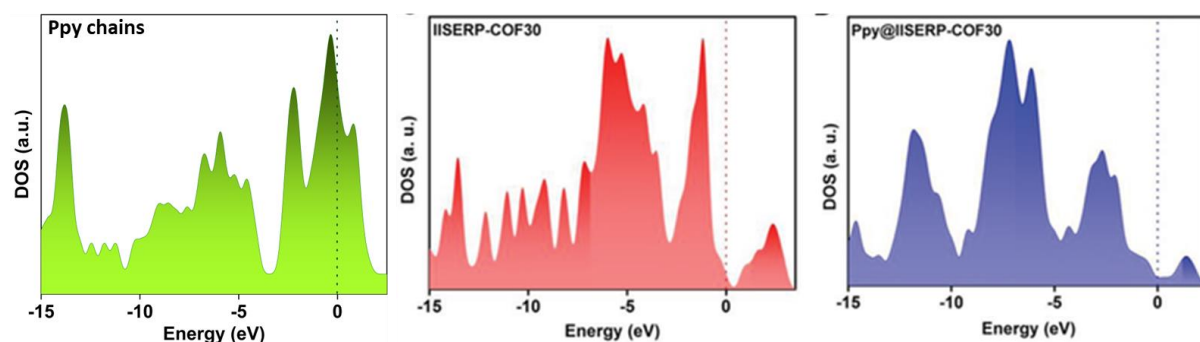


**Figure 3.32:** Density of States (DOS) diagrams for the neat Ppy, COF and the Ppy@COF. Note the presense of significant electron density even at the fermi level in the latter.

-14803 eV/unit-cell vs. -19564 eV/unit-cell) (under external electric field) (with no external field) at 0 K, (Figure 3.33). Thus the observations from computations match well with the trends observed from experiments and they suggest that even a defect-limited[2] partial

translation of the modules/monomers intrinsic electronics to the COF's polymeric structure imparts excellent electrochemical activity to it.
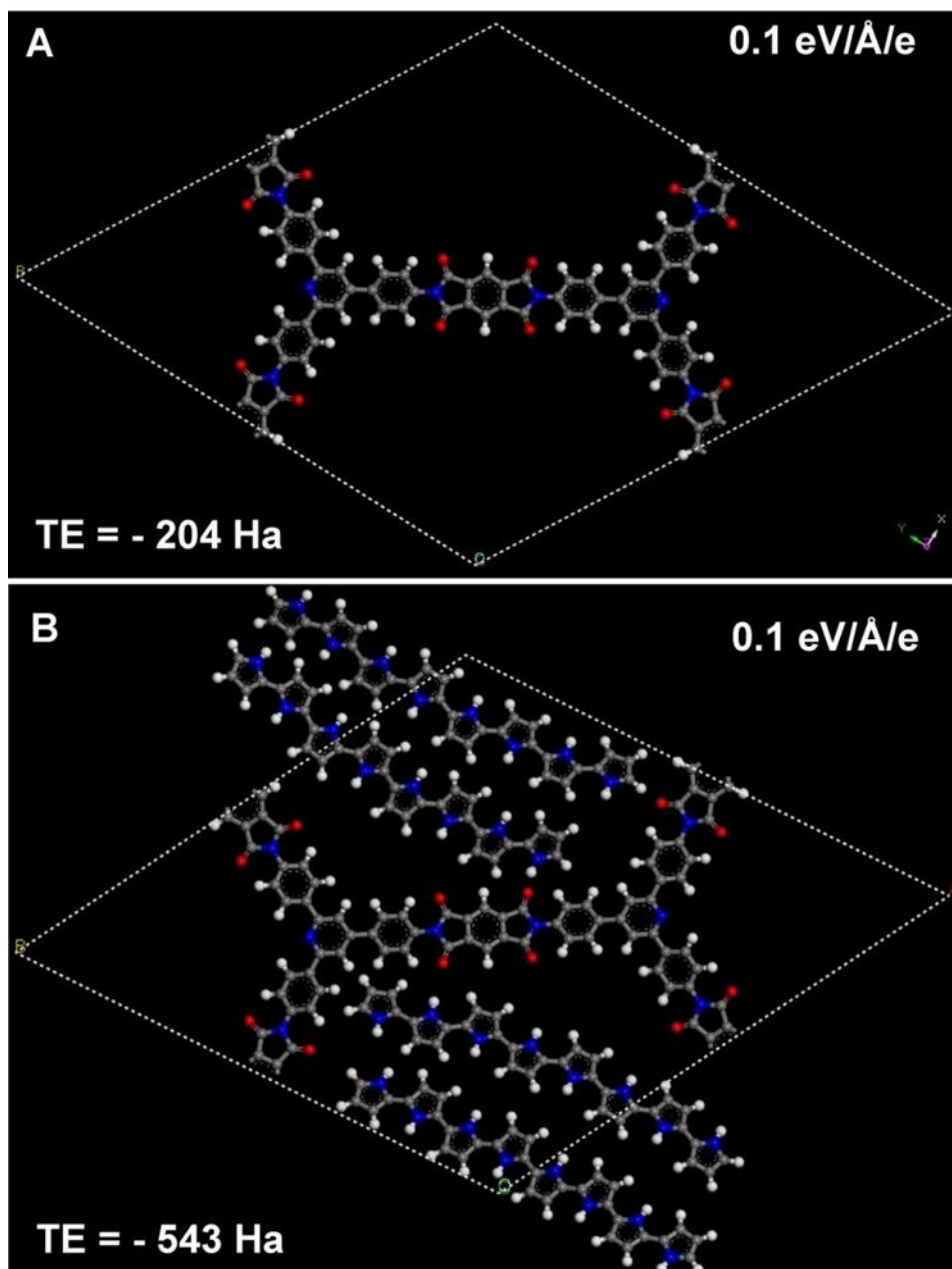


**Figure 3.33:** Optimized structures of the IISERP-COF30 and the Ppy@COF minimized under an applied potential. No unacceptable bond distances or angles were found. Note that the total energy of these structures is higher than the COF structure modeled from ground state DFT methods without any applied potential and at 0 K. The applied potential is expressed per unit cell.

## 3.3 Conclusion

This chapter describes an approach to improve COF-derived storage systems' electronic activity by increasing the number of redox-active heteroatoms within the system. We realize that only so much heteroatom can be blended directly into the COF framework. Hence the

inclusion of guests rich in interactive atoms offers an effective route. Thus, incorporating conducting polypyrrole into COF's ordered nanochannels further enhances its activity by creating facile electron conjugation pathways. The profound charge storage ability of the Ppy@COF in stabilizing all the dissociated electrolytes (cations and anions) in its skeleton is promptly investigated and justified with comprehensive electrochemical studies. The incessant electron dissipation under applied voltage within the COF framework electronically stimulates all its redox moieties producing high specific capacitance even at a very high current density. Also, the non-volatile and electrochemically stable Ppy units widen the effective voltage window yielding ultra-high energy density through additional pseudo interactions with the negatively charged ions ($SO_4^{2-}$ and $BF_4^-$). Importantly, coupling the porous Ppy@COF system with stable but bulky organic electrolytes appropriates a wider working voltage (0 to 2.5 V) that delivers a more balanced energy and power density. Stability displayed by the carbon-free Ppy@COF under both aqueous and organic electrolytes is noteworthy and lays a route for more hybrid systems. The prospect of Ppy units offering more electrons into the HOMO levels, which, under a potential, can be transferred to the LUMOs residing on the COF units, is captured by the DFT-optimized structures. The lowering of the electrochemical and optical bandgap of the COF by the incorporation of PPy is well augmented by the DFT studies, and this explains the abrupt enhancement of the power density and the energy densities without using any hybrid storage system. These make our finding unique, exciting and set the scene for constructing COF-based lightweight high-energy capacitors for futuristic applications.

## 3.4 Acknowledgements

## 3.5 References

[1]     A. P. Cote, A. I. Benin, N. W. Ockwig, M. O'Keeffe, A. J. Matzger, O. M. Yaghi, *Science* **2005**, *310*, 1166.

[2]     F. Haase, B. V. Lotsch, *Chem. Soc. Rev.* **2020**, *49*, 8469.

[3]     M. Wang, H. Guo, R. Xue, Q. Li, H. Liu, N. Wu, W. Yao, W. Yang, *ChemElectroChem* **2019**, *6*, 2984.

[4]     Y. Yusran, H. Li, X. Guan, D. Li, L. Tang, M. Xue, Z. Zhuang, Y. Yan, V. Valtchev, S. Qiu, Q. Fang, *Adv. Mater.* **2020**, *32*, 1907289.

[5]     N. Huang, P. Wang, D. Jiang, *Nat. Rev. Mater.* **2016**, *1*, 16068.

[6]     C. R. DeBlase, K. E. Silberstein, T.-T. Truong, H. D. Abruña, W. R. Dichtel, *J. Am. Chem. Soc.* **2013**, *135*, 16821.

[7]     X. Y. Yu, L. Yu, H. B. Wu, X. W. Lou, *Angew. Chem.* **2015**, *127*, 5421.

[8]     P. Bhanja, K. Bhunia, S. K. Das, D. Pradhan, R. Kimura, Y. Hijikata, S. Irle, A. Bhaumik, *ChemSusChem* **2017**, *10*, 921.

[9]     S. Haldar, R. Kushwaha, R. Maity, R. Vaidhyanathan, *ACS Mater. Lett.* **2019**, *1*, 490.

[10]    S. Haldar, D. Kaleeswaran, D. Rase, K. Roy, S. Ogale, R. Vaidhyanathan, *Nanoscale Horiz.* **2020**, *5*, 1264.

[11]    S. Haldar, K. Roy, R. Kushwaha, S. Ogale, R. Vaidhyanathan, *Adv. Energy Mater.* **2019**, *9*, 1902428.

[12]    X. Zhao, P. Pachfule, A. Thomas, *Chem. Soc. Rev.* **2021**, *50*, 6871.

[13]    M. Li, J. Liu, T. Zhang, X. Song, W. Chen, L. Chen, *Small* **2021**, *17*, 2005073.

[14]    D. Mullangi, V. Dhavale, S. Shalini, S. Nandi, S. Collins, T. Woo, S. Kurungot, R. Vaidhyanathan, *Adv. Energy Mater.* **2016**, *6*, 1600110.

[15]    E. Troschke, D. Leistenschneider, T. Rensch, S. Grätz, J. Maschita, S. Ehrling, B. Klemmed, B. V. Lotsch, A. Eychmüller, L. Borchardt, S. Kaskel, *ChemSusChem* **2020**, *13*, 3192.

[16]    D. Chakraborty, S. Nandi, D. Mullangi, S. Haldar, C. P. Vinod, R. Vaidhyanathan, *ACS Appl. Mater. Interfaces* **2019**, *11*, 15670.

[17]    S. Nandi, S. K. Singh, D. Mullangi, R. Illathvalappil, L. George, C. P. Vinod, S. Kurungot, R. Vaidhyanathan, *Adv. Energy Mater.* **2016**, *6*, 1601189.

[18]    B. Sun, J. Liu, A. Cao, W. Song, D. Wang, *ChemComm* **2017**, *53*, 6303.

[19]    C. Portet, G. Yushin, Y. Gogotsi, *J. Electrochem. Soc.* **2008**, *155*, A531.

[20]    A. J. R. Rennie, V. L. Martins, R. M. Smith, P. J. Hall, *Sci. Rep.* **2016**, *6*, 22062.

[21]    M. Sajjad, W. Lu, *J. Energy Storage* **2021**, *39*, 102618.

[22]    S. Haldar, D. Chakraborty, B. Roy, G. Banappanavar, K. Rinku, D. Mullangi, P. Hazra, D. Kabra, R. Vaidhyanathan, *J. Am. Chem. Soc.* **2018**, *140*, 13367.

[23]    S. P. Armes, *Synth. Met.* **1987**, *20*, 365.

[24] S. C. Rasmussen, in *Conductive Polymers*, CRC Press, **2018**, pp. 1.

[25] S. C. Rasmussen, *ChemPlusChem* **2020**, *85*, 1412.

[26] J. Stejskal, M. Trchová, P. Bober, Z. Morávková, D. Kopecký, M. Vrňata, J. Prokeš, M. Varga, E. Watzlová, *RSC Adv.* **2016**, *6*, 88382.

[27] J. Prokeš, M. Varga, M. Vrňata, S. Valtera, J. Stejskal, D. Kopecký, *Eur.* **2019**, *115*, 290.

[28] C. R. Mulzer, L. Shen, R. P. Bisbey, J. R. McKone, N. Zhang, H. c. D. Abruña, W. R. Dichtel, *ACS Cent. Sci.* **2016**, *2*, 667.

[29] E. Vitaku, C. N. Gannett, K. L. Carpenter, L. Shen, H. D. Abruña, W. R. Dichtel, *J. Am. Chem. Soc.* **2020**, *142*, 16.

[30] R. Kushwaha, S. Haldar, P. Shekhar, A. Krishnan, J. Saha, P. Hui, C. P. Vinod, C. Subramaniam, R. Vaidhyanathan, *Adv. Energy Mater.* **2021**, *11*, 2003626.

[31] L.-Q. Mai, A. Minhas-Khan, X. Tian, K. M. Hercule, Y.-L. Zhao, X. Lin, X. Xu, *Nat. Commun.* **2013**, *4*, 2923.

[32] S. Roldán, M. Granda, R. Menéndez, R. Santamaría, C. Blanco, *J. Phys. Chem. C* **2011**, *115*, 17606.

[33] H. Li, J. Chang, S. Li, X. Guan, D. Li, C. Li, L. Tang, M. Xue, Y. Yan, V. Valtchev, *J. Am. Chem. Soc.* **2019**, *141*, 13324.

[34] M. L. Aubrey, J. R. Long, *J. Am. Chem. Soc.* **2015**, *137*, 13594.

[35] H. Chen, H. Tu, C. Hu, Y. Liu, D. Dong, Y. Sun, Y. Dai, S. Wang, H. Qian, Z. Lin, L. Chen, *J. Am. Chem. Soc.* **2018**, *140*, 896.

[36] S. Chandra, T. Kundu, S. Kandambeth, R. BabaRao, Y. Marathe, S. M. Kunjir, R. Banerjee, *J. Am. Chem. Soc.* **2014**, *136*, 6570.

[37] A. V. Volkov, H. Sun, R. Kroon, T.-P. Ruoko, C. Che, J. Edberg, C. Müller, S. Fabiano, X. Crispin, *ACS Appl. Energy Mater.* **2019**, *2*, 5350.

[38] Q.-X. Wang, C.-Y. Zhang, *Macromol. Rapid Commun.* **2011**, *32*, 1610.

[39] B. Dhara, S. S. Nagarkar, J. Kumar, V. Kumar, P. K. Jha, S. K. Ghosh, S. Nair, N. Ballav, *J. Phys. Chem. Lett.* **2016**, *7*, 2945.

[40] S. Kandambeth, J. Jia, H. Wu, V. S. Kale, P. T. Parvatkar, J. Czaban-Jóźwiak, S. Zhou, X. Xu, Z. O. Ameur, E. Abou-Hamad, A.-H. Emwas, O. Shekhah, H. N. Alshareef, M. Eddaoudi, *Adv. Energy Mater.* **2020**, *10*, 2001673.

[41] Y. Wang, G. A. Sotzing, R. Weiss, *Chem. Mater.* **2008**, *20*, 2574.

[42] P. Li, X. Li, Y. Guo, C. Li, Y. Hou, H. Cui, R. Zhang, Z. Huang, Y. Zhao, Q. Li, *Adv. Energy Mater.* **2022**, 2103648.

[43] M. Szkoda, K. Siuzdak, A. Lisowska-Oleksiak, *Journal of Solid State Electrochemistry* **2016**, *20*, 563.

[44] A. C. Ramírez-Pérez, J. Quílez-Bermejo, J. M. Sieben, E. Morallón, D. Cazorla-Amorós, *Electrocatalysis* **2018**, *9*, 697.

[45]   M. Šetka, R. Calavia, L. Vojkůvka, E. Llobet, J. Drbohlavova, S. Vallejos, *Sci. Rep.* **2019**, *9*, 1.

[46]   X. Yang, J. Yang, J. Khan, H. Deng, S. Yuan, J. Zhang, Y. Xia, F. Deng, X. Zhou, F. Umar, *Nano-micro letters* **2020**, *12*, 1.

[47]   S. Kandambeth, V. Venkatesh, D. B. Shinde, S. Kumari, A. Halder, S. Verma, R. Banerjee, *Nat. Commun.* **2015**, *6*, 1.

[48]   L. Li, Q. Yun, C. Zhu, G. Sheng, J. Guo, B. Chen, M. Zhao, Z. Zhang, Z. Lai, X. Zhang, *J. Am. Chem. Soc.* **2022**.

[49]   S. Bi, F. Meng, D. Wu, F. Zhang, *J. Am. Chem. Soc.* **2022**, *144*, 3653.

[50]   C. Li, Z. Mao, H. Chen, L. Zheng, J. Huang, B. Zhao, S. Tan, G. Yu, *Macromolecules* **2015**, *48*, 2444.

[51]   Y. K. Koh, D. G. Cahill, *Phys. Rev. B* **2007**, *76*, 075207.

[52]   R. Van Der Jagt, A. Vasileiadis, H. Veldhuizen, P. Shao, X. Feng, S. Ganapathy, N. C. Habisreutinger, M. A. van der Veen, C. Wang, M. Wagemaker, *Chem. Mater.* **2021**, *33*, 818.

[53]   D.-H. Yang, Z.-Q. Yao, D. Wu, Y.-H. Zhang, Z. Zhou, X.-H. Bu, *J. Mater. Chem. A* **2016**, *4*, 18621.

[54]   H. Duan, K. Li, M. Xie, J.-M. Chen, H.-G. Zhou, X. Wu, G.-H. Ning, A. I. Cooper, D. Li, *J. Am. Chem. Soc.* **2021**, *143*, 19446.

[55]   W. Yan, C. Wang, J. Tian, G. Zhu, L. Ma, Y. Wang, R. Chen, Y. Hu, L. Wang, T. Chen, *Nat. Commun.* **2019**, *10*, 1.

[56]   A. A. Arrieta Almario, R. L. Tarazona Caceres, *Journal of the Chilean Chemical Society* **2009**, *54*, 14.

[57]   B. Pang, R. Köhler, V. Roddatis, H. Liu, X. Wang, W. Viöl, K. Zhang, *ACS omega* **2018**, *3*, 6841.

[58]   J. Lee, P. Srimuk, S. Fleischmann, X. Su, T. A. Hatton, V. Presser, *Prog. Mater. Sci.* **2019**, *101*, 46.

[59]   Z. Dai, C. Peng, J. H. Chae, K. C. Ng, G. Z. Chen, *Sci. Rep.* **2015**, *5*, 1.

[60]   C. Zhong, Y. Deng, W. Hu, J. Qiao, L. Zhang, J. Zhang, *Chem. Soc. Rev.* **2015**, *44*, 7484.

[61]   J. G. Huddleston, A. E. Visser, W. M. Reichert, H. D. Willauer, G. A. Broker, R. D. Rogers, *Green Chem.* **2001**, *3*, 156.

[62]   M. Earle, *Ionic Liquids in Synthesis* **2004**, *45*, 7043.

[63]   S. K. Ujjain, R. Bhatia, P. Ahuja, P. Attri, *PloS one* **2015**, *10*, e0131475.

[64]   F. Wang, X. Wu, X. Yuan, Z. Liu, Y. Zhang, L. Fu, Y. Zhu, Q. Zhou, Y. Wu, W. Huang, *Chem. Soc. Rev.* **2017**, *46*, 6816.

[65]   B. Delley, *J. Chem. Phys.* **2000**, *113*, 7756.

[66]   C. Hua, P. W. Doheny, B. Ding, B. Chan, M. Yu, C. J. Kepert, D. M. D'Alessandro, *J. Am. Chem. Soc.* **2018**, *140*, 6622.

[67]   A. Molina-Ontoria, G. Fernández, M. Wielopolski, C. Atienza, L. Sánchez, A. Gouloumis, T. Clark, N. Martín, D. M. Guldi, *J. Am. Chem. Soc.* **2009**, *131*, 12218.

[68]   Y. Li, J. Chen, C. Zhao, *RSC Adv.* **2017**, *7*, 56676.

[69]   A. Ghoufi, K. Benhamed, L. Boukli-Hacene, G. Maurin, *ACS Cent. Sci.* **2017**, *3*, 394.

[70]   G. Ying, Z. Gui-Lin, W. Jian-Guo, *Chinese J. Inorg. Chem.* **2012**, *28*, 2587.

## Appendix for chapter 3

### A3.1. Synthesis of IISERP-COF30:

Pyridinyl triamine (4,4',4''-(pyridine-2,4,6-triyl)trianiline) (107 mg, 0.3 mmol) and a linear pyromellitic dianhydride (1H,3H-benzo[1,2-c:4,5-c']difuran-1,3,5,7-tetraone) (98 mg, 0.45 mmol), were weighed into a Pyrex tube and were dissolved in NMP (3.0 mL) and mesitylene (3.0 mL) and stirred until a homogeneous yellow colour was observed. To this mixture, 0.3 mL of Isoquinoline was added. Then the Pyrex tube was flash frozen in a liquid nitrogen bath and sealed. The Pyrex tube along with its contents was placed in an oven at 160°C for 5 days and gradually cooled to room temperature over 12 hrs. This yielded about 165 mg of bright yellow coloured solid which was washed with hot DMF, dioxane, MeOH, acetone and THF (80%, isolated yield). This product was also subjected to a Soxhlet extraction using hot DMF/methanol/THF as solvent and filtered solid was characterized by $^{13}$C solid state NMR (Figure S7) and IR (Figure S8).
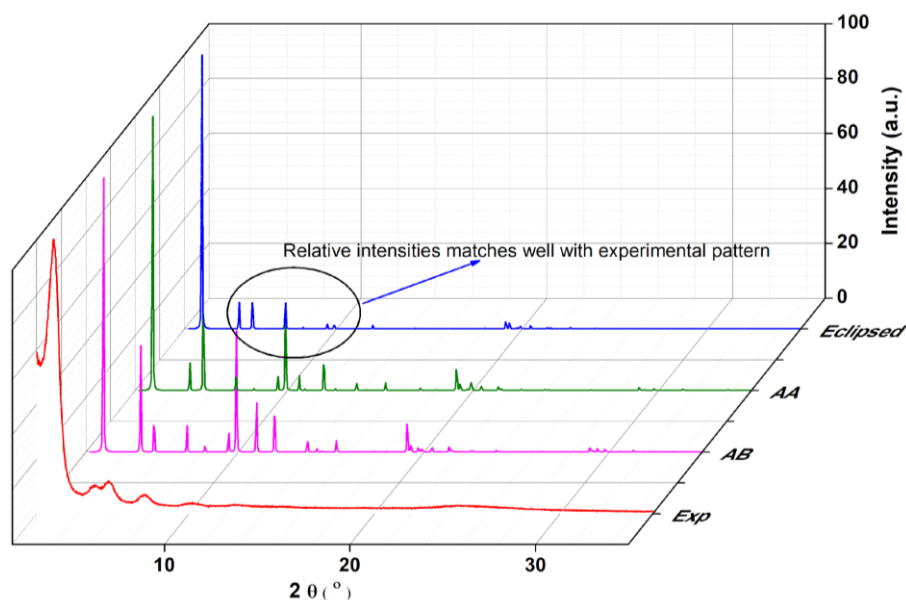


**Figure A3.1.** Comparisons of the experimental Powder X-ray Diffraction (PXRD) with the simulated PXRD calculated for different configurations of the modeled COF. The circle denotes the 2θ region where the relative intensities of the eclipsed configuration matches much better with the experimental PXRD compared to the other staggered configurations.

### A3.2. Synthesis and characterization of the Ppy-I₃ polymer:

To the 5 mL pyrrole (Py) in a glass tube, 10mL of a I$_2$ in hexane (0.05 M L$^{-1}$) was added dropwise to induce polymerization at –16 °C for 48 hours and kept standing for 24 hours at room temperature. The solid polymer obtained was washed with ample hexane to remove excess iodine. Then it was washed with o-DCB and m-cresol to dissolve polypyrrole oligomers. In the end, the polymer was washed with hexane and dried in the oven for 6 hours and used as it is for further characterization.

The PXRD shows the typical polymeric nature of polypyrrole.[1] [2] The IR band centred at 1704 cm$^{-1}$ (ring –C=N asymmetric); 1510 cm$^{-1}$ (ring –C=C symmetric); 1174 and 1023 cm$^{-1}$ (-C-N stretching); 3860, 3740, 3610 cm$^{-1}$ (polypyrrole –NH) confirm the formation of the polypyrrole polymer.[3]

The sharp $^{13}$C CPMAS signals around 23 (a) and 30 ppm (b) originate from the carbon connected to the protonated nitrogen of the polypyrrole. The less intense signal at 70 ppm (c) originates from the carbon connected to the non-protonated nitrogen of the quinoid part of the polypyrrole structure. The shoulder signal around 125 (d) ppm is attributed to fully conjugated carbons in the polymer backbone.[4]

The absorption peak at 620 nm in UV-Visible spectra signifies possible charge transfer between positively charged Ppy and $I_3^-$ .[5] This lowers down the overall band gap of the polypyrrole to 1.46 eV. The XPS of Ppy showing the peaks from I 3d peaks assigned to $I_3^-$. Each of the iodine peak in XPS consists of the binding energy of I-I bond of $I_3^-$ species and also a terminal $I^-$ (of $I_3^-$) interaction with $NH^+$ of polypyrrole. The distance between the I 3d$_{5/2}$ and I 3d$_{3/2}$ is 11.5 eV which remained constant even when we synthesized the polypyrrole in presence of the COF host. If $I^-$ solely presents as a counter anion, the binding energy for I-I should not even appear in the XPS. This indicates the presence of $I_3^-$ which is the energetically stable form of the polyiodide species. Also the C 1s XPS peak centred at 288.5 eV for C-NH$^+$---$I_3^-$ confirms the ionic interaction between Ppy and $I_3^-$. The N 1s XPS peak centred at 400 eV also shows similar interaction of pyrrole nitrogen with $I_3^-$. The morphology analysis by FESEM shows tiny nanosized particles are connected to each other to construct the threads of polymer. The absence of any host material could not control the growth of the polymer in a linear way. A lot of branching with different directional growth has been noticed. EDX shows homogeneous distribution of carbon, nitrogen and iodine throughout the skeleton of these threads of polypyrrole.
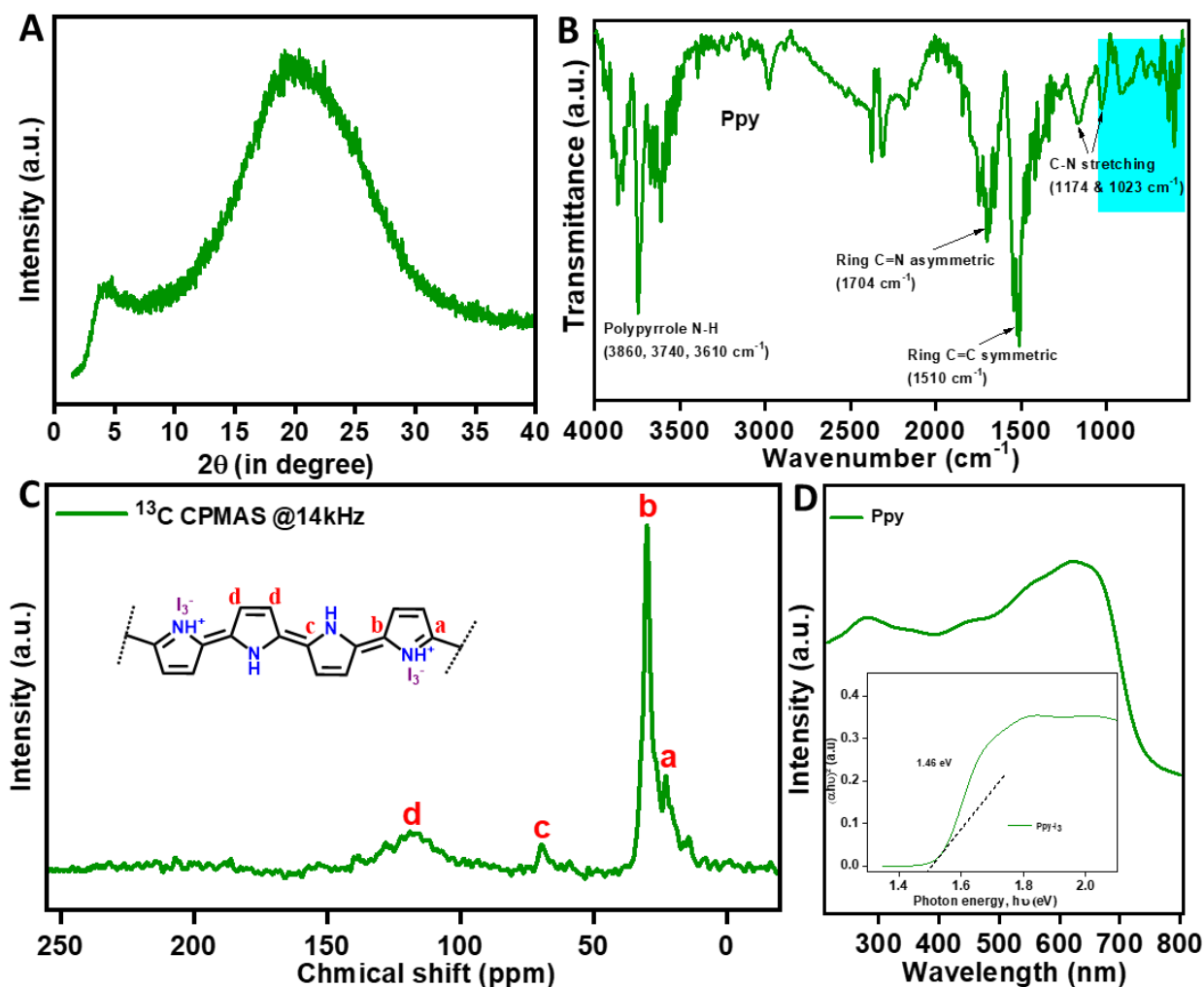
**Figure A3.2: A.** PXRD, **B.** FT-IR, **C.** $^{13}$C SSNMR, **D.** UV-Visible with Tauc plot (inset) of freshly prepared polypyrrole.
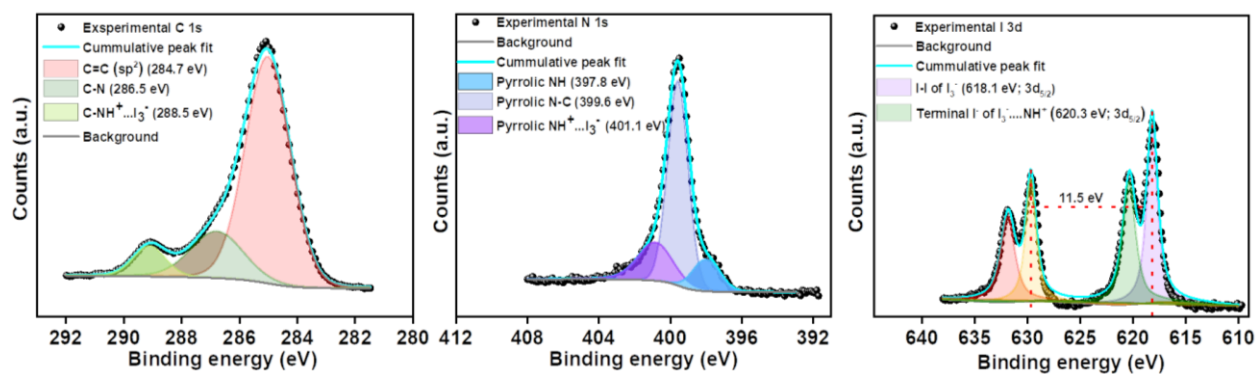


**Figure A3.3:** C 1s, N 1s and I 3d (left to right) XPS analysis of freshly prepared polypyrrole and assigned peaks
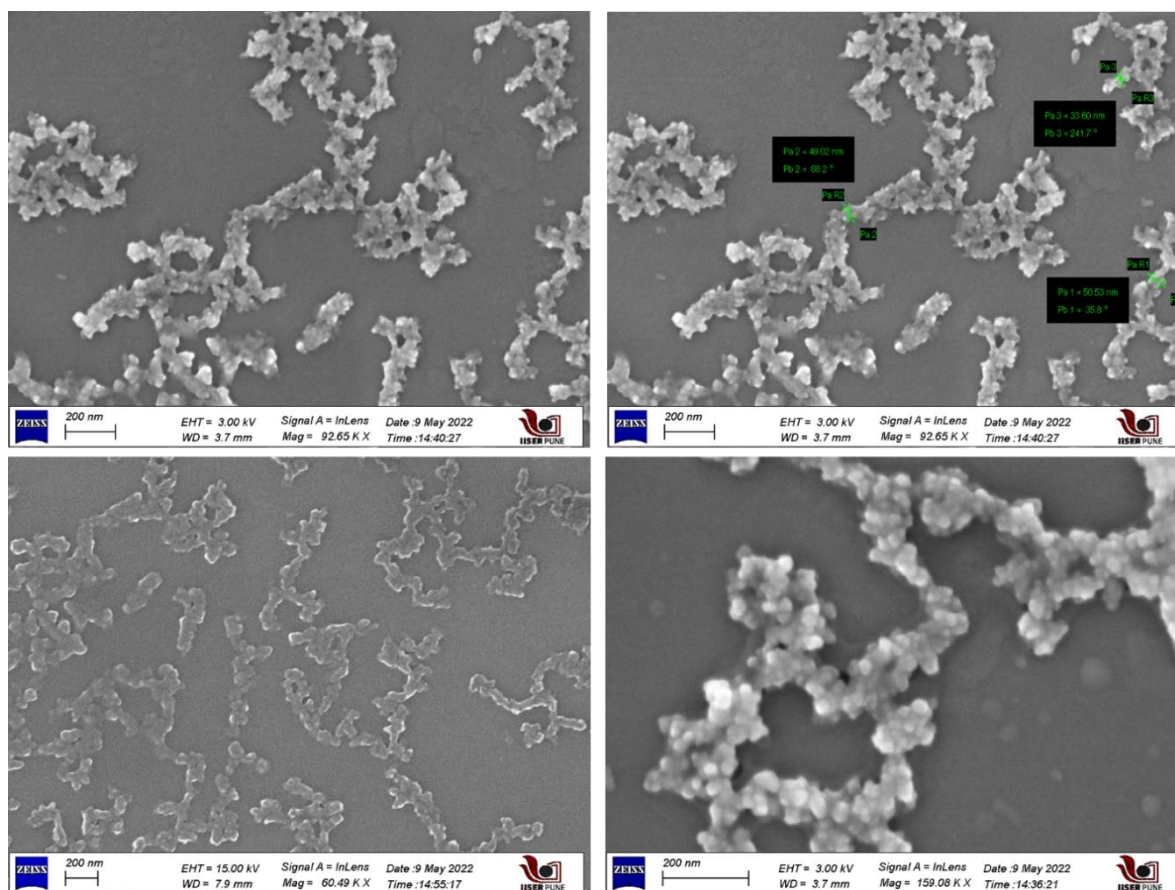
**FigureA3.4:** FE-SEM images of Polypyrrole polymers in different magnifications.

Notes on neat Polypyrrole synthesis: The attempted polypyrrole synthesis without having COF-host leads to thicker threads (30 nm to 70 nm) formation, consisting of small particles of Ppy and induces a lot of branching therefore.[6] But COF as a host material is expected to restrain its branching growth (Figure A3.2-A3.4). This template synthesis could potentially restrict rotational and vibrational motions leading to the gradual growth of the unidirectional polymer inside the porous nano-channel of the COF (Scheme 3.3, Figure 3.3).

| Element | Weight % | Atomic % |
|---------|----------|----------|
| C K | 69.72 | 84.28 |
| N K | 13.28 | 13.77 |
| I L | 16.99 | 1.94 |
| Totals | 100.00 | |
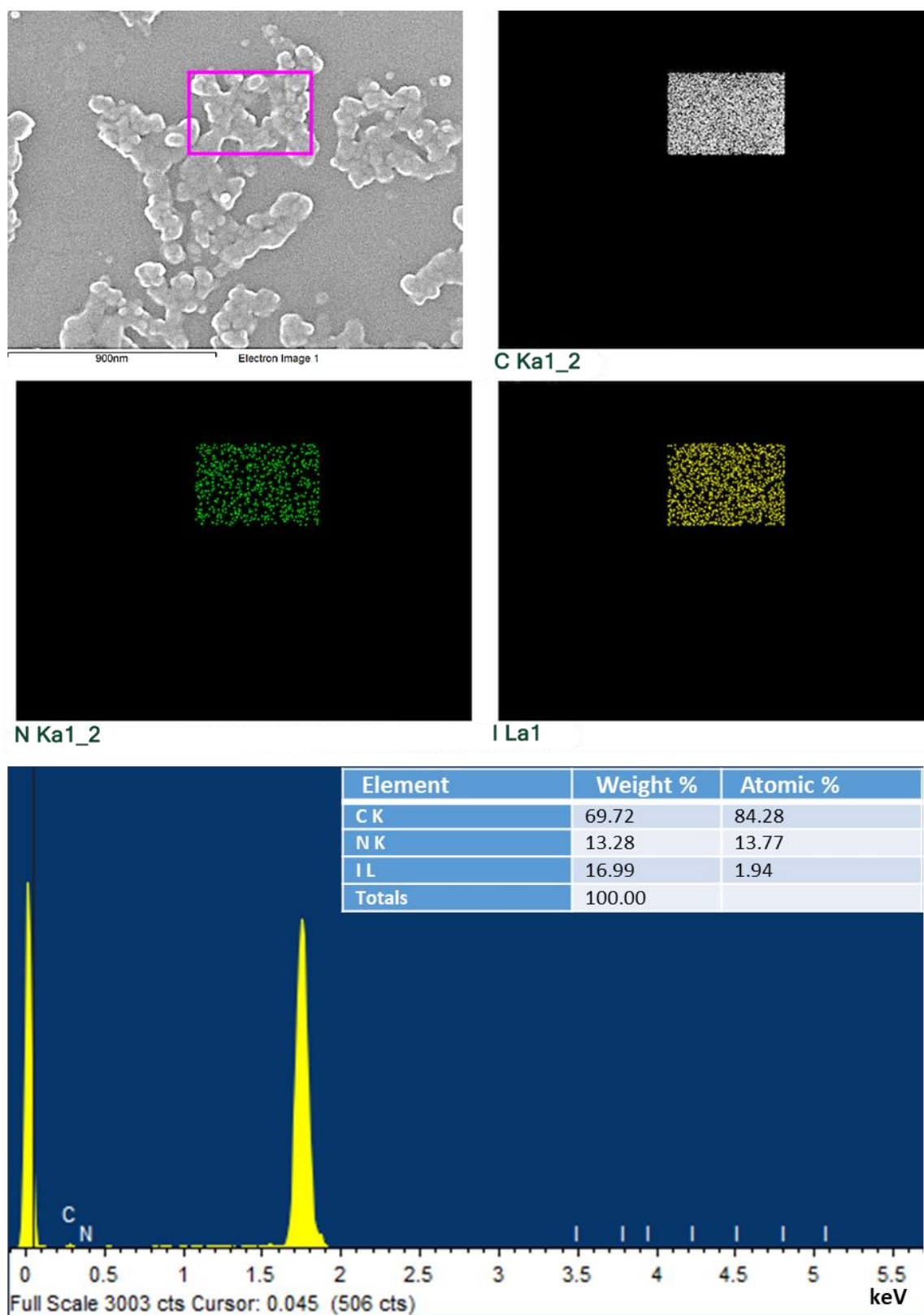
**Figure A3.5:** EDX analysis on portion of the polypyrrole threads.
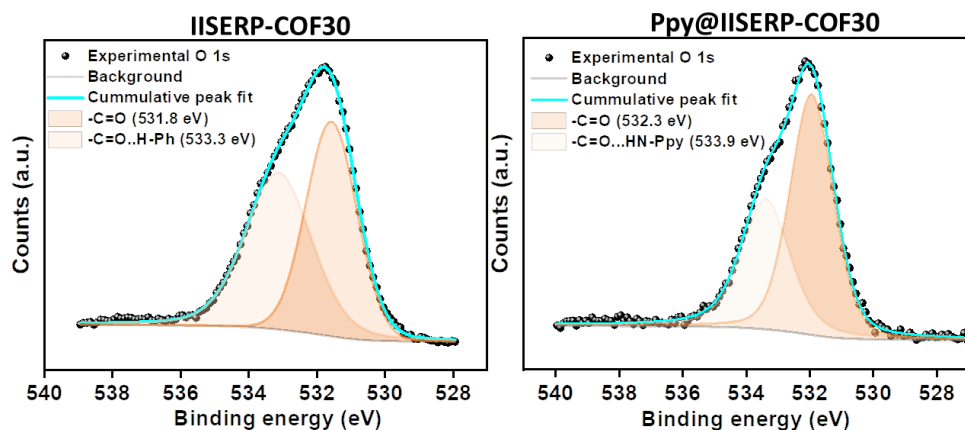
**Figure A3.6:** The comparison of O 1s XPS of Ppy@COF with as made COF.
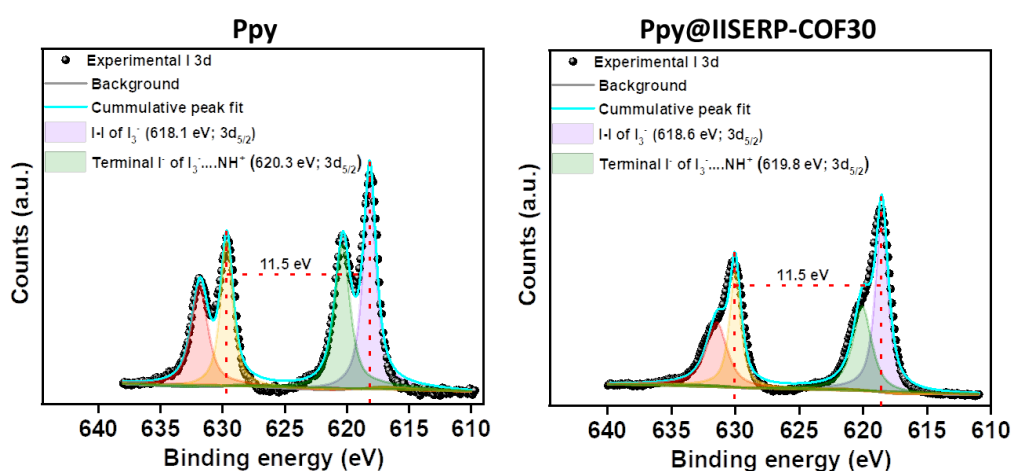


**Figure A3.7:** The comparison of I 3d XPS of Ppy@COF with as made Ppy.[8]
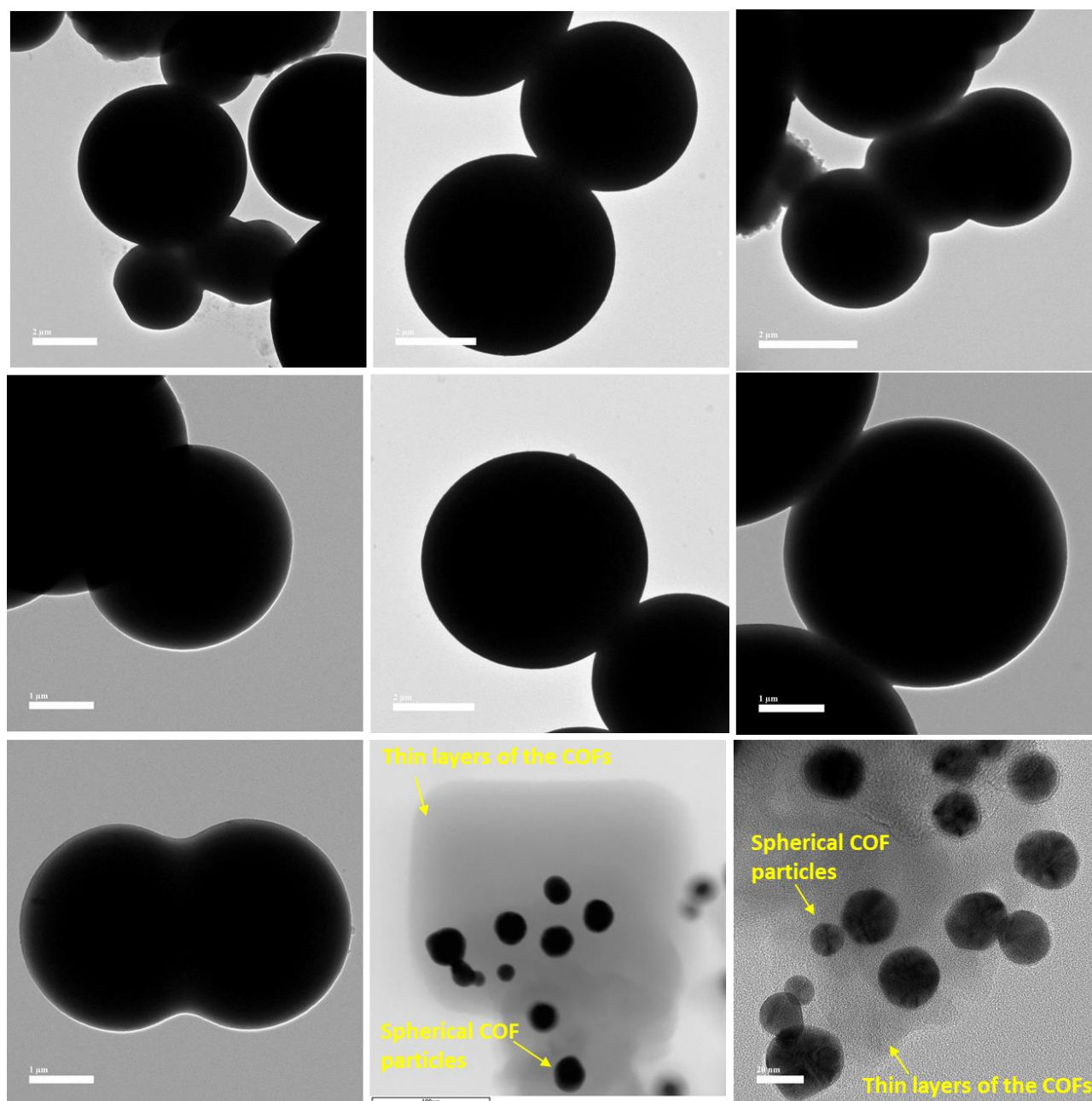
**Figure A3.8:** Thin layers of the COF and wrapped-up COF flakes constructing spherical balls. The size of these balls varies from microns (2 µm) to nanometre (20 nm) range.
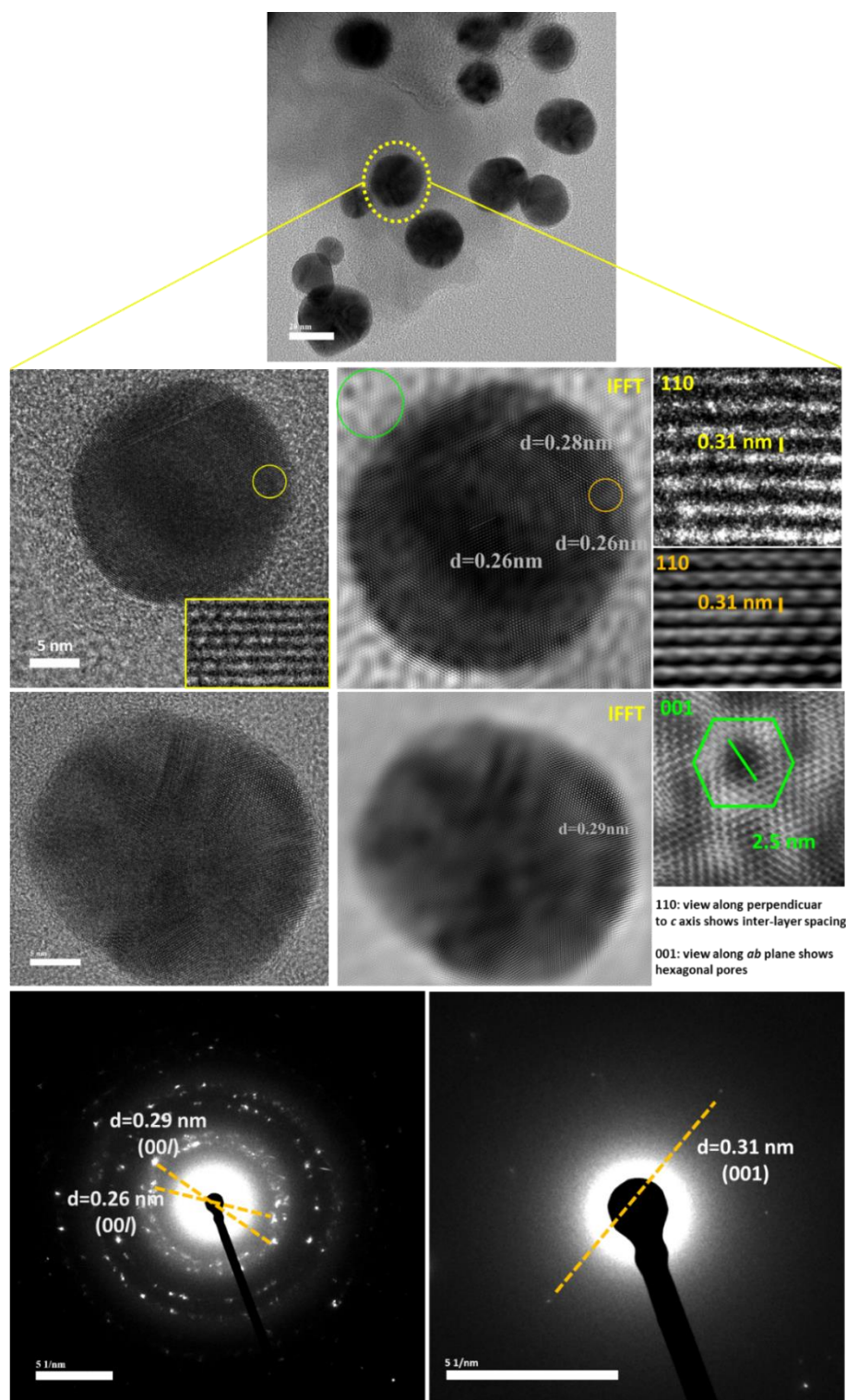
**Figure A3.9:** A transparent thin spherical particle of the COF has been focused for HRTEM imaging. The spherical dark images are made-up of wrapped COF flakes and this exposes the interlayer stacking. This stacks can be better seen from the HRTEM images. Meanwhile the thin flakes at the background display the hexagonal pores whose sizes match the modelled structure. (Below) The corresponding SAED pattern shows the lattice fringes observed on the flakes.
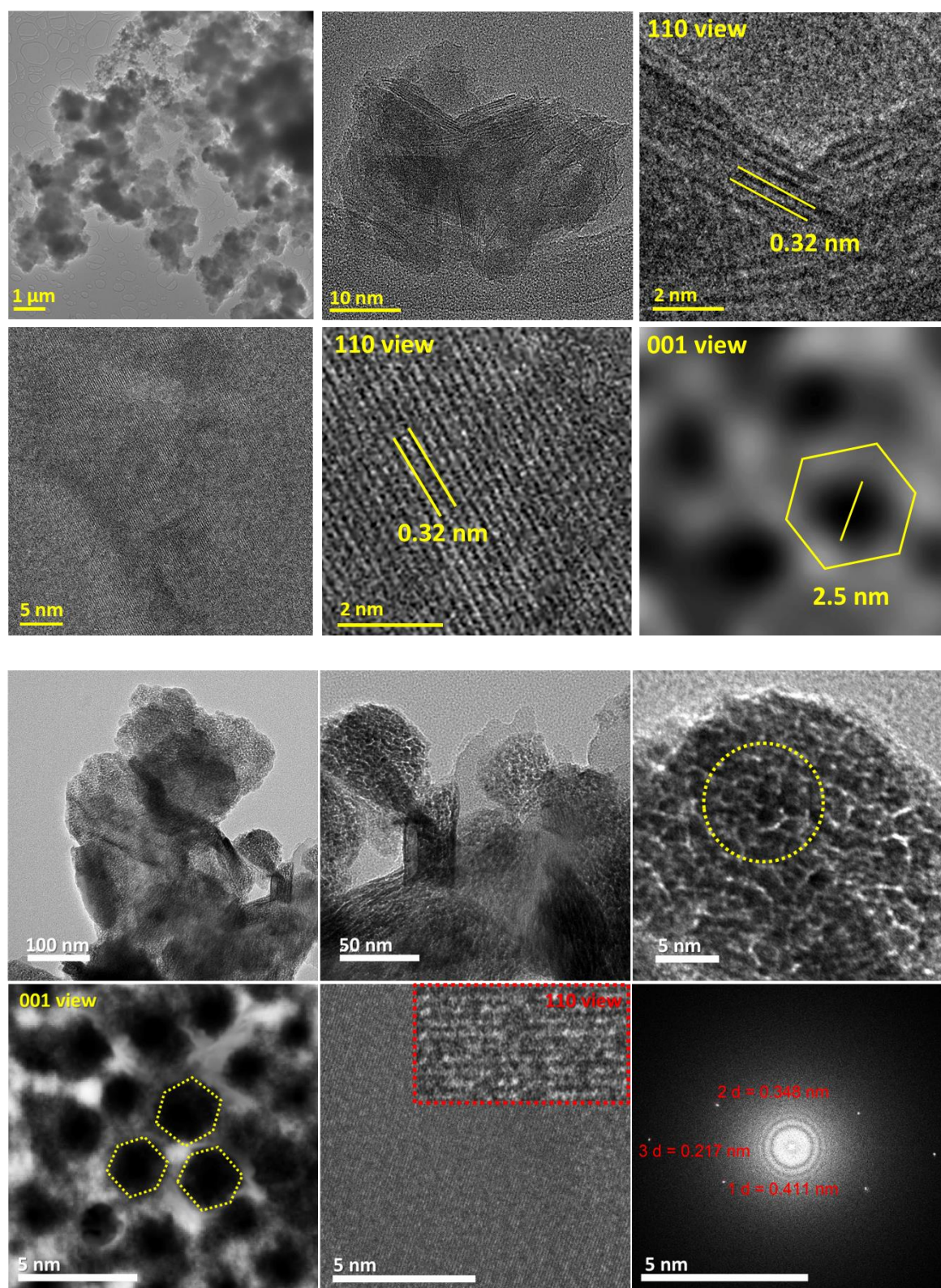
**Figure A3.10:** The big spheres of COF particles were opened up into constructing COF flakes by vigorous probe sonication in ethanolic dispersion of COF. The layer distances and hexagonal pores were detected well in these smaller flakes.
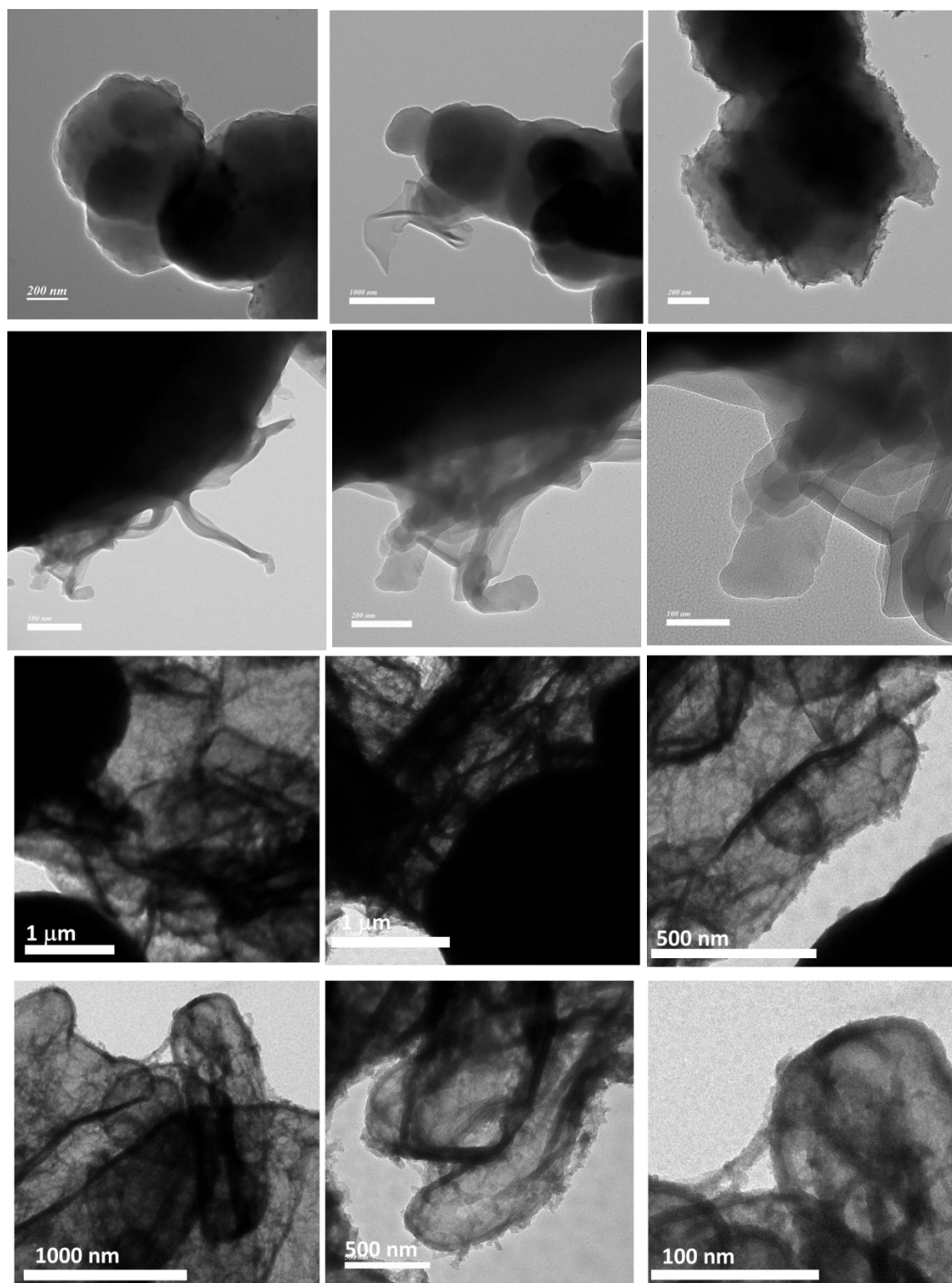
**Figure A3.11:** HRTEM images of the Ppy@COF. A few COF flakes are opened up from the big spheres and these expose loading of polypyrrole-thread.
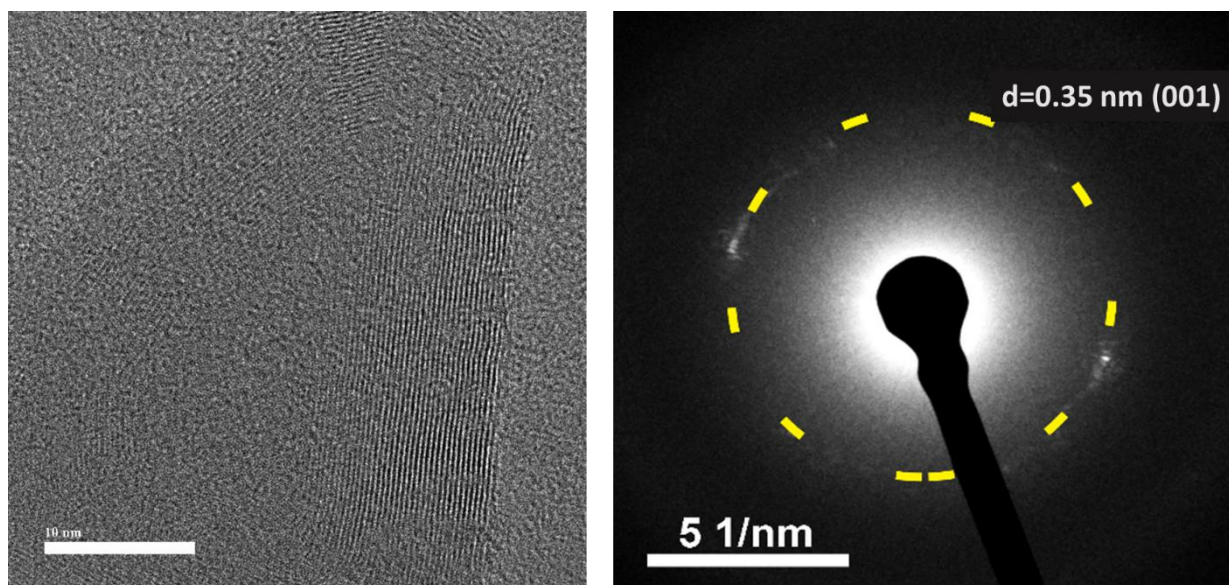
**Figure A3.12: (Left)** HRTEM images of the Ppy@COF showing the lattice fringes. **(Right)** The SAED pattern of Ppy@COF showing the d-spacing between layers.

Electrodes were fabricated by coating an ethanolic dispersion of the COFs on carbon paper. Coating was maintained over a $1 \times 1$ cm$^2$ area. Then it was dried in vacuum for 24 hrs. The electrodes were subjected to CV measurements in a non-aqueous electrolyte system (*t*-butyl ammonium hexafluorophosphate dissolved in acetonitrile, $^t$BuNH$_4$Br$_6$/ACN) under argon atmosphere. A nonaqueous Ag/Ag$_+$ reference electrode and platinum flag counter electrodes were used. CV measurements were carried in 50 mV/s scan rate from –1.2 to 2.0 V potential window. Following the convention, the highest oxidation potential has been taken to evaluate the position of the HOMO and lowest reduction potential to evaluate the position of the LUMO.[9]

**COF:**

$E_{HOMO}$ = - [$E_{OX} - E_{(Fc/Fc+)}$+4.8] eV= -(1.74 -0.58 +4.8) eV = 5.96 eV

$E_{LUMO}$ = - [$E_{Red} - E_{(Fc/Fc+)}$+4.8] eV= -(-0.42 -0.58 +4.8) eV = 3.8 eV

$E_{Ag/Ag+ \text{(non-aqueous)}}$ vs. NHE: 0.696 V and $E_{(Fc/Fc+)}$ : 0.58 V

$E_{bandgap}$ = $E_{HOMO} - E_{LUMO}$ = 2.16 eV

**Ppy@COF**:

$E_{HOMO}$ = - [$E_{OX} - E_{(Fc/Fc+)}$+4.8] eV= -(1.26 -0.58 +4.8) eV = 5.48 eV

$E_{LUMO}$ = - [$E_{Red} - E_{(Fc/Fc+)}$+4.8] eV= -(-0.31 -0.58 +4.8) eV = 3.91 eV

$E_{Ag/Ag+ \text{(non-aqueous)}}$ vs. NHE: 0.696 V and $E_{(Fc/Fc+)}$ : 0.58 V

$E_{\text{bandgap}} = E_{HOMO} - E_{LUMO} = 1.57$ eV

**$E_{HOMO} = - [EOX – E(Fc/Fc+) + 4.8]$ eV**

**$E_{LUMO} = - [ERed – E(Fc/Fc+) + 4.8]$ Ev**

**$E_{Ag/Ag+ \text{(non-aqueous)}}$ vs. NHE: 0.696 V and $E_{(Fc/Fc+)}$ : 0.58 V**

Where, NHE: Normal Hydrogen Electrode

SCE: Saturated Calomel Electrode

Fc/Fc+ : Ferrocene/Ferrocenium ion couple

## A3.3. Electrochemical measurement of Polypyrrole.

We also performed the CVs and GCD in acidic electrolyte for the neat polypyrrole using a three-electrode setup (Figure S31). The setup was constructed with polypyrrole-coated glassy carbon as a working electrode, platinum wire as the counter electrode, and Ag-AgCl as the reference electrode. The CV data analysis brings more perceptions to the redox activity of the polypyrrole chains. This polymer's neutral nitrogen centers also undergo facile protonation in positive potential (at 0.05 V; R4), similar to Ppy@COF (http://dx.doi.org/10.4067/S0717-97072009000100004). In addition, the protonated Ppy-$I_3^-$ polymer thread's added cationic-charge centers induce the interaction of the $SO_4^{2-}$ with polypyrrole in the negative potential region, too (at 0.37 V; R5). This implies withdrawing the electron density from the polypyrrole-derived working electrode, Figure S31A). The presence of these additional redox reactions (R4 and R5) also in Ppy@COF certainly enhances the charge storing capacity of the composite system. With the increase in the scan rate, the current density of these redox reactions also increases. This confirms the diffusive type ionic interaction of $H^+$ with the polypyrrole (Figure S31B). However, due to its high conducting behaviour and lack of a structured surface area, polypyrrole quickly dissipates the applied electron density. Hence during the discharging it shows abrupt dissipation of charge (Figure S31C).

## A3.4. Electrochemical measurement of COF and Ppy@COF
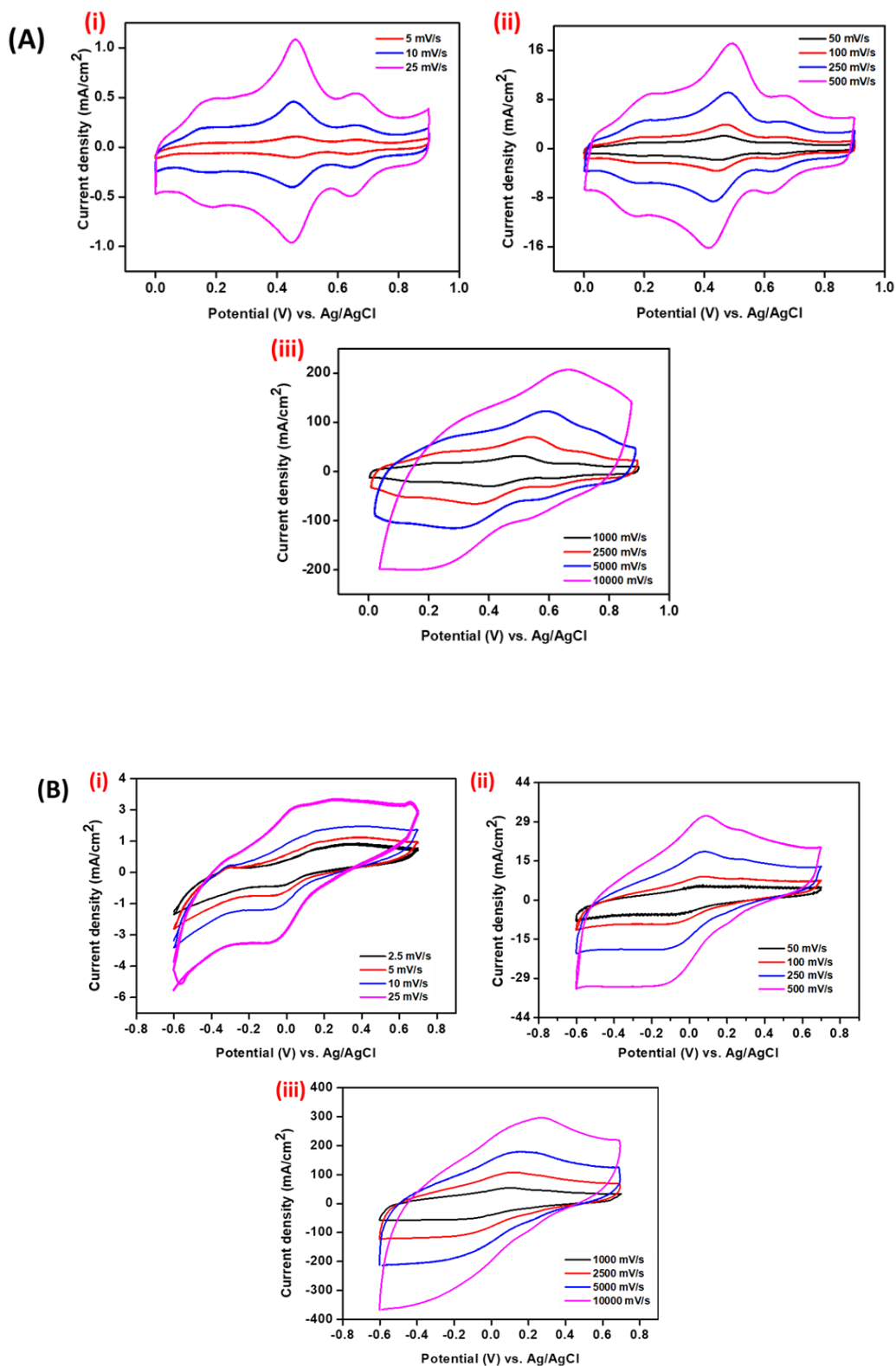


**Figure A3.13:** Different scan rate Cyclic Voltammograms (CV) of **A.** IISERP-COF30 and **B.** Ppy@COF in aqueous acid electrolyte in liquid state.
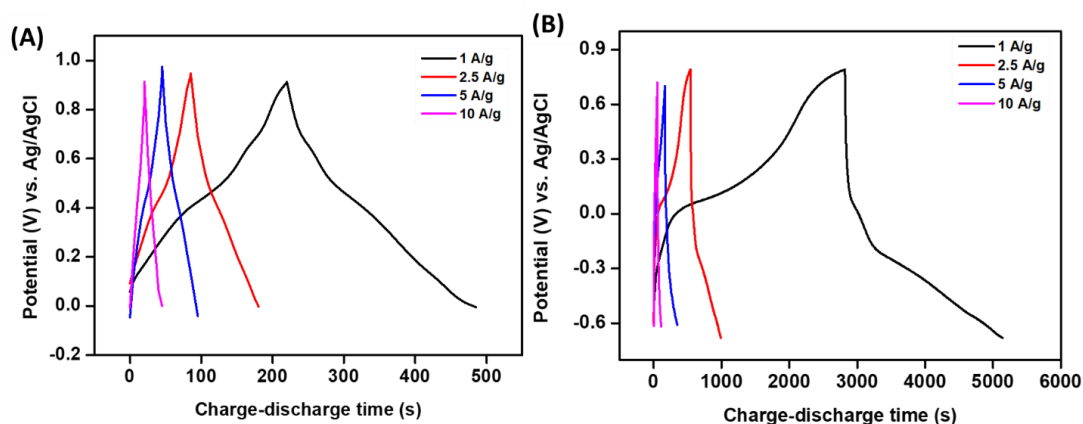
**Figure A3.14:** Charge-discharge curves at different current densities for **A.** COF and **B.** Ppy@COF in aqueous acid electrolyte in liquid state.
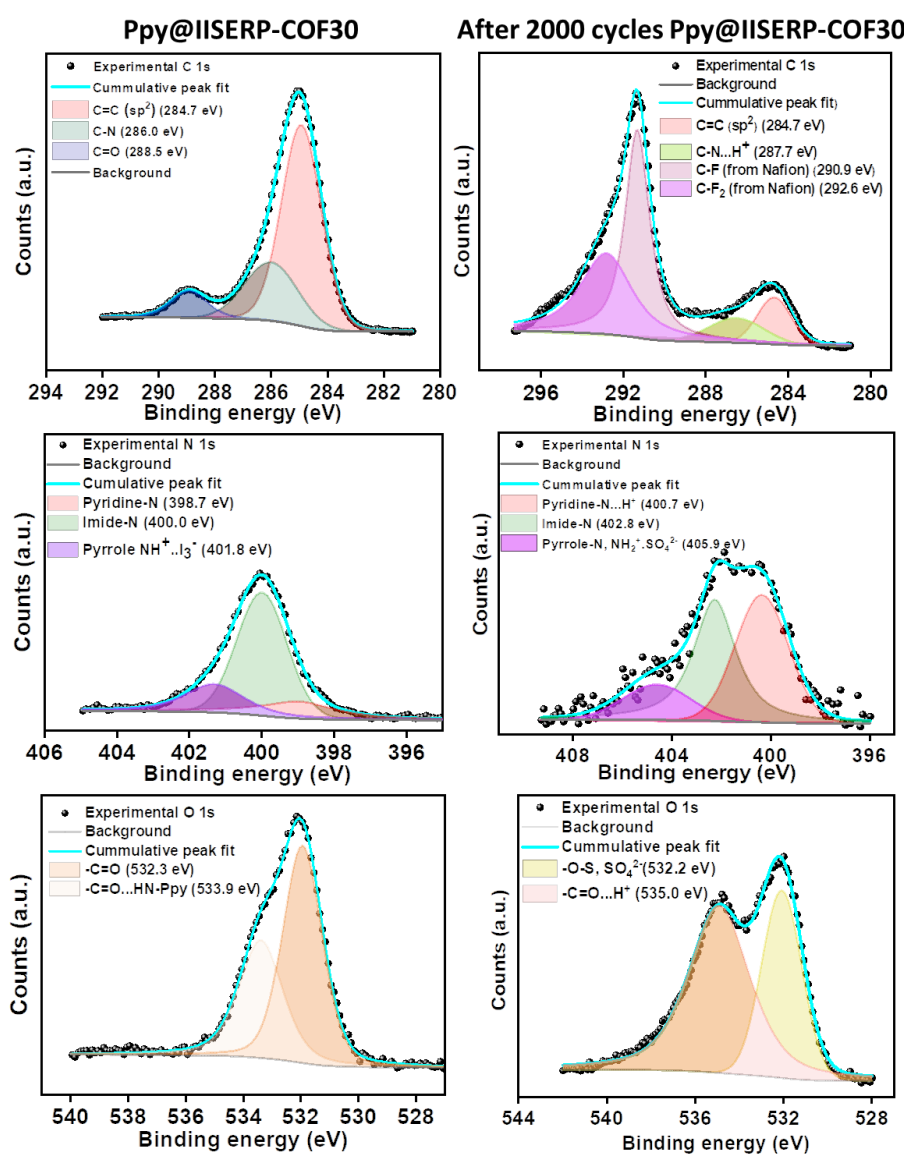


**Figure A3.15:** The C 1s, N 1s and O1s XPS data analysis of Ppy@COF before and after 2000 cycles showing the interaction of H⁺ with different functional groups.
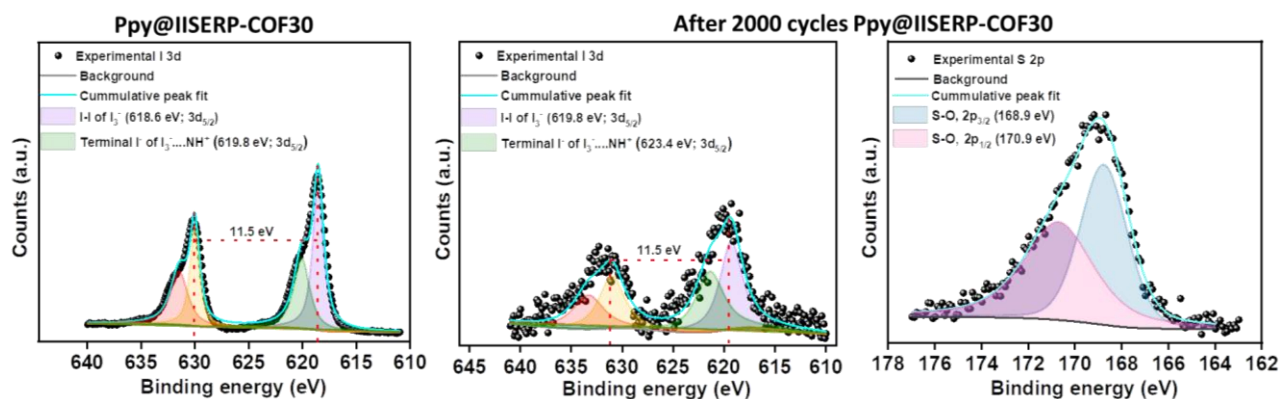
**Figure A3.16:** The I 3d and S 2p XPS data analysis of Ppy@COF before and after 2000 cycles showing $SO_4^{2-}$ incorporation.

## 14. Electrochemical measurements in acid-gel electrolyte:
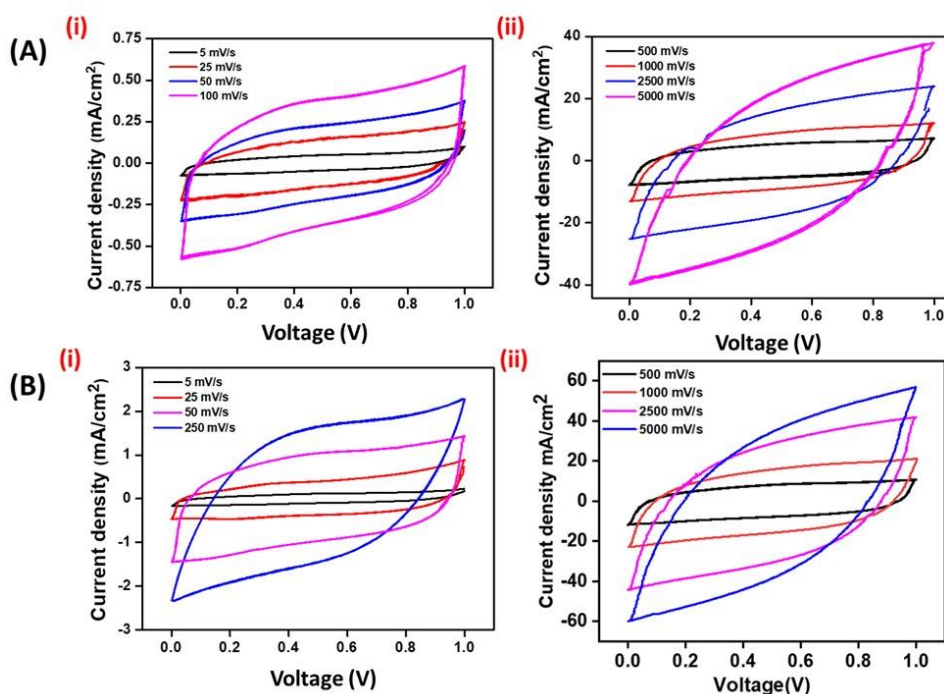


**Figure A3.17:** Different scan rate CVs of **A.** COF and **B.** Ppy@COF in acidic gel electrolyte system.
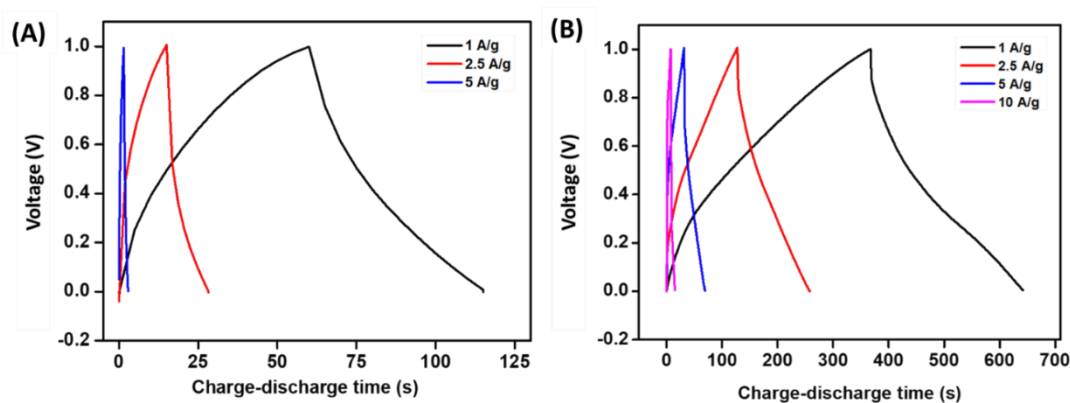


**Figure A3.18:** Charge-discharge curves at different current densities for A. IISERP-COF30 and B. Ppy@COF in acidic gel electrolyte system.
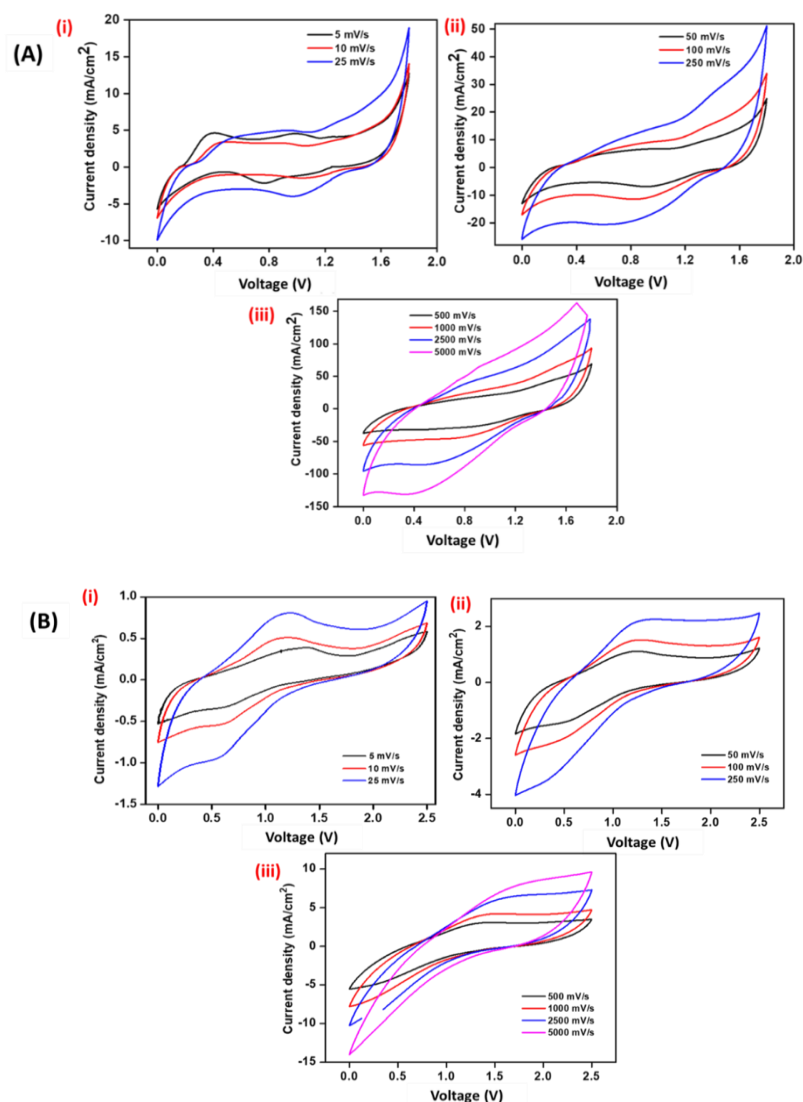
**Figure A3.19:** Different scan rate CVs of Ppy@COF in A. 1M tetraethyl NH4+BF4- electrolyte. B. EMIMBF4 gel-electrolyte systems.
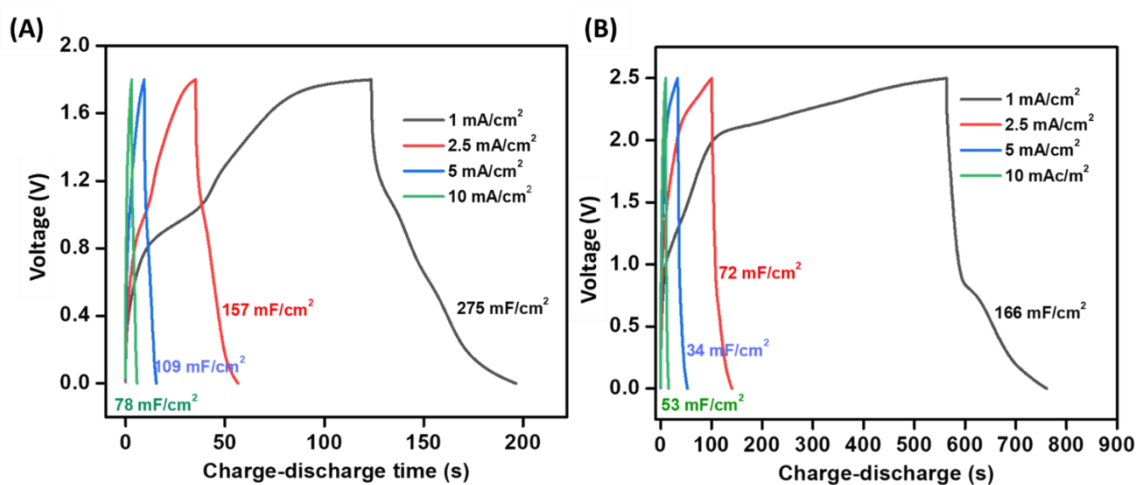


**Figure A3.20:** Charge-discharge curves at different current densities for Ppy@COF in **A.** 1M tetraethyl $NH_4^+$ $BF_4^-$ electrolyte. **B.** EMIMBF$_4$ gel-electrolyte systems.
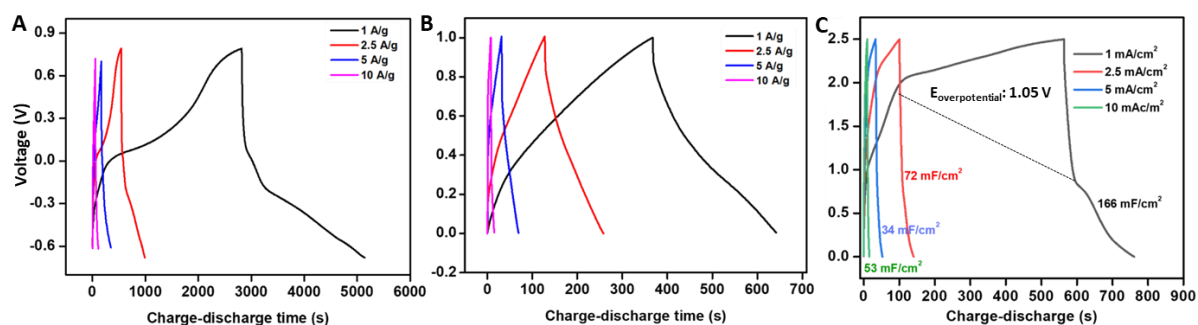
**Figure A3.21:** The comparison of GCD plot of Ppy@COF in **A.** liquid $H_2SO_4$ electrolyte. **B.** PVA-$H_2SO_4$ gel-electrolyte. **C.** $EMIMBF_4$ electrolyte.

Having carbon-free active material makes the post-cycle characterization more steadfast. The Ppy@COF, scratched from the device, shows a decrease of crystallinity from 200 to 2000 cycles. However, the intensity ratio of the first two peaks remains intact, and the amorphous hump becomes a bit prominent; we expect some disruption of the ordered structure of the COF after multiple cycles (Figure S43 A). Nevertheless, we confirmed the chemical integrity of the sample, even after 2000 cycles from the IR and UV-Visible spectra (Figure S43 B and C). From the FESEM, we find that the electrolyte ion percolation through the Ppy@COF-spheres opens it up into flakes (Figures S43 D (i)-(ii); Figure S44). Interestingly the homogeneous distribution of sulfur from $SO_4^{2-}$ species is seen from EDX analysis of the Ppy@COF subjected to 2000 cycles which augments the compositional ruggedness evidenced by the XPS spectra of the post-cycle sample (Figure 43 D(iii); Figure S34, Figure S35 and Figure S45). These observations from the cycled sample affirm the COF-derived electrodes as promising charge-storage candidates.
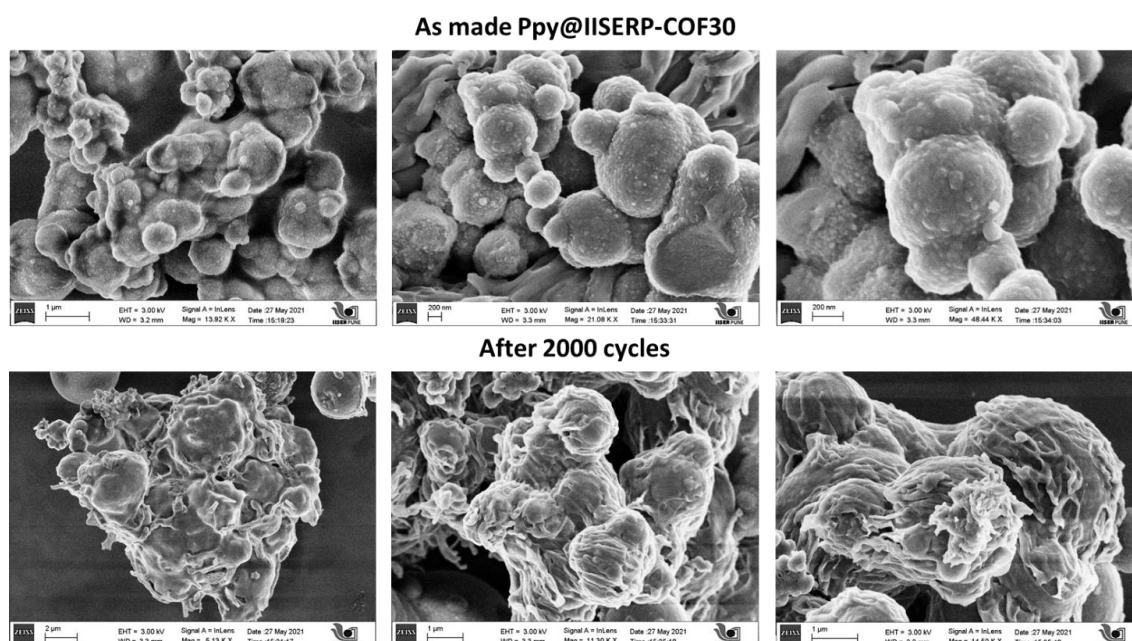


**Figure 3.22:** The FESEM images of Ppy@COF before and after GCD cycling.

| Element | Weight % | Atomic % |
|---------|----------|----------|
| C K | 53.47 | 69.76 |
| N K | 6.46 | 7.22 |
| O K | 20.29 | 19.87 |
| S K | 1.93 | 0.95 |
| I L | 17.84 | 2.20 |

| Elements | Weight % | Atomic % |
|----------|----------|----------|
| C K | 50.19 | 70.77 |
| N K | 3.98 | 4.82 |
| O K | 19.04 | 20.16 |
| S K | 1.72 | 0.91 |
| I L | 25.07 | 3.35 |



| Elements | Weight % | Atomic % |
|----------|----------|----------|
| C K | 54.77 | 75.23 |
| N K | 4.64 | 5.46 |
| O K | 14.83 | 15.29 |
| S K | 1.73 | 0.89 |
| I L | 24.03 | 3.12 |
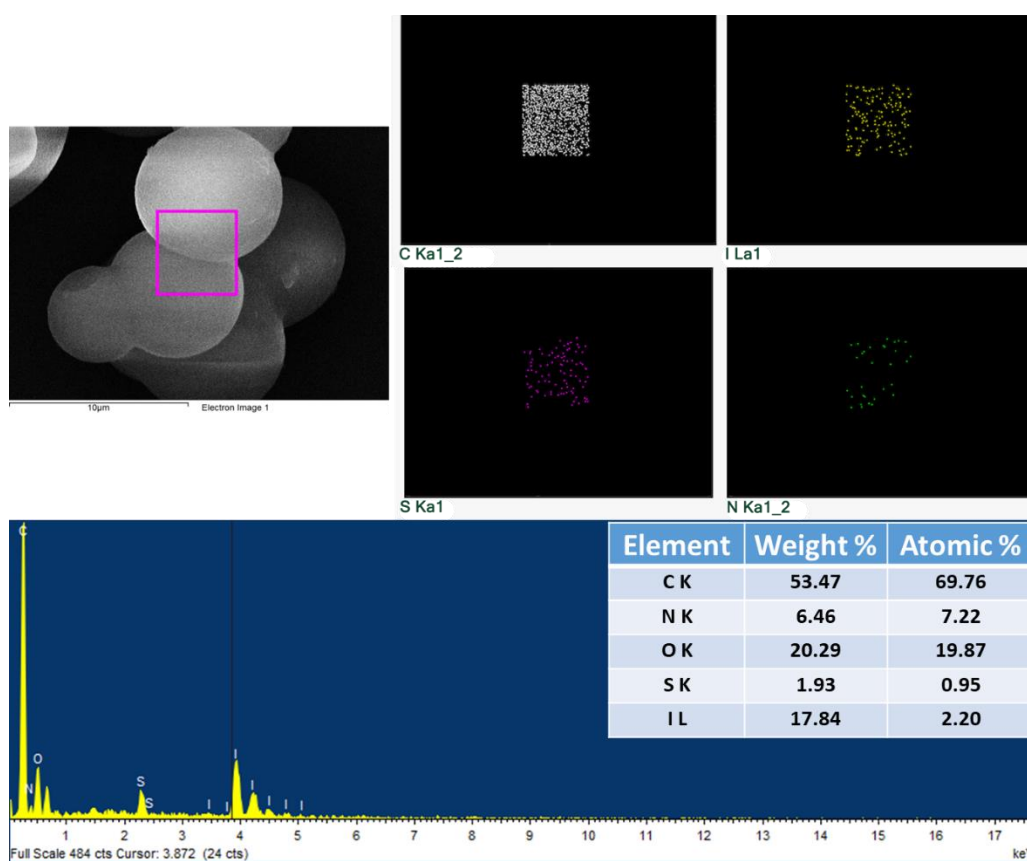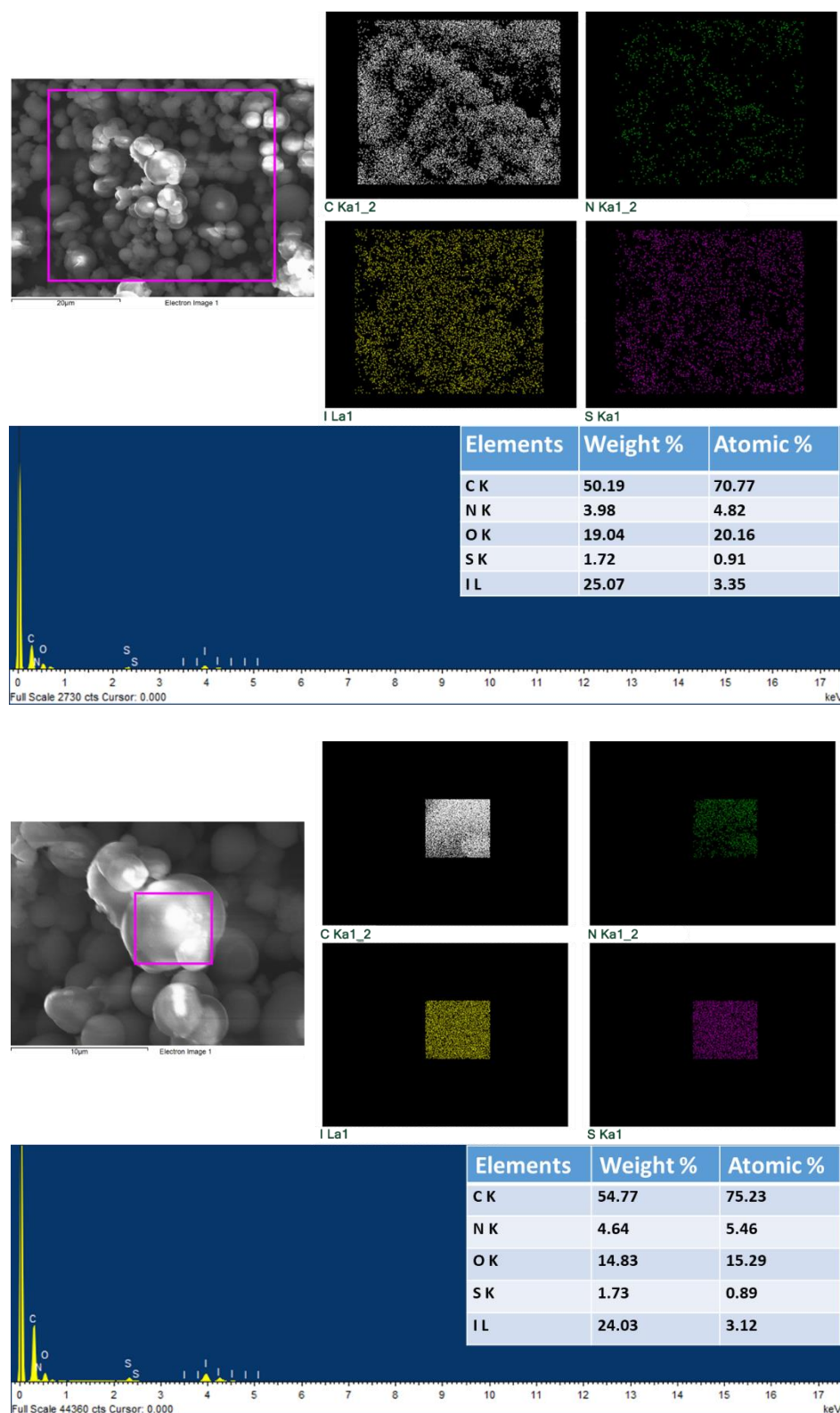
**Figure 3.23:** The EDX analysis of Ppy@COF in different portions of the sample after 2000 GCD cycles.

## A3.5. Computational details:

All calculations were performed using the different packages implemented in the Materials Studio V8 (*Accelrys Program*). Simulation of the lowest energy structural configuration: All calculations were spin polarized and dispersion corrected.

***To solve the structure of the COF***, an initial structure was developed via atomic-simulation using the Materials Studio V.8.0. Both the eclipsed and staggered configurations were simulated. The comparison of the simulated PXRDs against the experimental PXRD revealed that the eclipsed configuration matched better (Figure S4). The eclipsed model with pore-size of ~33.1 Å (not factoring the vander Waal radii of atoms) explains the meso porosity observed in the COF (experimental: 27 Å). Hence considering this configuration to be the initial model, we performed Pawley refinements employing the experimental PXRD pattern of the COF. An excellent fit was obtained with 110, 200, 220 reflections being prominent. Importantly, the 001 reflection occurring at 24.8 matches well with the interlayer separation of 3.53 Å, suggestive of strong p-stacking. This Pawley refined structure was used in all other calculations. The total energy of this refined COF was obtained using a rigorous CASTEP routine, which yielded the stable structure. CASTEP optimization parameters: LJ dispersions were used to determine van der Waals interactions, and self-consistent charges were used to determine the Coulombic interaction between partial atomic charges. UFF-based Lennard-Jones dispersion corrections were included in Energy, Force and Displacement calculations and the cell was optimized. All calculations are at 0K and were spin-unrestricted, adopting the formal spin as the initial spin. The smearing parameter of 0.005 to 0.02 Ha was applied. The dispersion corrected DFT calculations employed a plane wave basis cut-off of 500 eV. For our dispersion-corrected DFT (DFT-D) optimizations, we used Generalized Gradient Approximation (GGA) for calculating the exchange and the correlation energies and employed the Perdew-Wang 91 (PW91) functional. Pulay density mixing scheme were used. The total energy/eigen energy tolerance was kept high at a value of $0.5 \times 10^{-6}$ eV. The total energy of the refined IISERP-COF30's structure stabilized at -19564 eV/unit cell at 0K. Space group: C222; a = b = 37.2929, c = 3.5393 Å; g = 120.0. Formula: $C_{76}H_{24}N_8O_{12}$, M.wt. = 1241.1 (IISERP-COF30).

***For the Ppy@COF***, the COF framework was kept frozen and the Ppy chains were freely dispersed into it using Simulated annealing routine (See below). The COF was not relaxed considering the fact that the experimental PXRD pattern of the Ppy@COF sample did not show any appreciable peak shifts when compared to that of the pristine COF. Final structure was optimized using periodic DFT embedded in the CASTEP module. Same parameters as used for the COF energy optimizations were used. The total energy of the refined Ppy@COF structure was -54908 eV/unit cell at 0 K. Formula: $C_{204}H_{34}N_{40}O_{12}$, M.wt. = 3236.77 (Ppy@IISERP-COF30).

***Parameters employed for the Simulated Annealing:*** Automatic temperature control and 100000 cycles/cell were used to optimize the structure. Universal force field (UFF) in conjugation with a Qeq charge equilibration method was employed for the geometry optimization. However, we noticed that applying the equilibration (Qeq) did not significantly affect the final configurations. No constraints were placed during the optimizations. The optimized structure of the Ppy@COF had relative energy higher than the empty COF. We obtained uniform loading of 4 chains per unit cell of the COF and the chains arranged in and out of the COF plane.

Independently, all the structures of the Dimer and PPy Chain were geometry optimized using a DMOL$^3$ program with a high tolerance of $1\times10^{-8}$ for the SCF convergence and a global cut-off of 3.7 Å. This was for comparisons with the Ppy@COF.

***The HOMO-LUMO gaps*** of the COF and the Ppy@COF and other substructures such as the pyrrole dimers, chain were all calculated using the DMOL$^3$ program. For these, a Norm-conserving pseudopotentials with a plane wave basis cut-off of 500 eV was employed and the B3LYP functional was used. Electronic minimizations were achieved using an All 41 Bands/EDFT algorithm. All calculations were performed on the unit cell.

***We calculated the band-gap of the COF and the poly@COF*** using the DFTB package built within the MS package. For these, a Norm-conserving pseudopotentials with a plane wave basis cut-off of 500 eV was employed and the Universal Force Field was used. Only the energy was optimized. Electronic minimizations were achieved using an All 41 Bands/EDFT algorithm. All calculations were performed on the unit cell. The gradient-corrected exchange correlation were applied using the Generalized Gradient Approximation (GGA) and Perdew-Wang 91 (PW91) functional. A DFT-D correction was applied; a Global scheme was used for the orbital cut-off (5.1 Å) with a SCF tolerance of 1x e-006. A smearing parameter of 0.01 Ha was applied. In our opinion, the calculation could be displaying the best-case scenario by overestimating the electrostatics. Nonetheless, it is pointing in the right direction.

# Chapter 4

# Sulphonated Covalent Organic Framework For Solid State Li Ion Conduction

## 4.1 Introduction

Because of the revolutionary usage of covalent organic frameworks (COFs) as electrolytes, recent developments in energy storage have resulted in the introduction of cutting-edge solid-state batteries that are endowed with the capability to be folded.[1,2] In particular, the kinetics of ion transport have been a persistent problem with conventional ceramic and polymer electrolytes. These state-of-the-art batteries represent a considerable divergence from the traditional issues that solid-state batteries have been grappling with for a long time. This research presents a novel and cutting-edge variation of solid-state batteries that display remarkable ionic conductivity, ease of manufacture, and mechanical flexibility. This is accomplished by incorporating COF-based electrolytes into the architecture of the battery.

There is a lot of excitement surrounding solid-state batteries (SSBs) that use lithium-metal anodes because of their promise to provide high safety and energy density, which is essential for the next generation of energy storage devices. In order for these batteries to be successful, it is necessary to design high-performance ionic conductors for solid-state electrolytes (SSEs). Due to their capacity to dissolve lithium salts at elevated temperatures and to offer adaptive interfacial contact with electrodes, solid polymer electrolytes (SPEs) have traditionally been regarded to be prospective possibilities. In particular, ether-based polymers have been considered to be particularly promising.[3-6]

Increasing the conductivity of lithium ions has been accomplished through the utilisation of a method that involves the incorporation of ceramic single-ion conductors (SICs) into solid polymer electrolytes (SPEs). Polymer-ceramic composite electrolytes, also known as CPEs, are of great assistance in reducing the brittleness that is commonly observed in ceramic electrolytes. This brittleness frequently leads to inadequate interfacial lithium-ion transport and the production of dendrites at grain boundaries.[7-11] Despite the fact that several composite electrolytes have been investigated ever since their birth in 1981, it is still difficult to strike a balance between ionic conduction, transference number, and mechanical strength. There is a tendency for a higher SIC content in CPEs to decrease their mechanical toughness. Furthermore, the lithium-ion conductivity at ambient temperature seldom exceeds $10^{-4}$ S cm$^{-1}$. This is because the conductivity enhancements are primarily localised to the interface rather than being disseminated across the majority of the hybrid electrolyte.[12,13] Furthermore, in order to achieve the required structural integrity, a large thickness is required. This thickness has a negative impact on the conductance of lithium ions and the specific energy of the cells. For this reason, it is abundantly clear that pioneering approaches to the development of solid-state ionic conductors that possess balanced properties are absolutely necessary in order to fulfil the requirements of future batteries.

In this chapter, we propose a design approach for solid-state Li+ conductors that involves utilising solvating structural channels and separating Li+ from polymer segments. Initially, we showcase this method by employing electrolytes to mediate in ionic covalent organic frameworks (COFs). COFs,

which are chemically synthesised using periodic organic building units, exhibit exceptional stability and possess persistent pore channels.[14-18] We have discovered a novel liquid electrolyte called DMA@LiTFSI, which consists of a 2 M of lithiumbis(trifluoromethanesulfonyl)imide (LiTFSI) dissolved in dimethylacrylamide (DMA). Additionally, it was found that the presence of lithium salt can initiate the copolymerization of DMA solvent, resulting in the formation of a polymer electrolyte with exceptional flexibility. Building upon the observed conversion behaviour, we strategically incorporated the DMA@LiTFSI solution into the pores of a LiCOF material, and then initiated polymerization in that environment. Within the COF channels, the functional groups of flexible DMA chains have the ability to liberate $Li^+$ ions from the rigid COF backbone while also separating the lithium salt. The modified pore environment significantly enhanced the orderly transport of Li+ ions. The DMA@LiTFSI-mediated COF (DLC) electrolyte demonstrated a much higher solid-state ionic conductivity of $1.5 \times 10^{-3}$ S cm$^{-1}$ and a high $t_{Li}$+ value of 0.90 at room temperature.[19-26]

## 4.2 Results and Discussion

### 4.2.1 Synthesis of lithiated COF (Li@COF)

The S-COF was initially synthesized through a condensation reaction between the monomers. Tr (0.6 mmol) and Pa-SO3H (0.9 mmol) were introduced into a Pyrex tube containing 6 mL of a 1,4-dioxane/mesitylene solvent mixture (4:1 volume ratio) and 1.2 mL of 6 M acetic acid. After sonication for 10 minutes, the mixture was flash-frozen, then heated at 120 °C for 5 days. The resulting product was purified by washing with tetrahydrofuran, deionized water, and ethanol, followed by vacuum drying at 120 °C. The prepared S-COF was subsequently stirred with an excess of 3 M aqueous lithium acetate solution at 50 °C for 3 days. The lithiated product, Li@S-COF, was obtained by thoroughly washing with ultrapure water (70 °C) and vacuum drying.
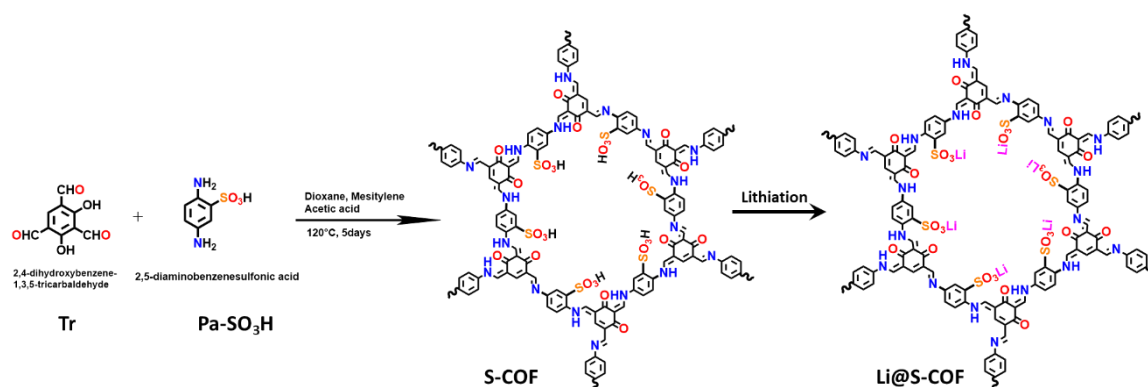


and its lithiation to form Li@S-COF.

The single-ionic-conducting COF (Scheme 4.1) was created by lithiating a standard S-COF, which itself was synthesized through a Schiff-base condensation reaction between 1,3,5-triformylresorcinol and 1,4-phenylenediamine-2-sulfonic acid. This lithiated version of the S-COF is referred to as Li@S-COF. The chemical structure of Li@S-COF is illustrated in Scheme 4.1 and confirmed in Figures XX.
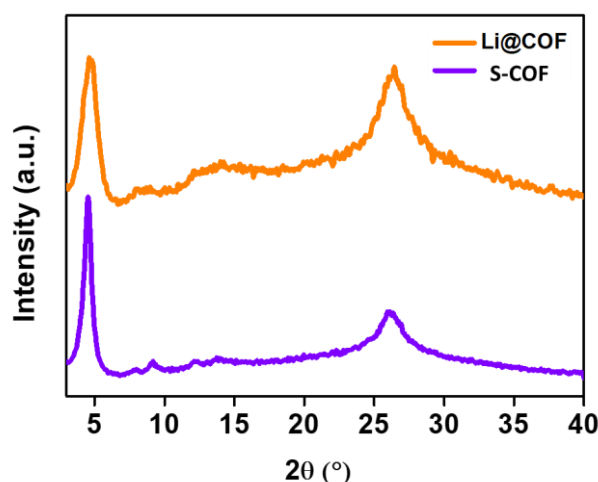


**Figure 4.1:** Comparative PXRD patterns of as made S-COF and Li@S-COF.

### 4.2.2 Charecterisation of S-COF and Li@S-COF

Powder X-ray diffraction (PXRD) analysis (Figure 4.1) shows a significant level of crystalline structure, indicated by diffraction peaks at 2θ = 4.54° and 26.16°, corresponding to the (100) and (001) planes, respectively.
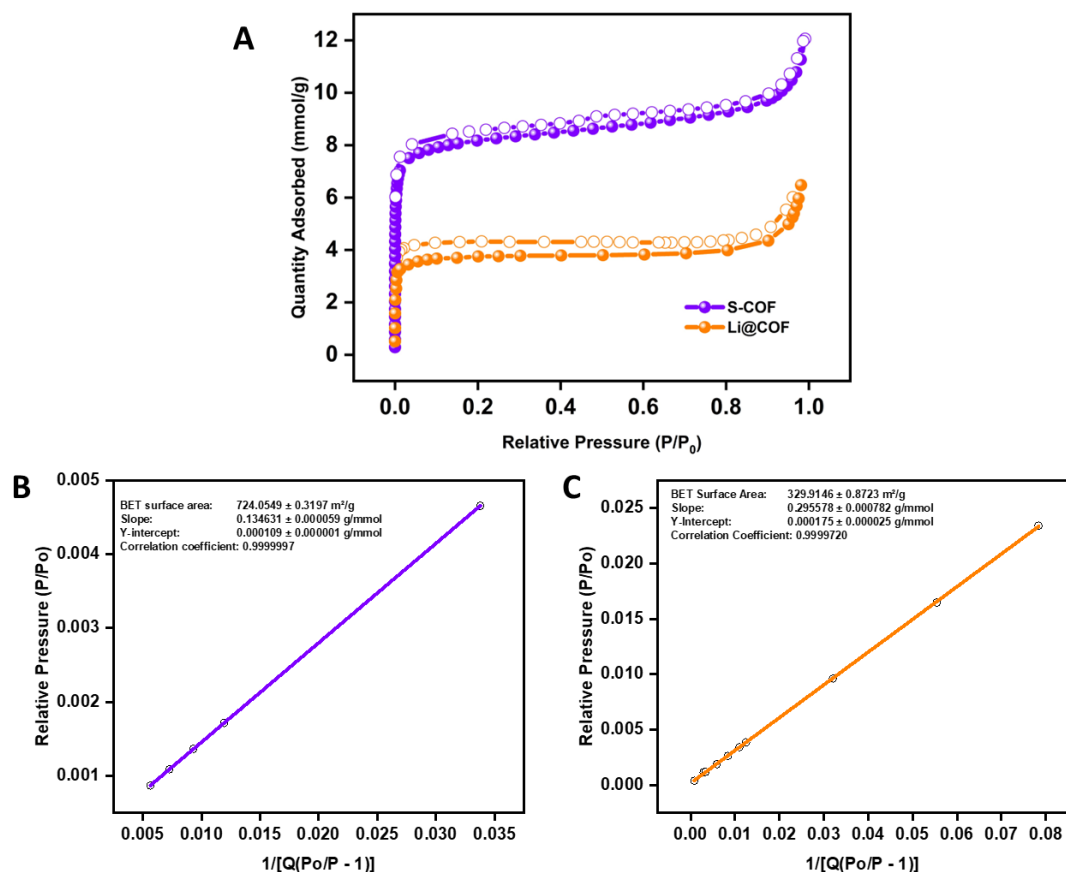


**Figure 4.2:** (A) A nitrogen 77 K adsorption–desorption isotherm. (B) A BET fit obtained using the low-pressure region data of the N2 adsorption isotherm of S-COF. (C) A BET fit obtained using the low-pressure region data of the N2 adsorption isotherm of Li@S-COF.

It was determined through the use of N2 sorption isotherms that Li$^+$ ions were incorporated into the S-COF. Initially, the S-COF displayed a surface area (SBET) of 724 m$^2$ g$^{-1}$, which is a high value according to the Brunauer–Emmett–Teller measurements. On the other hand, when loaded with 40 wt% DMA@LiTFSI, this SBET value dropped to 330 m$^2$ g$^{-1}$. It appears that the COF pores are gradually being filled, as indicated by the decrease in SBET.

The Li@S-COF powder was analysed using field emission scanning electron microscopy (FE-SEM), which disclosed a spherical morphology with the presence of micro-bubbles on the surface. HRTEM photos, obtained at different resolutions, illustrate the arrangement of layers in the COF flakes and the process of these flakes coming together to form thicker sheets through self-assembly (Figure 4.3).

The crystallinity of the COF flakes in all batches was confirmed by examining their lattice fringes and
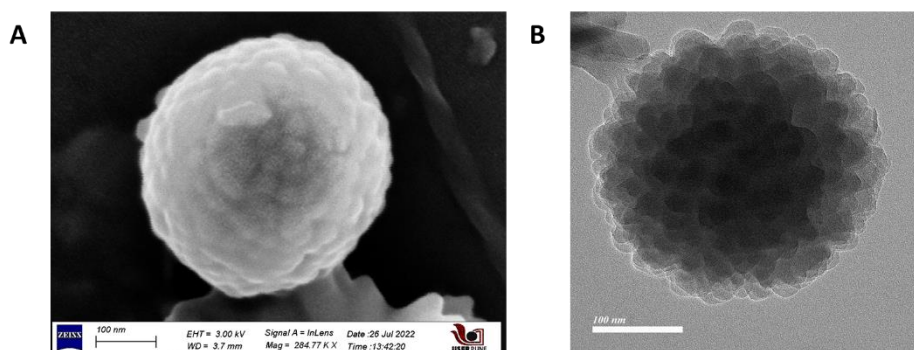


**Figure 4.3:** (A) FESEM and (B) HRTEM image of Li@S-COF showing thin layers and wrapped-up flakes forming spherical balls.**Scheme 4.1:** Schematic showing synthesis of S-COF

capturing the selected area electron diffraction (SAED) pattern from the identical flakes (Figures 4.4).

Figure 4.4A displays in-plane pictures of a Li@S-COF flake, demonstrating consistently aligned lattice fringes across the whole flake, suggesting the development of massive, extremely crystalline flakes. Robust SAED diffraction patterns were consistently detected from several flakes of the Li@S-COF sample and flakes from different preparation batches. In addition, high-resolution transmission electron microscopy (HRTEM) shows that the aggregated flakes are formed by the layering of thick multi-layers that have micro sized hexagonal pores on the surface, as depicted in Figure 4.4C-D.
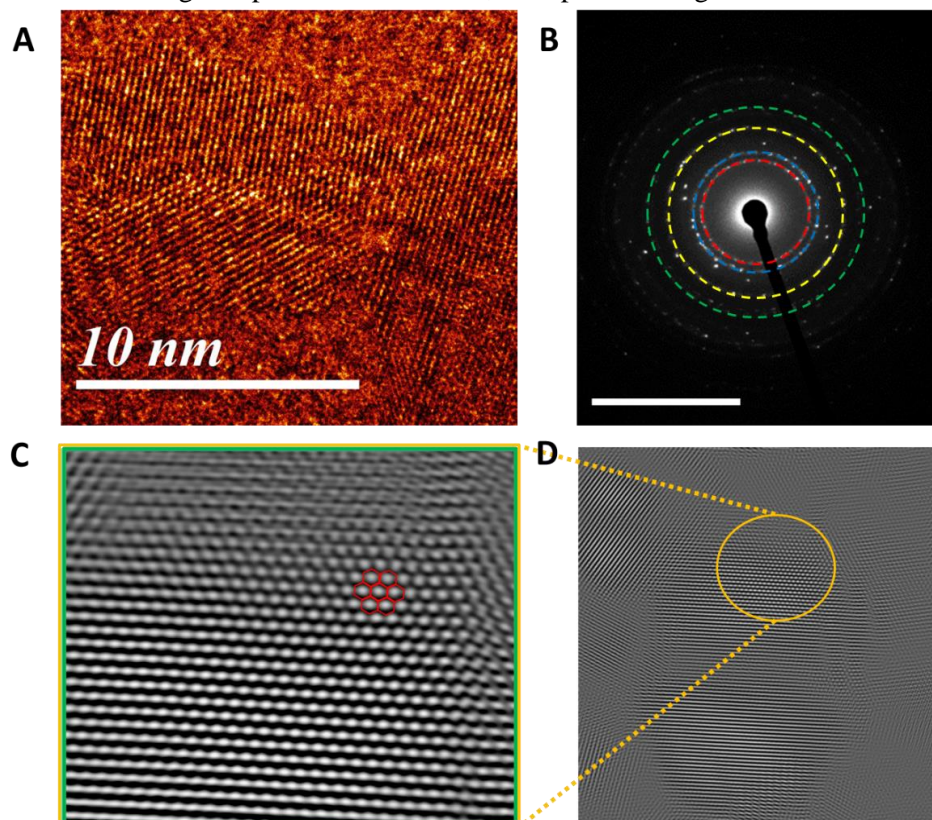


**Figure 4.4:** (A) A part of spherical particle shows the interlayer stacking of the COF. (B) SAED patterns of the COF observed for higher angle diffraction of the [00l] planes. (C-D) The big spheres of COF particles were opened up into constructing COF flakes by vigorous probe sonication in ethanolic dispersion of COF. The layer distances and hexagonal pores were detected well in these smaller flakes.

### 4.2.3 Conductivity studies of Li@S-COF powder

The lithium ion conductivity ($\sigma$) of the Li@S-COF was evaluated using electrochemical impedance spectroscopy over a frequency range of 1 Hz to 10 MHz with a Solartron Impedance Analyzer. The Li@S-COF was pelletized for this analysis. Conductivity measurements were performed three times on pellets with varying thicknesses (0.6 to 0.8 mm) and a diameter of 10 mm to ensure the consistency of the results. Each sample was equilibrated at a specific temperature without humidity for 2 hours prior to measurement. The lithium ion conductivity of the pellet was measured across a range of temperature from 25 °C to 150 °C (Figure 4.5 and Figure 4.6) and was calculated using the following equation.

$$\sigma\ (S\ cm-1) = \frac{l}{RA}$$
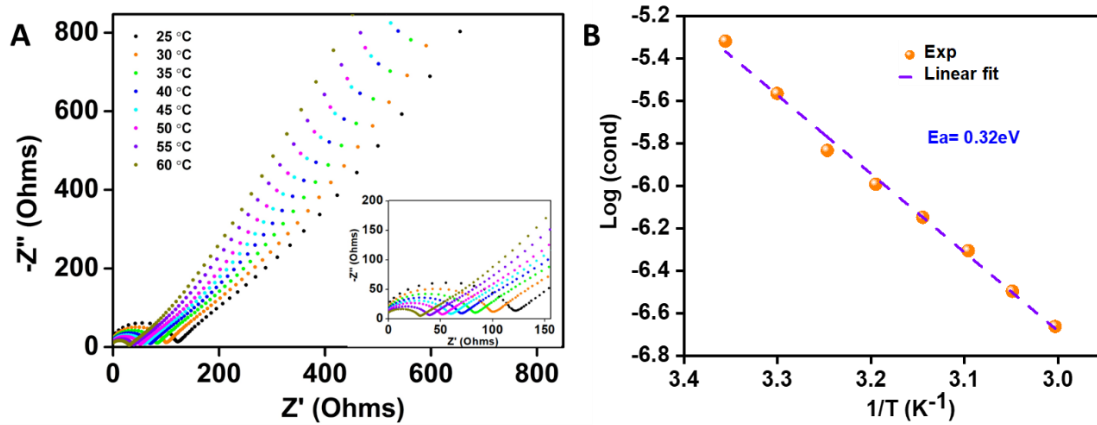


**Figure 4.5:** (A) Nyquist plots from the temperature-dependent conductivity measurements of Li@S-COF. (B) Arrhenius plots to investigate the activation energy of Li@S-COF at lower temperatures.

where l is the thickness of the pellet (cm), R is the resistance of the sample ($\Omega$) obtained from the x-axis intercept, and A is the cross-sectional area of the pellet ($cm^2$).
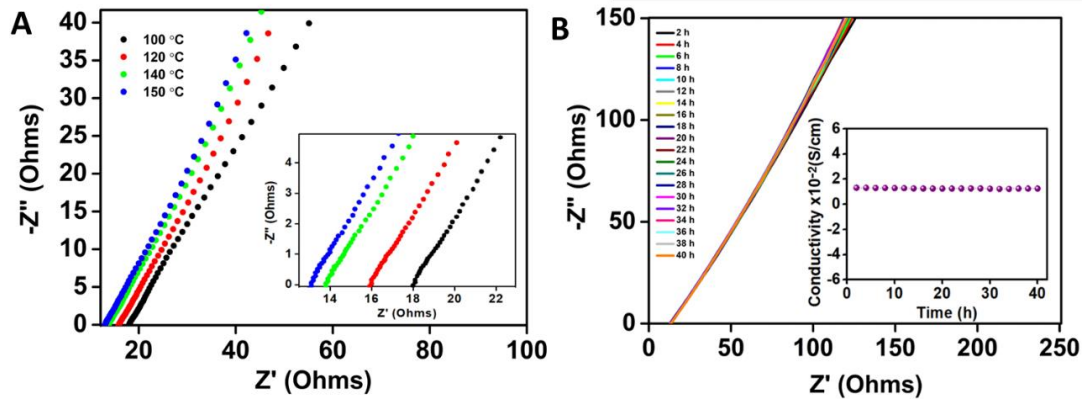


**Figure 4.6:** (A) Nyquist plots from the temperature-dependent conductivity measurements of Li@S-COF. (B) Nyquist plots of Li@S-COF recorded for 40 hours at 150°C, inset showing retention of conductivity over the time.

As the temperature increased, the Li+ conductivity of Li@S-COF showed a consistent rise, starting from $3.7 \times 10^{-4}$ S $cm^{-1}$ at 25 °C and reaching $8.6 \times 10^{-3}$ S $cm^{-1}$ at 150 °C. The activation energy (Ea) for Li$^+$ ion conduction in Li@S-COF was determined to be 0.39 eV from temperature-dependent Arrhenius plots (Figure 4.5B), indicating a notably low value. This suggests that Li@S-COF operates via the Grotthuss mechanism (Ea < 0.4 eV).

In addition, the Li$^+$ ion conductivity of Li@S-COF can be retained upon continuous run over 40 hours at 150 °C suggesting that high conductivity stability of Li@S-COF (Figure 4.6B). The Zview-4 software was used to fit the equivalent circuit for all Nyquist curves. Comparing the Nyquist plots of Li@S-COF at 25 °C and 150 °C, it is evident that the series and charge-transfer resistance are slightly greater for the plot recorded at 25 °C (R = 124 Ω) compared to the one recorded at 150 °C (R = 12.9 Ω) (Figure 4.7).
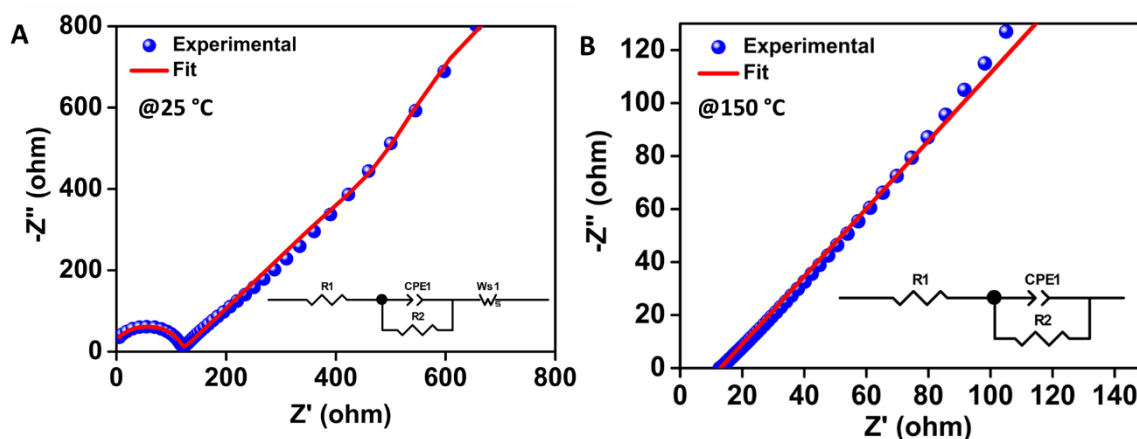


**Figure 4.7:** Equivalent circuit fitted for impedance plots of Li@S-COF recorded at (A) 25 °C and (B)150 °C.

### 4.2.4 Synthesis of DLC (**D**MA@**L**iTFSI_**C**OF) electrolyte

LiTFSI was dissolved in DMA solvent to create a 2 M electrolyte solution. The infiltration of this liquid electrolyte into the pores of Li@S-COF was achieved using a low-pressure-driven method. Initially, a specific amount of the electrolyte was added to the degassed Li@COF. The sample was then subjected to a vacuum for 2 hours to facilitate the electrolyte's infiltration and solidification within the COF channels, Subsequently, the DLC solid-state electrolyte is formed through thermal annealing at a temperature of 80 °C. The dried samples were subsequently pressed into a solid electrolyte film using a uniaxial hydraulic press, applying 3 tons of pressure at 120 °C for 1 hour.

The local chemical environments of Li@S-COF and DLC and were well studied with solid-state NMR, all the characteristics peaks were intact for monomers (112, 118 & 140 ppm for Pa-SO$_3$H and 178 ppm for Tr). The newly observed C-C chemical shift was measured at 33 ppm, providing confirmation of the successful conversion of DMA. Meanwhile, the characteristic C=O group of DMA exhibits resonance at 177 ppm in DLC. (Figure 4.8).
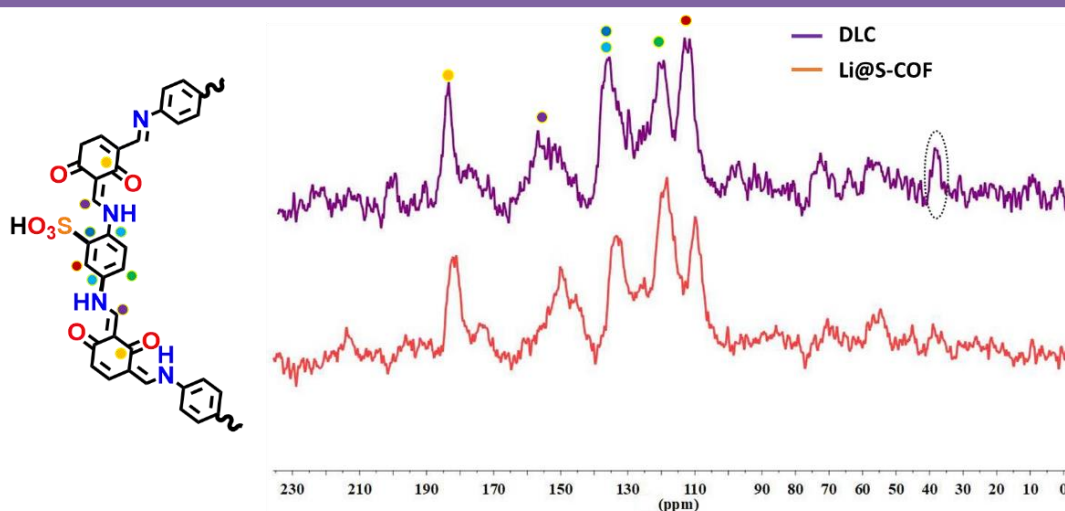
**Figure 4.8:** $^{13}$C NMR of the Li@S-COF and DLC electrolyte.

**4.2.5 Thermal stability and flexibility studies of DLC electrolyte**

The inclusion of flexible DMA@LiTFSI in the DLC allows it to endure different stress conditions like folding, twisting, and stretching (Figure 4.9). These mechanical properties are vital for preserving the integrity of the SSE/electrode interface, which typically undergoes significant volume changes. Furthermore, when compared to PP (Polypropylene) membranes, the DLC shows no noticeable dimensional shrinkage even at testing temperatures up to 200 °C, demonstrating outstanding chemical and thermal stability (Figure 4.9).



**Figure 4.9:** Thermal shrinkage of DLC and PP separator after heating at different temperatures for 60 min.

It is observed that DLC may be compressed into a thin (≈112 μm) and free of cracks membrane (Figure 4.10A) using a uniaxial hydraulic press (3 tonnes) at a temperature of 120 °C. On the other hand, bulk Li@S-COF powders can only be produced as a thick film, exceeding 140 μm, which clearly has empty spaces between particles (Figure 4.10B).
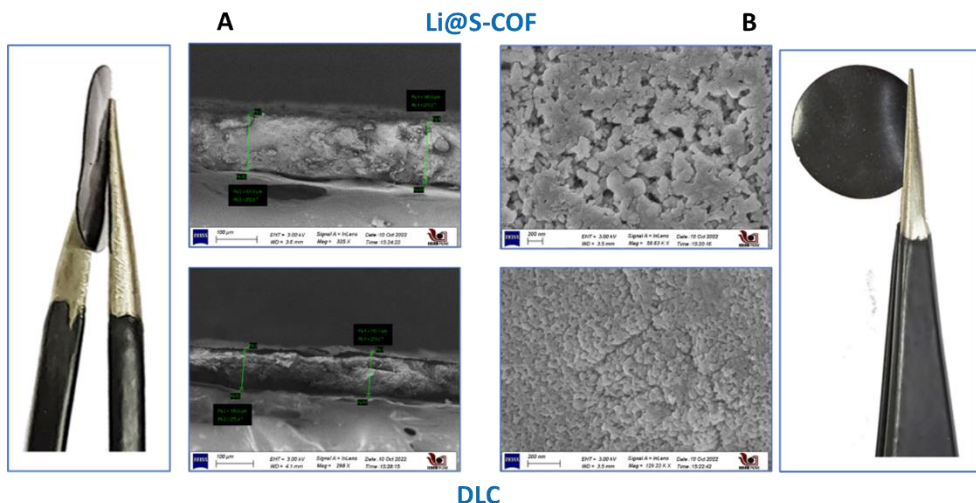
**Figure 4.10:** (A) Cross sectional FESEM images of the Li@S-COF and DLC electrolyte showing lowering of the thickness in case of DLC. (B )The top view of the Li@S-COF and DLC electrolyte revealing the reduction of grain boudaries on formation of the DLC electrolyte.

### 4.2.6 Electrochemical studies of DLC electrolyte

To enhance the efficiency of Li$^+$ transfer between particles and improve the mechanical characteristics of the solid electrolyte, the DMA@LiTFSI concentration in DLC was optimised at 40 wt%. The symmetric cell containing SS/DLC-x%/SS were pressed and subjechted to impedance analysis (x= 20, 40 and 60). The electrochemical performance of the DLC with varying DMA@LiTFSI loading is compared in the following analysis Figure 4.11.

The critical coupling of increased Li$^+$ concentration, favourable chemical environment, and ordered channels facilitates enhanced ionic conductivity (σ). Calculated from the plots in Figure 4.12, DLC has a σ of $1.5 \times 10^{-3}$ S cm$^{-1}$ (≈20 times that of Li@COF pellet) at 25 °C. The σ reaches $4.7 \times 10^{-3}$ S cm$^{-1}$
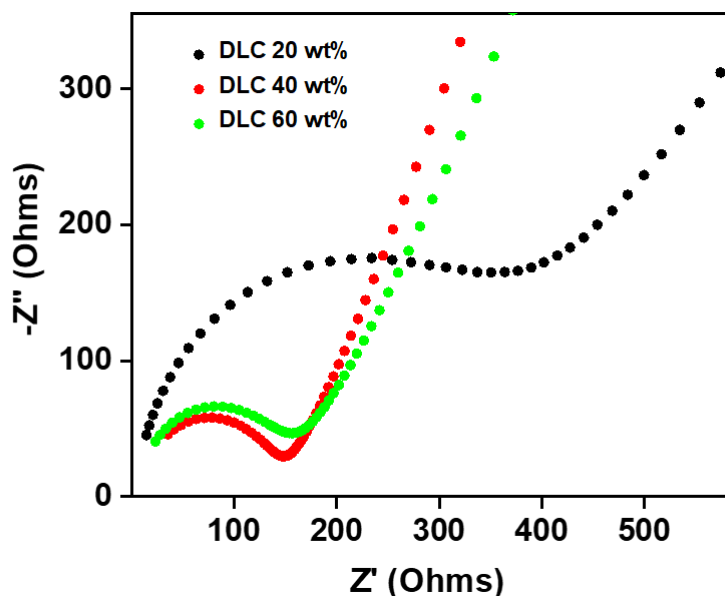


**Figure 4.11:** (a) Nyquist plots of the SS/DLC-20%/SS, SS/DLC-40%/SS, and SS/DLC60%/SS cells at 40 °C.

at 60 °C. Obviously, the Li$^+$ conductivity in DLC relies on the bulk phase transport within COF because it increases with the DMA@LiTFSI loading, as shown in Figure 4.12.
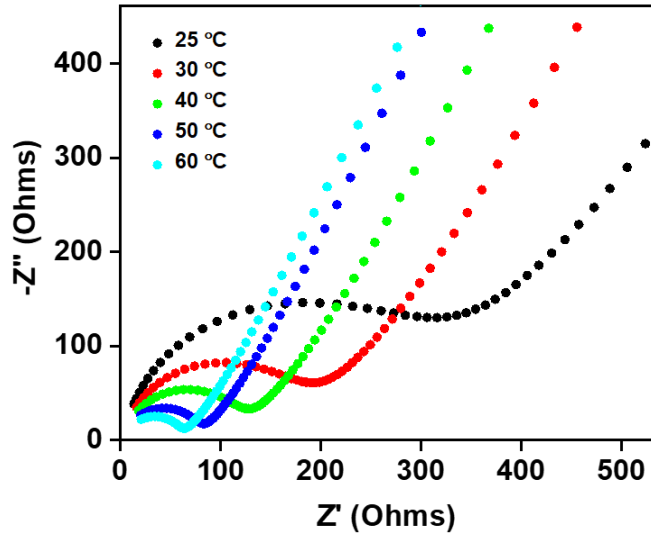


**Figure 4.12:** Temperature dependent Nyquist plots for SS/DLC-40%/SS showing improvement in Li+ ion conductivity up to 60 °C.

In addition, we conducted tests on the Li│DLC│Li symmetric cell to determine the lithium-ion transference number ($t_{Li}^+$). This value was obtained using the chronoamperometry method and calculated using the Vincent-Evans equation.

The variables $I_0$ and Is represent the initial and steady-state currents, respectively. $\Delta V$ refers to the potential applied across the cell. $R_0$ and Rs represent the initial and steady-state interfacial resistances of the passivation layers on the Li electrode.

$$t_+ = \frac{I_{ss}(\Delta V - I_0 R_0)}{I_0(\Delta V - I_{ss} R_{ss})}$$

Figure 4.13B displays the impedance spectra and the time-dependent response of DC polarisation for the DLC. The Li$^+$ ion transference numbers for the DLC were determined by comparing the initial and final current values, resulting in a computed value of 0.90. This number is deemed satisfactory in comparison to the value given in the literature and is deemed appropriate for future implementation of the DLC. The high lithium transference number of the DLC is likely due to the decrease in the distance between two Li$^+$ ions in the DLC electrolyte.
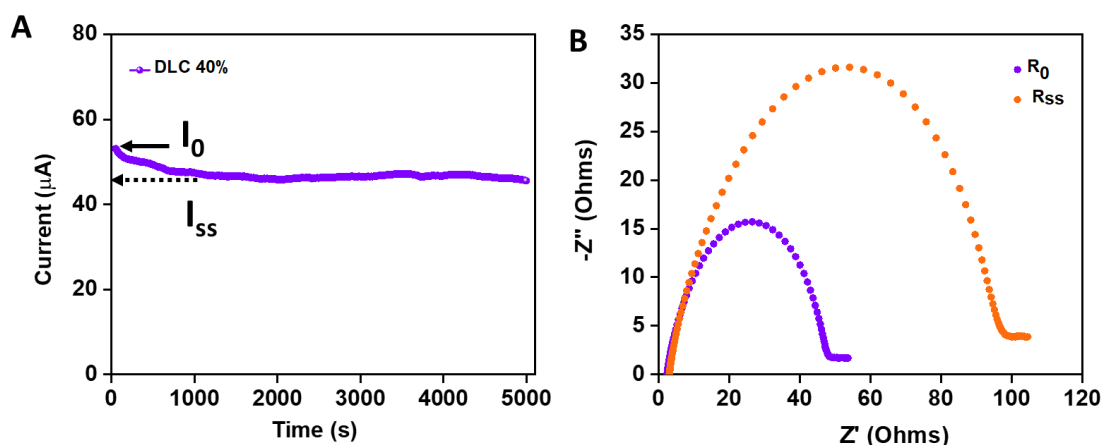
**Figure 4.13:** (A) Chronoamperometry of Li|DLC-40%|Li symmetric cell. (B) the corresponding Nyquist plots before and after polarization.

## 4.3 Conclusion

In conclusion, a single-ionic-conducting covalent organic framework (COF), Li@S-COF, was successfully synthesized through a Schiff-base condensation reaction followed by lithiation with a lithium acetate solution. The lithiation process resulted in a highly crystalline material with a BET surface area of 330 m$^2$ g$^{-1}$. The Li@S-COF exhibited good lithium-ion conductivity (3.7 x 10$^{-4}$ S cm$^{-1}$ at 25 °C), which increased significantly with temperature (8.6 x 10$^{-3}$ S cm$^{-1}$ at 150 °C) and showed excellent stability over 40 hours at 150 °C. Furthermore, by incorporating DMA@LiTFSI into the Li@S-COF, a composite solid-state electrolyte (DLC) was fabricated. The DLC displayed enhanced ionic conductivity (1.5 x 10$^{-3}$ S cm$^{-1}$ at 25 °C), superior mechanical flexibility, and outstanding thermal stability with no dimensional shrinkage even at 200 °C. Importantly, the DLC achieved a high lithium transference number of 0.90, indicating efficient Li$^+$ ion transport. This study highlights the potential of Li@S-COF and its derivatives (like DLC) as high-performance solid-state electrolytes candidate for solid-state lithium batteries.

## 4.4 References

1. A. Manthiram, X. Yu, S. Wang, Nat. Rev. Mater. 2017, 2, 16103.

2. Y. Zheng, Y. Yao, J. Ou, M. Li, D. Luo, H. Dou, Z. Li, K. Amine, A. Yu, Z. Chen, Chem. Soc. Rev. 2020, 49, 8790.

3. C. Yang, Q. Wu, W. Xie, X. Zhang, A. Brozena, J. Zheng, M. N. Garaga, B. H. Ko, Y. Mao, S. He, Y. Gao, P. Wang, M. Tyagi, F. Jiao, R. Briber, P. Albertus, C. Wang, S. Greenbaum, Y. Y. Hu, A. Isogai, M. Winter, K. Xu, Y. Qi, L. Hu, Nature 2021, 598, 590.

4. K. M. Diederichsen, E. J. McShane, B. D. McCloskey, ACS Energy Lett. 2017, 2, 2563.

5. D. G. Mackanic, X. Yan, Q. Zhang, N. Matsuhisa, Z. Yu, Y. Jiang, T. Manika, J. Lopez, H. Yan, K. Liu, X. Chen, Y. Cui, Z. Bao, Nat. Commun. 2019, 10, 5384.

6. X. Yu, A. Manthiram, Energy Storage Mater. 2021, 34, 282.

7. S. Randau, D. A. Weber, O. Kötz, R. Koerver, P. Braun, A. Weber, E. Ivers-Tiffée, T. Adermann, J. Kulisch, W. G. Zeier, F. H. Richter, J. Janek, Nat. Energy 2020, 5, 259.

8. M. Balaish, J. C. Gonzalez-Rosillo, K. J. Kim, Y. Zhu, Z. D. Hood, J. L. M. Rupp, Nat. Energy 2021, 6, 227.

9. Z. Gao, H. Sun, L. Fu, F. Ye, Y. Zhang, W. Luo, Y. Huang, Adv. Mater. 2018, 30, 1705702.

10. J. Zhang, N. Zhao, M. Zhang, Y. Li, P. K. Chu, X. Guo, Z. Di, X. Wang, H. Li, Nano Energy 2016, 28, 447.

11. Y. Ren, Z. Cui, A. Bhargav, J. He, A. Manthiram, Adv. Funct. Mater. 2021, 32, 2106680.

12. W.-P. Chen, H. Duan, J.-L. Shi, Y. Qian, J. Wan, X.-D. Zhang, H. Sheng, B. Guan, R. Wen, Y.-X. Yin, S. Xin, Y.-G. Guo, L.-J. Wan, J. Am. Chem. Soc. 2021, 143, 5717.

13. S. Tang, W. Guo, Y. Fu, Adv. Energy Mater. 2020, 11, 2000802.

14. J. Li, X. Jing, Q. Li, S. Li, X. Gao, X. Feng, B. Wang, Chem. Soc. Rev. 2020, 49, 35652.

15. K. Jeong, S. Park, G. Y. Jung, S. H. Kim, Y. H. Lee, S. K. Kwak, S. Y. Lee, J. Am. Chem. Soc. 2019, 141, 5880.

16. C. Niu, W. Luo, C. Dai, C. Yu, Y. Xu, Angew. Chem., Int. Ed. 2021, 60, 24915.

17. J. Kim, A. Elabd, S.-Y. Chung, A. Coskun, J. W. Choi, Chem. Mater. 2020, 32, 4185.

18. X. Li, H. Wang, Z. Chen, H. S. Xu, W. Yu, C. Liu, X. Wang, K. Zhang, K. Xie, K. P. Loh, Adv. Mater. 2019, 31, 1905879.

19. X. Wu, Y. L. Hong, B. Xu, Y. Nishiyama, W. Jiang, J. Zhu, G. Zhang, S. Kitagawa, S. Horike, J. Am. Chem. Soc. 2020, 142, 14357.

20. K. Dey, M. Pal, K. C. Rout, H. S. Kunjattu, A. Das, R. Mukherjee, U. K. Kharul, R. Banerjee, J. Am. Chem. Soc. 2017, 139, 13083.

21. Z. Shan, M. Wu, Y. Du, B. Xu, B. He, X. Wu, G. Zhang, Chem. Mater. 2021, 33, 5058.

22. Y. Kong, X. He, H. Wu, Y. Yang, L. Cao, R. Li, B. Shi, G. He, Y. Liu, Q. Peng, C. Fan, Z. Zhang, Z. Jiang, Angew. Chem., Int. Ed. 2021, 60, 17638.

23. D. Guo, F. Ming, D. B. Shinde, L. Cao, G. Huang, C. Li, Z. Li, Y. Yuan, M. N. Hedhili, H. N. Alshareef, Z. Lai, Adv. Funct. Mater. 2021, 31, 2101194.

24. Z. Cheng, M. Xie, Y. Mao, J. Ou, S. Zhang, Z. Zhao, J. Li, F. Fu, J. Wu, Y. Shen, D. Lu, H. Chen, Adv. Energy Mater. 2020, 10, 1904230.

25. M. A. Khayum, M. Ghosh, V. Vijayakumar, A. Halder, M. Nurhuda, S. Kumar, M. Addicoat, S. Kurungot, R. Banerjee, Chem. Sci. 2019, 10, 8889.

26. X. Li, K. P. Loh, ACS Mater. Lett. 2019, 1, 327.

**First author (*Included in thesis*)**

1. **<u>Rase, D</u>**.; Illathvalappil, R.; Singh, H. D.; Shekhar, P.; Leo, L. S.; Chakraborty, D.; Haldar, S.; Shelke, A.; Ajithkumar, T. G.; Vaidhyanathan, R., Hydroxide ion-conducting viologen–bakelite organic frameworks for flexible solid-state zinc–air battery applications. Nanoscale Horizons 2023, 8, 224-234.

2. **<u>Rase, D.</u>**; Manna, N.; Kushwaha, R.; Jain, C.; Singh, H. D.; Shekhar, P.; Singh, P.; Singh, Y. K.; Vaidhyanathan, R., Designed Enhancement in Hydroxide Ion Conductivity of Viologen-Bakelite Organic Frameworks for Flexible Rechargeable Zinc-Air Battery. Chem. Sci. 2024.

3. Haldar, S.[†]; **<u>Rase, D.</u>**[†]; Shekhar, P.; Jain, C.; Vinod, C. P.; Zhang, E.; Shupletsov, L.; Kaskel, S.; Vaidhyanathan, R., Incorporating Conducting Polypyrrole into a Polyimide COF for Carbon-Free Ultra-High Energy Supercapacitor. Adv. Energy Mater. 2022, 12, 2200754. (**[†]co-first authors**)

**Co-authored**

4. Haldar, S.; Kaleeswaran, D.; **Rase, D.**; Roy, K.; Ogale, S.; Vaidhyanathan, R., Tuning the electronic energy level of covalent organic frameworks for crafting high-rate Na-ion battery anode. Nanoscale Horizons 2020, 5, 1264-1273.

5. Singh, H. D.; Singh, P.; **Rase, D.**; Vaidhyanathan, R., Pore volume regulated $CO_2$ adsorption in C–C bonded porous organic frameworks. Mater. Adv. 2023, 4, 3055-3060.

6. Kushwaha, R.; Jain, C.; Shekhar, P.; **Rase, D.**; Illathvalappil, R.; Mekan, D.; Camellus, A.; Vinod, C. P.; Vaidhyanathan, R., Made to Measure Squaramide COF Cathode for Zinc Dual-Ion Battery with Enriched Storage via Redox Electrolyte. Adv. Energy Mater. 2023, 13, 2301049.

7. Singh, H. D.; Singh, P.; Vysyaraju, R.; Balasubramaniam, B. M.; **Rase, D.**; Shekhar, P.; Jose, A.; Rajendran, A.; Vaidhyanathan, R., Unlocking the Separation Capacities of a 3D-Iron-Based Metal Organic Framework Built from Scarce Fe4O2 Core for Upgrading Natural Gas. Chem. Mater. 2023, 35, 8261-8271.

8. Jain, C.; Kushwaha, R.; **Rase, D.**; Shekhar, P.; Shelke, A.; Sonwani, D.; Ajithkumar, T. G.; Vinod, C. P.; Vaidhyanathan, R., Tailoring COFs: Transforming Nonconducting 2D Layered COF into a Conducting Quasi-3D Architecture via Interlayer Knitting with Polypyrrole. J. Am. Chem. Soc. 2023, 146, 487-499.

9. Chandran, C.; Singh, H. D.; Leo, L. S.; Shekhar, P.; **Rase, D.**; Chakraborty, D.; Vinod, C. P.; Vaidhyanathan, R., A covalent organic framework with electrodeposited copper nanoparticles–a desirable catalyst for the Ullmann coupling reaction. J. Mater. Chem. A 2022, 10, 15647-15656.

10. Shekhar, P.; Kosugi, K.; Singh, H. D.; Kushwaha, R.; **Rase, D.**; Matsuzaki, T.; Jain, C.; Singh, P.; Singh, Y.; Vinod, C. P.; Kondo, M.; Masaoka, S.; Vaidhyanathan, R., Resorcinol-Azodianiline COF Supported FeOOH QDs Catalyzed Electrochemical Ammonia Synthesis Under Ambient Conditions. Chem. Mater. 2024. ***Just accepted***

**IISER PUNE**

Rase Deepak <rase.deepak@students.iiserpune.ac.in>

## RE: Request for permission to reuse two of my articles published with RSC publication.

2 messages

**CONTRACTS-COPYRIGHT (shared)** <Contracts-Copyright@rsc.org>          Thu, Jul 4, 2024 at 6:50 AM
To: "rase.deepak@students.iiserpune.ac.in" <rase.deepak@students.iiserpune.ac.in>

Dear Deepak Rase

The Royal Society of Chemistry (RSC) hereby grants permission for the use of your paper(s) specified below in the printed and microfilm version of your thesis. You may also make available the PDF version of your paper(s) that the RSC sent to the corresponding author(s) of your paper(s) upon publication of the paper(s) in the following ways: in your thesis via any website that your university may have for the deposition of theses, via your university's Intranet or via your own personal website. We are however unable to grant you permission to include the PDF version of the paper(s) on its own in your institutional repository. The Royal Society of Chemistry is a signatory to the STM Guidelines on Permissions (available on request).

Please note that if the material specified below or any part of it appears with credit or acknowledgement to a third party then you must also secure permission from that third party before reproducing that material.

Please ensure that the thesis includes the correct acknowledgement (see http://rsc.li/permissions for details) and a link is included to the paper on the Royal Society of Chemistry's website.

Please also ensure that your co-authors are aware that you are including the paper in your thesis.

Best wishes

Becky